Pyrolysed Carbon Scaffold for Bioelectrochemistry in Life Science

Amato, Letizia

Publication date:
2013

Document Version
Publisher's PDF, also known as Version of record

Pyrolysed Carbon Scaffolds for Bioelectrochemistry in Life Science

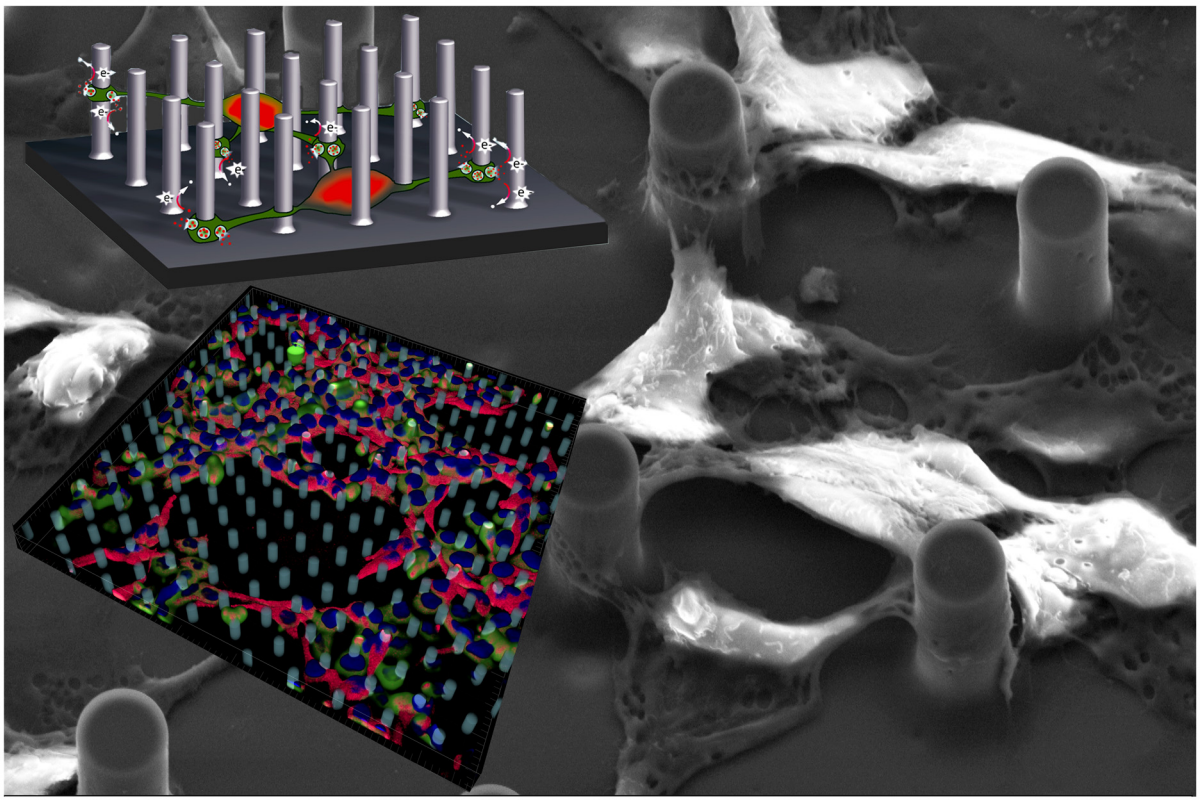

Letizia Amato

Ph. D. Thesis

December, 2013

Department of Micro- and Nanotechnology

Abstract

The research carried out in this thesis aimed to develop two-dimensional (2D) and three-dimensional (3D) carbon-based micro –and nano- electrodes to improve the electrochemical measurements in a wide range of applications. These electrode structures can, for instance, be used to run measurements on cells or as a part of the bio-fuel cells. Specifically, the research has focused on three distinct but interrelated areas: (1) The fabrication of 2D and 3D of carbon -based micro -and nano- electrodes and the characterization of their physical, electrical and electrochemical properties. (2) The surface treatment of these electrode structures to enhance their electrochemical performance, but also to make it possible to change the electrode surface properties so that small or large chemical / biological molecules can be attached onto them, e.g. for bio-sensors that may be developed, or to make them more compatible with cell biological applications (biocompatibility). (3) The study and application of functionalized 3D carbon electrodes for measuring the neurotransmitter dopamine emitted from neurons derived- stem cells that are clinically relevant in research on Parkinson's disease.

Résumé

Forskningen som er udført i denne afhandling havde til formål at udvikle todimensionelle (2D) og tredimensionelle (3D) kulstof baserede mikro- og nanoelektroder for at forbedre elektrokemiske målinger i en lang række af applikationer. Disse elektrodestrukturer kan f.eks. bruges for at lave målinger direkte på celler eller som en del af biobrændselsceller. Konkret har forskningen haft fokus på tre forskellige men indbyrdes afhængige områder: (1) Fabrikationen af 2D- og 3D kulstofs baserede mikro- og nanoelektroder og undersøgning af deres fysiske, elektriske og elektrokemiske egenskaber. (2) Overfladebehandling af disse elektrodestrukturer for at forbedre deres elektrokemiske præstation, men også for gøre det muligt at forandre elektrodernes overfladeegenskaberne så at små eller store kemiske/biologiske molekyler kan bindes fast på dem, f. eks for at biosensorer kan konstrueres, eller for at de skal blive mere kompatible med cellebiologiske applikationer (biokompatibilitet). (3) Undersøgelse og anvendelse af overfladebehandlede 3D kulstofelektroder til måling af neurotransmittorn dopamin som afgives fra neurale stamceller som er klinisk relevante indenfor forskning omkring Parkinson's sygdom

Contents

List of Publications, Submitted Papers and Manuscripts

Paper I. Fabrication of high-aspect ratio SU-8 micropillar arrays. Letizia Amato, Stephan S. Keller, Arto Heiskanen, Maria Dimaki, Jenny Emnéus, Anja Boisen, and Maria Tenje, *Microelectronic Engineering* 98 (2012) 483–487.

Paper II. Dense High-Aspect Ratio 3D Interdigitated Carbon Pillar Microelectrode Arrays. Letizia Amato, Arto Heiskanen, Rasmus Hansen, Maria Tenje, Lauge Gammelgaard, Tomas Rindzevicius, Anja Boisen, Jenny Emnéus, and Stephan S. Keller. *Manuscript*.

Paper III. Tailoring the Surface of 2D and 3D Pyrolysed Carbon Structures Using Plasma Treatment and Electrochemical Reduction of an Aryl Diazonium Compound for Bioelectrochemistry. Letizia Amato, Arto Heiskanen, Niels Bent Larsen, Anja Boisen, Stephan Sylvest Keller, and Jenny Emnéus. *Manuscript.*

Paper IV. Conducting 3D-carbon Scaffolds for Enhanced Differentiation of Neural Stem Cells and Dopamine Detection. Letizia Amato, Arto Heiskanen, Claudia Caviglia, Fozia Shah, Kinga Zór, Maciej Skolimowski, Marc Madou, Lauge Gammelgaard, Rasmus Hansen, Emma G. Seiz, Milagros Ramos, Tania Ramos Moreno, Alberto Martínez-Serrano, Anja Boisen, Stephan S. Keller, and Jenny Emnéus. *Submitted.*

My Contribution to the Papers

Paper I. I designed, planned, and performed the experiments. I evaluated the result and had a major contribution in writing the manuscript.

Paper II. I took major part in the design of experiments, carried out most of the experimental work and the evaluation of the results, and had a major contribution in writing the manuscript.

Paper III. The idea of this paper was initiated by me. I did most of the experimental design and experimental work. I also had a major contribution to the evaluation of the results and writing the paper.

Paper IV. I had a major contribution to this paper; work included: design and fabrication of the microelectrodes, planning, design and execution of the experiments, evaluation of the results and drafting the manuscript.

Other Publications not Included in This Thesis:

Pyrolyzed Photoresist Electrodes for Integration in Microfluidic Chips for Transmitter Detection from Biological Cells. Simon Tylsgaard Larsen, Aikaterini Argyraki, Letizia Amato, Simone Tanzi, Stephan S. Keller, Noemi Rozlosnik, Rafael J.Taboryski. *ECS Electrochemistry Letters*, 2 (2013), B5-B7.

Compact potentiostat for cellular electrochemical imaging with 54 parallel channels. Marco Vergani, Marco Carminati, Giorgio Ferrari, Marco Sampietro, Letizia Amato, Arto Heiskanen, Maria Dimaki, Winnie Edith Svendsen, Jenny Emnéus. *Proceedings of IEEE Biomedical Circuits and Systems Conference* (2012).

Titanium tungsten coatings for bioelectrochemical applications. Rafal Wierzbicki, Letizia Amato, Joanna Łopacińska, Arto Heiskanen, Jenny Emnéus, Maria Tenje, Michael Stenbæk Schmidt, Peter Bøggild, Kristian Mølhave, Alison Downard, Keith Baronian. *Technical Proceedings of the 2011 NSTI Nanotechnology Conference and Expo*, Vol. 3 Nano Science and Technology Institute (2011) 252-255.

Chapter 1

Introduction

Conductive substrates and scaffolds (e.g. based on metal[1,2], carbon[3–5], conductive polymers[6],etc.) offer the possibility for electrical sensing, and can thus provide a micro-environment for real-time monitoring of cell population dynamics[7]. Several methodologies have enabled fabrication of two-dimensional (2D) and three-dimensional **(**3D) electrodes. However, fabrication of 2D and especially 3D electrodes still poses limitations for high-throughput, reproducibility, and large-scale production, which are very important for both fundamental and more application-oriented studies. For instance, 3D metal electrodes may require complex processing and the use of expensive metal electroplating, sputtering or evaporation equipment, which often restrict high-yields and could result in more expensive electrodes, not amenable for mass-production[8,9]. Additionally, microfabricated electrodes using e.g. noble metals can only operate in a limited electrochemical potential window[10–12] and are prone to fouling[13,14], thus restricting their electrochemical applications. For these reasons, carbonaceous materials[15] such as graphene, graphene foam[16], CNTs, diamond-like carbon[17], carbon composites[18] and pyrolysed carbon are emerging for development of 2D and 3D electrodes. The carbon MEMS technique is a very simple, high-yield, and cost-effective method for electrode fabrication, and consists of heat treatment of a patterned polymer in presence of inert atmosphere, leading to production of pyrolysed carbon electrodes[19]. This process enables easy and reproducible fabrication of 2D and 3D carbon electrodes with novel custom-made designs and unique sensitivities, and may even be suitable for mass production. Pyrolysed carbon electrodes exhibit a wide electrochemical potential window[11,12], chemical inertness towards a range of solvents and electrolytes[20], good biocompatibility[21], and the possibility to tune the electrical[22–24] and mechanical[25] properties of the electrodes. These properties have already facilitated several applications of 2D and 3D pyrolysed carbon electrodes, such as chemical sensing[26], heavy metal detection[27], biosensors[28–31], cell substrates[21,32,33], and microbatteries[34–36].

2D and 3D pyrolysed carbon electrodes have great potential as sensing substrates and sensing scaffolds for cells, which could e.g. help to understand mechanisms of diseases, as well as improve screening and testing of drugs. Moreover, electrical activity of pyrolysed carbon electrodes could be explored in nerve tissue regeneration studies, like it has been already done for other conductive scaffolds[37–41]. Compared to other scaffolds, the advantages with pyrolysed carbon scaffolds are several: (1) Organised[42] and random[43] structured scaffolds can

be fabricated in a simple process at small or semi-large scale with high-reproducibility, high-yield and cost-effectiveness. Micro/nanostructures can be placed in precisely defined positions without restrictions in shape or cross section and the features and scale depend on the process used for making the polymer precursor[44]. (2) By changing the chemical composition of the polymer precursor and the pyrolysis conditions, the carbon conductivity can be tailored[23,45]. (3) Similarly, the mechanical properties of the scaffold can be tuned[44] to match the stiffness cells experience *in vivo*[46]. This fabricational degree of freedom provides possibilities for mass production, facilitating novel custom-made designs with unique properties to support various biomedical and pharmaceutical applications.

1.1. Objectives of the thesis

The research conducted for this thesis was aimed at developing 2D and 3D carbon micro and nano-electrodes for bioelectrochemistry in general and for biological applications, such as conductive substrates and scaffolds for cell biology, biofuel cells, etc. Specifically, the research has focused on three areas: (i) fabrication of 2D and 3D carbon micro- and nanostructures and their subsequent interfacing with external measurement setups (chapter 2); (ii) characterization of the microfabricated carbon electrodes before and after surface modification for their bulk microstructure, surface and electrical properties, and their electrochemical performances (chapter 3 and 4); (iii) investigation and application of the 3D carbon electrodes for measuring exocytosis of dopamine events from clinically relevant stem cells derived neurons (chapter 5).

Chapter 2

Fabrication of Carbon-Based Micro and Nanostructures

This chapter starts by describing the structural properties of different carbon allotropes that have been used for fabrication of various 2D and 3D electrode materials. Then, the steps leading to production of pyrolysed carbon structures and the different variables affecting the pyrolysis process are discussed. Finally, the pyrolysed 2D and 3D electrode structures fabricated for this thesis are presented, and the different electrode interfacing used during the work will be illustrated.

2.1. Carbon Allotropes and Their Structural Properties

Carbon has many allotropes[15,47], such as graphite, diamond, fullerene, and glass-like carbons. The latter are carbons obtained through pyrolysis, which means carbonization of organic polymers[15] at high temperature in inert atmosphere, a process that will be described in more details in the following sections. The structural properties of the above mentioned allotropes are briefly reported below.

The graphite structure consists of ideally infinite sheets of graphene stacked in parallel and bound through weak Van der Waals forces (Fig. 2.1A). Graphene has a polycrystalline structure, consisting of several crystallites. It is characterized by the atomically ordered hexagonal surface containing the "a" axis known as the "basal plane" (Fig. 2.1B), and the irregular plane parallel to the "c" axis known as "edge plane" (Fig. 2.1C), where L_a and L_c are the characteristic dimensions of the basal plane and edge plane, respectively[15,48].

The carbon atoms in graphite are all sp^2 hybridized, with an intra-planar C-C bond length of 0.14 nm (Fig. 2.1B) and inter-planar spacing (d_{002}) of 0.34 nm (Fig. 2.1C). The conductivity[a] of graphite is $2 - 4 \times 10^5$ S/m[49].

In diamond, carbon is sp^3 hybridized and tetrahedral, with a C-C bond length of 0.15 nm (Fig. 2.1D). Diamond has a very low conductivity ($\sigma = 1 \times 10^{-18}$ S/m) and is thereby an electrical insulator. It usually contains dopants, such as boron, to provide sufficient conductivity when being used as an electrode material[15,50].

Among the fullerenes, carbon nanotubes (CNTs) are very commonly used as an electrode material. CNTs are "rolled up" single or multiple layers of graphene sheets[15], which form single-walled CNTs (SWNTs) or multi-walled CNTs (MWNTs), respectively (Fig. 2.1E).

[a] Graphite conducts electricity preferentially in the plane parallel to the covalently bonded graphene sheets (basal plane), due to delocalization of one of the outer electrons of each atom to form a π-cloud. This results in lower bulk conductivity for graphite ($\sigma = 2 \times 10^5 - 4 \times 10^5$ S/m) than for most metals (i.e. for Au, $\sigma = 4.1 \times 10^7$ S/m; for Pt, $\sigma = 9.4 \times 10^6$ S/m). The conductivity of graphite on the c-axis is 333 S/m[49].

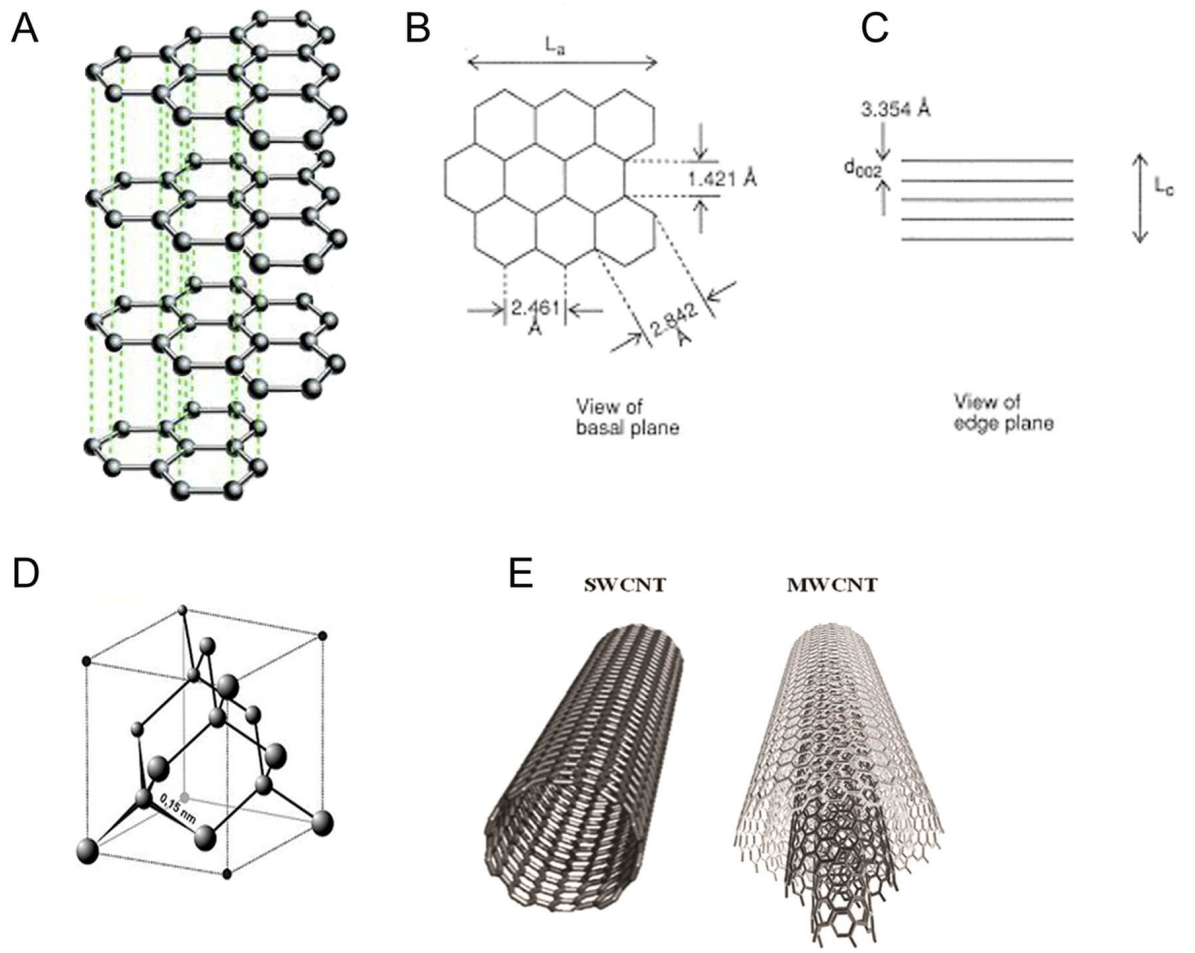

Figure 2.1. A) Graphene sheets stacked in parallel to form graphite. Characteristic dimensions of the graphite crystallite, L_a on the basal plane (B), and L_c on the edge plane (C), adapted from[48]. (D) Tetrahedrically bonded carbon atoms in the diamond structure. (E) Rolled up single and multilayers of graphene forming SWCNT and MWCNT, adapted from[51].

Glassy carbon (GC) electrodes are obtained by pyrolysis between 1000-3000 °C of polyacrylonitrile (PAN) or phenol/formaldehyde polymeric resin precursors. GC electrodes exhibit excellent electrochemical properties, thus are often used as the 'gold standard' to compare the electrochemical behavior of other electrodes. The microstructure of GC comprises a mixture of carbon atoms, sp^2 (graphitic regions) and sp^3 hybridized (disordered regions)[52–55]. In the 1970s, the structure of GC was considered to have a ribbon-like geometry with entangled graphitic planes[56] (Fig. 2.2A). High-resolution transmission electron microscopic (TEM) analysis of commercially available GC (Fig.2.2B) showed that carbons derived from pyrolysed polymers contain small isolated crystals of graphite. During carbonization, the C-C bonds of the polymer precursor backbone do not break, thus the

graphitic regions cannot fully develop into graphene sheets. The carbon can form graphitic regions of only limited size, with L_a and L_c in the range of 3-7 nm, and inter-planar spacing (d_{002}) larger than 0.34 nm[15,48].

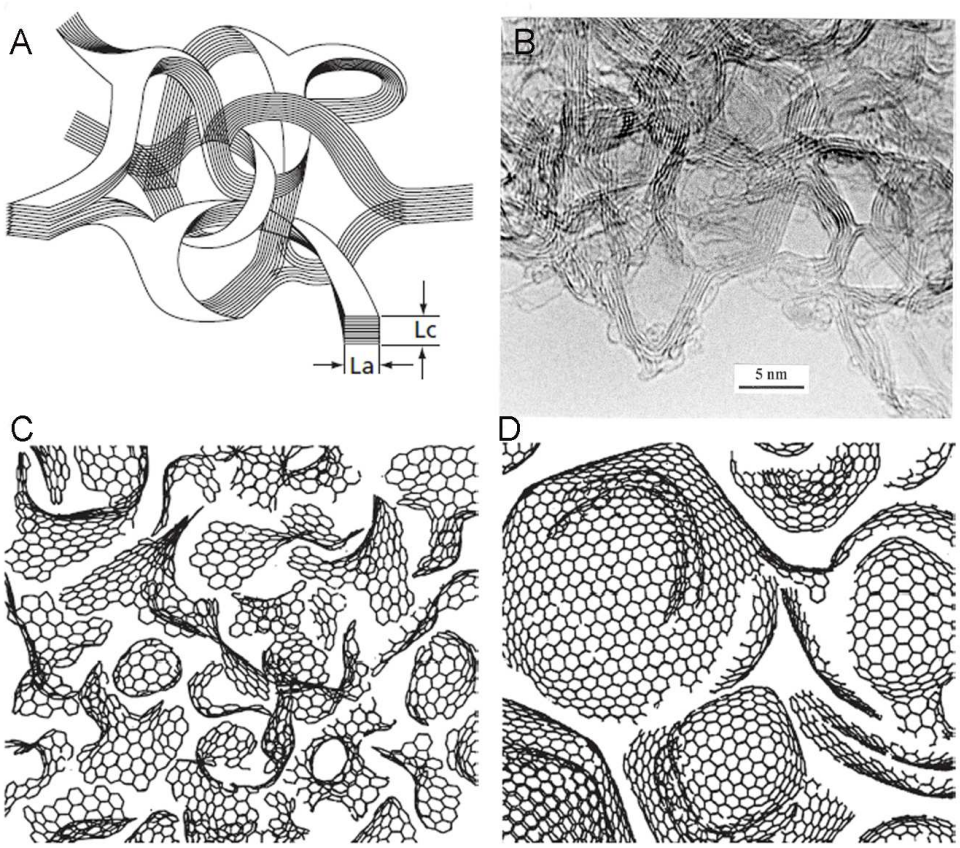

Figure 2.2. (A) Structural model for glassy carbon proposed by Jenkins-Kawamura[57]. (B) TEM images of glassy carbon prepared at 3000 °C[58]. Models for the structure of glassy carbon prepared by (C) low-temperature and (D) high- temperature treatment[58].

Based on these observations, Harris[58] suggested that GC consists of sp^2 hybridized carbons (such as those found in fullerenes) forming six-membered rings as well as five and seven membered rings. According to this 'fullerene-related structure', GC prepared at different temperatures results in different amount of dispersed graphene sheets (Fig. 2.2C-D). The amount of graphitic regions in the carbon matrix, i.e. the degree of microstructural disorder, can be evaluated with Raman spectroscopy (discussed in Chapter 3).

2.2. 2D and 3D Carbon Electrodes

Different carbon materials, such as graphene, CNTs, and pyrolysed carbon, have been used to develop various types of electrodes. Due to their structural properties, not all of them are suitable for fabrication of 2D and 3D micro and nano-electrodes. For instance, finely patterned 3D electrodes in graphene and CNT-based materials are difficult to achieve. For graphene electrodes, this is due to its 'two dimensional' structural properties.

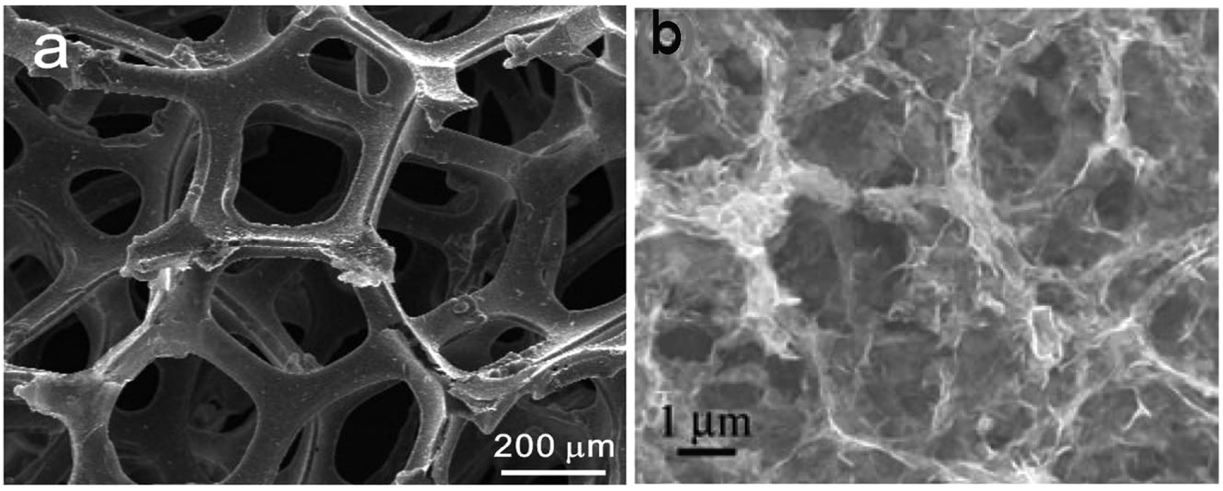

Figure 2.3. SEM images of a) graphene foam[16] and b) graphene composite hydrogels[15].

Recently, graphene foam[16] (Fig 2.3A) and graphene composite hydrogels[59,60] (Fig. 2.3B) have enabled fabrication of 3D electrodes[61]. However, these materials are difficult to pattern and are utilized as fabricated entities of bulk material instead of 3D micro- and nanostructures based on e.g. lithographic patterning.

CNTs have been the basis of various kind of structures, such as 2D substrates[62], forests[63], bundles[64], finely patterned multi-electrode arrays[65], nanostructured sponges[66] (Fig. 2.4), and CNT-composite hydrogels[67].

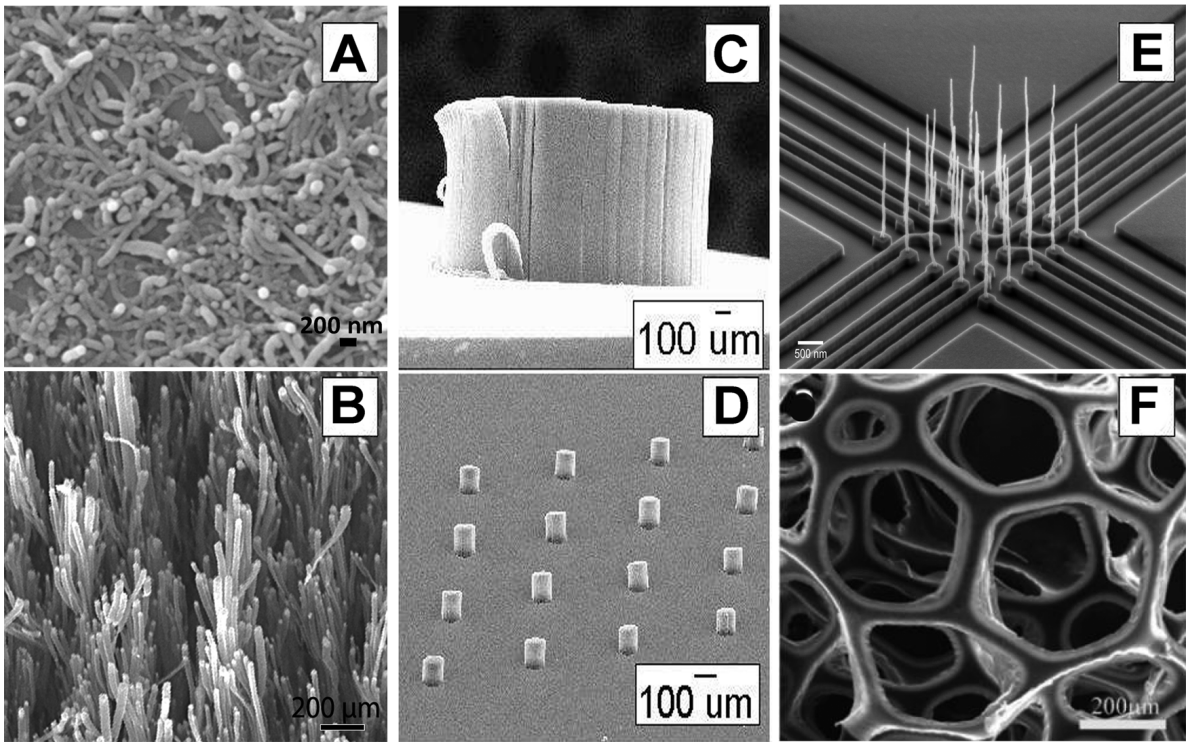

Figure 2.4. SEM images of different CNTs-based structures. (A) 2D substrates[62], (B) forests[63], (C-D) bundles[64], (E) finely patterned multi-electrode arrays[65], (F) nanostructured sponge[66].

Compared to fabrication of other carbon-based electrodes, pyrolysis of 2D and 3D polymeric micro- and nanoscale template structures is a very attractive method for obtaining, in a facile and cost-effective manner, various 2D and 3D carbon micro- and nanostructures. The advantage of using polymers as starting material for carbon microfabrication is that they can be very finely patterned by micromachining techniques. Hence, a wide variety of shapes and cross-sections in the macro to the nano length scale can be obtained for the entire fabricated system. Different polymer micromachining techniques (e.g. microcontact printing, 3D printing, e-beam lithography, photo- and soft lithography, moulding, embossing, etc.) enable nano- and micropatterning of polymeric precursor, which may then be pyrolysed to obtain the corresponding carbon structures[24,68–70]

Different considerations need to be made when developing pyrolysed carbon electrodes depending on the desired electrode size, dimensionality (i.e. 2D or 3D), and the final application. The characteristics of the pyrolysed product e.g. in terms of conductivity (related to carbon yield [b], ratio of sp^2 to sp^3 carbon atoms, and heteroatom contents), as well as

[b] Carbon yield is the ratio of the weight of carbon to the weight of the original polymer sample

surface properties, vary greatly with fabrication parameters and process conditions. Some of these variables will be dwelled on in the following sections.

2.3. What Happens During Pyrolysis?

The pyrolysis process involves step-wise carbonization of organic polymers at different temperatures, atmospheres (e.g. nitrogen, argon, forming gas[c]) and pressures (e.g. ambient, vacuum). Initially during the process, intra-molecular reactions occur within the C-C chain of the polymer. Depending on the kind of polymer, different reactions take place, resulting in one of the following possibilities for the C-C chains[57]:

1. Degradation into small molecules which are eliminated as gases, thus leaving very little or no carbon behind. This happens e.g. during pyrolysis of polyethylene[57].
2. Collapse and pass, at least partly, through a liquid or liquid-crystalline state, leading to formation of coke, which upon heating to 2700 °C will develop graphitic regions approximately parallel to each other (graphitizing carbon)[71] (Fig. 2.5A). The transformation of such a structure into crystalline graphite may be expected relatively facile (graphitization)[71]. An example showing this behavior is polyvinylchloride[71].
3. Remain intact without passing through a fluid state. The final product will retain the characteristic shape of the precursor, albeit smaller in size. Due to the difficulty of breaking C-C bonds, homogeneous development of graphitic regions is inhibited (non-graphitizing carbon)[71] (Fig. 2.5B). An example of this behaviour is pyrolysis of thermosetting polymers, such as polyfurfuryl alcohol and phenolic polymers[72] (e.g. SU-8 based materials).

[c] Forming gas is composed of 95% N_2 and 5% H_2.

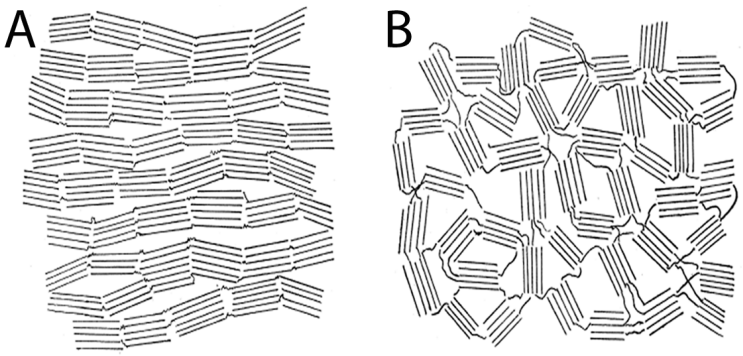

Figure 2.5.
Schematic representation of the structure of (A) a graphitizing carbon – the graphitic regions are approximately parallel to each other; (B) non-graphitizing carbons – the graphitic regions are oriented randomly, and their cross-links are sufficiently strong to impede movement of the layers into a more parallel arrangement. Modified from[71].

Jenkins and Kawamura[57] elucidated the different steps leading to the formation of carbon from pyrolysis of thermosetting resins (case 3 above). During pyrolysis, many reactions take place concurrently in a multi-step process (Fig. 2.6), including dehydrogenation, cyclization, condensation, hydrogen transfer and isomerization. During the pre-carbonization phase (below 300 °C), unreacted monomers and molecules of solvent are eliminated from the polymeric precursor structure. Removal of halogens (e.g. Cl) and heteroatoms (e.g. oxygen, nitrogen) occurs during the carbonization phase I (between 300°C and 500°C), leading to a rapid polymer mass loss, while a network of conjugated carbon systems is formed. Towards the end of this phase, removal of hydrogen atoms starts to take place (dehydrogenation stage). During carbonization phase II (from 500 °C to 1200 °C), remaining hydrogen, oxygen and nitrogen atoms attached to carbon atoms are completely cleaved off and removed, thus forcing the aromatic network to become interconnected. Finally, at the so-called 'annealing stage' (above 1200 °C) most of the remaining impurities are eliminated. The final pyrolysis temperature ultimately determines the residual content of foreign material, and thereby the final carbon content, as well as the conductivity of the carbonization product, as will be discussed in section 2.3.2.

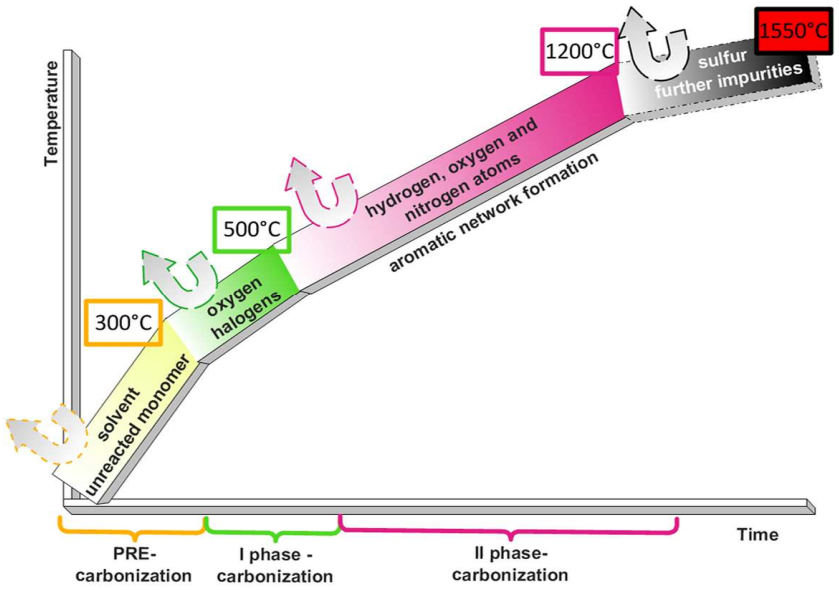

Figure 2.6. Schematic of the multi-step carbonization process taking place during pyrolysis.

2.3.1. Choice of Polymer Precursor

Not all polymers are suitable for obtaining glass-like carbon structures. Different precursors for carbonization have been used, including epoxy resins[73], phenolic resins[74], polyfurfuryl alcohols[74], furfuryl alcohol resins[75], polyimides[54], polyvinyl chloride[76], polyvinylidene[76], polyacrylonitrile[76], parylene[77], as well as various block copolymers (such as polystyrene-block-poly(2-vinylpyridine)[78], poly(ethylene oxide)-block-polystyrene[79]). Depending on the polymer precursor, different carbon yields are obtained. For instance, polyfurfuryl alcohol and phenol-formaldehyde resins result in more than 80% carbon yield[72].

It is also possible to "dope" the polymer precursor as well as the final product with various heteroatoms (e.g. silicon[80], halogens[81,82]) and metal catalysts[83], or to combine the pyrolysed carbon structure with other carbon materials, such as CNTs[84] or graphene[85] (Fig. 2.7).

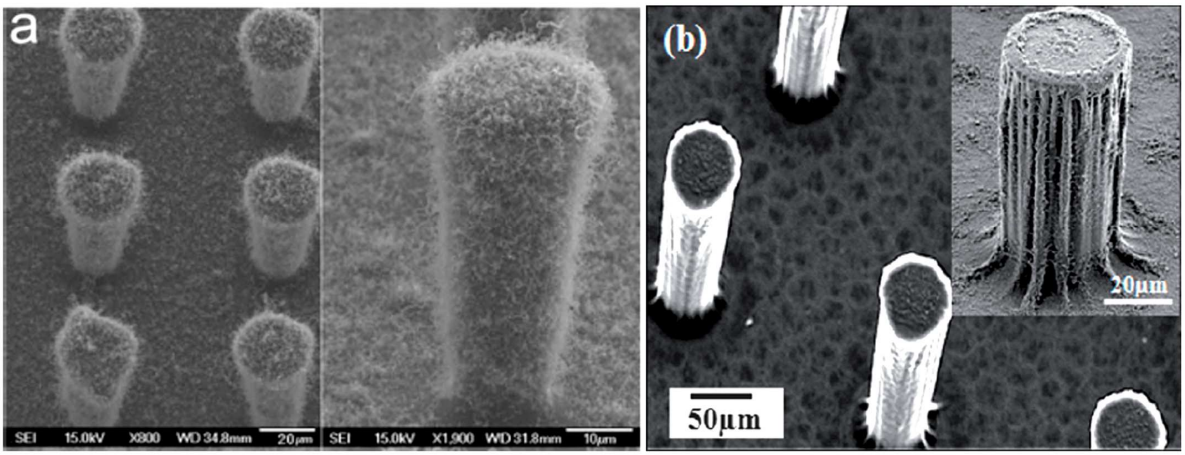

Figure 2.7. Pyrolysed carbon structures combined with (a) CNTs[84] and (b) graphene[85].

The choice of polymer also depends on the technique used for patterning of the polymer precursor, which in turn is dictated by the desired electrode dimensions. Due to the structural reproducibility and the availability of standard processing equipment, photoresists such as acid-catalyzed phenol formaldehyde resins and novolac-epoxy resins have during the past 15 years become the preferred materials to derive carbon structures with micro- and nanometer dimensions. The first reports on patterned pyrolysed carbon microstructures concerned carbon features of very low aspect ratio[d] derived from micromolded resin (such as poly furfuryl alcohol)[24,75], UV patterned positive[52,86,87] and negative photoresists[22,52–54].

Moreover, the nature and chemical structure of the polymer precursor, in this case the photoresist, affects the formation of graphitic zones in the pyrolysed carbon. For instance, in positive photoresist (such as AZ resists from Clariant), graphite-like areas begin to form at lower temperatures than in negative photoresist films[52,54]. In AZ resist precursors, the monomer units have a hexagonal benzene ring structure. Hence the bond rearrangement that is needed to form graphite-like areas is not drastic[54]. However, due to difficulties in designing a thick positive photoresist with low UV absorption (to easily control exposure dose) and necessary transparency to UV light[88], the carbon structures derived from them are low aspect ratio (1:1 – same height and width). To meet the challenging demands posed by fabrication of high aspect ratio (HAR) carbon structures, a photoresist with excellent transparency, wide range of viscosities (to enable different resist film thicknesses), and high

[d] The ratio between the height and the width of a structure is referred to as the 'aspect ratio'.

contrast is needed. SU-8, an epoxy based negative photoresist, developed by IBM, meets all these requirements, and is commonly used to fabricate HAR micro- and nanostructures[31,89–93], which can be achieved using, e.g. X-ray, e-beam and two-photon lithography. However, for high-throughput fabrication of arrays these methods require long processing times, are very costly, and therefore have limited applicability. Therefore, standard UV photolithography is preferred if possible.

In this thesis, SU-8 was used as precursor materials for the fabrication of micro- and nanostructured electrodes. Additionally, a study with polystyrene (PS) and polystyrene-blockpolydimethylsiloxane (PS-PDMS) copolymers, obtained from the Nanoporous group at DTU Nanotech, was performed. Fig. 2.8 shows the structures obtained after pyrolysis of PS and PS-PDMS. Our results show that PS-PDMS contains an atomic percentage of 29% silicon in the corresponding pyrolysed material (as will be discussed more in Chapter 3.1). The silicon content may be a limiting factor for obtaining high-conductive structures due to lower carbon content (19%) compared to polystyrene (96%) and SU-8 photoresist (98%), but at the same time the silicon is functioning as support for the 3D structure, shown in fig. 2.8B.

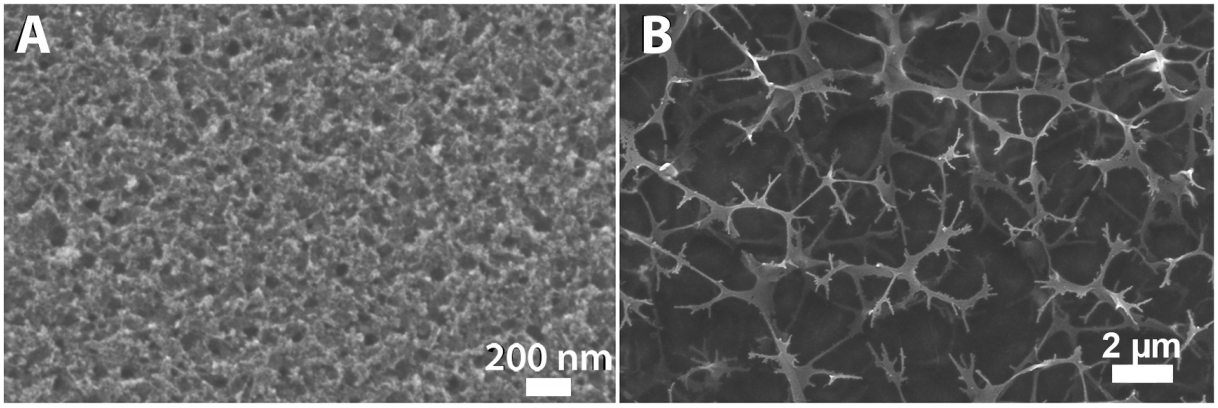

Figure 2.8. SEM images of pyrolysed PS (A) and PS-PDMS (B).

2.3.2. Pyrolysis Temperature

The final pyrolysis temperature significantly affects the properties of the carbonized product. For instance, carbon films from both positive[22,52,53] and negative[27,54] photoresists prepared at pyrolysis temperatures at 1000 °C or higher exhibit lower resistivity and better electrochemical behavior than those prepared at lower temperatures. Lyons et al.[22] have attributed this phenomenon to the increasing degree of graphitization with higher

temperature: the volume fraction of the conductive graphitic regions increases, and thereby the material as a whole becomes more conductive when treated at higher temperatures[22].

Since aromatization and film densification take place at higher heat treatment temperatures[54], weight loss and thereby shrinkage depend on the final temperature, i.e., higher film shrinkage will occur at higher pyrolysis temperatures. Although this lead to higher conductivity, extensive shrinkage may result in distortion of the carbon structures. This might jeopardize the outcome of the process, as observed in the case for SU-8 based carbon nanopillars obtained by colloidal lithography (Fig. 2.9, see also section 2.4.2). During my experiments, the pyrolysis temperature was 900°C, due to limited performance of the furnace available at the DTU Danchip facilities.

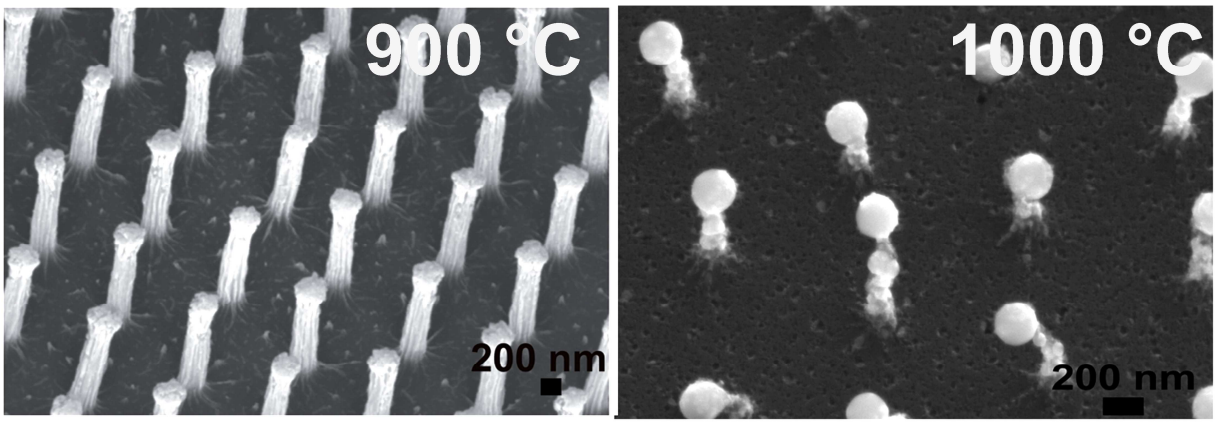

Figure 2.9. Effect of the pyrolysis temperature on the structure shrinkage: At 1000 °C, distortion of the nanopillars takes place. Tests at 1000 °C were performed at Marc Madou's Lab, UC Irvine (CA).

2.3.3. Furnace Atmosphere

Pyrolysis of photoresist in presence of inert environment (N_2, H_2, forming gas, or vacuum) leads to surfaces with low oxygen content. For pyrolysis in forming gas or vacuum[52], the produced carbon surfaces have the lowest oxygen to carbon ratio (O/C) of all. In vacuum, however, removal of gaseous by-products tends to be faster, and can result in the formation of micro-cracks in SU-8 structures, which may corrupt the sample[11]. During our experiments, N_2 atmosphere was used.

Due to air leakage in the furnace at DTU Danchip, several tests were performed to optimize the N_2 flow to avoid complete oxidation of the precursor polymer structures during pyrolysis (some results of these tests are shown in Fig. 2.10). At flow rates below 24 L/min no

pyrolysed carbon was left on the samples. In the available furnace, one sample with a maximum size of a 4-inch-wafer could be processed in one experimental run.

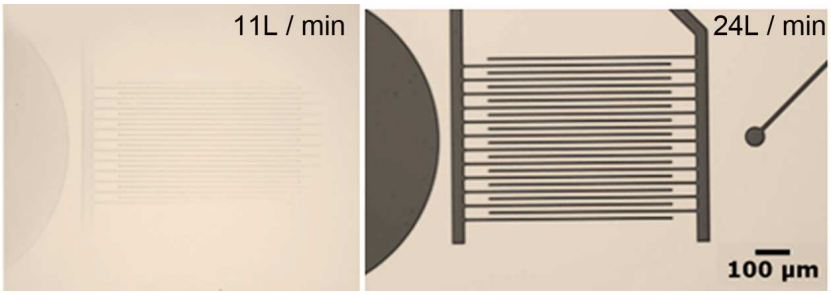

Fig. 2.10. Optical microscope images of carbon microstructures resulting from pyrolysis conducted in presence of two different N_2 flows, 11L/min and 24L/min. This indicates that the higher flow reduces structure oxidation, which is instead taking place with a flow of 11L/min.

2.4. Micro and Nanostructures Fabricated Using Pyrolysis in This Thesis

2.4.1. Standard UV Lithography

Part of the research conducted for this thesis was aimed at optimizing the SU-8 processing for SU-8 micropillar arrays, with dimensions close to the resolution limit of standard UV-lithography (paper I) (Fig. 2.11).

During optimization, different pillar diameters were obtained, which then were pyrolysed to obtain the corresponding carbon micropillars (Table 1) (paper II). The smallest dimensions of carbon micropillars were 1.4 µm in diameter, 11 µm in height, and ~6 µm in spacing. These dimensions are much smaller compared to micropillar arrays reported previously, which have spacing and diameters higher than 10 µm[31,88,93].

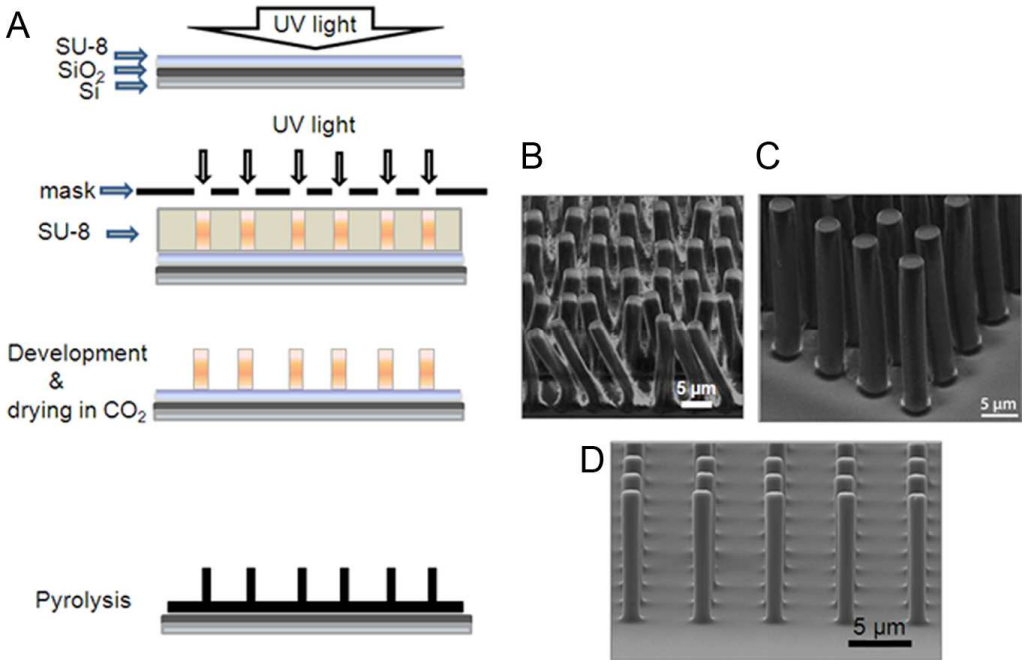

Figure 2.11. Fabrication of carbon micropillars. (A) Schematics of the process flow. (B-C) Result of the SU-8 processing before (B) and after (C) optimisation (paper I). (D) Micropillars obtained after pyrolysis of (C) (paper II).

Table 2.1 – Dimensions (average +- sem (n=48) of micropillars before and after pyrolysis; ND=Nominal diameter on the lithographic mask; C=Carbon

	Pillar diameter		Pillar height	
ND [µm]	SU-8 [µm]	C [µm]	SU-8 [µm]	C [µm]
3	3.07 ± 0.02	1.44 ± 0.02	23.44 ± 0.07	11.07 ± 0.10
3.5	3.49 ± 0.03	1.66 ± 0.02	23.49 ± 0.21	11.37 ± 0.04
4	4.16 ± 0.03	1.98 ± 0.04	24.48 ± 0.17	11.69 ± 0.06
5	4.97 ± 0.04	2.50 ± 0.03	24.40 ± 0.15	11.77 ± 0.06
10	9.35 ± 0.06	5.08 ± 0.03	24.13 ± 0.08	11.98 ± 0.06
15	13,68 ± 0.10	7.58 ± 0.05	24.01 ± 0.14	11.20 ± 0.08

Furthermore, 2D structures using SU-8 and AZ photoresists as precursor were photolitographically defined to obtain the corresponding carbon electrodes with different designs (Fig. 2.12).

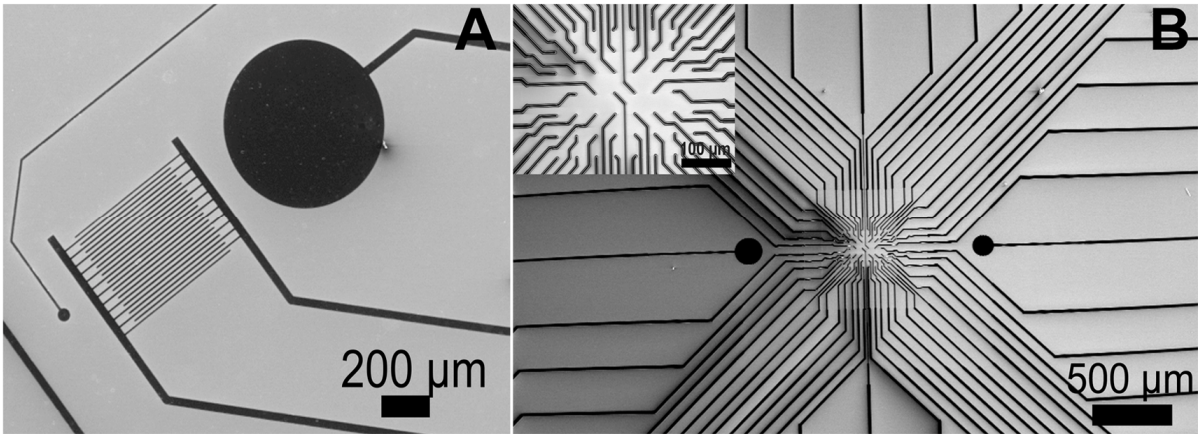

Figure 2.12. SEM images of three-electrode systems in two different carbon electrodes designs derived from SU-8 patterned with photolitography. (A) Interdigitated structures; (B) 54 individually addressable micro-electrode arrays.

Moreover, micropillar arrays were finely patterned on the interdigitated structures (shown in Fig. 2.12A) to obtain 3D interdigitated carbon microelectrodes (Fig. 2.13) (paper II).

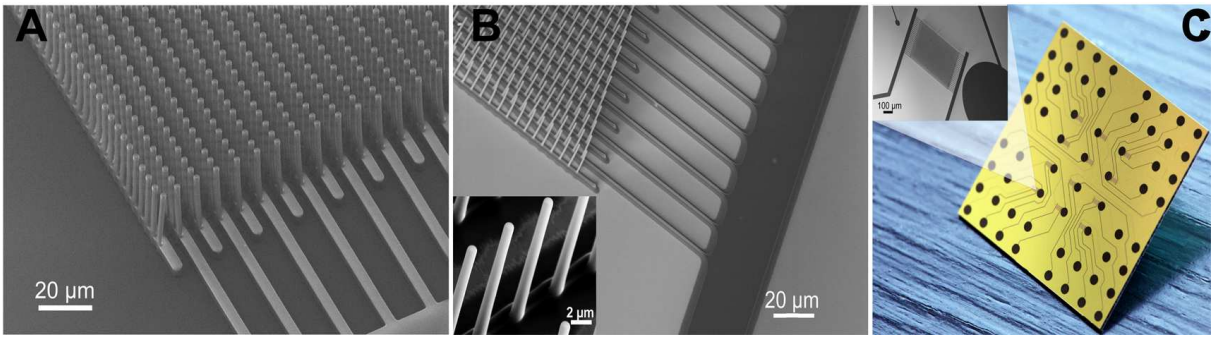

Figure 2.13. SEM images of pillars interconnected on interdigitated structures (A) before and (B) after pyrolysis. (C) Photograph of a silicon chip with the pyrolysed carbon electrode arrays structures (12 three-electrode systems at the centre with surrounding contact pads).

2.4.2. Colloidal Lithography

For fabrication of large areas of carbon nanopillar arrays, a method combining colloidal lithography and pyrolysis, was developed (Fig. 2.14). This was done in collaboration with the Company Plasmore S.r.l. (Milano, Italy). Colloidal lithography has been previously used for nanostructuring polymer films[94], metal[95,96] and silicon surfaces[97,98]. However, by combining colloidal lithography and pyrolysis, we were able to achieve fabrication of SU-8 nanopillar arrays with different aspect ratios (Table 2.2) and the corresponding carbon nanopillars.

During the process, a monolayer of polystyrene beads (nominal diameter: 500 or 1000 nm) were deposited[99] on SU-8 film substrates (5µm thick SU-8 on Si wafer) (Fig. 2.14 A). The beads are then used as etching mask during O_2 plasma treatment, similarly to a previously described method[99] (Fig. 2.14 B). After etching, the residual beads are removed with ultrasonication in isopropanol as a lift-off technique (Fig. 2.14 C). Combination of etching time, plasma etching parameters and nanoparticle size resulted in SU-8 nanopillar arrays with different aspect ratios (Table 2.2). Finally, the SU-8 nanostructures were carbonized to obtain the corresponding carbon nanopillar arrays (Fig. 2.14 D-E).

This method can easily be scaled-up to generate wafer-scale carbon nanopillar arrays, by using equipment suitable for larger scale fabrication.

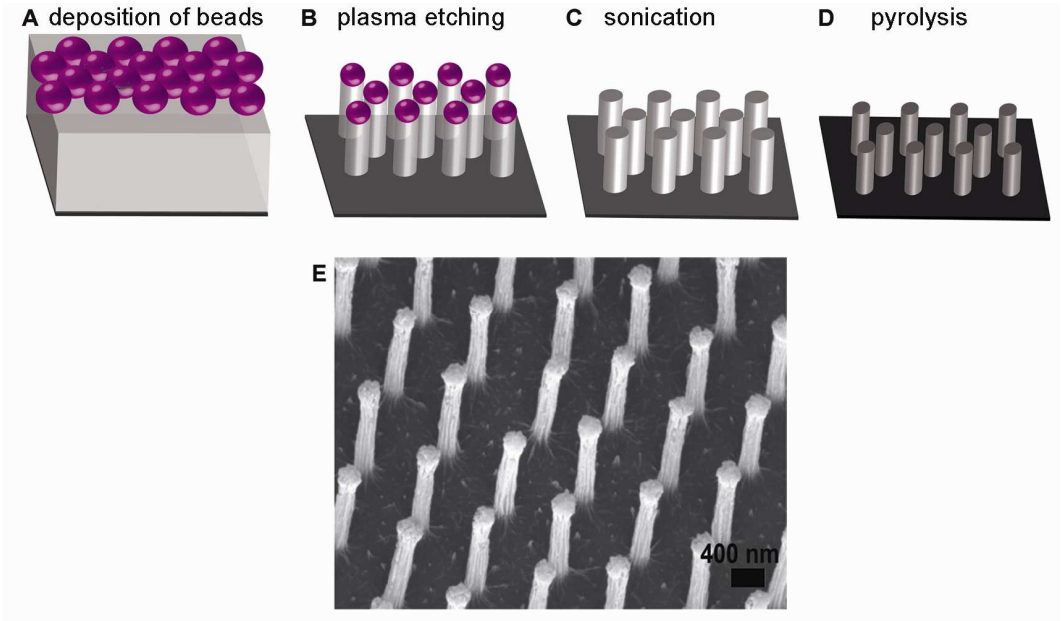

Figure 2.14. (A-D) Process flow of the fabrication of carbon nanopillar arrays via colloidal lithography and pyrolysis. (E) SEM image of carbon nanopillar arrays.

Table 2.2 Different dimensions of polystyrene nanoparticles and etching time during O_2 plasma treatment used for obtaining SU-8 nanopillars with different height and width.

Nanoparticle diameter [nm]	etching time [min]	height [nm]	width [nm]	aspect ratio
1000	3x5'	1470	420	3.5
1000	4x5'	1900	250	7.6
500	4'	283	406	0.7
500	2x4'	450	321	1.4

2.4.3. Deep UV Lithography

For high-throughput fabrication of carbon nanostructures, deep UV (DUV) lithography is a promising technique. SU-8 photoresist is compatible with DUV lithography. However, SU-8 is not optimal for this kind of technique due to high-absorption of the photo-initiator in the SU-8 formulation at the operational wavelength of DUV (248 nm). This makes the fabrication of SU-8 nanostructures with DUV lithography challenging. By changing the exposure dose (100 – 600 mJ cm^{-2}), baking temperatures (room temperature, 40 °C, 50 °C, 60°C) and baking times (1-4 minutes), we successfully optimized the fabrication of SU-8 nanostructures with 300 nm in width. The processing parameters are reported in Table 2.3. Briefly, 150 nm thick SU-8 films were spin coated on top of 4-inch silicon wafer with a 2 µm thick thermal silicon dioxide layer. This was followed by solvent evaporation at room temperature (RT) and mask-exposure with DUV radiation (100 mJ/cm^2). The exposed samples were subjected to a post-exposure-bake (PEB) on a hotplate (1 min at 40 °C) and the uncrosslinked SU-8 was developed in Propylene Glycol Monomethyl Ether Acetate.

Table 2.3 Processing parameters for obtaining SU-8 nanostructures with DUV lithography

Soft bake	Exposure	PEB	Development
5 minutes at RT (solvent evaporation)	100 mJ/cm^2	1 minute at 40 °C	1 minute

The obtained structures were pyrolysed to obtain the corresponding carbon nanostructures (Fig. 2.15). This work was done in collaboration with two bachelor students, Henrik Teglborg and Joachim Thomsen, and DTU Danchip.

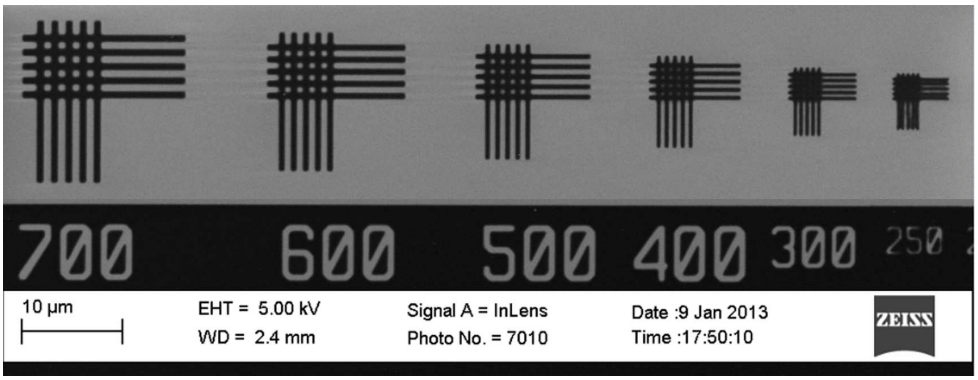

Figure 2.15. SEM image of carbon nanostructures of different width (from 700 nm to 250 nm), obtained with DUV lithography of SU-8 films and subsequent pyrolysis. The smallest well-resolved carbon nanostructure was 300 nm in width.

2.5. Interfacing Electrode Chip for Electrochemical Measurements

For electrochemical characterization of microfabricated electrodes, three different set-ups were employed for interfacing with external measurement apparatus.

2.5.1. Glass Electrochemical Cell

The electrodes were mounted horizontally between a metal base plate, insulated with a PTFE rubber pad, and a glass cell. A Viton O-ring and four springs from the base plate to the glass cell sealed the solution above the electrode, while defining the working area of 0.34 cm^2 (Fig. 2.16).

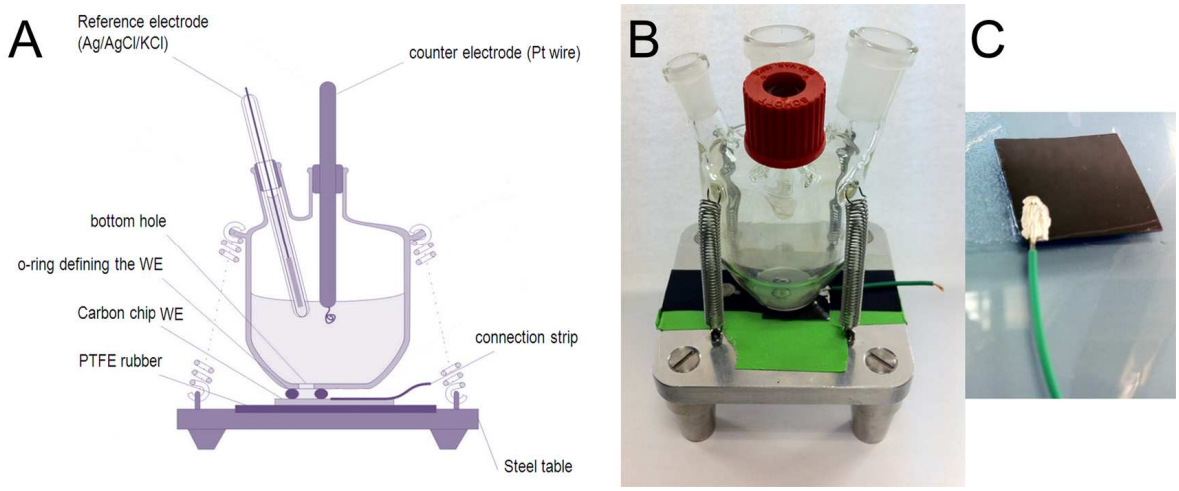

Figure 2.16. (A) Conceptual drawing of the electrochemical cell used to interface the pyrolysed carbon chips. (B) Photo of the electrochemical cell mounted with the chip. (C) Close up of the chip with a copper wire bonded using silver-saturated epoxy connections.

This setup configuration was developed and obtained from the Downard's group (Canterbury University, New Zealand)[100,101], where I spent 2 months in one of my external research stays at the start of my PhD. The carbon film layer served as the working electrode (WE). The contact to the carbon layer was made from the top with a copper wire bonded with silver-saturated epoxy connections to minimize parasitic capacitances and which served as lead to the potentiostat[102,103] (Fig. 2.16C). The setup facilitated preliminary characterization of the electrochemical properties of pyrolysed material, such as SU-8, PS, and PS-PDMS block-copolymer. The measurements were performed using a three-electrode configuration with a commercial Ag/AgCl reference electrode (RE) and a Pt wire serving as counter electrode (CE). This set up was not convenient for patterned electrodes or for experiments with biological samples and, thus a different setup had to be developed, as will be described below.

2.5.2. Glued Electrochemical Cell

For patterned electrodes, the area of the carbon working electrode was defined with a piece of plastic tubing (inner diameter 3.5 mm; length 6 mm), glued on the carbon chip with epoxy glue and serving as a vial[102] (Fig. 2.17). In this way, the projected areas for all types of electrode arrays were identical. Similarly to the previous setup, the contact to the working electrodes was a copper wire bonded with silver-saturated epoxy. In this configuration, a

500-µm diameter chlorinated Ag pseudo RE and a 500-µm diameter Pt CE were used, by placing them in the vial.

This setup had several drawbacks: i) it was not convenient when surface modification on the assembled setup (e.g. plasma treatment) needed to be performed since the silver epoxy would contaminate the surface during the plasma treatment; ii) electrode interfacing became very time consuming and cumbersome when multiple areas needed to be glued and contacted. For these reasons a third final set-up was fabricated, as will be described below.

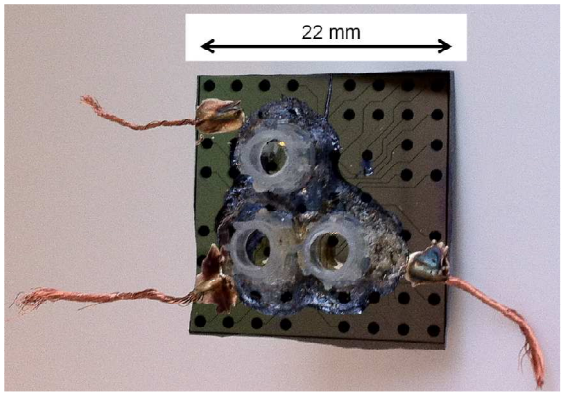

Figure 2.17. Photograph of a patterned carbon electrode chip, described in figure 2.12, with vials defining the working electrode area, and copper wires bonded with silver-saturated epoxy.

2.5.3. Micromilled Electrochemical Cell

For electrochemical evaluation of different surface modifications and for detection of dopamine from different types of cells, a different chip was designed and fabricated (Fig. 2.18A). This chip consisted of four areas with carbon micropillars to be used as WE interconnected by a carbon film. The micropillar dimensions were 1.4 µm in diameter for the x and y squares (Fig 2.18A) and 5.1 or 7.6 µm for the z and w squares (see other dimensions in Table 2.1). Cr/Au pads on the flat part of the carbon chip served as electrical contacts for easy interfacing with the external set-up (Fig. 2.18A). The Cr/Au metal layers (20/200nm) were patterned by sputtering through a shadow mask made by micromilling of polycarbonate (Fig. 2.18B).

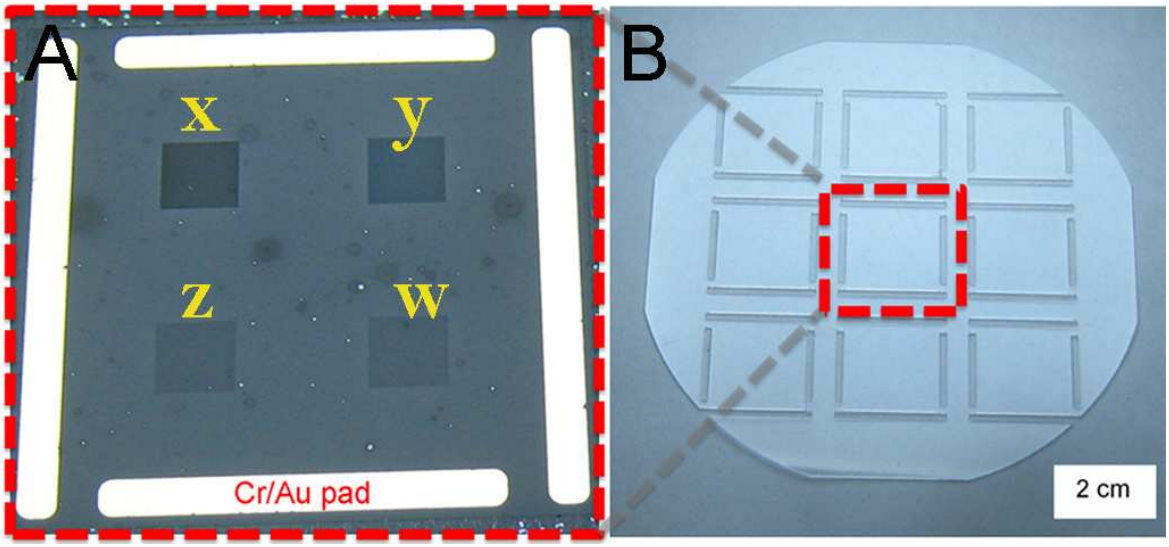

Figure 2.18. Photograph of (A) a carbon chip having four squares with carbon micropillar structures for use as WE interconnected by a carbon film. On the carbon film Cr/Au contacts were made; (B) a shadow mask in polycarbonate used for depositing metal contacts on the carbon chips seen in (A).

For this chip a new electrochemical set up was designed and fabricated. The carbon electrode chips were placed in a micromilled polymethyl methacrylate (PMMA) holder (Figs. 2.19), which formed a 70-µL vial on top of the electrode chip to facilitate liquid handling during experiments. Interconnections between the electrode chip and the potentiostat were obtained using a tailor-made PCB having gold plated spring loaded pins. Similarly to the previous configuration, in this setup a chlorinated Ag pseudo RE and a 500-µm diameter Pt CE were used, by placing them in the vial. This electrochemical cell was used in papers II, III and IV.

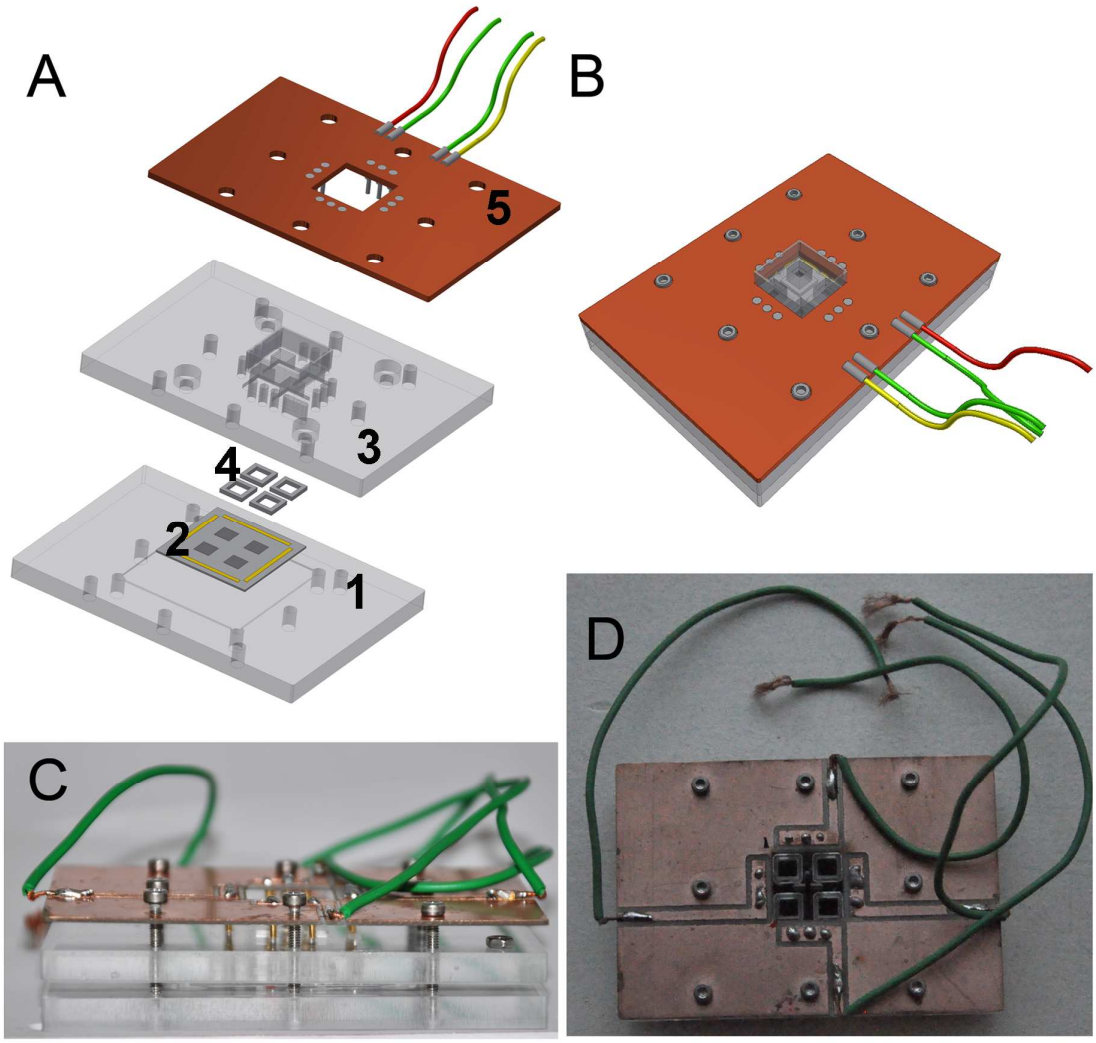

Figure 2.19. Conceptual drawing of the micromilled electrochemical cell: (A) Exploded view of the different parts ((1) bottom plate with place for (2) the electrode chip with 4 different WE areas, mid-plate defining 4 WE vials with (4) o-rings on top, and (5) a PCB as a top plate with spring loaded pins for connection to Cr/Au pads connected to the WEs)) fully assembled in (B). Photographs of the assembled electrochemical cell: (C) Side view and (D) top view.

Chapter 3

Methods for Material Characterization and Analysis

This chapter is an overview of the methods used for characterization of the micro and nanostructures developed in this thesis.

The surface characteristics of a material (i.e. topography, roughness) as well as its chemical/physical properties (chemical composition, surface energy, wettability, and surface reactivity) can affect its interaction with e.g. a biological element[104,105]. In the case of a conducting material used as an electrode, characterization of the bulk composition and microstructure, surface- and the electrical properties are also of great importance. For this project, the surface morphology was characterized using scanning electron microscopy (SEM), atomic force microscopy (AFM), and profilometry. The chemical/physical surface and bulk properties were evaluated by X-ray photoelectron spectroscopy and Raman spectroscopy. For studying surface hydrophobicity/wettability, contact angle measurements were performed. Four-point probe measurements allowed electrical characterization of the electrode materials. Finally, the electrochemical properties were evaluated using voltammetric methods (cyclic voltammetry and amperometry) and electrochemical impedance spectroscopy.

3.1. X-Ray Photoelectron Spectroscopy (XPS)

A XPS spectrum is derived from the binding energies of electrons characteristic of atoms, and can thus give information about the atomic composition of surfaces[106]. The XPS technique analyses the composition of the most external atomic layer of a surface (1-10 nm)[106]. Upon irradiation of a solid surface with X-rays, the core electrons have the highest probability to match the X-ray energy, and thereby gain enough energy to be ejected from the surface (Fig 3.1). The core electrons are close to the nucleus and have binding energies characteristic of the particular element. The emitted electrons have characteristic kinetic energies, which are proportional to the radiation energy, according to eq.1:

$$K_E = hv - E_b - \varphi \qquad \text{Equation 1}$$

where K_E is the kinetic energy of the electron, hv is the photon energy (h is Planck's constant, v is the frequency of the incident radiation, which is related to the X-ray source), E_b is the binding energy, and φ is the work function, a constant dependent on the spectrometer.

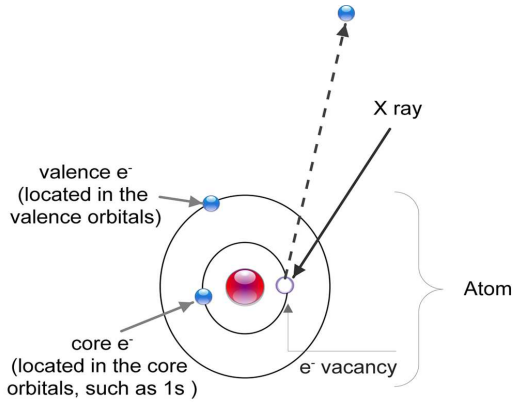

Figure 3.1. A schematic illustration of the emission process of electrons from an atom excited by X-rays

By measuring the kinetic energies of the emitted electrons, their binding energies in the atomic orbitals can be evaluated and plotted as a spectrum. Since each element has its own unique set of binding energies, it is possible to identify elements that contribute to a XPS survey spectrum, and determine the relative concentration of the atomic elements in the surface layer.

XPS survey spectra were used to evaluate the atomic percentage composition of various pyrolysed materials derived from different polymer precursors. Table 3.1 shows the atomic percentage of pyrolysed carbon derived from PS-PDMS, PS, and the SU-8, which were analysed during the work done for this thesis. Moreover, survey spectra gave information about changes in surface composition of electrodes caused by e.g. oxygen plastma treatment, as shown in Fig. 3.2A.

Table 3.1. Atomic percentage composition of pyrolysed carbon derived from polystyrene-block-polydimethylsiloxane (PS-PDMS), polystyrene (PS), and the negative photoresist SU-8 (SU-8). The results indicate that the C content is higher in PS and in SU-8 compared to PS-PDMS.

	PS-PDMS	PS	SU-8
C_{1s}	19	96	98
O_{1s}	52	4	2
Si_{2p}	29		

Moreover, survey spectra gave information about changes in surface composition of electrodes caused by e.g. oxygen plasma treatment, as shown in Fig. 3.2A.

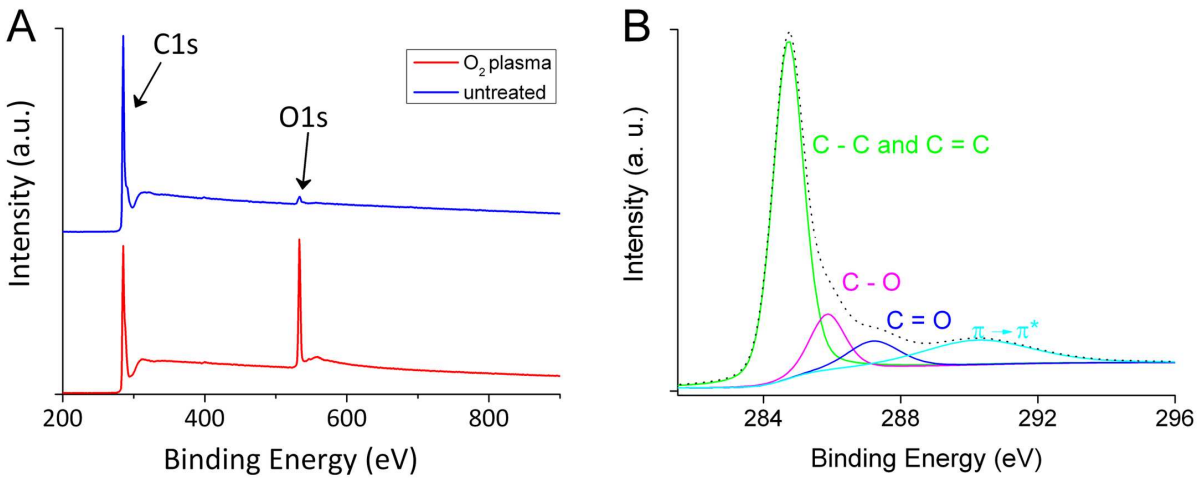

Figure 3.2. (A) Characteristic XPS survey spectra of flat pyrolysed carbon before (untreated) and after oxygen plasma treatment (O_2 plasma). (B) Curve fit to the C1s spectra of pyrolysed carbon derived from SU-8 photoresist (sum of spectra-dotted line), resulting in four individual peaks.
The main peak corresponds to sp^2-hybridized graphite-like carbon (C=C) atoms and sp^3-hybridized carbon (C-C) atoms. C-O are e.g. alcohol, ether species; C=O are e.g. ketone, aldehyde species; π–π* are shake-up satellite peaks due to π–π* transitions in the aromatic rings of the graphitic areas[107].

In addition to the identification of elements in a material surface layer, it is possible to obtain information about the functional groups present on a surface. For any given element, the binding energy of the core electron depends on its chemical environment, caused by the chemical bonds the element is participating in. This phenomenon results in 'chemical' shifts in the binding energies of the elements, giving different peaks in high-resolution spectra for different compounds. For instance, the chemically shifted C_{1s} peaks differ in their binding energies depending on whether they are linked to e.g. an oxygen atom by a single bond (e.g. alcoholic group), a double bond (e.g. carbonyl group), or two oxygen atoms (e.g. carboxylic group)[108]. These peaks will often overlap to produce a spectrum, which is the sum of the individual peaks. Extraction of information from such spectra requires curve fitting. For instance, in high-resolution C_{1s} spectra of pyrolysed carbon films derived from SU-8 photoresist, the C_{1s} signal exhibits an asymmetric tailing, due to the intrinsic asymmetry of the graphite peak and to the contribution of oxygen functionalities on the surface, see Fig. 3.2B.

XPS was used in this work for determining elemental composition of electrode surfaces (Papers II, III, and IV), as well as for monitoring the changes in surface composition, e.g. during electrode modification (Papers III and IV).

3.2. Raman Spectroscopy

Raman spectroscopy is used for elucidating the microstructure of materials[109]. Pyrolysed carbon consists of a mixture of graphite-like regions and disordered carbon and its microstructural disorder ranges between that of amorphous carbon and graphite. A Raman spectrum can give an indication of the relative amount of graphitic and amorphous regions, i.e. it can provide information about the degree of disorder of pyrolysed carbon[109].

Molecules are excited to a higher energy state by light and the following relaxation causes emission of light, which is referred to as scattering. When light with frequency ν_0 interacts with the molecular vibrations in a system, the molecule passes from the ground state of energy through an intermediate level, called 'virtual energy state' (Fig. 3.3).

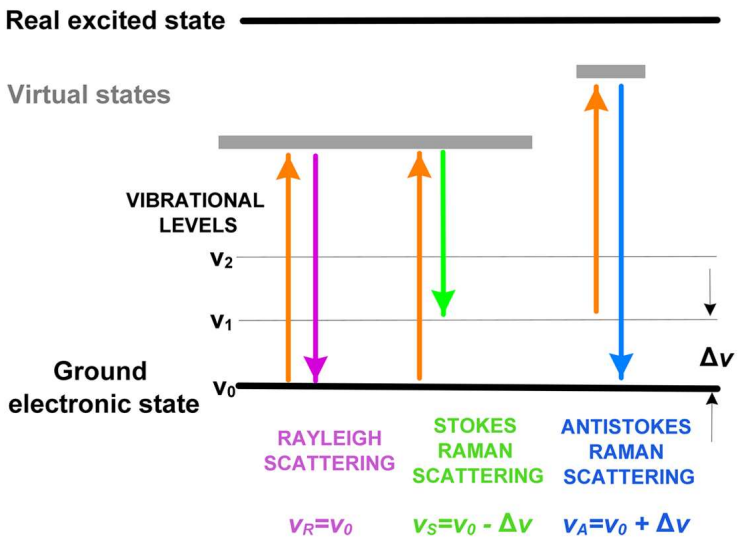

Figure 3.3. The energy level diagram and transitions, which are responsible for Rayleigh, Stokes, and Anti-Stokes scattering

The virtual state does not correspond to a real energy level of the molecule, however the closer its energy is to the energy of a real excited state, the higher the scattering probability. Upon relaxation, the molecule emits photons via two different scattering processes:

- Elastic scattering (Rayleigh scattering), where the scattered radiation is at the same frequency as the incident radiation ($\nu_{R=}\nu_o$). In this case both the photon energy and molecular energy are conserved. Rayleigh scattering has the highest probability of taking place[109].
- Inelastic scattering (Raman scattering), where the frequency of the scattered radiation differs from the frequency of the incident radiation. In this case the total photon plus molecular energy is conserved but the vibrational energy changes and the frequency in the scattered radiation is altered by a shift, $\Delta\nu$, from the excitation wavelength[109].

There are two types of Raman scattering phenomena, which differ by whether the frequency of incident light is shifted up ($\nu_0 + \Delta\nu$) or down ($\nu_0 - \Delta\nu$) (Fig. 3.3). If the final vibrational state of the molecule is more energetic than the initial state, then the emitted photon will be shifted to a lower frequency (ν_S) (Stokes shift), in order for the total energy of the system to remain balanced. If the final vibrational state of the molecule is less energetic than the initial state, then the emitted photon will be shifted to a higher frequency (ν_A) (anti-Stokes shift).

At room temperature most of the molecules are in the ground vibrational state (v = 0) with a much lower population in the first vibrationally excited state (v = 1). Since there is much higher probability that the molecule is in the ground vibrational state, the Stokes lines in the Raman spectrum are much more intense than the anti-Stokes lines. The wavelengths close to the one of the exciting laser (Rayleigh scattering) are removed by filtering, while the remaining wavelengths (Raman scattering) are collected by a detector.
In pyrolysed carbon, the E_{2g} vibrational mode at 1582 cm^{-1} (also present in graphite) and the A_{1g} vibrational mode at 1360 cm^{-1} are Raman active[110]. Fig. 3.4 shows the Raman spectra obtained from pyrolysed films derived from PS-PDMS, PS, and SU-8.

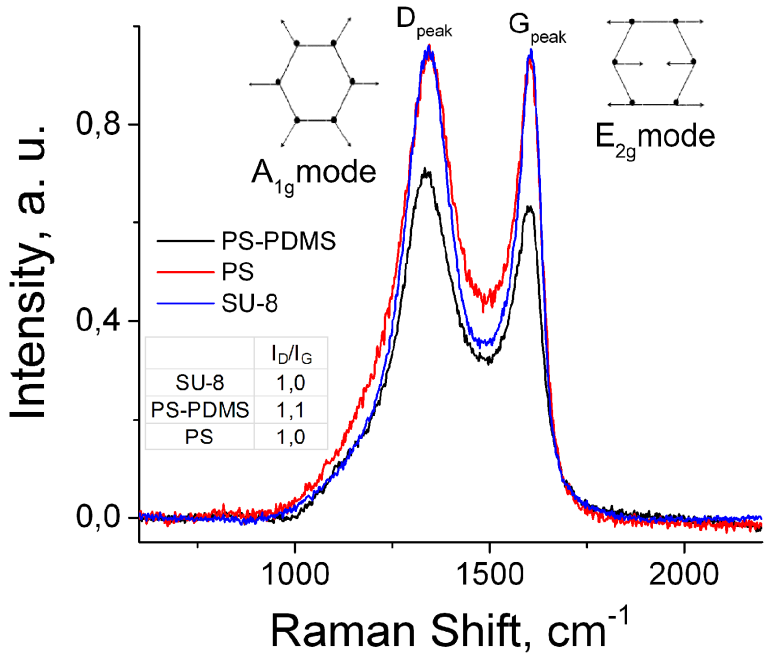

Figure 3.4. Raman spectra of pyrolysed films derived from PS-PDMS, PS, and SU-8. The spectra show the D and G peaks, due to the A_{1g} and E_{2g} modes, respectively.

The E_{2g} mode at 1582 cm^{-1} results in a peak, called "G" peak, where G stands for "graphite". The G peak is caused by bond stretching of all sp^2 hybridized C atoms in rings (e.g. aromatic molecule) as well as in chains (e.g. olefinic molecules[e])[111]. When the symmetry in the graphite lattice is broken due to presence of disordered regions, the A_{1g} mode becomes active[111]. This results in a new peak near 1360 cm^{-1}, called the "D" peak where D stands for disordered[111]. For instance, in Raman spectra of pyrolysed carbon derived from SU-8 photoresist both D and G peaks are present (Fig. 3.4), which means that both amorphous and graphitic regions are contributing. This phenomenon has been reported for other pyrolysed carbon materials as well as other kinds of amorphous and nanocrystalline carbon films[111].

It is known that the peak intensity ratio of the D and G peaks varies inversely with the crystallite size La ($I_D/I_G \propto 1/La$)[110] (see also Fig. 2.1C). Hence, the higher the microstructural disorder of the carbon matrix, i.e. the higher the number of defects, the higher the D peak intensity and, thus, the smaller L_a[110–112]. From the Raman spectra in Fig. 3.4, the calculated I_D/I_G is higher for pyrolysed films of PS-PDMS (I_D/I_G = 1.1) compared to SU-8 and PS (I_D/I_G = 1), indicating higher microstructural disorder of pyrolysed PS-PDMS.

[e] Olefins are unsaturated hydrocarbon containing one or more pairs of carbon atoms linked by a double bond, C=C.

Raman spectroscopy was use to evaluate the microstructure of pyrolysed carbon derived from SU-8 with different thicknesses (Papers II).

3. 3. Electrical Measurements

Four point probe (4PP) measurements can be used to investigate the electrical properties of materials[113]. During 4PP measurements a known current (I) is applied between two outer probes using a current source while a potential drop (V) is measured between two inner probes (Fig. 3.5).

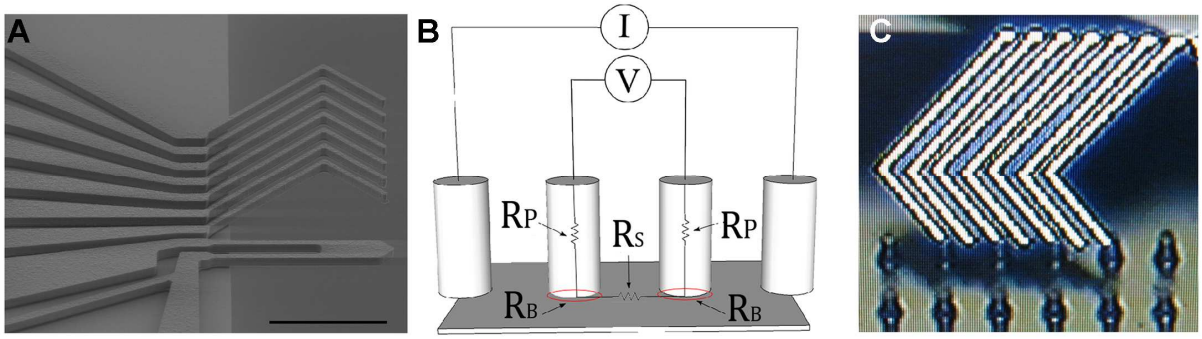

Figure 3.5. (A) SEM image of the probe used for electrical measurements (courtesy of L. Gammelgaard; scale bar: 100 µm). (B) Conceptual illustration of the 4PP measurements on top of carbon pillar structures (R_P = pillar resistance; R_B = contact resistance between the pillars and the flat interface; R_S = resistance of flat interface). (C) A micrograph of a micro 4PP during the measurement on micropillar carbon electrodes.

The resistance of the sample is calculated using Ohm's law ($R = V/I$) with ohm (Ω) as unit. When measuring on a thin homogeneous sheet, the sheet resistance (R_S), expressed in Ω/sq (ohm per square[f]), can be obtained by considering a correction factor (k), which is dependent on the geometry of the sample and the probe, according to equation 2 and 3[114,115].

$$R_S = k \times \frac{V}{I} \qquad \text{Equation 2}$$

[f] Ohms per square is dimensionally equal to an ohm, but is exclusively used for sheet resistance. Sheet resistance of 1 Ω could be misinterpreted as bulk resistance of 1 Ω, whereas sheet resistance of 1 Ω/sq cannot be misinterpreted.

Based on knowledge of layer thickness, the resistivity of the material can be calculated from the sheet resistance using:

$$\rho = R_S \times t \qquad \text{Equation 3}$$

Where ρ is the resistivity, R_S is sheet resistance, and t is the layer thickness. Conventional 4PP measurements are based on direct current, while the set-up employed in the work for this thesis was from the company Capres A/S, using alternating current, which can measure the phase shift (φ) of the electrical signal[113]. The alternating current has a sinusoidal waveform and can be expressed as:

$$I(t) = I \sin(\omega t + \varphi) \qquad \text{Equation 4}$$

where *I(t)* is the current as a function of time (t), ω is the angular frequency, and φ is the phase shift. The phase shift is used by the Capres system to check that a good ohmic contact between the tips of the probe (in this case an L-shaped micro-machined cantilever, shown in Fig. 3.5A and C) and the surface is established. For $\varphi < 1°$, the contact is considered good.
The Capres system was used for measuring the sheet resistance of pyrolysed carbon films as well as to evaluate the presence of contact resistance at the interface between 3D carbon structures and the flat interface carbon layer (Fig. 3.5B-C) (Papers II and IV). Resistance values were used to compare measurements of pillars versus measurements on a flat surface, since sheet resistance is not applicable when measuring on 3D structures, such as the carbon pillars. When measuring on the pillars, a bad ohmic contact can either be at the cantilever/pillar contact or at the pillar/flat interface. If the contact is bad at either of these sites, there will be a significant phase shift. However, it will not be possible to identify specifically at which site the contact is bad. If the ohmic contact is good in both places, there will be hardly any phase shift. For all measurements, the phase shift was 0.2 degree, which is below 1, and thereby considered good. This measurement does not directly give a value of the interface resistance, but it indicates that there is a good ohmic contact between the pillars and the flat interface, i.e. the interface has a negligible contact resistance, and should therefore not interfere with the electrode performance.

3.4. Contact Angle Measurement

Analysis of surface wettability, expressed as the contact angle (CA) between the liquid and the surface enables functional and structural characterization of the surface. CA gives information about e.g. hydrophobicity, surface energy, roughness, contamination, and surface heterogeneity [116,117]. For determination of CA, the Sessile drop method (Fig 3.6A)[118] involves measuring the CA α directly from a liquid drop profile after placing it on the surface. α is the equilibrium CA, described by Young's equation[118]:

$$\gamma_{LV}\cos(\alpha) = \gamma_{SV} - \gamma_{SL} \qquad \text{Equation 5}$$

where γ_{LV}, γ_{SV} and γ_{SL} are liquid-vapor, surface-vapor and surface-liquid interfacial tensions, respectively.

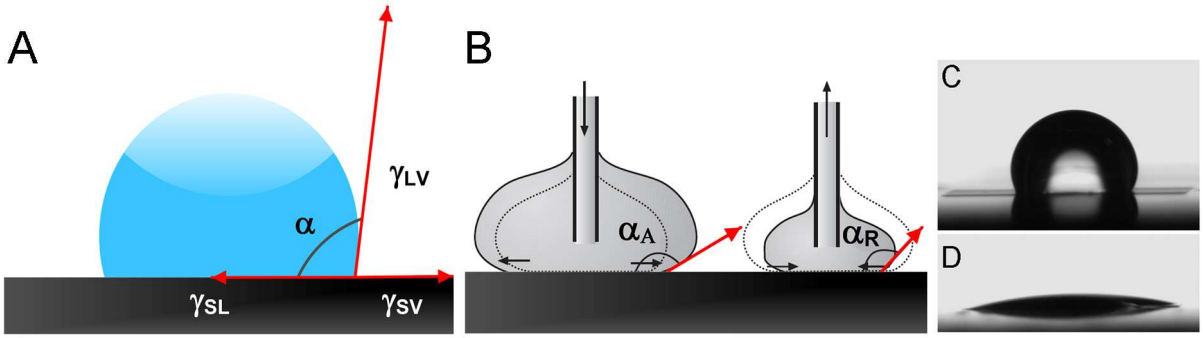

Figure 3.6. (A) Sessile drop method[116] for measuring the static contact angle α where γ_{LV} is the liquid-vapor, γ_{SV} the surface-vapor and γ_{SL} the surface-liquid interfacial tension, respectively. (B) Contact angles for evaluating the advancing contact angle, α_A, and the receding contact angle, α_R[118]. Static contact angle, using water as liquid on carbon pillar electrode arrays, before (C) and after (D) O_2 plasma treatment.

Young's equation is only valid for ideal systems, e.g. chemically homogeneous, rigid, and smooth at an atomic scale. In these cases, a single unique CA exists[119]. The failure of the system to meet the ideal conditions is the theoretical basis for the hysteresis, which is defined as the difference between the advancing, α_A, and the receding contact angle, α_R , α_A - α_R[118,119]. The equilibrium CA is between the $\alpha_A$and α_R contact angles. Hence, a drop on a surface has CA values ranging from the α_A to the α_R.

The α_A and α_R CAs are obtained by increasing and decreasing the liquid volume of a droplet on the solid surface until the drop-surface boundary starts to move over the surface. This is done by keeping a syringe needle immersed in the droplet, while adding or withdrawing liquid from it during the measurement (Fig. 3.6B). In Fig. 3.6C and D, static CA measurements on 3D carbon pillar electrodes are shown before (C) and after O_2 plasma treatment (D) using water as liquid. Aside from the static CA, the CA hysteresis should also be measured to better describe the surface heterogeneity[118,119], in terms of e.g. roughness, micro-and nanostructuring, as well as surface functionality Hence, CA measurements were used to evaluate the effect of surface modifications, such as plasma treatment (Papers III and IV in chapters 6) and electrochemical modification using diazonium salt (Paper III), on the wettability of 2D and 3D electrodes.

3.5. Electrochemistry

Electrochemical techniques can be used to study the characteristics of electrode surfaces, but also as a strict analytical detection tool. Both approaches have been used in this thesis. Among the electrochemical characterization techniques, cyclic voltammetry (CV) and electrochemical impedance spectroscopy (EIS) are the most widely used and described in this thesis. The electrochemical performance of carbon produced by pyrolysis of e.g. photoresists has been extensively studied[27,52–54,86,87,120,121]. Electrochemical reactions at pyrolysed photoresist electrodes exhibit electron transfer kinetics (the rate at which an electron can be transferred from the electron donor to the electron acceptor) very similar to those at commercial glassy carbon electrodes[52]. During the research for this thesis, applications of electrochemical techniques were explored for:

- Characterization of the electrochemical behaviour of microfabricated 2D and 3D carbon electrodes, e.g. pyrolysed films with different thicknesses derived from SU-8 photoresist.
- Evaluation of surface modification of 2D and 3D carbon electrodes, e.g. CV for dopamine before and after oxygen plasma treatment; CV and EIS in presence of a

redox couple that has reversible behavior, such as ferri- and ferrocyanide, to compare the effect of plasma treatment and electrochemical grafting of carboxylic acids.

- Amperometry monitoring of dopamine exocytosis from populations of a model cell line, pheochromocytoma (PC12) cells, as well as of human neural stem cells (hNSCs)

3.5.1. General Introduction to Electrochemistry

An electrochemical cell consists of two half-cells, one anode and one cathode, which are in contact through an external conductor and at least one electrolyte solution. A reduction always takes place at the cathode and an oxidation always takes place at the anode.

3.5.1.1. Thermodynamic Cell Potential

At equilibrium, when no current is flowing through the electrochemical cell, the thermodynamic cell potential or Nernst potential (E_{Nernst}) is referred to as the open circuit potential (OCP) for the electrochemical cell and is given by the expression,

$$E_{Nernst} = E_c - E_a \qquad \text{Equation 6}$$

where E_c is the electrode potential for the cathode reaction, and E_a is the electrode potential for the anode reaction. E_{Nernst} is the theoretically calculated cell potential for a galvanic cell or the theoretically calculated cell potential necessary to apply in order to drive an electrolytic cell.

Conventionally, half-cell reactions are written as reduction reactions. For the general reaction $M^{n+} + ne^- \rightleftharpoons M(s)$, it is possible to write the Nernst equation, which relates the electrode potential to the concentration of electroactive species in solution, approximating that for dilute solutions, the activity for the ion M^{n+}, $a_{M^{n+}} \approx [M^{n+}]$, and where $a_{M(s)}$ =1.

$$E_M = E_M^0 - \frac{RT}{nF} \ln \frac{1}{[M^{n+}]} \qquad \text{Equation 7}$$

where $E_M{}^0$ is the standard electrode potential *at standard conditions* (where the activity a_{Mn+} = 1 and the temperature T = 298.15 °K), n is the number of electrons, R is the gas constant

=8.3145 (J/mol K), F is Faraday's constant = 96485 (C/mol), T is the absolute temperature, and $[M^{n+}]$ is the concentration of the electroactive species in solution.

Electrode potentials for half-cell reactions are defined as the thermodynamic cell potential (E_{Nernst}) in an electrochemical cell in which a theoretical standard hydrogen electrode (SHE) serves as the anode, where E_{SHE} has been assigned the potential 0 V (at all temperatures) at standard conditions of a_{H+} =1, p_{H2} = 1 atm, and T = 298.15 °K. For the general reaction according to equations (6) and (7) this means that:

$$E_{Nernst} = E_M - E_{SHE} = E_M - 0 = E_M^0 - \frac{RT}{nF}\ln\frac{1}{[M^{n+}]} \qquad \text{Equation 8}$$

where E_{Nernst} becomes a direct measure of the E_M, which at standard condition means that it becomes a measure of E_M^0. E^0 values for numerous half-cell reactions are available in the literature and are by definition a value for the tendency for reduction. The higher the E^0 is, the higher is the tendency for reduction, and vice versa, the lower the E^0 is, the higher is the tendency for oxidation.

By converting the natural logarithm to the log10, a more commonly used expression for Nernst equation is obtained:

$$E_M = E_M^0 - \frac{0.0592}{n}\log\frac{1}{[M^{n+}]} \quad or \quad E_M = E_M^0 + \frac{0.0592}{n}\log[M^{n+}] \qquad \text{Equation 9}$$

The Gibbs free energy for a redox reaction (ΔG) is related to E_{Nernst} through the expression $\Delta G = -nFE_{Nernst,}$ where $\Delta G = \Delta G° + RT\ lnK$. Here, K is the equilibrium constant for the redox reaction, and $\Delta G°$ is the Gibbs free energy at standard conditions, giving an indication whether the reaction will take place spontaneously or not.

A true SHE does not exist since it is virtually impossible to obtain a condition that provides a pH=0. Instead a well-defined reference electrode, e.g. Ag/AgCl ($E_{Ag/AgCl}$ = 0.198 V *vs.* SHE) or saturated calomel electrode (SCE, E_{SCE} = 0.245 V *vs.* SHE), is employed as a reference point to obtain the OCP or to measure a current at an electrode.

The *standard electrode potential* E^0 is often replaced in the Nernst equation by the *formal electrode potential* $E^{0'}$. The latter can be used for any set of conditions, not just when all activities are at unity. This is an important entity when, e.g. protons take part in the redox reaction, which is the case for the oxidation of dopamine and many other biochemical reactions. Biochemists therefore define the formal potential at physiological pH.

At equilibrium conditions without current flow in an electrochemical cell, when a redox couple is present in solution, the concentration of the oxidised ([Ox]) and reduced ([Red]) species at the electrode surface is equal to the corresponding bulk concentration. Nernst equation can be written as:

$$E = E^{0\prime} + \frac{0.059}{n} \log \frac{[Ox]}{[Red]} \qquad \text{Equation 10}$$

For a redox couple present in equimolar concentration the corresponding form of equation 10 is:

$$E = E^{0\prime} + \frac{0.059}{n} \log \frac{[Ox]^1}{[Red]} \qquad \text{Equation 11}$$

In this case, the logarithmic concentration-dependent term becomes zero and thereby $E = E^{0'}$.

3.5.1.2. Currents in Electrochemical Cells

When a potential (deviating from E_{Nernst}) is applied across the electrode/solution-interface, it drives the transfer of electrons between the electrode material and the electroactive species in the electrolyte, thus generating a current. The processes taking place at the electrode-electrolyte interface can be divided into faradaic and non-faradaic processes. Faradaic processes are governed by Faraday's law of electrolysis[g], which states that the current is directly proportional to the number of molecules reduced or oxidised. Hence, faradaic processes involve electron transport across the electrode-electrolyte interface, whereas the non-faradaic processes comprise modulation effects of charge distributions at the interface.

The poised potential at the electrode shifts the energy level of the free electrons, resulting in electron transfer between the conductive material and the molecular orbitals of the redox species in solution energetically favourable (Fig. 3.7). By applying a negative potential to an

[g] Faraday's law of electrolysis: $I = \frac{Q}{t} = \frac{nFn_x}{t}$ where Q is the total charge carried by electrons that are accepted or donated, t is the time during which the current is recorded, n is the number of accepted or donated electrons, F is the Faraday constant (96.485 C mol^{-1}), and n_x is the number of moles of the chemical species oxidized or reduced.

electrode, the energy of the electrons in the electrode material increases, resulting in a flow of electrons from the electrode to the Lowest Unoccupied Molecular Orbital (LUMO) of the species in the electrolyte. Consequently, reduction of the oxidised species (Ox) in solution takes place (Ox + e^- → Red; reduction or cathodic current). Similarly, when the electron energy in the electrode material is decreased upon application of a positive potential electrons from the Highest Occupied Molecular Orbital (HOMO) are transferred from the reduced species in the solution to the conductive electrode material. This leads to oxidation of the reduced species in solution (Red → Ox + e^-; oxidation or anodic current) (Fig. 3.8)

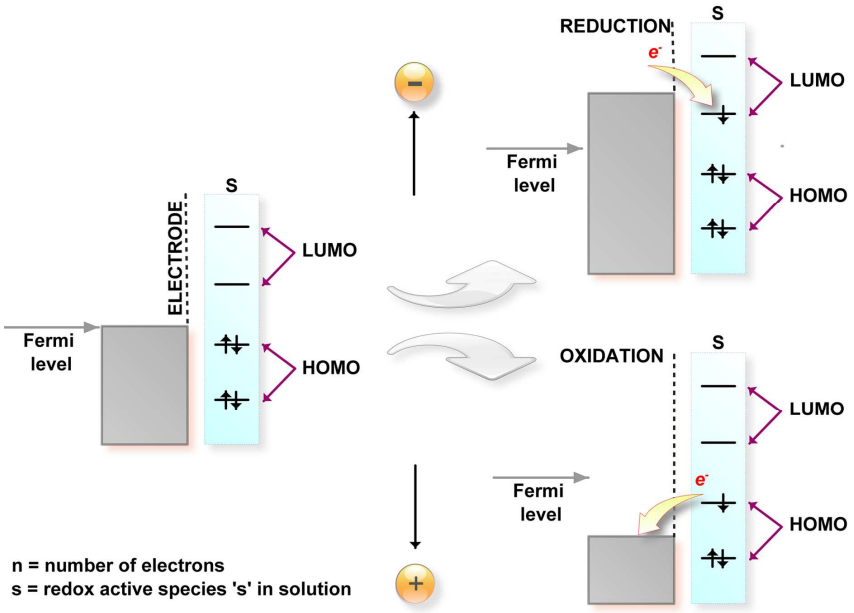

Figure 3.7. When the equilibrium potential is perturbed, applying a positive or negative potential to the WE, oxidation or reduction, respectively, will occur at the electrode/electrolyte interface.

For an electrochemical reaction to take place at the electrode surface, a positive or negative potential step must be applied deviating from the formal potential $E^{0'}$. The applied positive or negative potential difference with respect to the $E^{0'}$ is called the overpotential η, and serves as a driving force for the electrochemical reaction to occur. The values of potentials able to activate reduction and oxidation processes depend on several factors, such as: (i) the junction potential due to the construction of the electrochemical cell; (ii) the potential drop due to presence of the double layer and ohmic resistance; (iii) adsorption and reaction polarizations related to adsorption effects and intermediate limiting reactions, and (iv) charge transfer resistance due to the material properties.

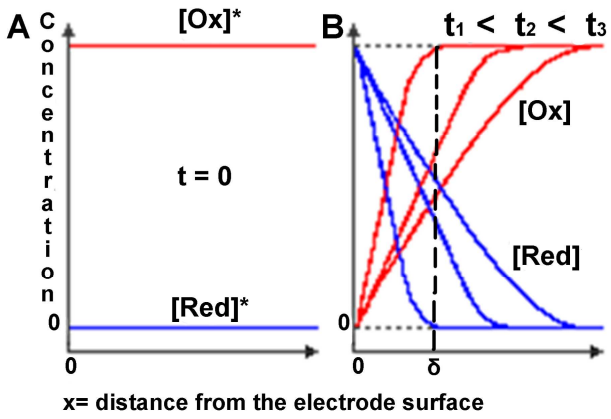

Figure 3.8. The concentration profile before (A) and after (B) application of a potential step: When no potential is applied, the concentration of Red and Ox species is uniform in the system and equal to the bulk concentration. Upon application of a potential to the electrode surface, a stagnant layer called the *Nernst diffusion layer* (δ_{ox} for the oxidized species and δ_{red} for the reduced species) is present. The consumed redox species are replenished through this layer by diffusion, regardless of the overall mode of mass transfer in the bulk solution. During reduction $[Ox]_{x=0}$ decreases with the time, whereas during oxidation $[Red]_{x=0}$ decreases. Modified from [h].

The amplitude of the obtained cathodic or anodic current is directly related to the amplitude of the negative or positive potential applied until a limiting current is reached. The limiting current is regulated by the mass transfer of the redox species in the bulk solution e.g. by diffusion. Assuming for simplicity that diffusion of the redox species is equal ($D_{Ox}=D_{Red}$ and and $\delta_{OX}= \delta_{RED}$), the measured current ($i_{measured}$) can be related to the applied η through the equation:

$$\eta = \frac{RT}{nF} \ln \frac{i_{l,c} - i_{measured}}{i_{measured} - i_{l,a}} \qquad \text{Equation 12}$$

where $i_{l,c}$ is the cathodic limiting current for reduction of the oxidized species, and $i_{l,a}$ is the anodic limiting current for oxidation of the reduced species. Fig. 3.9 depicts a current-overpotential curve, where the measured current is plotted as a function of the applied η. In the curve, η = 0 indicates the equilibrium position.

[h] http://www.chem.uoa.gr/applets/AppletDiffus/Appl_Diffus2.html

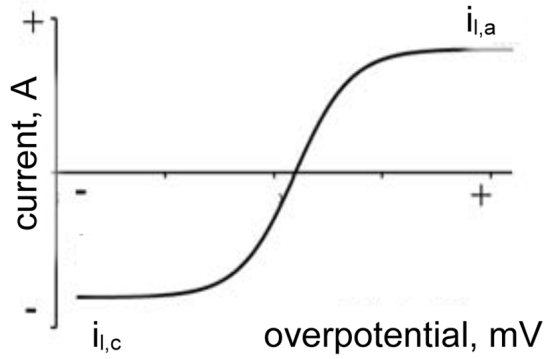

Figure 3.9 An arbitrary current-overpotential curve for a redox couple having equivalent mass transfer for both Ox and Red.

3.5.2. Inner and Outer Sphere Redox Systems

Depending on the mechanism of electron transfer taking place between the electrode and the electroactive species[122,123] (Fig. 3.10), it is possible to distinguish different classes of reactions:

- Outer sphere redox system - the electron transfer occurs through a solvent layer, which is in contact with the surface. The chemical interaction between the electrode and the electroactive species can be considered as non-existent.
- Inner sphere redox system - the electrode and the electroactive species are in direct contact and therefore the electron transfer occurs directly.

The first generally accepted theory of inner and outer sphere systems was initially elaborated by R. Marcus[124] to explain different rates of electron transfer reaction. McCreery and co-workers intensively studied inner and outer sphere redox systems in relation to their electrochemical behaviour at carbon material surfaces[125,126], distinguishing between inner-sphere reactions, which depend on the electrode surface chemistry, and outer-sphere routes, which are essentially insensitive to it[123]. An example of inner sphere redox system is $Fe^{3+/2+}$, whose redox reaction is facilitated by transient interactions with surface oxides[15]. Hence, this redox system is inhibited significantly if surface oxides are absent or obscured by adsorbates[126].

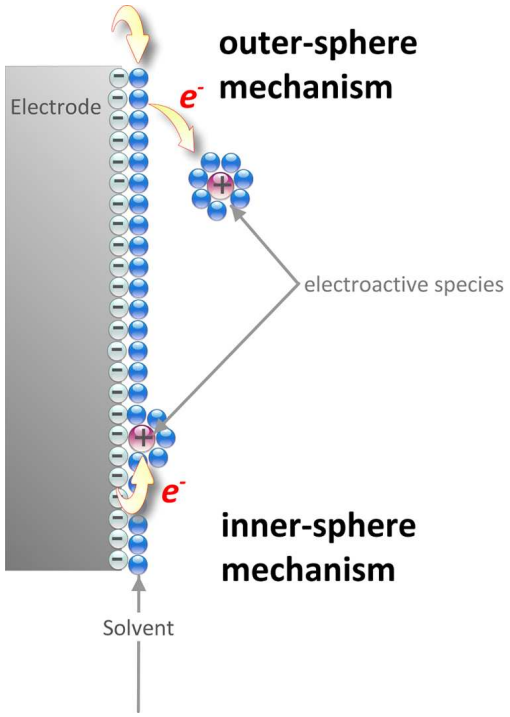

Figure 3.10. Mechanisms of electron transfer.

The $Ru(NH_3)_6^{3+/2+}$ redox system is considered as outer sphere and should not be influenced by impurities and different surface characteristics of electrodes, since it does not interact with any surface sites or functional groups on the electrode[123,126,127]. The $Fe(CN)_6^{3-/4-}$ couple is considered a 'non-ideal' outer sphere system[15], due to its sensitivity to impurities and negatively charged surface oxides (e.g. carboxylates)[15,123,126,127]. When surface carboxylates are present and deprotonated at neutral pH, electrostatic effects take place, affecting electron transfer kinetics of the $Fe(CN)_6^{3-/4-}$ couple[126]. This phenomenon was observed at pyrolysed carbon electrode surfaces after modification with oxygen plasma and electrochemical grafting of diazonium salt (paper III). The $Ru(NH_3)_6^{3+/2+}$ couple was used to compare carbon electrodes derived from different polymer precursors for electron transfer reactivity, as reported in section 3.5.4.

3.5.3. Measurements with Two and Three-Electrode Systems

During electrochemical experiments, where techniques such as cyclic voltammetry and amperometry are used, a three-electrode setup is a common configuration. In this setup, one of the electrodes is utilized for controllable electrochemical processes, and is defined as the working electrode (WE). The potential of the WE is adjusted to a desired value versus a

reference electrode (RE), such as a Ag/AgCl electrode, which has a stable and known potential. The RE is connected to a lead of the potentiostat having high impedance, thus eliminating the possibility of current flowing through this lead. A third electrode, the counter electrode (CE), closes the electrical circuit, and current passes between CE and WE through the electrolyte.

When small currents are flowing in the system, a two-electrode configuration can be used, consisting just of a WE and a CE. This configuration was applied during electrochemical impedance spectroscopy (EIS) measurements (section 3.2.6).

3.5.3.1. The Working Electrode (WE)

Different materials, such as a metal or carbon, can constitute the WE, and can be used as it is or modified in different ways. Reactive sites, surface functionalities, modifications and electronic properties of an electrode can affect the electrode kinetics[127]. Moreover, electron transfer at semiconductor electrodes is often much slower than on metals, because of a low density of electrons (charge carriers[i])[127]. The conductivity of different carbon allotropes varies greatly due to their different structures, ranging from insulators (such as diamond) to semimetals (graphite)[15]. For pyrolysed carbon materials, derived from different polymers and at various pyrolysis temperatures, the electrical properties range from an insulator to a semiconductor and semimetal[22].

3.5.3.2. The Reference Electrode (RE)

In micro- and nanofabricated systems, pseudo-reference electrodes (pseudo-REs), such as a Ag wire coated with a layer of solid silver chloride (AgCl), or a plain metal electrode (e.g. gold or platinum), are used as reference electrodes (REs). Pseudo-REs are common in microfabricated systems due to their possibility of being miniaturized and to their simplicity of manufacture[128]. Contrarily to conventional REs, pseudo-REs do not have an internal electrolyte to ensure the stability of the reference electrode potential. The electrochemical potential of a pseudo-RE is not defined, and may thereby be affected by contaminating species (such as adsorption of proteins in solution) or variation of the conditions in the

[i] Electrons that are free to move and carry charges within e.g. metal electrodes, are responsible for conduction of electric current.

electrochemical cell. These effects are eliminated in conventional REs by using highly concentrated filling solutions, e.g. saturated KCl in the Ag/AgCl reference electrode[128]. Due to this, it is important to check the pseudo-REs potential regularly and adjust the potential accordingly. A pseudo-RE, i.e., Ag wire coated with AgCl, was used for most of the experiments performed for this thesis. Due to toxicity of Ag/AgCl electrodes[j] on biological systems[129], a Pt wire was used as pseudo-RE in paper IV.

3.5.3.3. The Counter Electrode (CE)

Typically, no reactions under study occur at the surface of the counter electrode (CE) to not adversely influence the reactions occurring at the WE. The same number of electrons is transferred at the CE as is transferred at the WE. Due to this a fast electron transfer as well as a larger area than the WE are important in order for the CE not to become a limiting factor in an electrochemical system. Platinum is one commonly used material for the CE, due to its inertness and the fast electron transfer kinetics occurring at its surface. Platinum was also used during the experiments performed for this thesis. However, less expensive materials may also be used, such as carbon, other metals, etc.

3.5.4. Cyclic Voltammetry

In cyclic voltammetry, the current response is measured upon application of a linear potential with a triangular waveform (Fig. 3.11). This triangular potential excitation signal sweeps the electrode potential between two extreme values (switching potentials $E_{\lambda 1}$ and $E_{\lambda 2}$). Important parameters, such as the peak currents (i_{pa} – anodic and i_{pc} – cathodic) and the peak potentials (E_{pc} - cathodic and E_{pa} – anodic) can be extracted from the cyclic voltammogram (CV).

For a diffusion controlled and reversible electron transfer process at 25°C (298 K), the peak current (i_p) is given by the Randles-Sevcik equation[20]:

$$i_p = (2.687\ x\ 10^5)\ n^{3/2}\ v^{1/2} D^{1/2} A C \qquad \text{Equation 13}$$

[j] Ag ions are toxic for cells.

where *n* is the number of electrons exchanged in the redox reaction, *v* the potential scan rate in Vs^{-1}, *D* the diffusion coefficient of the reduced or oxidized species in cm^2s^{-1}, *A* is the area in cm^2, *C* the concentration in mol cm^{-3}.

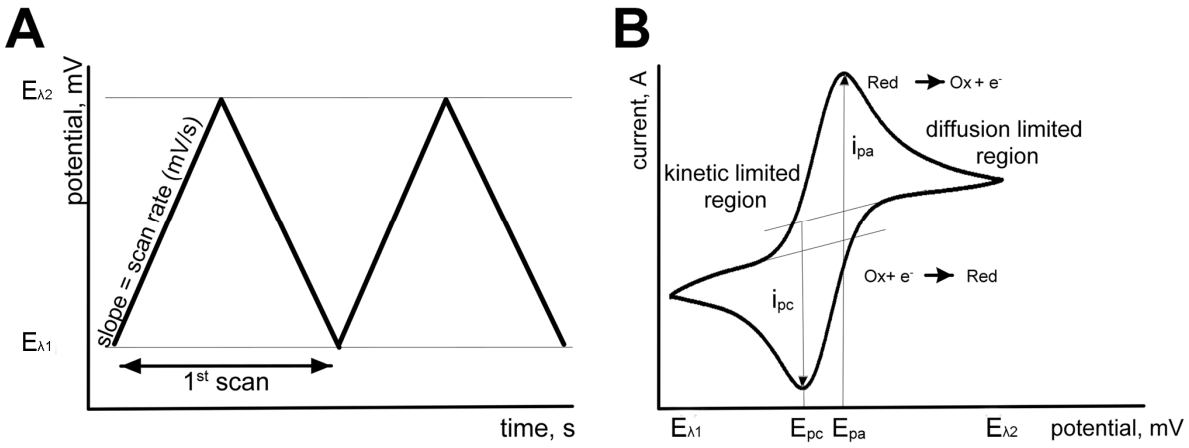

Figure 3.11 Principles of cyclic voltammetry. (A) Triangular potential waveform. (B) A typical cyclic voltammogram (CV) recorded at an SU-8-derived pyrolysed carbon film electrode in the presence of a redox couple that has reversible behaviour, e.g. $Ru(NH_3)_6^{3+/2+}$. The figure shows the parameters that can be derived from a CV. $E_{\lambda1}$ and $E_{\lambda2}$ are the switching potentials; i_{pa} and i_{pc} are the anodic and cathodic peak currents, respectively; E_{pc} and E_{pa} are the cathodic and anodic peak potentials, respectively.

From the peak potential values it is possible to estimate the degree of electrochemical reversibility of the redox process by analysing the difference between the cathodic and anodic peak potential ($\Delta E_p = |E_{pa} - E_{pc}|$), where ΔE_p is close to 59/n mV[k] at 25 °C for a reversible redox reaction[130,131]. Moreover, it is possible to estimate the formal potential ($E^{0'}$) of the redox couple involved in the reaction through the expression $E^{0'} \approx E_{1/2} = (E_{pa}+E_{pc})/2$. Cyclic voltammetry is therefore a very useful tool to characterize the electrochemical behaviour of novel electrode materials or surface modifications. Another important parameter that can be derived from cyclic voltammetry is the i_{pa}/i_{pc} ratio that for nernstian systems is equal to unity, regardless of scan rate, E_λ, and diffusion coefficients.

By studying the behaviour of a chosen redox compound, different electrode modifications can be compared (as was done for dopamine in Paper III and ferri-ferrocyanide in Paper IV). Aside from electrochemical properties, other factors can affect parameters such as ΔE_p and

[k] For a fully nernstian system the value 59/n mV is related to Nernst equation (equation 7) (n is the number of electrons involved in the reaction).

peak current. Examples are increased resistance due to: (i) thin carbon film (Paper II) (Fig. 3.12), (ii) thin leads from the WE to the electrical contacts, and (iii) bad external contacts, all resulting in an increased ΔE_p and lower peak currents.

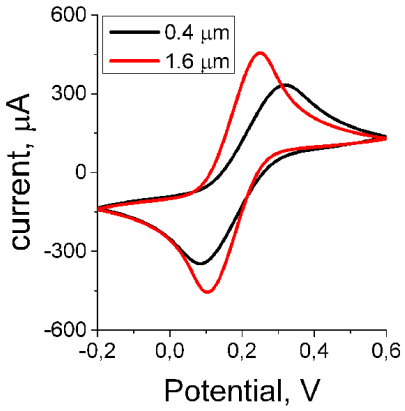

Figure 3.12 Representative CVs at pyrolysed carbon films of 0.4 µm and 1.6 µm thickness (in 10 mM potassium hexacyanoferrate (II/III) in PBS pH7, scan rate 100 mV s^{-1} versus Ag/AgCl pseudo-reference electrode). The acquired CVs showed lower ΔE_p values for 1.6 µm carbon films compared to 0.4 µm films as well as an increase in peak current for the 1.6 µm film. The decrease in ΔE_p values and increase in peak current with increased film thickness are likely due to decreased resistivity for thicker films, which are thus more favourable for electron transfer at the electrode surface.

Cyclic voltammetry also facilitates evaluation of kinetic parameters of a redox reaction at an electrode surface. The method of Nicholson allows to determine the standard rate constant for electron transfer (k^0) from the experimental ΔE_p[131,132]. Knowing the scan rate v, k^0 can be calculated from:

$$k^0 = \psi \ (D_0 \pi v)^{½} \left(\frac{nF}{RT}\right)^{½} \left(\frac{D_R}{D_0}\right)^{\alpha/2} \qquad \text{Equation 14}$$

where values of the numerical charge transfer parameter, ψ, can be obtained from the working function introduced by Nicholson[132] that relates the variation of ΔE_p with ψ (Fig. 3.13). D_R and D_0 are the diffusion coefficients for the reduced and oxidized form of the redox couple, respectively. α is the charge transfer coefficient, which for most general cases is 0.5.

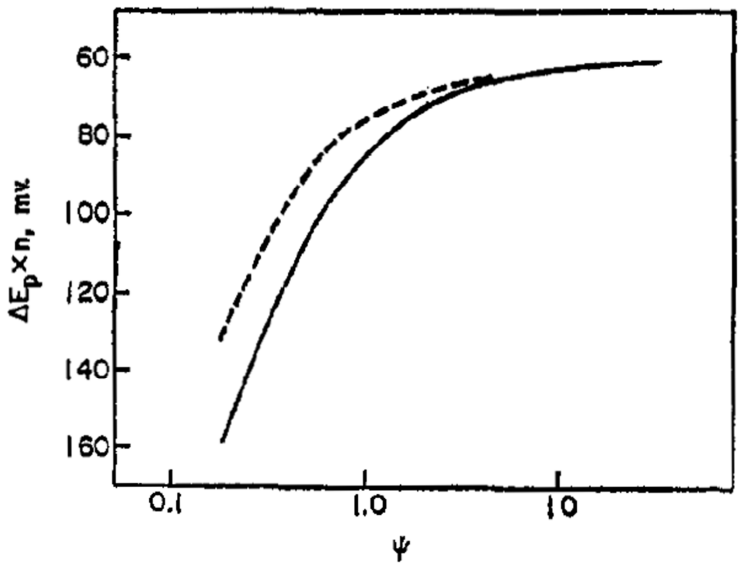

Figure 3.13 Working curve relating ΔE_p with ψ[132]

For evaluation of k^0 at pyrolysed carbon electrodes derived from different polymer precursor templates, the $Ru(NH_3)_6^{3+/2+}$ redox couple was used. In this case, D_R is the diffusion coefficient of $Ru(NH)_6^{2+}$ ($6.7x10^{-6}$ cm^2 s^{-1})[133], and D_0 is the diffusion coefficient of $Ru(NH)_6^{3+}$ ($8.4x10^{-6}$ cm^2 s^{-1})[134]. Table 3.2 shows k^0 values for different pyrolysed carbon materials, calculated from ΔE_p values obtained at a scan rate of 10 mVs^{-1}.

Table 3.2. k^0 values calculated with equation 14 from the experimental ΔE_p of the CVs obtained in 1mM $Ru(NH_3)_6^{3+/2+}$, scan rate 10 mV s^{-1}. SU-8 – 0.5 µm and SU-8 - 11 µm indicate two different thicknesses of the analysed carbon film, PS is polystyrene, and PS-PDMS is polystyrene-block-polydimethylsiloxane.

Electrode	ΔE_p (mV)	k^0 (cm s^{-1})
PS-PDMS	109	8,0E-02
PS	78	3,3E-01
SU-8 - 0.5 µm	92	1,2E-01
SU-8 - 11 µm	72	5,4E-01

The increased electron transfer kinetics of a pyrolysed SU-8 film with 11 µm thickness compared to the one with 0.5 µm thickness is in accordance with the lower resistivity for thicker carbon films (paper II). Moreover, the slower electron transfer kinetics of PS-PDMS compared to PS and SU-8 films may be related to its lower carbon content (as shown by XPS

analysis in Table 3.1), as well as to its higher microstructural disorder (as shown by Raman spectroscopy in Fig. 3.4).

Moreover, electron transfer kinetics are very useful for determination of the surface characteristics of an electrode, e.g. after surface modification. For instance, compared to untreated carbon surfaces for surfaces modified with O_2 and H_2O/O_2 plasma higher ΔEp values (derived from the CVs) and hence slower electron transfer of the $Fe(CN)_6^{3-/4-}$ redox were observed (paper III). This is caused by increased electron density conveyed by increased oxygen functionalities introduced by the plasma.

3.5.5. Amperometry

In amperometry, the measured current is dependent on an applied constant potential. The necessary applied constant potential value can be determined from a CV, based on the obtained anodic and cathodic peak potential. The overpotential at which the desired electrochemical reaction, i.e. reduction or oxidation, is driven must be high enough to ensure rapid depletion of the electroactive species at the electrode surface, such that the process is controlled by diffusion to the electrode. For example, if the formal potential of the redox couple is 0 mV vs. Ag/AgCl, the WE needs to be poised at a more negative potential value in order to follow the reduction, or at a more positive potential value for the oxidation. The recorded current includes contributions from:

- The faradaic current due to oxidation or reduction of a species, caused by the shift in the electrode potential from the equilibrium position;
- The charging current due to charging of the electrical double layer capacitance on the electrode surface. After the initial potential step, the charging current level reaches a maximum value (at $t \approx 0$) and then decays exponentially; the magnitude of which is essentially determined by the magnitude of the potential step and the resistance of the solution according to Ohm's law.

The exponential decay of the charging current is completed in a period of microseconds. After that the registered current (i) primarily comprises a contribution of the faradaic current, which decays with time asymptotically approaching zero when large electrodes with linear

diffusion pattern are used. This behaviour is valid under diffusion-controlled conditions, where the current is limited by diffusion of the analyte to the electrode surface (unstirred solution) and follows the Cottrell equation:

$$i\,(t) = \frac{nFAD_i^{½}C_i^*}{\pi^{½}t^{½}} \qquad \text{Equation 15}$$

where A is the electrode area (cm^2), C_i* is the bulk concentration ($mol\,cm^{-3}$) of the reduced or oxidized component i of a redox couple, depending on whether an oxidation or reduction reaction, respectively, is being studied, n is the number of electrons involved, F is the Faraday constant ($C\,mol^{-1}$), D_i is the diffusion coefficient for the electroactive species i ($cm^2\,s^{-1}$), and t is the time (s).

When amperometry is used for detecting an electroactive analyte that for instance is released by cells, the sample electrolyte does not initially contain the electroactive species in question. An applied potential step causes, nevertheless, an initial decay of current comprised of the double layer charging current and the ionic current in the electrolyte. When the current has decayed to a constant level a baseline is obtained for the subsequent measurements of the released electroactive species. Upon release its oxidation or reduction results in formation of a current-time trace (peak) as seen in Fig. 3.14. Amperometric detection was used to evaluate the capabilities of 3D-carbon scaffolds for monitoring dopamine exocytosis from two different cell lines grown on the scaffolds (paper IV).

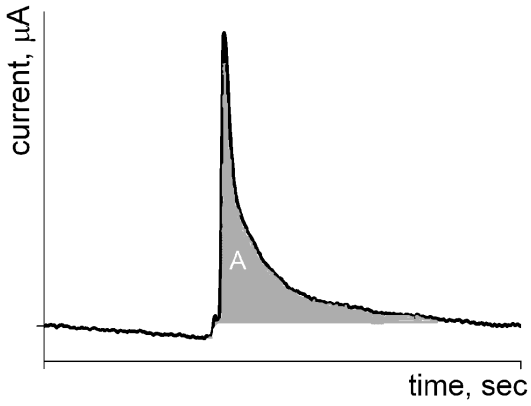

Figure 3.14 Typical current-time trace recorded during exocytosis measurements. (**A** – peak area)

3.5.6. Electrochemical Impedance Spectroscopy (EIS)

3.5.6.1. General Introduction to EIS

Electrochemical impedance spectroscopy (EIS) is a useful technique for characterization of materials as well as for evaluation of electrode surface modifications[135]. In EIS a small-amplitude sinusoidal excitation potential, E(t), is applied to a two-electrode system (a WE and CE) in a chosen frequency (f) range. The applied potential, E(t), can be expressed as function of time t:

$$E(t) = E_0 \, sin\,(2\pi f t) = E_0 \, sin\,(\omega t) \qquad \text{Equation 16}$$

where ω is the radial frequency of the applied potential and E_0 is the amplitude of the potential. The sinusoidal potential E(t) results in a sinusoidal current response, I(t), with the same frequency but shifted in phase (φ), which can be expressed as a function of time:

$$I(t) = I_0 \sin(\omega t + \varphi) \qquad \text{Equation 17}$$

where I_0 is the amplitude of the current. In analogy to Ohm's law, the total impedance of the system *Z* can be expressed as:

$$Z(\omega) = \frac{E(t)}{I(t)} = \frac{E_0 \sin(\omega t)}{I_0 \sin(\omega t + \varphi)} = |Z| \, \frac{\sin(\omega t)}{\sin(\omega t + \varphi)} \qquad \text{Equation 18}$$

Hence Z is expressed in terms of a magnitude |Z| and a phase shift φ. The phase shift is determined by the resistive and capacitive components of the system:

- The sinusoidal potential across a resistor generates a sinusoidal current response that has the same phase angle as the applied potential (φ = 0° - purely resistive behaviour) (Fig. 3.15A).

- The sinusoidal potential across a capacitor results in a current that is delayed by 90°[l] (φ = -90° - purely capacitive behaviour) (Fig. 3.15B).

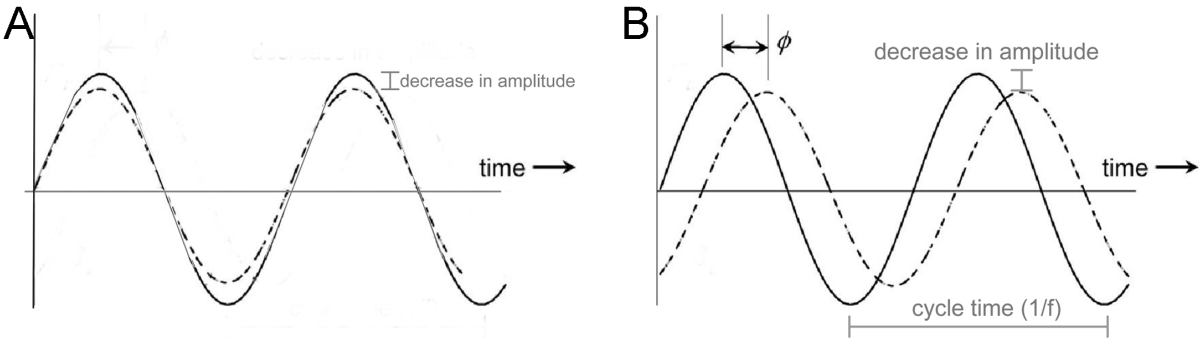

Figure 3.15 (A) A sinusoidal potential (solid line) across a resistor generates a sinusoidal current response (dashed line) that has the same phase angle as the potential (φ=0). (B) The same sinusoidal potential across a capacitor results in a current that is delayed by a phase angle of φ=-90°.

Using Euler's relationship, $e^{j\varphi} = \cos\varphi + j\sin\varphi$, where $j = \sqrt{-1}$, the impedance Z can be written as a combination of a real (Z_{RE}) and an imaginary (Z_{IM}) component:

$$Z(\omega) = \frac{E(t)}{I(t)} = \frac{E\, e^{j\omega t}}{I\, e^{j\omega t - j\varphi}} = |Z|\, e^{j\varphi} = |Z|\,(cos\varphi + jsin\varphi) = Z(\omega)_{RE} + jZ(\omega)_{IM}$$

Equation 19

Where $Z(\omega)_{RE}$ (in-phase) results from the resistive components of the system, and $Z(\omega)_{IM}$, (out-of-phase) from the capacitive ones[m].

3.5.6.2. Electrical Double Layer

The structure that describes the charge distribution at the electrode-electrolyte interface at atomic level is called electrical double layer. The solution side of the double layer consists of multiple layers, schematically represented in Fig. 3.16. The layer closest to the electrode is called *inner Helmholtz layer* and is composed of solvent molecules and specifically adsorbed ions. The Inner Helmholtz plane (IHP) contains these specifically adsorbed ions define. The next thicker layer of solvated ions, the *outer Helmholtz layer*, covers the transition of ionic

[l] Impedance of a capacitor decreases as the frequency increases. The impedance behaviour of a capacitor versus frequency is opposite to that of an inductor.

[m] If the descriptive equivalent circuit is very complex, as is often the case in electrochemistry for real systems, both real and imaginary components comprise contributions of resistive and capacitive properties.

concentration from the electrode surface to the bulk solution. The solvated ions are nonspecifically adsorbed, and since they are shielded by the first layer, they interact more weakly by long-range electrostatic forces with the charged electrode surface. The Outer Helmholtz Plane (OHP) comprises these nearest solvated ions. Due to thermal agitation in the solution, the nonspecifically adsorbed ions are distributed in the region that extends from the OHP into the bulk of the solution, called the *diffuse layer*[131].

Since the charged electrode is separated from the charged ions[n], the electrical double layer resembles a parallel-plate capacitor[o].

The overall impedance of an electrochemical cell, consisting of a WE, a CE, and an electrolyte, has three main contributions: (1) Impedance of the electrolyte R_s, (2) interface impedance of the WE, and (3) interface impedance of the CE. Usually, the CE has a larger dimension than the WE. Thus, the CE interface impedance is much smaller and thereby negligible compared to the WE interface impedance[p].

[n] The separation distance is in the order of Angstroms.

[o] Charges separated by an insulator form a capacitor. In a normal case there is no insulator in a double layer capacitance but due to electrode modifications this is exactly what can be the consequence.

[p] Impedance is directly proportional to resistance ($Z \propto R$) and inversely proportional to capacitance ($Z \propto 1/C$). Since capacitance is proportional to the area of a capacitor ($C \propto A$), and the resistance is inversely proportional to the area of a resistor ($R \propto 1/A$), the total impedance of the system is inversely proportional to the area of the system ($Z \propto 1/A$).

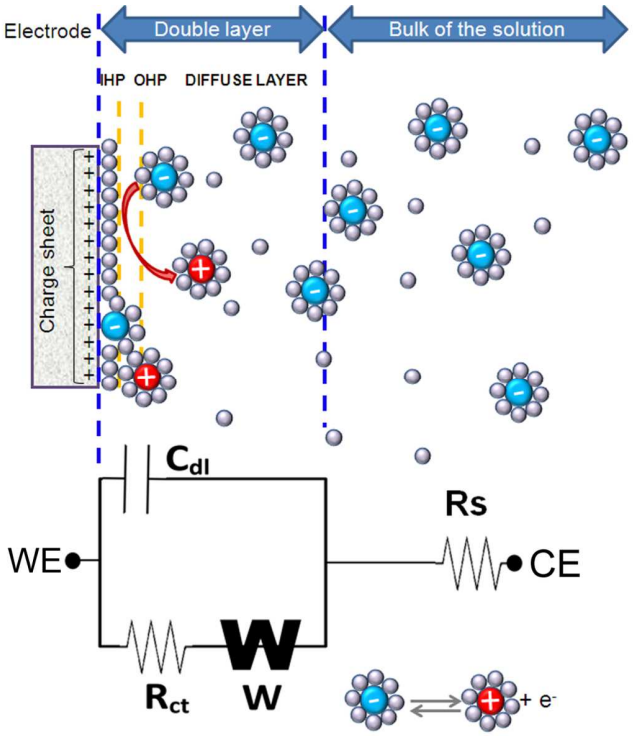

Figure 3.16. An interfacial electrochemical reaction with diffusion- and double layer component with the Randles electrical equivalent circuit describing the interface. Abbreviations: C_{DL}, double-layer capacitance; CE, counter electrode; IHP, Inner Helmholtz Plane; OHP, Outer Helmholtz Plane; R_{ct}, charge transfer resistance; R_S, solution resistance; WE, working electrode; W, Warburg impedance

EIS data are commonly analysed by fitting them to an equivalent electrical circuit model using non-linear regression. The circuit elements in the model are electrical elements such as capacitors, resistors, and inductors. The simplest general equivalent circuit for an electrode/electrolyte interface[q] comprises the series of the double layer capacitance C_{DL} and the solution resistance R_S[r] (Fig. 3.17).

Figure 3.17 Equivalent circuit for electrode/electrolyte interface.

[q] The impedance of a series circuit containing a resistor and a capacitor is: $Z(\omega) = R - (j/C\,\omega)$

[r] The R_S depends on the ionic concentration, type of ions, temperature, and the geometry of the area in which current is carried, while the value of the C_{DL} depends on electrode potential, temperature, ionic concentrations, types of ions, oxide layers, electrode roughness, and impurity adsorption.

For low frequencies the capacitive term dominates and the impedance is determined by the charged interface, while for high frequencies the impedance is purely resistive and determined by the bulk solution. Hence, by varying the frequency, different individual contributions to the overall impedance of an electrochemical system can be investigated. This facilitates, e.g. understanding and troubleshooting of anomalous results, which can be related to problems with an electrode surface or contacts to external instrumentation, whereas the same information cannot be obtained by CVs.

If the electrolyte also contains a redox couple, the occurring redox reactions lead to charge transfer and thus mass transfer affects the electrochemical behavior of the system. The WE interface impedance includes two main components and is described by Randles equivalent circuit model shown in Fig. 3.16[136], describing the contribution of the system to the total impedance:

- Non-faradaic - due to the contribution of the electrical double layer capacitance (C_{dl})
- Faradaic - due to (i) redox reactions taking place across the interface by overcoming an activation barrier, namely the charge transfer resistance R_{ct} (kinetically controlled property of the system), (ii) mass transfer of the redox species, affecting the rate of electron transfer at the electrode surface (mass transfer resistance), defined as Warburg impedance W (diffusion controlled property of the system).

3.5.6.3. Representation of EIS Measurements

Recorded data from EIS measurements can be plotted in different ways, such as:

- Bode plot: The magnitude of impedance ($|Z|$) and the phase angle (φ) are plotted as a function of the frequency (f) on a logarithmic scale.
- Nyquist plot: The negative of the imaginary impedance ($-Z_{IM}$) is plotted as a function of the real impedance (Z_{RE}) (Fig. 3.18).

A Nyquist plot provides a clear visualization of the system characteristics. It consists of a semicircle and a linear portion (Fig. 3.18).

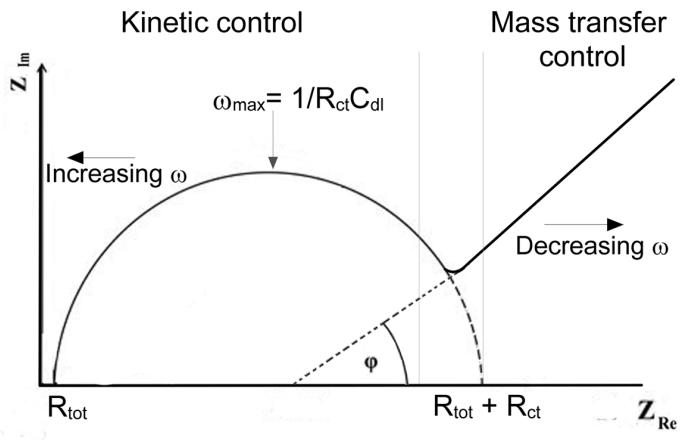

Figure 3.18 A Nyquist plot, resulting from measurement in a solution containing redox active compounds, showing the relationship between the phase angle (φ), and the real- and imaginary-component of the impedance.

The semicircle portion at higher frequencies (increasing in direction ← of the plot) represents the capacitive behaviour. The semicircle diameter represents the charge-transfer resistance, R_{CT}, i.e. the electron transfer limitation. The highest point of the semicircle gives the electrical double layer capacitance. The intercept of the Nyquist plot at the real-axis indicates the magnitude of the solution resistance. However, in systems where external contacts have significant resistances, these are also included in the resistance indicated by the intercept of the semicircle, R_{TOT}. The linear portion at lower frequencies (decreasing in direction → of the plot) corresponds to the diffusion-limited process and is characteristic of systems with mass transfer control properties. The linear part forms ideally a 45° angle (phase angle, φ[s]) with the Z_{Re}-axis, i.e. mass transfer related properties cause a 45-degree phase shift in the response signal.

On solid electrodes, such as carbon electrodes, the non-faradaic component of the interface (the double layer capacitor) does not behave purely as a capacitor, but instead as a constant phase element[137] (CPE). This indicates the presence of non-uniform current distribution, which in carbon electrodes is originated by, e.g. the presence of both edge and basal planes[138]. The electron transfer reaction rates of redox systems at basal planes are more sluggish compared to the ones at the edge plane[48], resulting in inhomogeneous reaction rates

[s] $\varphi = \tan^{-1}(Z_{IM} / Z_{RE})$

and hence giving rise to non-ideal capacitive behaviour, modelled as CPE[t]. The centre of the obtained semicircle of a Nyquist plot is often situated below the real-axis (Fig. 3.19). By rotating the Nyquist plot, corresponding to an "ideal" behaviour (solid line in Fig. 3.19), by an angle $\varphi = \alpha\,\pi/2$ it is possible to represent the "CPE" behaviour (dotted line). α is an empirically derived constant that for CPE is < 1 and can give an idea of the degree of resistive and capacitive properties: α = 1 indicates a purely capacitive interface (i.e. the CPE resembles a pure double-layer capacitance); α = 0 indicates the presence of a pure resistance. Generally, for increased surface inhomogeneity, such as roughness and inhomogeneous reaction rates, alfa decreases. For pyrolysed carbon films the decreasing α value seems to be related to the roughness increase for thicker films (paper II). Moreover, for untreated pyrolysed carbon films, α is quite low (0.74) in comparison with smooth e-beam evaporated gold surfaces (~0.9)[139] and increases upon modification with diazonium salt (0.91), indicating that the degree of inhomogeneity decreases (paper III).

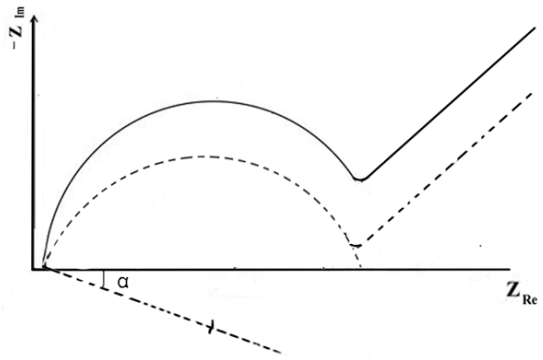

Figure 3.19 Nyquist plot with α = 1 (solid line) and 0< α <1 (dashed line).

If the acquired impedance spectra of a system are better described using a CPE instead of C_{DL}, the C_{DL} value can be obtained using the relation[135,137]:

$$C_{DL} = \left(\frac{Q\,R_S\,R_{CT}}{R_S + R_{CT}}\right)^{1/\alpha} \frac{R_S + R_{CT}}{R_S\,R_{CT}} \qquad \text{Equation 20}$$

[t] CPE is an empirical quantity given by: CPE = $Q(j\omega)^{-\alpha}$, where Q is the magnitude of CPE at ω = 1 and α is the multiplication factor of the phase angle.

Where Q is the magnitude of CPE at frequency ω=1, and the other parameters are the same as previously described. The C_{DL} value can also be obtained from the Hsu and Mansfeld formula[140]:

$$C_{DL} = Q\ (\omega''_{max})^{\alpha-1} \qquad \text{Equation 21}$$

Where ω''_{max} is the angular frequency at which the absolute value of Z_{Im} reaches its maximum (Fig. 3.17), Q is the magnitude of CPE at frequency ω=1, and α is the multiplication factor of the phase angle.

Aside from the Nicholson method, which allows to evaluate the kinetic parameters k^0 from ΔE_p derived from CV (section 3.2.6), estimation of k^0 can also be done by considering the electrochemical basis of the R_{CT}, as indicated in eq.22[131]:

$$R_{CT} = \frac{RT}{C^* n^2 F^2 A k^0} \qquad \text{Equation 22}$$

where *R* is the molar gas constant, *T* is the absolute temperature of the system, *C** is the equal concentration of the oxidized and reduced form of the used redox probe, *n* is the number of electrons involved in the redox process, *F* is Faraday's constant, *A* is the area of the electrode surface available for the redox process, k^0 is the apparent standard rate constant of the redox process at a very small sinusoidal potential which only causes a small perturbation of the system from the equilibrium, characterized by the OCP.

EIS facilitated characterization of pyrolysed carbon films derived from SU-8 of different thicknesses in relation to their resistance (paper II). Moreover, evaluation of different surface modifications (plasma treatment and electrochemical modification with diazonium salt) was possible (paper III).

3.3. Immunocytochemistry and Image Analysis

Immunocytochemistry is used to detect specific molecules or proteins (antigens) in cells or tissues. This is done by exploiting antibodies that can bind specifically to the target molecules, allowing unique detection of molecules and proteins of interest in a sample[141]. By

tagging the antibody to, e.g. a fluorophore, the antibody-antigen interaction can be visualised with a fluorescent or a confocal laser-scanning microscope. For immunocytochemistry detection, antibodies are classified as primary or secondary (Fig. 3.20A). A primary antibody (first layer) specifically recognises and binds to the target antigen and is typically unlabelled. The secondary antibody (second layer) is usually labelled with a tag and reacts with the primary antibody, enabling detection of the target antigen.

In the work performed for this thesis, immunocytochemistry was used to label tyrosine hydroxylase (TH) and beta tubulin in neural stem cells. TH is the rate-limiting enzyme for production of the neurotransmitter dopamine, and beta tubulin is the characteristic cytoskeletal component of neuronal axons. This was done to indirectly confirm dopaminergic phenotype of stem cell-derived neurons growing and differentiating on commercial plasticware, as well as on different 3D carbon scaffolds (Paper IV). The staining of the nuclei allows estimation of the number of cells expressing TH out of the total number of cells (example shown in Fig. 3.20 B).

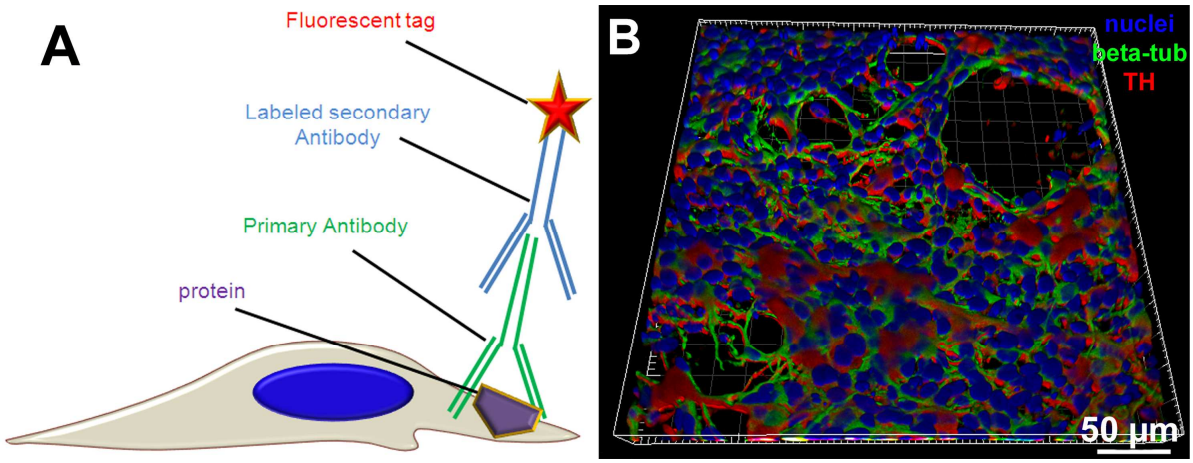

Figure 3.20 (A) Conceptual drawing of immunocytochemistry. (B) Confocal laser scanning image showing differentiated neural stem cells on carbon scaffolds. Nuclei are blue, beta tubulin positive cells are green, and TH positive cells are red.

Chapter 4

Surface Modification of Carbon Structures for Biological Applications

This chapter describes the treatment methods that have been investigated to modify the surface of 2D and 3D carbon electrodes during the work performed for this thesis.

The surface chemistry of pyrolysed carbon electrodes is important for their electrochemical behaviour and application[126,142]. Modification prior to their use is therefore often a necessity. To introduce specific surface functionalities, which confer properties suited for a desired application, carbon materials can be modified with different physical and chemical treatments. Moreover, functionalization of the surfaces can facilitate physisorption or covalent tethering of molecules, such as enzymes, antibodies, DNA, and cell adhesion factors that are required for biological applications[143–146]. For instance, increasing the surface functionalities on pyrolysed carbon material is necessary when using it as a substrate[21] or scaffold for cell growth (paper IV).

4.1. Surface Characteristics of Pyrolysed Carbon Electrodes

Similarly to GC electrodes[126,147126,147], the surface of pyrolysed carbon materials is heterogeneous and consists of basal and edge planes of graphene sheets which is not graphitized[108]. The atoms on the edge plane of the graphene sheets are much more reactive than the atoms on the basal plane, the latter of which are atomically ordered. Hence chemisorbed foreign elements, such as oxygen, are predominantly located on the edges[48,108,142].

Generally, the pyrolysis process conditions as well as the precursor polymer material strongly affect the nature and the distribution of surface functional groups and heteroatoms, which determine the surface chemistry of the pyrolysed carbon structures. For instance, an oxide terminated surface is produced when pyrolysis is conducted in non-reducing atmosphere (e.g. in presence of argon and nitrogen)[52,121]. Moreover, exposure of a pristine carbon surface to even trace amounts of oxygen results in a submonolayer coverage of carbon–oxygen complexes, which are thought to be located near the edges of polyaromatic sheets in carbon[108,126,142]. Figure 4.1 shows a representative but non comprehensive list of oxygen functionalities present on carbon surfaces[48,126].

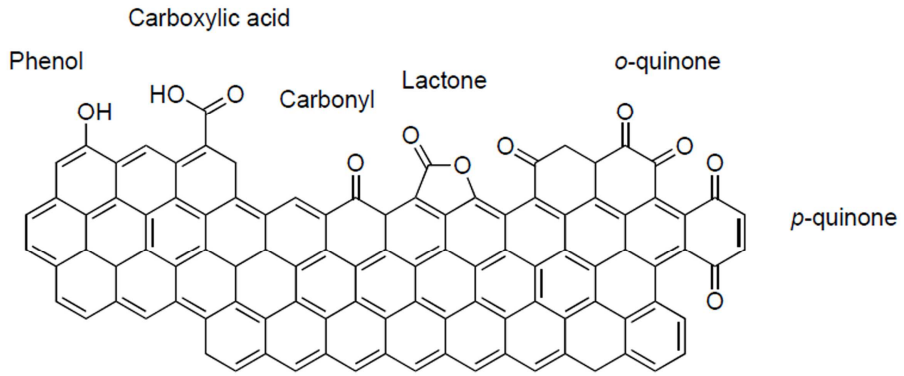

Figure 4.1. Oxygen functionalities that can be present on pyrolysed carbon surfaces[108,126]

These functional groups have been extensively studied with different techniques, such as optical spectroscopy, XPS, thermal desorption mass spectrometry[15], and infrared spectroscopy[21,148,149]. In this thesis, the functional groups on pyrolysed carbon were identified by XPS, which revealed that on untreated surfaces, phenolic (C-OH) and carbonyl groups (C=O) were the most abundant functionalities (Table 4.1) (paper III).

Table 4.1. Relative percentage (average ± SD. n= 3) of functional groups obtained from deconvolution of C_{1s} spectra for untreated samples of pyrolysed carbon surfaces derived from SU-8. Deconvolution gives four individual component groups that represent graphitic carbon (C=C) and sp^3 hybridized C (C-C), phenolic (C-OH) and carbonyl (C=O) functionalities, and shake-up satellite[u]

Functional groups	
C-C & C=C	63.14 ± 0.76
COH	12.05 ± 0.04
C=O	8.77 ± 0.29
shake up	16.05 ± 0.61

The oxide coverage and the type of functional groups can vary widely with e.g. the original polymer material precursor used (Table 3.2). Moreover, the tendency of oxygen terminated surfaces to adsorb impurities leads to variable surface functionalities[150]. Contamination by adsorbates increases the oxygen/carbon atomic (O/C) ratio on samples exposed to the

[u] Shake-up satellite peaks are found in structures with conjugated π systems, such as aromatic rings in graphite.

ambient atmosphere in the laboratory (Fig. 4.2), a phenomenon that has been also observed for glassy carbon[7] and pyrolysed positive photoresist[52]. Possible mechanisms responsible for adsorption of nonpolar adsorbates are the creation of e.g. induced dipole[151].

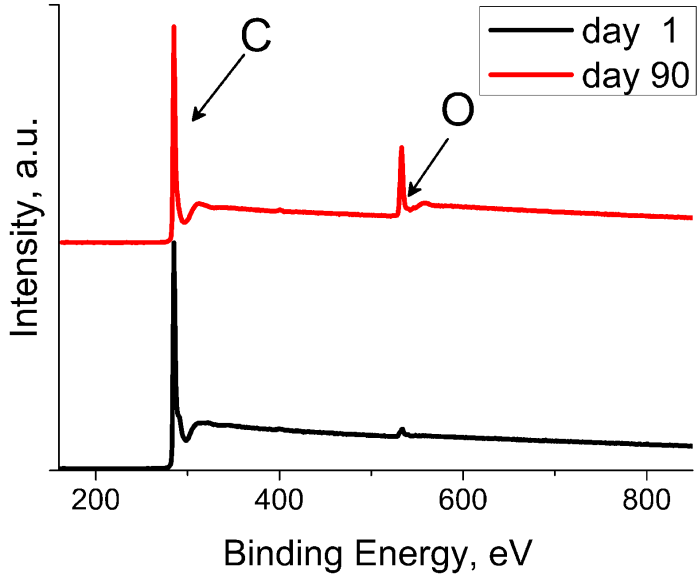

Figure 4.2. Survey spectra of pyrolysed carbon derived from SU-8 photoresist films. The O/C ratio increases from 0.02 at day 1 to 0.1 at day 90 after pyrolysis.

Pyrolysis in a reducing atmosphere (e.g. in presence of forming gas) minimizes carbon oxidation, leading to a low O/C ratio[52]. This may result in a hydrogen-terminated carbon surface, which is relatively stable towards oxidation in the ambient atmosphere during storage. The lower reactivity can be due to lower density of unsatisfied valences on hydrogen terminated surfaces[52], similarly to hydrogen plasma treated glassy carbon[151]. Hydrogen terminated carbon surfaces tend to be both unreactive[152] and hydrophobic[151], properties which limit their further application. For obtaining reproducible coverage of surface functionalities as well as for rendering carbon surfaces with properties suitable for electrochemistry and biological applications, modification of the surfaces is needed.

4.2. Tailoring the Surface Chemistry of Pyrolysed Carbon Electrodes for Electrochemical Detection and Cell-Based Applications

Different treatments have enabled modification of carbon materials, such as polymer coatings[35,153,154], plasma modifications[3,10,11,19], UV-assisted modification[92,157,158], oxidation using strong acids (e.g. HNO_3 or H_2SO_4)[148,159] or anodization[160], and electrochemically-assisted covalent modification[161]. Here, plasma treatment and electrochemical reduction of diazonium salt will be described.

4.2.1. Plasma Treatment

Plasma treatment of carbon surfaces is a rapid, effective, and versatile method that can easily be tuned to introduce a wide range of functional groups by varying the plasma parameters, such as power, pressure, gas mixture, and treatment time[149]. The excited species, i.e. electrons, radicals, and ions within the plasma, strongly interact with the pyrolysed carbon surface, breaking e.g. C=C bonds. The complex mixture of surface functionalities introduced by the plasma influence the physical and chemical properties of the surface. Specifically, it results in a dramatic change of the increased electron density (conveyed by e.g. increased oxygen functionalization) and roughness, which influences the wetting characteristics of the surface[116]. Moreover, the introduced functional groups on the pyrolysed carbon are active sites that can be further exploited for tethering molecules, such as antibodies[162], proteins[163], and DNA[92].

In this thesis oxygen plasma treatment was performed to increase the surface wettability of 2D and 3D carbon electrodes (Paper IV), and hence resulted in enhanced physisorption of adhesion factors that are required for cell adhesion, spreading, growth, and differentiation (see section 4.3). Moreover, the effect of oxygen plasma and water vapour/oxygen plasma treatments on pyrolysed carbon electrodes was evaluated in terms of wettability, surface composition, and electrochemical behaviour (Paper III).

4.2.2. Diazonium Salt Modification

Although plasma treatment of carbon can generate different types of surface functionalities, and can be performed easily and on large areas, ultimately, the number of obtainable

functional groups is, nevertheless, limited (Fig. 4.1). Methods for electrochemically assisted modification of a carbon surface offer the possibility of selective grafting of functional groups[161]. The most commonly used electrochemically assisted modification of carbon materials are: (i) reduction of aryl diazonium salts, leading to aryl terminated carbon, and (ii) oxidation of aryl acetates or amines that graft aryl or amine groups covalently to the carbon surface[161].

In diazonium salt modification the molecule used during the reaction is commonly a substituted benzene ring (the substituent on the benzene is the aryl substituent)[161]. The presence of selected functional groups on the aryl substituent can lead to useful electrode surface properties[161], facilitating further chemistry for immobilization of enzymes[143,144], antibodies[145], and electroactive groups[146]. Moreover, since the reaction is induced electrochemically, it is possible to limit and direct the modification specifically to e.g. only some electrodes in an array of individually addressable working electrodes.

Electrochemical reduction of aryl diazonium salt was the modification used during the work in this thesis. This method was first applied to carbon electrodes (GC, carbon fibers, carbon powder, and highly oriented pyrolytic graphite) in 1992[164] and has since then been extensively studied[165]. However, it has been also successfully used on silicon[166,167], stainless steel[168], copper, gold, and platinum[169], CNTs[170], graphite[171], graphene[172], and PC[173,174]. The method yields a very stable surface functionalization, requiring mechanical abrasion for its removal (indicative of the covalent nature of the attachment)[175]. The modification (Fig. 4.3) involves reaction of phenyl amines with sodium nitrite ($NaNO_2$) to form a phenyl diazonium ion[v], capable of undergoing electrochemically induced one-electron reduction on carbon electrodes, thus generating a phenyl radical and N_2, the former of which reacts with the carbon surface by coupling to an unsatisfied valence or adding to a double bond[176].

[v] The phenyl amine is first dissolved in hydrochloric acid, and then a solution of sodium nitrite is added. The reaction between the hydrochloric acid and the nitrite ions produces the nitrous acid HNO_2. The positive ion, containing the $-N_2^+$ group, is known as a diazonium ion.

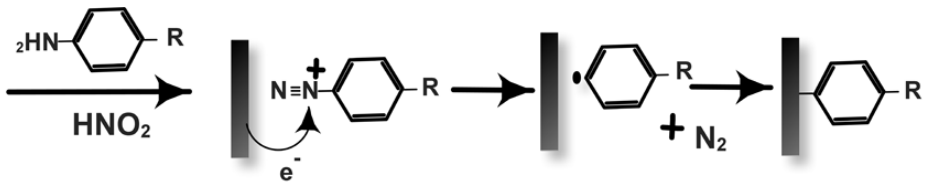

Figure 4.3 Modification of carbon surfaces by phenyl amines reduction[165,177].

Similar to alkanethiol mixed layers on gold[178], obtained from solutions of different alkanethiols[w], it is possible to use mixed layers of aryl diazonium salts[179].

During the research performed for this thesis, reduction of aryl diazonium salt with a carboxylic substituent was performed and compared to plasma modification in terms of electrochemical behaviour and wettability (Paper III).

4.3. Biocompatibility

The traditional concept of biocompatibility of materials implicates a "do not harm" mission[180] (i.e. nontoxic, nonmutagenic, etc.) and is often evaluated using measurements of cell morphology, viability, and growth. However, these parameters are not sufficient to assess their effects on the molecular level, such as alterations of gene expression[181]. Due to the link between gene expression and disease mechanism, the impact of an experimental system on cellular functions should be minimal, or at least known[181]. Hence, the choice of investigated biocompatibility parameters for novel biomaterial as well as microfabricated 2D and 3D structures is vital. It has therefore been suggested that the concept of material biocompatibility should be modified, i.e., a material is biocompatible when it: (1) does not induce cell death, (2) supports cell proliferation, and (3) does not alter the transcriptome profile compared to a reference material such as polystyrene (biocomparability)[182]. In the work performed in this thesis, the biocompatibility and biocomparability of pyrolysed carbon electrodes were tested at different conditions (with and without oxygen plasma treatment as well as with and without polylysine coatings) (Fig. 4.4) and compared with polystyrene plastic ware (paper IV).

[w] Organic thiols adsorb onto gold surfaces from solution and form ordered monolayers (self-assembled monolayers).

Based on a more 'positive' concept of biocompatibility, materials bring an enhancement of the desired biological functions[180], which in the case of neural stem cells can result in an increased manifestation of dopaminergic properties (paper IV). For instance, our immunocytochemistry experiments for the enzyme tyrosine hydroxylase (TH) have revealed that the obtained percentage of TH positive cells for growing cells on pyrolysed carbon is tremendously increased (>70%) compared to cells growing on common plasticware (~2%) (Fig. 4.5).

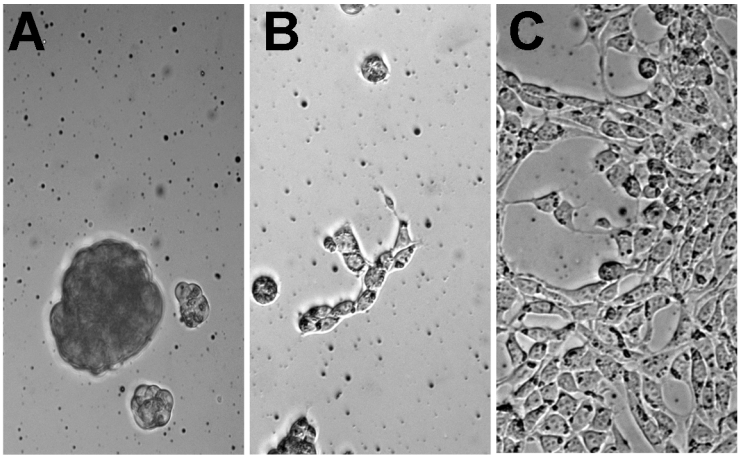

Figure 4.4. Representative micrographs after 24-h culturing of human neural stem cells (hNSCs) on differently treated carbon surfaces. On untreated (A) or plasma treated (B) pyrolysed carbon surface, hNSCs adhere poorly, forming clusters that do not promote cell spreading to acquire the proper morphology. Oxygen functionalities on plasma treated surfaces provide anchoring points for improved physisorption of the primary amine groups of polylysine that mediate cell attachment (C) (paper IV).

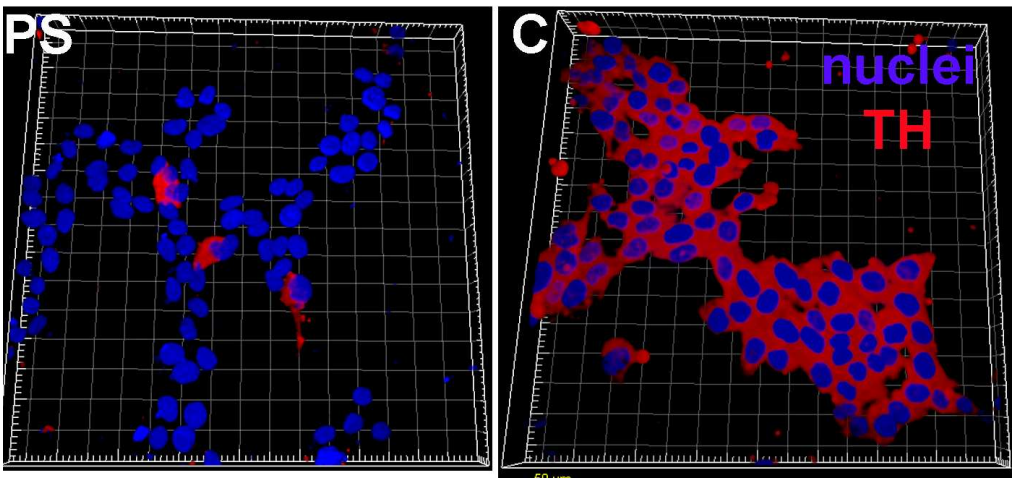

Figure 4.5. Confocal fluorescence images of immunostained growing neuronal stem cells (48h) on: (PS) PLL modified polystyrene (PS) and (C) oxygen plasma and PLL treated flat carbon surfaces. The images show that a much higher % of cells on C is TH positive.

Chapter 5

Micro- and Nanostructures for Cell-Based Research

In this chapter, a brief explanation of Parkinson's disease and different ways of detecting dopamine is presented. Moreover, the mechanism of interaction between cells and the in vivo and in vitro environment will be described.

Micro and nano-engineering techniques are exploited in fabrication of biomaterials to obtain good interfaces and substrates where cells can adhere, divide, grow, and differentiate[183]. Different materials (e.g. hydrogels, polymers, ceramics, composites, silicon, carbon) are currently explored for building substrates and scaffolds for tissue engineering and biomedical research[184–188]. Micro and nanostructured surfaces may be able to tune the response of cells, which could be useful within technologies relevant to e.g. tissue engineering and regenerative medicine[104,188]. Recently, conductive 3D scaffolds (e.g. based on silicon nanowire field-effect transistors, conductive polymers, carbon nanotube (CNT)-doped hydrogels, graphene foam) have emerged as a new approach[187,189–192] to provide both the necessary structural support for cell or tissue growth and a means for localized stimulation/monitoring of the functional dynamics in a cell population. These conductive scaffolds are of particular interest in neuroscience since neuronal functions are strongly influenced by electrical stimuli due to the inherent nature of signal transmission in nerve tissue. During the work done in this thesis, the suitability of conductive carbon scaffolds has been demonstrated for dopamine detection from a neural stem cell line that is clinically relevant for treatment of Parkinson's disease (paper IV).

5.1. Parkinson´s Disease

In the central nervous system (CNS), dopamine is as a neurotransmitter, which belongs to the catecholamine family, modulating e.g. motor functions, memory and learning, feelings of reward and attention, as well as sleep[193]. In patients with Parkinson's disease (PD), the dopaminergic neurons (able to produce dopamine) in *substantia nigra* of the CNS are dysfunctional or dying, causing a subsequent lack of dopamine, which is manifested as e.g. slow movement, tremor, rigidity, inability to initiate movement, as well as involuntary movement[194–196]. Treatments with, e.g. deep brain stimulation, enzyme inhibitors, L-3,4-dihydroxyphenylalanine (L-DOPA), have been shown to be quite effective in alleviating the symptoms influencing motor functions[197,198]. However, therapies for treatment of non-motor symptoms, such as dementia, are still lacking, and disease progression cannot be counteracted[197]. Clinical trials within cell replacement therapy (CRT) with transplantation of neural fetal tissue into the brain (*striatum* area) have provided proof of principle that

neuronal replacement can result in clinical improvement of PD patients (Fig. 5.1)[196,199–201]. The fraction of dopaminergic neurons that form from the transplanted tissue can re-innervate the striatum and restore dopamine production, giving rise to clear symptomatic relief in some patients[196,199,201].

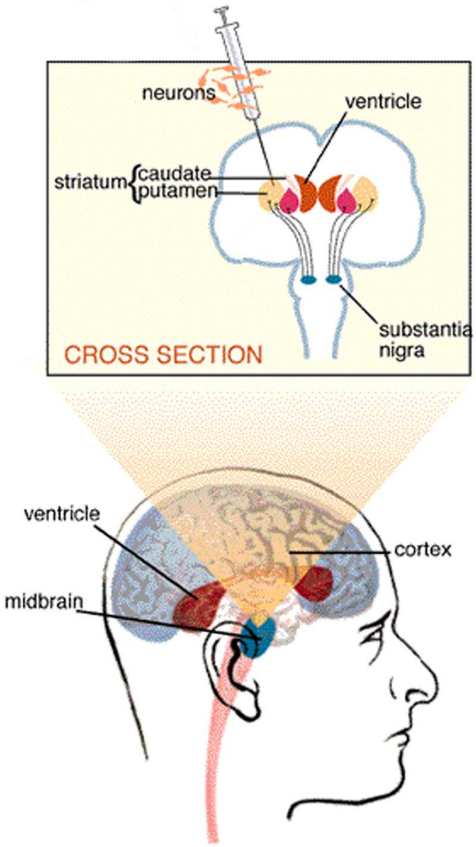

Figure 5.1. Treatment of Parkinson's disease by transplantation of dopaminergic neurons in the brain (cell replacement therapy (CRT)). Adapted from[249].

Stem cells are undifferentiated cells that are able to: (i) differentiate into many specialized adult cell types (e.g. hepatocytes, erythrocytes, neurons, etc.) in response to proper stimuli (*potency*); (ii) proliferate and reproduce themselves maintaining their potency (*self-renewal*). These cells can be classified according to their origin: embryonic stem cells (ES), neural stem cells (NSC) and mesenchymal stem cells (MSC)[202]. NSCs are multipotent cells, derived from the nervous system, with ability to give rise to cells of the three neural lineages: neurons (some of which can be dopaminergic), astrocytes, and oligodendrocytes[198].

In development of NSCs able to differentiate to a dopaminergic lineage, the main concern is how large a fraction of a cell population can show the manifestation of dopaminergic properties. For preclinical transplantation, dopaminergic neurons from stem cells have been

produced *in vitro* from different sources and species[203–219]. Previous studies have shown that the human neural stem cell (hNSC) line hVMbcl-x_L, derived from the ventral mesencephalon, after differentiation generates the highest obtained percentage of dopaminergic neurons, 17.2%[219]. This still imposes a limitation for effective implementation of CRT. Hence, novel substrates and scaffolds for directing the fate of hNSCs to dopaminergic neurons are essential for the field of stem cell research.

The confirmation of a true dopaminergic property (phenotype) necessitates detection of the actually released dopamine. Dopamine is electrochemically active and thus detectable by e.g. amperometry or fast scan cyclic voltammetry[220]. Therefore, conductive substrates and scaffolds could enable e.g. evaluation of chosen differentiation conditions on the number of dopaminergic neurons in a cell population.

Due to the clinical relevance of hVMbcl-x_L NSCs, this cell line was used in the work presented in this thesis (paper IV).

5.2. Neurotransmitter Exocytosis and its Detection

Single-cell studies using fluorescence detection[221] and electrophysiology[222], have revealed the mechanism of dopamine release - exocytosis. Upon electrical, mechanical, and chemical stimulation of neurons (e.g. using an elevated concentration of K^+ ions[223,224]) the Ca^{2+} ion channels present in the presynaptic neuron are depolarized, causing a Ca^{2+} ion influx[223,225]. This event triggers fusion of the vesicles that store neurotransmitters (e.g. dopamine) with the plasma membrane, causing opening of a fusion pore and leading to release of dopamine[223,225](Fig. 5.2).

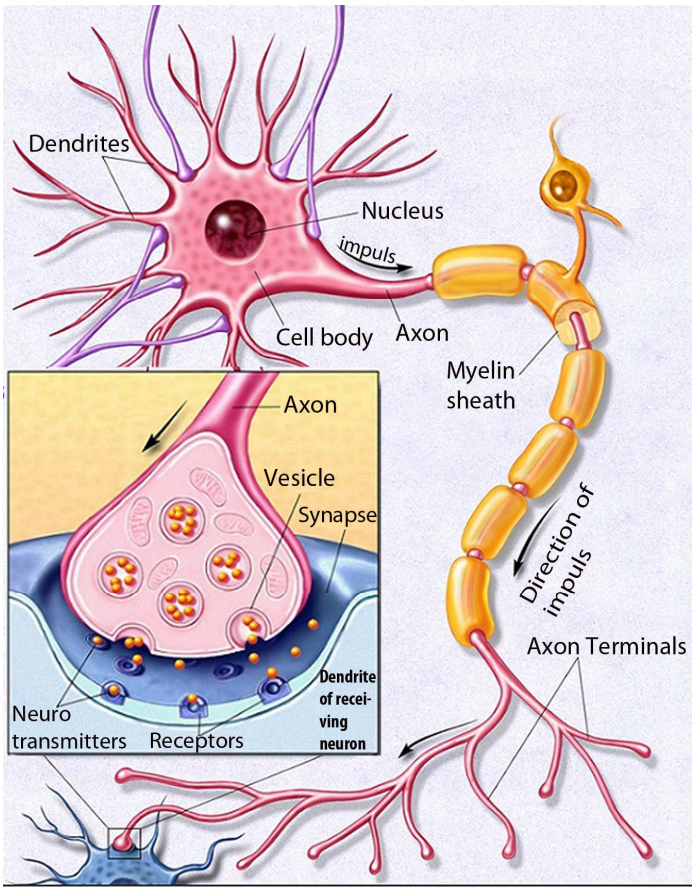

Figure 5.2. Within the nervous system, neurons transmit information to other nerve cells through dendrites, which extend from the neuron cell body, and receive messages from other neurons. Synapses are the contact points where one neuron communicates with another. Inset: mechanism of neurotransmitter release - When an electrical impulse arrives to the gap between two neurons (synaptic cleft), it causes opening of Ca^{2+} ion channels and increases the intracellular Ca^{2+} concentration. This event triggers fusion of the membrane of vesicles containing neurotransmitters with the plasma membrane of the pre-synaptic neuron, leading to release of neurotransmitter. In this way, the electrical signal is converted into its chemical counterpart. Modified from[226].

Real-time monitoring of exocytotic release of dopamine and other catecholamines can be achieved only by electrochemical detection. This has been demonstrated on single cells belonging to different model cell lines (e.g. chromaffin and pheochromocytoma (PC12) cells), which have the Ca^{2+} dependent machinery for releasing catecholamines, such as dopamine. Chromaffin and PC12 cells are not neurons and hence *in vivo* the dopamine in their vesicles does not function as neurotransmitter, but the release mechanism is the same as the release of dopamine and other neurotransmitters from neurons. Hence, information about the process of neurotransmitter exocytosis originates from studies using these model cell lines. Amperometric measurements of catecholamine secretion have been conducted using

carbon fiber microelectrodes[227,228] (placed immediately adjacent to these cells – Fig. 5.3A), and exhibit current spikes corresponding to packages of one vesicle at a time (quantal release)[227,229] (Fig. 5.3B - C).

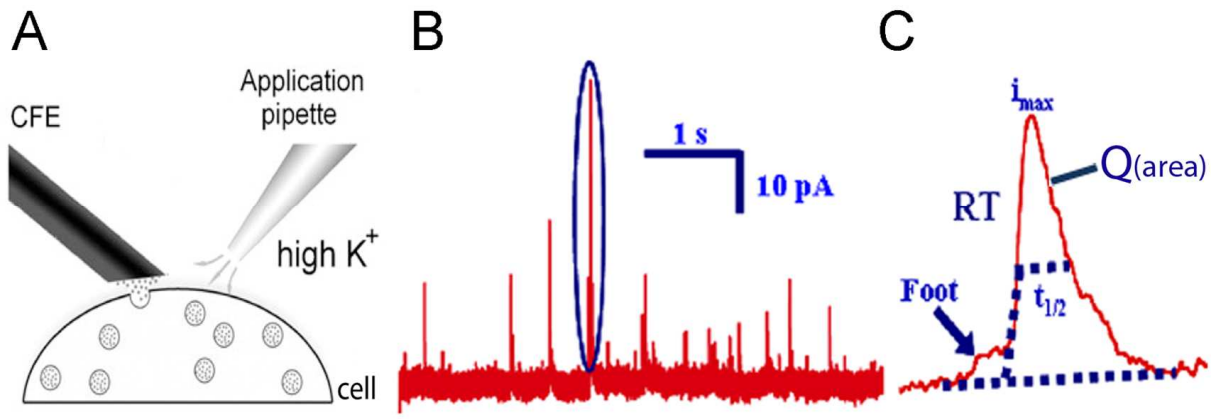

Figure 5.3. (A) Illustration of amperometric measurements on a single-cell using a carbon fibre microelectrode (CFE)[230]. (B) Typical amperometric recording of current spikes from a single cell[231]. (C) Magnification of one current spike with different parameters that can be obtained to characterize exocytotic events, e.g. the spike amplitude (i_{max}), the peak width half height ($t_{½}$), the rise time (RT – time required for recording 25-75% of the i_{max}), the total charge (Q^x- integration of the current of each peak)[231].

In order to lower the cost of these types of experiments and to increase their throughput, amperometric recordings of exocytosis events using planar (2D) microelectrode chips[232–238] are becoming popular, and enable depending on the design dopamine detection from both single cell[232–238] and cell populations[237,238] (Fig. 5.4).

The propensity of metal electrodes to fouling due to polymerization of dopamine on the electrode surface poses limitations for dopamine detection[13]. Therefore, microfabricated electrodes based on carbon represent a very good alternative, and have been employed during the work done for this thesis.

[x] From Q, the total charge, it is possible to derive the total number of released dopamine molecules[227] with the following equation based on Faraday's law of electrolysis: $molecules = QA/nF$, where Q is the total charge, n is the number of electrons involved in the oxidative process (2 for dopamine), F is the Faraday constant (9.6485 x 10^4 C mol^{-1}), and A is the Avogadro's constant.

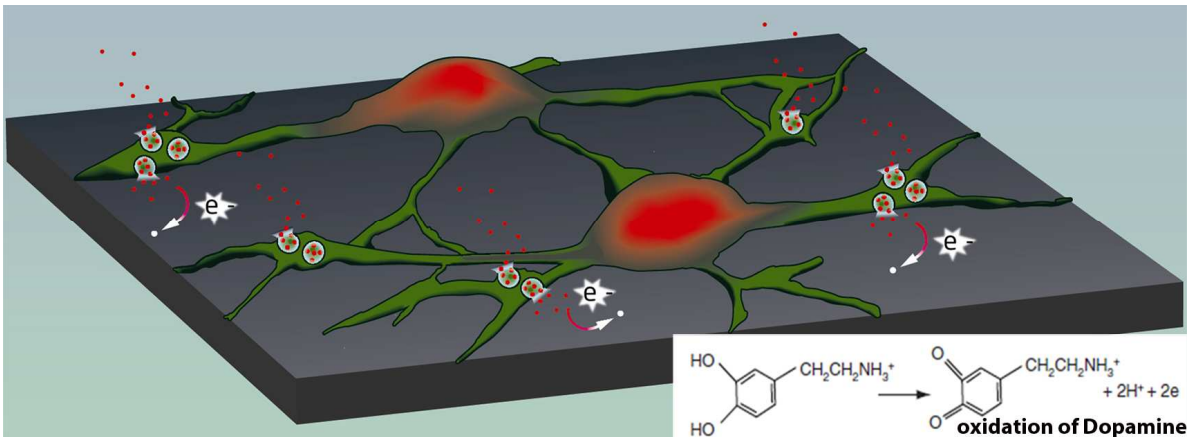

Figure 5.4. Amperometric detection of dopamine at planar microelectrodes from a cell population: the dopamine is immediately oxidized at the potential poised at the electrode. Inset: reaction of dopamine oxidation.

Experiments on single cells have been very useful to elucidate the mechanism of dopamine exocytosis. However, single cell studies cannot be conducted to evaluate dopaminergic properties of cell lines such as hVMbcl-x_L NSCs, due to their dependence on surface anchorage and cytokines produced by neighbouring cells in a population. Traditionally, their capability to release dopamine is determined by collecting samples of culture medium containing dopamine released by a cell population, followed by subsequent HPLC analysis[219,239]. During the work done for this thesis, electrochemical real-time detection of dopamine exocytosis from populations of stimulated NSCs has for the first time been demonstrated using 3D carbon pillar scaffolds (paper IV) (Fig. 5.5).

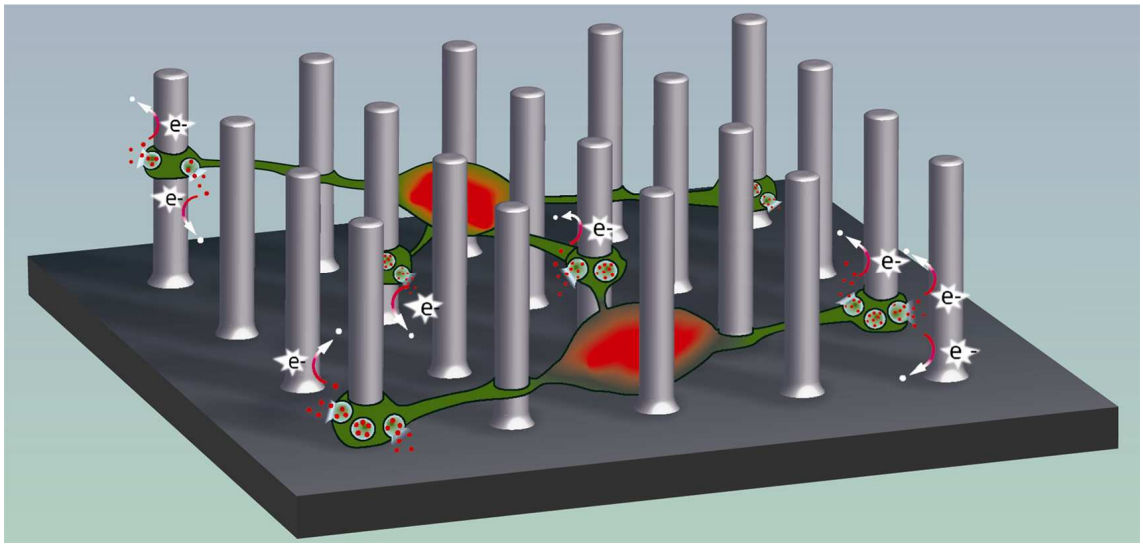

Figure 5.5. Dopamine detection on 3D scaffold from population of differentiated neurons.

5.3. Interaction of Cells With the *In Vivo* and *In Vitro* Environment

Typically in *in vivo* environment, cells interact and respond to features from the macro scale down to the molecular scale[104]. Cells sense most extracellular signals via transmembrane receptors (integrins) that recognize and tether the cell cytoskeleton by forming focal adhesions through motifs within proteins (for instance laminin, fibronectin and vitronectin) that constitute the fibers of the extracellular matrix (ECM)[240]. Upon binding, integrins elicit complex biochemical cascades of intracellular signaling, which together act to regulate cell physiology[241]. Consequently, topographies ranging from nano- to microscale, for instance topographies composed of networks of nanoscale pores, ridges, and fibers made by ECM molecules, affect cell physiology[2]. At the same time, cells are inherently sensitive to their surroundings, thus they are influenced by multiple cues (Fig. 5.6), including: (1) mechanical and biochemical-interactions with the ECM, (2) gradients of secreted signals (e.g. hormones, cytokines, and growth factors), and (3) cell–cell contacts[242]. These cues dynamically influence and regulate cell behavior, such as expression of ECM proteins, proliferation, activation of growth factors, maintenance of survival signals to prevent programmed cell death (apoptosis), and differentiation[241,243–245].

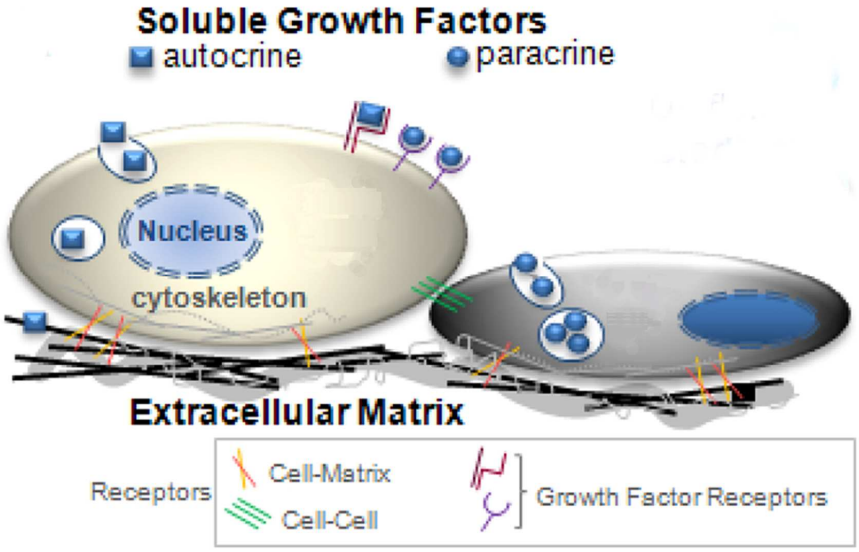

Figure 5.6. Different factors affect cell behavior and direct their fate: soluble and matrix bound factors, cell-cell contact, cell-matrix adhesion. Modified from [246].

Most *in vitro* studies with adherent mammalian cells are performed using standard 2D culture systems in which cells are plated onto commercial polystyrene cell culture plastic ware that, depending on the cell type, is treated or not with pre-coatings to initiate cell adhesion.

Some cells e.g. fibroblasts, which are one of the main components of connective tissue, can grow directly on the plastic ware since they secret ECM components that coat the plastic thus mediating cell adhesion. Other cells, such as neural cells, whose capacity to secrete ECM proteins is essentially non-existent, requires pre-coating of the plastic ware with adhesion factors. However, 2D formats are poor mimics of the *in vivo* environment. Compared to cells on 2D plastic ware, cells growing in a more physiologically resembling environment, such as a 3D one, vary considerably in their morphology, their cell/cell and cell/matrix interactions, and their differentiation levels[247].

5.3.1. Interaction of Cells with Micro- and Nanotopographies

It has been shown that micro- and nanotopographies, their order (e.g. pillars, grooves, ridges, steps, and pits), and their symmetry (e.g. hexagonal or orthogonal or packing of nanopits) can regulate cell behavior[188]. Therefore, structuring of nano- and microscale material to control cell behavior has important implications when designing new materials, which could be used e.g. for tissue engineering.

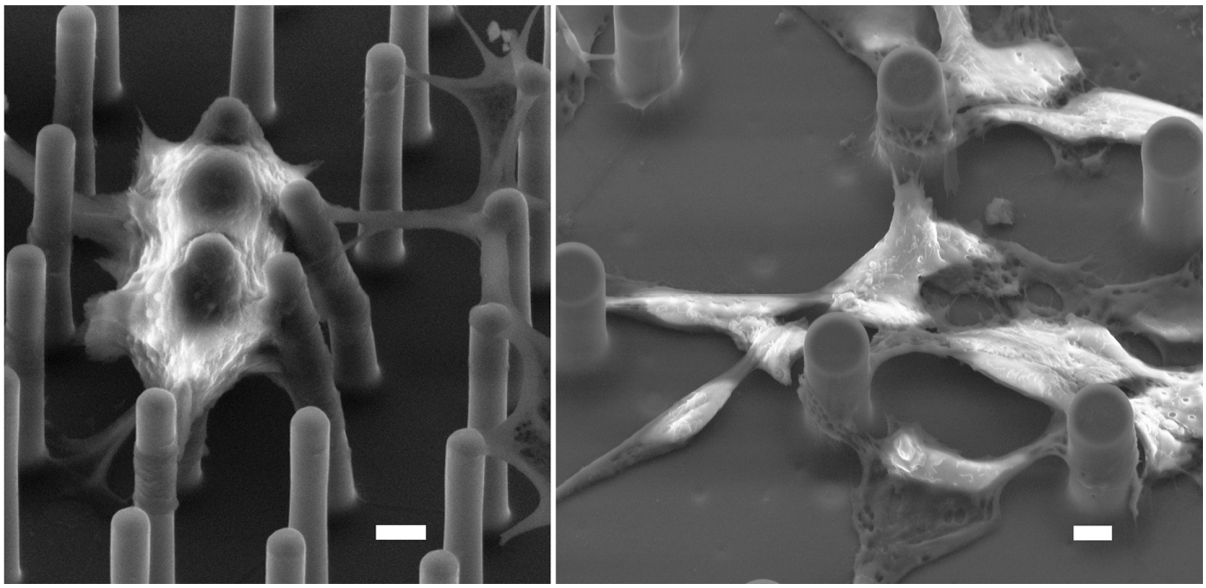

Figure 5.7. SEM images of growing (A) PC12 cells on 1.4 µm pillar scaffolds, and (B) hNSCs on 5.1 µm pillars. Scale bar: 2 µm.

One early response of cells to microtopographies is to increase the number of their 'sensing' organelles, such as filopodia and microspikes. Fig. 5.7A shows PC12 cells and Fig. 5.7B hNSCs grown on micropillar scaffolds developed during this thesis (paper IV). Regardless of cell type or substrate, cells exhibit filopodial and spindle shape protrusions, which serve as anchoring points to pull the cell body. This phenomenon has been shown before[248].

Chapter 6

Summary of the Papers

Paper I describes the process optimization of SU-8 for fabrication of high-aspect ratio micropillar arrays. Different process parameters were changed during the optimization related to the baking steps, temperature, ramping rate and duration, and the results were compared. Large areas of pillar arrays with various diameter and ~22 µm height were fabricated. The optimized process yielded pillars close to the resolution limit of UV photolithography with diameter 1.8 µm, AR = 11.

Paper II presents the fabrication and thorough characterization of the micropillar arrays described in Paper I before and after pyrolysis. The carbon micropillar arrays and three carbon film thicknesses were characterized for their shrinkage, and different properties: electrical, electrochemical, bulk microstructure (i.e. disorder and crystallite formation). Finally, fabrication of high-aspect ratio micropillars on interdigitated electrodes and their electrochemical behaviour is described. Due to their good properties, the obtained 3D interdigitated electrodes can be further used for bioelectrochemical applications.

Paper III shows the surface modification of pyrolysed carbon films and of micropillar arrays presented and characterized in Paper II. The carbon surfaces were modified with electrochemical reduction of diazonium salt, oxygen and a mixture of water/oxygen plasma treatments. The effect of the treatments was analyzed and compared using XPS, electrochemical impedance spectroscopy, cyclic voltammetry, and contact angle measurements.

Paper IV presents the application of the micropillar electrodes as 3D scaffolds for growth and differentiation of clinically relevant neural stem cells developed for cell replacement therapy of Parkinson's disease. The obtained results show that the pyrolysed carbon itself strongly increases the cells' development to mature dopamine releasing neurons and the 3D environment enhances the growth of neurites. Due to the conductive properties of the 3D-carbon scaffolds, these are optimal for electrochemical detection of exocytotic dopamine release from stem cell populations, functioning as a dopamine trap capable of detecting a much larger quantity of the released dopamine compared to conventional microchip-based systems relying on planar electrode configuration.

Chapter 7

Conclusions and Outlook

2D and 3D scaffolds in pyrolysed carbon could represent a new direction in bioelectrochemical applications. The tailoring possibility of the scaffold in terms of shape and surface functionalization could facilitate the developments of novel biosensors. The surface treatment of these electrode structures enhances their electrochemical performance, but also to make it possible to change the electrode surface properties so that small or large chemical / biological molecules can be attached onto them, e.g. for bio-sensors that may be developed, or to make them more compatible with cell biological applications. Moreover, 3D carbon scaffold opens up new possibilities in stem cell research and therapy. The combination of a conducting 3D carbon scaffold and electrochemistry gives unique possibilities to enhance hNSCs differentiation into TH^+ phenotype (material) and neurite elongation (3D topography), and at the same time enables direct confirmation of true dopaminergic phenotype and neuronal maturation (electrochemical dopamine trap).

Acknowledgments

I would like to express my sincere gratitude to my supervisors Jenny Emnéus, Arto Heiskanen, Stephan Keller and Anja Boisen for their constant guidance, support and professional advice. Their profound knowledge of cleanroom fabrication, electrochemistry, bioanalytical techniques, and great overall experience were invaluable for completing this thesis.

A large part of the experimental work presented here, including microfabrication and characterization of the carbon electrodes, has been performed using the Danchip facilities. Therefore, I would like to thank Katarina Nilson, Conny Hougaard, and Thomas Anhøj, for their assistance, supervision, and fruitful discussion during my work there. I received great help from Jens Hemmingsen, especially during the 'KS Spinner panicking moments', and therefore I would like to specially thank him.

I am also indebted to the Bioanalytics and Nanoprobes groups for sharing their competences and creating a stimulating atmosphere.

Special thanks to Kinga, for being a good friend and colleague, and for constant moral support…devi stare molto calmo ☺

Grazie Claudia for being a sweet friend, for the many many many lunches you provided me, for your funny irony , for trying hard to understand and even adapt to my southern Italian accent, for being patient, for 'teaching' me the art of 'diplomacy' and for initiating me to the 'philosophy' of the cells…e comunque, la seccia, NO!! ☺ siempre!

Grazie a Chiara C., for sharing her coffee and chewing gum addictions.

Thanks to my patient students, Andrea, Rasmus, Henrik, and Joachim.

To the Italian community at DTU I would like to express my gratitude. In random order: Pavel, Adele, Filo, Simo, Marco, Paolino, Chiara for our pleasant italian coffee breaks; Albe and Filli for sharing their ideas and experience about graphene; Luisa and Claudia G. for being good friends and such a funny company during the endless waiting times in the clean room.

Outside DTU I would like to thank Maria and Romén, for being great friends and always a funny company. Eli, for our crazy and funny dances.

Grazie Jacob for your ‘infinite’ patience, for being a good friend, a lovely partner, a great coffee-maker, and an excellent pizzaiolo. Tak for your support and for constantly reminding me the important things in life.

Outside DK, I wish to thank Francesco for his constant ‘Skype support’ and our long nerdy/funny discussions. Dora, for being a good friend, and her long and warm emails.

Finally, help, support, and love I received from my family cannot be valued highly enough. Grazie Mari mia, Fó, Bart, e papa’. ☺ ☺ ☺

References

1. Dvir, T., Timko, B. P., Brigham, M. D., Naik, S. R., Karajanagi, S. S., Levy, O., Jin, H., Parker, K. K., Langer, R. & Kohane, D. S. Nanowired three-dimensional cardiac patches. *Nature Nanotechnology* **6,** 720–725 (2011).

2. Shevach, M., Maoz, B. M., Feiner, R., Shapira, A. & Dvir, T. Nanoengineering gold particle composite fibers for cardiac tissue engineering. *Journal of Materials Chemistry B* **1,** 5210–5217 (2013).

3. Lovat, V., Pantarotto, D., Lagostena, L., Cacciari, B., Grandolfo, M., Righi, M., Spalluto, G., Prato, M. & Ballerini, L. Carbon nanotube substrates boost neuronal electrical signaling. *Nano Letters* **5,** 1107–1110 (2005).

4. Cha, C., Shin, S. R., Annabi, N. & Dokmeci, M. R. Carbon-based nanomaterials: multifunctional materials for. 2891–2897 (2013).

5. Li, N., Zhang, Q., Gao, S., Song, Q., Huang, R., Wang, L., Liu, L., Dai, J., Tang, M. & Cheng, G. Three-dimensional graphene foam as a biocompatible and conductive scaffold for neural stem cells. *Scientific Reports* **3,** 1604 (6pp) (2013).

6. Ghasemi-mobarakeh, L., Prabhakaran, M. P. & Morshed, M. Application of conductive polymers , scaffolds and electrical stimulation for nerve tissue engineering. *Journal of Tissue Engineering and Regenerative Medicine* **5,** 17–35 (2011).

7. Spegel, C., Heiskanen, A., Skjolding, L. H. D. & Emnéus, J. Chip based electroanalytical systems for cell analysis. *Electroanalysis* **20,** 680–702 (2008).

8. Voldman, J., Gray, M. L., Toner, M. & Schmidt, M. A. A microfabrication-based dynamic array cytometer. *Analytical Chemistry* **74,** 3984–3990 (2002).

9. Patel, J. N., Gray, B. L., Kaminska, B. & Gates, B. D. Flexible three-dimensional electrochemical glucose sensor with improved sensitivity realized in hybrid polymer microelectromechanical systems technique. *Journal of diabetes science and technology* **5,** 1036–1043 (2011).

10. Wang, J. *Analytical electrochemistry*. (John Wiley & Sons, Inc., 2006).

11. Wang, C., Taherabadi, L. H. & Madou, M. J. A novel method for the fabrication of high-aspect ratio C-MEMS structures. *Journal of Microelectromechanical Systems* **14,** 348–358 (2005).

12. Nlwa, O. & Tabel, H. Voltammetric measurements of reversible and quasi-reversible redox species using carbon film based interdigitated array microelectrodes. **6,** 285–289 (1994).

13. Lane, R. F. & Hubbard, A. T. Differential double pulse voltammetry at chemically modified platinum electrodes for in vivo determination of catecholamines. *Analytical chemistry* **48,** 1287–1292 (1976).

14. Baldwin, R. P. Electrochemical determination of carbohydrates: enzyme electrodes and amperometric detection in liquid chromatography and capillary electrophoresis. *Journal of Pharmaceutical and Biomedical Analysis* **19,** 69–81 (1999).

15. McCreery, R. L. Advanced carbon electrode materials for molecular electrochemistry. *Chemical reviews* **108,** 2646–2687 (2008).

16. Chen, Z., Ren, W., Gao, L., Liu, B., Pei, S. & Cheng, H.-M. Three-dimensional flexible and conductive interconnected graphene networks grown by chemical vapour deposition. *Nature materials* **10,** 424–428 (2011).

17. Sreenivas, G., Ang, S. S., Fritsch, I., Brown, W. D., Gerhardt, G. a & Woodward, D. J. Fabrication and characterization of sputtered-carbon microelectrode arrays. *Analytical chemistry* **68,** 1858–1864 (1996).

18. Khosla, A. & Gray, B. L. Preparation, characterization and micromolding of multi-walled carbon nanotube polydimethylsiloxane conducting nanocomposite polymer. *Materials Letters* **63,** 1203–1206 (2009).

19. Madou, M., Lal, A., Schmidt, G., Song, X., Kinoshita, K., Fendorf, M., Zettl, A. & White, R. Carbon micromachining (C-MEMS). in *Electrichemical Society Proceedings* **97-19,** 61–69 (1997).

20. Cowlard, F. C. & Lewis, J. C. Vitreous Carbon - A new form of carbon. *Journal of Materials Science* **2,** 507–512 (1967).

21. Teixidor, G. T., Gorkin, R., Tripathi, P. P., Bisht, G. S., Kulkarni, M., Maiti, T. K., Battacharyya, T. K., Subramaniam, J. R., Sharma, A., Park, B. Y. & Madou, M. Carbon microelectromechanical systems as a substratum for cell growth. *Biomedical Materials* **3,** 1–16 (2008).

22. Lyons, A. M. Photodefinable carbon films: electrical properties. *Journal of Non-Crystalline Solids* **70,** 99–109 (1985).

23. Park, B. Y., Taherabadi, L., Wang, C., Zoval, J. & Madou, M. J. Electrical Properties and Shrinkage of Carbonized Photoresist Films and the Implications for Carbon Microelectromechanical Systems Devices in Conductive Media. *Journal of The Electrochemical Society* **152,** J136–J143 (2005).

24. Schueller, B. O. J. A., Brittain, S. & Whitesides, G. M. Fabrication of glassy carbon microstructures by pyrolysis of microfabricated polymeric precursors. *Advanced Materials* **9,** 477–480 (1997).

25. Kawamura, K. & M, J. G. Mechanical properties of glassy carbon fibres derived from phenolic resin. *Journal of Materials Science* **7,** 1099–1112 (1972).

26. K. Zachek, M., Takmakov, P., Moodya, B., Wightman, R. M. & McCarty, G. S. Simultaneous decoupled detection of dopamine and oxygen using pyrolyzed carbon microarrays and FSCV. *Analytical Chemistry* **81,** 6258–6265 (2010).

27. Mardegan, A., Kamath, R., Sharma, S., Scopece, P., Ugo, P. & Madou, M. Optimization of carbon electrodes derived from epoxy-based photoresist. *Journal of the Electrochemical Society* **160,** B132–B137 (2013).

28. Xu, H., Malladi, K., Wang, C., Kulinsky, L., Song, M. & Madou, M. Carbon post-microarrays for glucose sensors. *Biosensors & Bioelectronics* **23,** 1637–1644 (2008).

29. Lee, J. a, Hwang, S., Kwak, J., Park, S. Il, Lee, S. S. & Lee, K.-C. An electrochemical impedance biosensor with aptamer-modified pyrolyzed carbon electrode for label-free protein detection. *Sensors and Actuators B: Chemical* **129,** 372–379 (2008).

30. Bisht, G. S., Holmberg, S., Kulinsky, L. & Madou, M. Diffusion-free mediator based miniature biofuel cell anode fabricated on a carbon-MEMS electrode. *Langmuir* **28,** 14055–14064 (2012).

31. Kassegne, S., Wondimu, B., Majzoub, M. & Shin, J. High-efficiency microarray of 3D carbon MEMS electrodes for pathogen detection systems. *Proceedings of SPIE* **7266,** 726615, 1–6 (2008).

32. Zhou, H., Gupta, A., Zou, T. & Zhou, J. Photoresist derived carbon for growth and differentiation of neuronal cells. *Molecular Science* **8,** 884–893 (2007).

33. Mitra, J., Jain, S., Sharma, A. & Basu, B. Patterned growth and differentiation of neural cells on polymer derived carbon substrates with micro/nano structures in vitro. *Carbon* **65,** 140–155 (2013).

34. Teixidor, G. T., Zaouk, R. B., Park, B. Y. & Madou, M. J. Fabrication and characterization of three-dimensional carbon electrodes for lithium-ion batteries. *Journal of Power Sources* **183,** 730–740 (2008).

35. Min, H.-S., Park, B. Y., Taherabadi, L., Wang, C., Yeh, Y., Zaouk, R., Madou, M. J. & Dunn, B. Fabrication and properties of a carbon/polypyrrole three-dimensional microbattery. *Journal of Power Sources* **178,** 795–800 (2008).

36. Wang, C., Taherabadi, L., Jia, G., Madou, M., Yeh, Y. & Dunn, B. C-MEMS for the Manufacture of 3D Microbatteries. *Electrochemical and Solid-State Letters* **7,** A435–A438 (2004).

37. Kotov, N. a., Winter, J. O., Clements, I. P., Jan, E., Timko, B. P., Campidelli, S., Pathak, S., Mazzatenta, A., Lieber, C. M., Prato, M., Bellamkonda, R. V., Silva, G. a., Kam, N. W. S., Patolsky, F. & Ballerini, L. Nanomaterials for Neural Interfaces. *Advanced Materials* **21,** 3970–4004 (2009).

38. Seil, J. T. & Webster, T. J. Electrically active nanomaterials as improved neural tissue regeneration scaffolds. *Wiley interdisciplinary reviews. Nanomedicine and nanobiotechnology* **2,** 635–47 (2010).

39. Ghasemi-mobarakeh, L., Prabhakaran, M. P. & Morshed, M. Application of conductive polymers , scaffolds and electrical stimulation for nerve tissue engineering. (2011). doi:10.1002/term

40. Srikanth, M. & Kessler, J. a. Nanotechnology-novel therapeutics for CNS disorders. *Nature reviews. Neurology* **8,** 307–18 (2012).

41. Saracino, G. a a, Cigognini, D., Silva, D., Caprini, A. & Gelain, F. Nanomaterials design and tests for neural tissue engineering. *Chemical Society reviews* **42,** 225–62 (2013).

42. Amato, L., Heiskanen, A., Hansen, R., Tenje, M., Gammelgaard, L., Rindzevicius, T., Boisen, A., Emnéus, J. & Keller, S. S. Dense high-aspect ratio 3D interdigitated carbon pillar microelectrode arrays. *To be determined* 1–16

43. Mohanty, S., Amato, L., Heiskanen, A., Keller, S. S., Boisen, A., Wolff, A. & Emnéus, J. Conducting pyrolysed carbon scaffold for tissue engineering. in *Proceeding of the 39th International Conference on Micro- and Nano-Engineering (MNE)* (2013).

44. Wang, C. & Madou, M. From MEMS to NEMS with carbon. *Biosensors & Bioelectronics* **20,** 2181–2187 (2005).

45. Schueller, O. J. A., Brittain, S. T. & Whitesides, G. M. Fabrication of glassy carbon microstructures by pyrolysis of microfabricated polymeric precursors. *Advanced Materials* **9,** 477–480 (1997).

46. Georges, P. C. & Janmey, P. A. Cell type-specific response to growth on soft materials. *Journal of Applied Physiology* **98,** 1547–1553 (2005).

47. Falcao, E. H. L. & Wudl, F. Carbon allotropes: beyond graphite and diamond. *Journal of Chemical Technology and Biotechnology* **82,** 524–531 (2007).

48. McCreery, R. L. in *Eletroanalytical Chemistry* (Bard, A. J.) 221–374 (Marcel Dekker, 1991).

49. Pierson, H. O. *Handbook of Carbon, Graphite, Diamond and Fullerenes*. Ch. 3 (Noyes Publications, 1993).

50. Robertson, J. Review Properties of diamond-like carbon. *Surface and Coatings Technology* **50,** 185–203 (1992).

51. http://www.intechopen.com/books/carbon-nanotubes-polymer-nanocomposites/polymer-carbon-nanotube-nanocomposites.

52. Ranganathan, S., McCreery, R., Majji, S. M. & Madou, M. Photoresist-derived carbon for microelectromechanical systems and electrochemical applications. *Journal of The Electrochemical Society* **147,** 277–282 (2000).

53. Kim, J., Song, X., Kinoshita, K., Madou, M. & White, R. Electrochemical studies of carbon films from pyrolyzed photoresist. *Journal of the Electrochemical Society* **145,** 2314–2319 (1998).

54. Singh, A., Jayaram, J., Madou, M. & Akbar, S. Pyrolysis of negative photoresists to fabricate carbon structures for microelectromechanical systems and electrochemical applications. *Journal of The Electrochemical Society* **149,** E78–E83 (2002).

55. Pesin, L. A. Structure and properties of glass-like carbon. *Journal of Materials Science* **7,** 1–28 (2002).

56. Jenkins, G. M.; Kawamura, K.; Ban, L. L. Formation and structure of polymeric carbons. *Royal Society* **327,** 501–517 (1972).

57. Jenkins, G. & Kawamura, K. *Polymeric Carbon - Carbon Fibre, Glass and Char*. (Cambridge University Press, 1976).

58. Harris, P. J. F. Fullerene-related structure of commercial glassy carbons. *Philosophical Magazine* **84,** 3159–3167 (2004).

59. Whiteside, N. J., Wallace, G. G. & in het Panhuis, M. Preparation and characterisation of graphene composite hydrogels. *Synthetic Metals* **168,** 36–42 (2013).

60. Xu, Y., Huang, X., Lin, Z., Zhong, X., Huang, Y. & Duan, X. One-step strategy to graphene/Ni(OH)2 composite hydrogels as advanced three-dimensional supercapacitor electrode materials. *Nano Research* **6,** 65–76 (2012).

61. Li, C. & Shi, G. Three-dimensional graphene architectures. *Nanoscale* **4,** 5549–5563 (2012).

62. Lovat, V., Pantarotto, D., Lagostena, L., Cacciari, B., Grandolfo, M., Righi, M., Spalluto, G., Prato, M. & Ballerini, L. Carbon nanotube substrates boost neuronal electrical signaling. *Nano Letters* **5,** 1107–1110 (2005).

63. Wierzbicki, R., Amato, L., Łopacińska, J. ., Heiskanen, A., Emnéus, J., Tenje, M. ., Schmidt, M. S., Bøggild, P., Mølhave, K., Downard, A. & Baronian, K. Titanium tungsten coatings for bioelectrochemical applications. in *Technical Proceedings of the 2011 NSTI Nanotechnology Conference and Expo — 2011* 252–255 (Nano Science and Technology Institute, 2011).

64. Liu, X., Baronian, K. H. R. & Downard, A. J. Direct growth of vertically aligned carbon nanotubes on a planar carbon substrate by thermal chemical vapour deposition. *Carbon* **47,** 500–506 (2009).

65. Ghavanini, F. A. Synthesis and characterization of vertically aligned carbon nanofibers. (2011).

66. Chen, W., Rakhi, R. B., Hu, L., Xie, X., Cui, Y. & Alshareef, H. N. High-performance nanostructured supercapacitors on a sponge. *Nano letters* **11,** 5165–5172 (2011).

67. Yang, Z., Cao, Z., Sun, H. & Li, Y. Composite films based on aligned carbon nanotube arrays and a poly(N-isopropyl acrylamide) hydrogel. *Advanced Materials* **20,** 2201–2205 (2008).

68. Martinez-Duarte, R., Renaud, P. & Madou, M. J. A novel approach to dielectrophoresis using carbon electrodes. *Electrophoresis* 2385–2392 (2011).

69. Penmatsa, V., Kawarada, H. & Wang, C. Fabrication of carbon nanostructures using photo-nanoimprint lithography and pyrolysis. *Journal of Micromechanics and Microengineering* **22,** 1–8 (2012).

70. Du, R., Ssenyange, S., Aktary, M. & McDermott, M. T. Fabrication and characterization of graphitic carbon nanostructures with controllable size, shape, and position. *Small* **5,** 1162–8 (2009).

71. Franklin, R. E. Crystallite growth in graphitizing and non-graphitizing carbons. *Proceedings of the Royal Society A* **209,** 196–218 (1951).

72. Fitzer, E. & Schafer, W. The effect of crosslinking on the formation of glasslike carbons from thermosetting resins. *Carbon* **8,** 353–364 (1970).

73. Kawamura, K. & Kimura, S. Glass-like carbon made from epoxy resin cured with 2,4,6-trinitrophenol. *The Chemical Society of Japan* **56,** 2499–2503 (1983).

74. Fitzer, E. & Schaefer, W. The formation of glasslike carbon by pyrolysis of polyfurfuryl and phenolic resin carbon alcohol. *Carbon* **7,** 643–648 (1969).

75. Schueller, O. J. A., Brittain, S. T. & Whitesides, G. M. Fabrication of glassy carbon microstructures by soft lithography. *Sensors and Actuators A: Physical* 125–139 (1999).

76. Kinoshita, K. *Carbon, Electrochemical and Physicochemical Properties.* (Wiley-Interscience, 1988).

77. Morton, K. C., Morris, C. A., Derylo, M. A., Thakar, R. & Lane, A. Carbon electrode fabrication from pyrolyzed parylene c. *Anal. Chem.* **83,** 5447–5452 (2011).

78. Wang, Y., Liu, J., Christiansen, S., Kim, D. H., Gösele, U. & Steinhart, M. Nanopatterned carbon films with engineered morphology by direct carbonization of UV-stabilized block copolymer films. *Nano Letters* **8,** 3993–3997 (2008).

79. Huang, J., Tang, C., Lee, H., Kowalewski, T. & Matyjaszewski, K. A novel route for the preparation of discrete nanostructured carbons from block copolymers with polystyrene segments. *Macromolecular Chemistry and Physics* **208,** 2312–2320 (2007).

80. Callstrom, M. R., Neenan, T. X., McCreery, R. L. & Alsmeyer, D. C. Doped glassy carbon materials (DGC): low-temperature synthesis, structure, and catalytic behavior. *Journal of the American Chemical Society* **112,** 4954–4956 (1990).

81. Hutton, H. D., Alsmeyer, D. C., McCreery, R. L., Neenan, T. X. & Callstrom, M. R. Synthesis, characterization and electrochemical activity of halogen doped glassy carbon. *Polym. Mater. Sci. Eng.* **67,** 237–241 (1992).

82. Hutton, H. D., Huang, W., Alsmeyer, D. C., Kometani, J., McCreery, R. L., Neenan, T. X. & Callstrom, M. R. Synthesis, characterization, and electrochemical activity of halogen-doped glassy carbon. 1110–1117 (1993).

83. Hutton, H. D., Pocard, N. L., Alsmeyer, D. C., Schueller, O. J. A., Spontak, R. J., Huston, M. E., Huang, W., McCreery, R. L., Neenan, T. X. & Callstrom, M. R. Preparation of nanoscale platinum (0) clusters in glassy carbon and their catalytic activity. **17,** 1727–1738 (1993).

84. Chen, W., Beidaghi, M., Penmatsa, V., Bechtold, K., Kumari, L., Li, W. Z. & Wang, C. (Peggy). Integration of carbon nanotubes to C-MEMS for on-chip supercapacitors. *IEEE Transactions on Nanotechnology* **9,** 734–740 (2010).

85. Penmatsa, V., Kim, T., Beidaghi, M., Kawarada, H., Gu, L., Wang, Z. & Wang, C. Three-dimensional graphene nanosheet encrusted carbon micropillar arrays for electrochemical sensing. *Nanoscale* **4,** 3673–3678 (2012).

86. Hebert, N. E., Snyder, B., McCreery, R. L., Kuhr, W. G. & Brazill, S. a. Performance of pyrolyzed photoresist carbon films in a microchip capillary electrophoresis device with sinusoidal voltammetric detection. *Analytical Chemistry* **75,** 4265–4271 (2003).

87. Kostecki, R., Song, X. & Kinoshita, K. Electrochemical analysis of carbon interdigitated microelectrodes. *Electrochemical and Solid-State Letters* **2,** 465–467 (1999).

88. Tang, Z., Shi, T., Gong, J., Nie, L. & Liu, S. An optimized process for fabrication of high-aspect-ratio photoresist-derived carbon microelectrode array on silicon substrate. *Thin Solid Films* **518,** 2701–2706 (2010).

89. Amato, L., Keller, S. S., Heiskanen, A., Dimaki, M., Emnéus, J., Boisen, A. & Tenje, M. Fabrication of high-aspect ratio SU-8 micropillar arrays. *Microelectronic Engineering* **98,** 483–487 (2012).

90. Campo, A. Del & Greiner, C. SU-8: a photoresist for high-aspect-ratio and 3D submicron lithography. *Journal of Micromechanics and Microengineering* **17,** R81–R95 (2007).

91. López-Romero, D., Barrios, C. a., Holgado, M., Laguna, M. F. & Casquel, R. High aspect-ratio SU-8 resist nano-pillar lattice by e-beam direct writing and its application for liquid trapping. *Microelectronic Engineering* **87,** 663–667 (2010).

92. De Volder, F. L., Vansweevelt, R., Wagner, P., Reynaerts, D., Hoof, C. Van & Hart, A. J. Hierarchical carbon nanowire microarchitectures made by plasma-assisted pyrolysis of photoresist. *ACS Nano* **5,** 6593–6600 (2011).

93. Wang, Chunlei; Madou, J. M. Carbon as a MEMS material: micro and nanofabrication of pyrolysed photoresist carbon. *International Journal Manufacturing Technology and Management* **13,** 360–375 (2008).

94. Denis, F. A., Hanarp, P., Sutherland, D. S. & Dufre, Y. F. Fabrication of nanostructured polymer surfaces using colloidal lithography and spin-coating. *Nano Letters* **2,** 1419–1425 (2002).

95. Dolatshahi-Pirouz, A., Sutherland, D. S., Foss, M. & Besenbacher, F. Growth characteristics of inclined columns produced by Glancing Angle Deposition (GLAD) and colloidal lithography. *Applied Surface Science* **257,** 2226–2230 (2011).

96. Dolatshahi-Pirouz, A., Jensen, T., Vorup-Jensen, T., Bech, R., Chevallier, J., Besenbacher, F., Foss, M. & Sutherland, D. S. Synthesis of functional nanomaterials via colloidal mask templating and Glancing Angle Deposition (GLAD). *Advanced Engineering Materials* **12,** 899–905 (2010).

97. Chen, J.-K., Qui, J.-Q., Fan, S.-K., Kuo, S.-W., Ko, F.-H., Chu, C.-W. & Chang, F.-C. Using colloid lithography to fabricate silicon nanopillar arrays on silicon substrates. *Journal of Colloid and Interface Science* **367,** 40–48 (2012).

98. Purwaningsih, L., Schoen, T., Wolfram, T., Pacholski, C. & Spatz, J. P. Fabrication of multi-parametric platforms based on nanocone arrays for determination of cellular response. *Beilstein Journal of Nanotechnology* **2,** 545–551 (2011).

99. Valsesia, A., Meziani, T., Bretagnol, F., Colpo, P., Ceccone, G. & Rossi, F. Plasma assisted production of chemical nano-patterns by nano-sphere lithography: application to bio-interfaces. *Journal of Physics D: Applied Physics* **40,** 2341–2347 (2007).

100. Brooksby, P. A. & Downard, A. J. Electrochemical and atomic force microscopy study of carbon surface modification via diazonium reduction in aqueous and acetonitrile solutions. *Langmuir* **20,** 5038–5045 (2004).

101. Rawson, F. J., Garrett, D. J., Leech, D., Downard, A. J. & Baronian, K. H. R. Electron transfer from Proteus vulgaris to a covalently assembled, single walled carbon nanotube electrode functionalised with osmium bipyridine complex: application to a whole cell biosensor. *Biosensors & Bioelectronics* **26,** 2383–2389 (2011).

102. Heiskanen, A. R., Spégel, C. F., Kostesha, N., Ruzgas, T. & Emnéus, J. Monitoring of saccharomyces cerevisiae cell proliferation on thiol-modified planar gold microelectrodes using impedance spectroscopy. *Langmuir* **24,** 9066–9073 (2008).

103. Kostesha, N., Heiskanen, A., Spégel, C., Hahn-Hägerdal, B., Gorwa-Grauslund, M.-F. & Emnéus, J. Real-time detection of cofactor availability in genetically modified living Saccharomyces cerevisiae cells--simultaneous probing of different geno- and phenotypes. *Bioelectrochemistry* **76,** 180–188 (2009).

104. Stevens, M. M. & George, J. H. Exploring and engineering the cell surface interface. *Science* **310,** 1135–1138 (2005).

105. Alves, N. M., Pashkuleva, I., Reis, R. L. & Mano, J. F. Controlling cell behavior through the design of polymer surfaces. *Small* **6,** 2208–2220 (2010).

106. DeVries, J. E. Surface characterization methods — XPS , TOF-SIMS , and SAM A complimentary ensemble of tools. *Journal of Materials Engineering and Performance* **7,** 303–311 (1998).

107. Desimoni, E., Casella, G. I., Morone, a. & Salvi, a. M. XPS determination of oxygen-containing functional groups on carbon-fibre surfaces and the cleaning of these surfaces. *Surface and Interface Analysis* **15,** 627–634 (1990).

108. Boehm, H. P. Surface oxides on carbon and their analysis: a critical assessment. *Carbon* **40,** 145–149 (2002).

109. Chu, P. K. & Li, L. Characterization of amorphous and nanocrystalline carbon films. *Materials Chemistry and Physics* **96,** 253–277 (2006).

110. Tuinstra, F. & Koenig, J. L. Raman spectrum of graphite. *The Journal of Chemical Physics* **53,** 1126–1130 (1970).

111. Ferrari, A. & Robertson, J. Interpretation of Raman spectra of disordered and amorphous carbon. *Physical Review B* **61,** 14095–14107 (2000).

112. Ferrari, A. C. Raman spectroscopy of graphene and graphite: Disorder, electron–phonon coupling, doping and nonadiabatic effects. *Solid State Communications* **143,** 47–57 (2007).

113. Petersen, D. H., Hansen, O., Hansen, T. M., Petersen, P. R. E. & Bøggild, P. Static contact micro four-point probes with <11 nm positioning repeatability. *Microelectronic Engineering* **85,** 1092–1095 (2008).

114. Perloff, D. S. Four Point Sheet resistance correction factors for thin rectangular samples. *Solid State Electronics* **20,** 681–687 (1977).

115. Smits, B. F. Measurement of sheet resistivities with the four-point probe. *The Bell System Technical Journal* 711–718 (1958).

116. Strobel, M. & Lyons, C. S. An essay on contact angle measurements. *Plasma Processes and Polymers* **8,** 8–13 (2011).

117. Yan, Y. Y., Gao, N. & Barthlott, W. Mimicking natural superhydrophobic surfaces and grasping the wetting process: a review on recent progress in preparing superhydrophobic surfaces. *Advances in Colloid and Interface Science* **169,** 80–105 (2011).

118. Yan, Y. Y., Gao, N. & Barthlott, W. Mimicking natural superhydrophobic surfaces and grasping the wetting process: a review on recent progress in preparing superhydrophobic surfaces. *Advances in Colloid and Interface Science* **169,** 80–105 (2011).

119. Good, R. J. Contact angle, wetting, and adhesion: a critical review. *Journal of Adhesion Science and Technology* **6,** 1269–1302 (1992).

120. Fairman, C., Yu, S. S. C., Liu, G., Downard, A. J., Hibbert, D. B. & Gooding, J. J. Exploration of variables in the fabrication of pyrolysed photoresist. *Journal of Solid State Electrochemistry* **12,** 1357–1365 (2008).

121. Ranganathan, S. & McCreery, R. L. Electroanalytical performance of carbon films with near-atomic flatness. *Analytical chemistry* **73,** 893–900 (2001).

122. Zanello, P. *Inorganic electrochemistry*. *Practice* (The Royal Society of Chemistry, 2003).

123. McCreery, R. L., Cline, K. K., McDermott, C. A. & McDermott, M. T. Control of reactivity at carbon electrode surfaces. *Colloids and Surfaces A: Physicochemical and Engineering Aspects* **93,** 211–219 (1994).

124. Marcus, R. a. On the theory of oxidation-reduction reactions involving electron transfer. I. *The Journal of Chemical Physics* **24,** 966–978 (1956).

125. Yang, H. & McCreery, R. L. Effects of surface monolayers on the electron-transfer kinetics and adsorption of methyl viologen and phenothiazine derivatives on glassy carbon electrodes. *Analytical Chemistry* **71,** 4081–4087 (1999).

126. Chen, P. & McCreery, R. L. Control of electron transfer kinetics at glassy carbon electrodes by specific surface modification. *Analytical Chemistry* **68,** 3958–3965 (1996).

127. Cline, K. K., Mcdermott, M. T. & McCreery, R. L. Anomalously slow electron transfer at ordered graphite electrodes: influence of electronic factors and reactive sites. *J. Phys. Chem.* **98,** 5314–5319 (1994).

128. Shinwari, M. W., Zhitomirsky, D., Deen, I. a, Selvaganapathy, P. R., Deen, M. J. & Landheer, D. Microfabricated reference electrodes and their biosensing applications. *Sensors* **10,** 1679–1715 (2010).

129. Jackson, W. F. & Duling, B. R. Toxic effects of silver-silver chloride electrodes on vascular smooth muscle. *Circulation Research* **53,** 105–108 (1983).

130. Kissinger, P. T. & Heineman, W. R. Cyclic voltammetry. *Journal of Chemical Education* **60,** 702–706 (1983).

131. Bard, A. J. & Faulkner, L. R. *Electrochemical methods*. (Wiley, New York, 2001).

132. Nicholson, S. R. Theory and application of cyclic voltammetry for measurement of electrode reaction kinetics. *Analytical chemistry* **37,** 1351–1355 (1965).

133. Wipf, D. O., Kristensen, E. W., Deakin, M. R. & Wightman, R. M. Fast-scan cyclic voltammetry as a method to measure rapid heterogeneous electron-transfer kinetics. *Analytical Chemistry* **60,** 306–310 (1988).

134. Buttry, D. A. & Anson, F. C. Electron hopping vs. molecular diffusion as charge transfer mechanisms in redox polymer films. *Journal of Electroanalytical Chemistry* **130,** 333–338 (1981).

135. Lvovich, V. F. *Impedance spectroscopy*. (Wiley-Interscience, 2012).

136. Randles, J. E. B. Kinetics of rapid electrode reactions. *Discussion of the Faraday Society* **1,** 11–19 (1947).

137. Brug, G. J., Van Den Eeden, A. L. G., Sluyters-Rehbach, M. & Sluyters, J. H. The analysis of electrode impedances complicated by the presence of a constant phase element. *Journal of Electroanalytical Chemistry* **176,** 275–295 (1984).

138. Kim, C.-H., Pyun, S.-I. & Kim, J.-H. An investigation of the capacitance dispersion on the fractal carbon electrode with edge and basal orientations. *Electrochimica Acta* **48,** 3455–3463 (2003).

139. Pardo-Yissar, V., Katz, E., Lioubashevski, O. & Willner, I. Layered polyelectrolyte films on au electrodes: characterization of electron-transfer features at the charged polymer interface and application for selective redox reactions. *Langmuir* **17,** 1110–1118 (2001).

140. Hsu, C. H. & Mansfeld, F. Technical note: concerning the conversion of the constant phase element parameter Yo into a capacitance. *Corrosion* **57,** 747–748 (2001).

141. Ramos-Vara, J. A. Technical aspects of immunohistochemistry. *Veterinary pathology* **42,** 405–426 (2005).

142. McCreery, R. L. in *Voltammetric Methods in Brain Systems* (Boulton, A. A. & Baker, G. B.) **27,** 1–26 (Humana Press, 1995).

143. Bourdillon, C., Delamar, M., Demaille, C., Hitmi, R., Moiroux, J. & Pinson, J. Immobilization of glucose oxidase on a carbon surface derivatized by electrochemical reduction of diazonium salts. *Journal of Electroanalytical Chemistry* **336,** 113–123 (1992).

144. Alonso-Lomillo, M. A., Domínguez-Renedo, O., Hernández-Martín, A. & Arcos-Martínez, M. J. Horseradish peroxidase covalent grafting onto screen-printed carbon electrodes for levetiracetam chronoamperometric determination. *Analytical biochemistry* **395,** 86–90 (2009).

145. Radi, A.-E., Muñoz-Berbel, X., Lates, V. & Marty, J.-L. Label-free impedimetric immunosensor for sensitive detection of ochratoxin A. *Biosensors & bioelectronics* **24,** 1888–1892 (2009).

146. Ghodbane, O., Chamoulaud, G. & Bélanger, D. Chemical reactivity of 4-bromophenyl modified glassy carbon electrode. *Electrochemistry Communications* **6,** 254–258 (2004).

147. Mcdermott, M. T. & McCreery, R. L. Scanning tunneling microscopy of ordered graphite and glassy carbon surfaces: electronic control of quinone adsorption. *Langmuir* **10,** 4307–4314 (1994).

148. Hirabayashi, M., Mehta, B., Vahidi, N. W., Khosla, A. & Kassegne, S. Functionalization and characterization of pyrolyzed polymer based carbon microstructures for bionanoelectronics platforms. *Journal of Micromechanics and Microengineering* **23,** 1–11 (2013).

149. Hirabayashi, M., Mehta, B., Khosla, A. & Kassegne, S. Functionalization of pyrolyzed carbon microstructures for bio-nanoelectronics platforms. *ECS Transactions* **50,** 325–331 (2012).

150. Ranganathan, S., Kuo, T.-C. & McCreery, R. L. Facile preparation of active glassy carbon electrodes with activated carbon and organic solvents. *Analytical Chemistry* **71,** 3574–3580 (1999).

151. Kuo, T. & McCreery, R. L. Surface chemistry and electron-transfer kinetics of hydrogen-modified glassy carbon electrodes. *Electroanalysis* **71,** 1553–1560 (1999).

152. Madou, M. & Sharma, S. Micro and nano patterning of carbon electrodes for bioMEMS. *Bioinspired, Biomimetic and Nanobiomaterials* **1,** 252–265 (2012).

153. Xu, H., Malladi, K., Wang, C., Kulinsky, L., Song, M. & Madou, M. Carbon post-microarrays for glucose sensors. *Biosensors & bioelectronics* **23,** 1637–44 (2008).

154. Emr, S. A. & Yucynych, A. M. Use of polymer films in amperometric biosensors. *Electroanalysis* **7,** 913–923 (1995).

155. Hirabayashi, M., Mehta, B., Khosla, A. & Kassegne, S. Functionalization of pyrolyzed carbon microstructures for bio-nanoelectronics platforms. *ECS Transactions* **50,** 325–331 (2012).

156. Evans, J. F. & Kuwana, T. Introduction of functional groups onto carbon electrodes via treatment with radio-frequency plasmas. *Analytical Chemistry* **51,** 358–365 (1979).

157. Yang, J.-H., Penmatsa, V., Tajima, S., Kawarada, H. & Wang, C. Direct amination on 3-dimensional pyrolyzed carbon micropattern surface for DNA detection. *Materials Letters* **63,** 2680–2683 (2009).

158. Sun, B., Colavita, P. E., Kim, H., Lockett, M., Marcus, M. S., Smith, L. M. & Hamers, R. J. Covalent photochemical functionalization of amorphous carbon thin films for integrated real-time biosensing. *Langmuir* **22,** 9598–605 (2006).

159. Banerjee, S., Hemraj-Benny, T. & Wong, S. S. Covalent surface chemistry of single-walled carbon nanotubes. *Advanced Materials* **17,** 17–29 (2005).

160. Alsmeyer, D. C. & Mccreery, R. L. In situ raman monitoring of electrochemical graphite intercalation and lattice damage in mild aqueous acids. *Analytical Chemistry* **64,** 1528–1533 (1992).

161. Downard, A. J. Electrochemically assisted covalent modification of carbon electrodes. *Electroanalysis* **12,** 1085–1096 (2000).

162. Lee, J., Hwang, S., Kwak, J., Park, S. Il, Lee, S. S. & Lee, K.-C. An electrochemical impedance biosensor with aptamer-modified pyrolyzed carbon electrode for label-free protein detection. *Sensors and Actuators B: Chemical* **129,** 372–379 (2008).

163. Lee, J., Lee, K.-C., Park, S. Il & Lee, S. S. The fabrication of carbon nanostructures using electron beam resist pyrolysis and nanomachining processes for biosensing applications. *Nanotechnology* **19,** 1–7 (2008).

164. Delamar, M., Hitmi, R., Pinson, J. & Savéant, J. M. Covalent modification of carbon surfaces by grafting of functionalized aryl radicals produced from electrochemical reduction of diazonium salts. *Journal American Chemical Society* **114,** 5883–5884 (1992).

165. Pinson, J. & Podvorica, F. Attachment of organic layers to conductive or semiconductive surfaces by reduction of diazonium salts. *Chemical Society reviews* **34,** 429–439 (2005).

166. De Villeneuve, C. H., Pinson, J., Bernard, M. C., Allongue, P. & Physique, L. De. Electrochemical formation of close-packed phenyl layers on Si (111). *Journal of Physical Chemistry B* **101,** 2415–2420 (1997).

167. Flavel, B. S., Garrett, D. J., Lehr, J., Shapter, J. G. & Downard, A. J. Chemically immobilised carbon nanotubes on silicon: Stable surfaces for aqueous electrochemistry. *Electrochimica Acta* **55,** 3995–4001 (2010).

168. Deniau, G., Azoulay, L., Bougerolles, L., Palacin, S. & Cedex, F.-G. V. Surface electroinitiated emulsion polymerization: grafted organic coatings from aqueous solutions. *Chemistry of Materials* **18,** 5421–5428 (2006).

169. Bernard, M., Chausse, A., Cabet-deliry, E., Chehimi, M. M., Pinson, J., Podvorica, F. & Vautrin-ul, C. Organic layers bonded to industrial, coinage, and noble metals through electrochemical reduction of aryldiazonium salts. *Chemical Materials* **15,** 3450–3462 (2003).

170. Bahr, J. L., Yang, J., Kosynkin, D. V, Bronikowski, M. J., Smalley, R. E. & Tour, J. M. Functionalization of Carbon Nanotubes by Electrochemical Reduction of Aryl Diazonium Salts: A Bucky Paper Electrode. *Journal of the American Chemical Society* **123,** 6536–6542 (2001).

171. Liu, Y. & Mccreery, R. L. Reactions of organic monolayers on carbon surfaces observed with unenhanced raman spectroscopy. *Journal American Chemical Society* **117,** 11254–11259 (1995).

172. Paulus, G. L. C., Wang, Q. H. & Strano, M. S. Covalent electron transfer chemistry of graphene with diazonium salts. *Accounts of chemical research* **46,** 160–70 (2013).

173. Anariba, F., DuVall, S. H. & McCreery, R. L. Mono- and multilayer formation by diazonium reduction on carbon surfaces monitored with atomic force microscopy "scratching". *Analytical chemistry* **75,** 3837–44 (2003).

174. Brooksby, P. a & Downard, A. J. Electrochemical and atomic force microscopy study of carbon surface modification via diazonium reduction in aqueous and acetonitrile solutions. *Langmuir* **20,** 5038–45 (2004).

175. Allongue, P., Delamar, M., Desbat, B., Fagebaume, O., Hitmi, R., Pinson, J. & Savéant, J.-M. Covalent modification of carbon surfaces by aryl radicals generated from the electrochemical reduction of diazonium salts. *Journal of the American Chemical Society* **119,** 201–207 (1997).

176. Downard, A. J. Electrochemically assisted covalent modification of carbon electrodes. *Electroanalysis* **12,** 1085–1096 (2000).

177. Baranton, S. & Bélanger, D. Electrochemical derivatization of carbon surface by reduction of in situ generated diazonium cations. *The journal of physical chemistry. B* **109,** 24401–10 (2005).

178. Folkers, J. P., Laibinis, P. E. & Whitesides, G. M. Self-assembled monolayers of alkanethiols on gold: comparisons of monolayers containing mixtures of short- and long-chain constituents with CH3 and CH2OH terminal groups. *Langmuir* **8,** 1330–1341 (1992).

179. Liu, G., Chockalingham, M., Khor, S. M., Gui, A. L. & Gooding, J. J. A comparative study of the modification of gold and glassy carbon surfaces with mixed layers of in situ generated aryl diazonium compounds. *Electroanalysis* **22,** 918–926 (2010).

180. Helmus, M. N., Gibbons, D. F. & Cebon, D. Biocompatibility: meeting a key functional requirement of next-generation medical devices. *Toxicologic pathology* **36,** 70–80 (2008).

181. Łopacińska, J. M., Grădinaru, C., Wierzbicki, R., Køber, C., Schmidt, M. S., Madsen, M. T., Skolimowski, M., Dufva, M., Flyvbjerg, H. & Mølhave, K. Cell motility, morphology, viability and proliferation in response to nanotopography on silicon black. *Nanoscale* **4,** 3739–3745 (2012).

182. Łopacińska, J. M., Emnéus, J. & Dufva, M. Poly(dimethylsiloxane) (PDMS) affects gene expression in PC12 cells differentiating into neuronal-like cells. *PloS One* **8,** 1–11 (2013).

183. Dolatshahi-Pirouz, A., Nikkhah, M., Kolind, K., Dokmeci, M. R. & Khademhosseini, A. Micro- and nanoengineering approaches to control stem cell-biomaterial interactions. *Journal of Functional Biomaterials* **2,** 88–106 (2011).

184. Zorlutuna, P., Annabi, N., Camci-Unal, G., Nikkhah, M., Cha, J. M., Nichol, J. W., Manbachi, A., Bae, H., Chen, S. & Khademhosseini, A. Microfabricated biomaterials for engineering 3D tissues. *Advanced Materials* **24,** 1782–1804 (2012).

185. Limongi, T., Cesca, F., Gentile, F., Marotta, R., Ruffilli, R., Barberis, A., Dal Maschio, M., Petrini, E. M., Santoriello, S., Benfenati, F. & Di Fabrizio, E. Nanostructured superhydrophobic substrates trigger the development of 3D neuronal networks. *Small* **9,** 402–412 (2013).

186. Papadopoulou, E. L., Samara, A., Barberoglou, M., Manousaki, A., Pagakis, S. N., Anastasiadou, E., Fotakis, C. & Stratakis, E. Silicon scaffolds promoting three-dimensional neuronal web of cytoplasmic processes. *Tissue engineering: Part C* **16,** 497–502 (2010).

187. Cha, C., Shin, S. R., Annabi, N., Dokmeci, M. R. & Khademhosseini, A. Carbon-based nanomaterials: multifunctional materials for biomedical engineering. *ACS Nano* **7,** 2891–2897 (2013).

188. Dalby, M. J., Gadegaard, N., Tare, R., Andar, A., Riehle, M. O., Herzyk, P., Wilkinson, C. D. W. & Oreffo, R. O. C. The control of human mesenchymal cell differentiation using nanoscale symmetry and disorder. *Nature Materials* **6,** 997–1003 (2007).

189. Tian, B., Liu, J., Dvir, T., Jin, L., Tsui, J. H., Qing, Q., Suo, Z., Langer, R., Kohane, D. S. & Lieber, C. M. Macroporous nanowire nanoelectronic scaffolds for synthetic tissues. *Nature Materials* **11,** 872–876 (2012).

190. Yow, S.-Z., Lim, T. H., Yim, E. K. F., Lim, C. T. & Leong, K. W. A 3D electroactive polypyrrole-collagen fibrous scaffold for tissue engineering. *Polymers* **3,** 527–544 (2011).

191. Shin, S. R., Jung, S. M., Zalabany, M., Kim, K., Zorlutuna, P., Kim, S., Nikkhah, M., Khabiry, M., Azize, M., Kong, J., Wan, K., Palacios, T., Dokmeci, M. R., Bae, H., Tang, X. & Khademhosseini, A. Carbon-nanotube-embedded hydrogel sheets for engineering cardiac constructs and bioactuators. *ACS Nano* **7,** 2369–2380 (2013).

192. Li, N., Zhang, Q., Gao, S., Song, Q., Huang, R., Wang, L., Liu, L., Dai, J., Tang, M. & Cheng, G. Three-dimensional graphene foam as a biocompatible and conductive scaffold for neural stem cells. *Nature Scientific Reports* **3,** 1–6 (2013).

193. Beaulieu, J.-M. & Gainetdinov, R. R. The physiology , signaling , and pharmacology of dopamine receptors. *Pharmacological Reviews* **63,** 182–217 (2011).

194. Jankovic, J. Parkinson's disease: clinical features and diagnosis. *Journal of Neurology, Neurosurgery, and Psychiatry* **79,** 368–376 (2008).

195. Seiz, E. G., Ramos-Gómez, M., Courtois, E. T., Tønnesen, J., Kokaia, M., Liste Noya, I. & Martínez-Serrano, A. Human midbrain precursors activate the expected developmental genetic program and differentiate long-term to functional A9 dopamine neurons in vitro. Enhancement by Bcl-X(L). *Experimental cell research* **318,** 2446–2459 (2012).

196. Arias-Carrión, O. & Yuan, T.-F. Autologous neural stem cell transplantation: a new treatment option for Parkinson's disease? *Medical hypotheses* **73,** 757–769 (2009).

197. Lindvall, O. & Kokaia, Z. Review series Stem cells in human neurodegenerative disorders — time for clinical translation? *the Journal of Clinical Investigation* **120,** 29–40 (2010).

198. Arenas, E. Stem cells in the treatment of Parkinson's disease. *Brain Research Bulletin* **57,** 795–808 (2002).

199. Spencer, D. S., Robbins, R. J. & Naftolin, F. Unilateral transplantation of human fetal mesencephalic tissue into the caudate nucleus of patients with Parkinson's disease. *The New England Journal of Medicine* **327,** 1541–1548 (1992).

200. Ganz, J., Lev, N., Melamed, E. & Offen, D. Cell replacement therapy for Parkinson's disease: how close are we to the clinic? *Expert Review of Neurotherapeutics* **11,** 1325–1339 (2011).

201. Lindvall, O. & Bjorklund, A. Cell therapy for Parkinson's disease. *The Journal of American Society for Experimental Neurotherapies* **1,** 382–393 (2004).

202. Wang, Y., Chen, S., Yang, D. & Le, W. Stem cell transplantation: a promising therapy for Parkinson's disease. *Journal of Neuroimmune Pharmacology* **2,** 243–250 (2007).

203. Studer, L., Tabar, V. & McKay, R. D. Transplantation of expanded mesencephalic precursors leads to recovery in parkinsonian rats. *Nature Neuroscience* **1,** 290–5 (1998).

204. Kawasaki, H., Mizuseki, K., Nishikawa, S., Kaneko, S., Kuwana, Y., Nakanishi, S., Nishikawa, S. I. & Sasai, Y. Induction of midbrain dopaminergic neurons from ES cells by stromal cell-derived inducing activity. *Neuron* **28,** 31–40 (2000).

205. O'Keeffe, F. E., Scott, S. A., Tyers, P., O'Keeffe, G. W., Dalley, J. W., Zufferey, R. & Caldwell, M. A. Induction of A9 dopaminergic neurons from neural stem cells improves motor function in an animal model of Parkinson's disease. *Brain* **131,** 630–41 (2008).

206. Sánchez-Pernaute, R., Studer, L., Bankiewicz, K. S., Major, E. O. & McKay, R. D. In vitro generation and transplantation of precursor-derived human dopamine neurons. *Journal of Neuroscience Research* **65,** 284–8 (2001).

207. Sanchez-Pernaute, R., Lee, H., Patterson, M., Reske-Nielsen, C., Yoshizaki, T., Sonntag, K. C., Studer, L. & Isacson, O. Parthenogenetic dopamine neurons from primate embryonic stem cells restore function in experimental Parkinson's disease. *Brain : a journal of neurology* **131,** 2127–39 (2008).

208. Bjorklund, L. M., Sánchez-Pernaute, R., Chung, S., Andersson, T., Chen, I. Y. C., McNaught, K. S. P., Brownell, A.-L., Jenkins, B. G., Wahlestedt, C., Kim, K.-S. & Isacson, O. Embryonic stem cells develop into functional dopaminergic neurons after transplantation in a Parkinson rat model. *Proceedings of the National Academy of Sciences of the United States of America* **99,** 2344–2349 (2002).

209. Cho, M. S., Lee, Y.-E., Kim, J. Y., Chung, S., Cho, Y. H., Kim, D.-S., Kang, S.-M., Lee, H., Kim, M.-H., Kim, J.-H., Leem, J. W., Oh, S. K., Choi, Y. M., Hwang, D.-Y., Chang, J. W. & Kim, D.-W. Highly efficient and large-scale generation of functional dopamine neurons from human embryonic stem cells. *Proceedings of the National Academy of Sciences of the United States of America* **105,** 3392–3397 (2008).

210. Wernig, M., Zhao, J.-P., Pruszak, J., Hedlund, E., Fu, D., Soldner, F., Broccoli, V., Constantine-Paton, M., Isacson, O. & Jaenisch, R. Neurons derived from reprogrammed fibroblasts functionally integrate into the fetal brain and improve symptoms of rats with Parkinson's disease. *Proceedings of the National Academy of Sciences of the United States of America* **105,** 5856–5861 (2008).

211. Rodríguez-Gómez, J. A., Lu, J.-Q., Velasco, I., Rivera, S., Zoghbi, S. S., Liow, J.-S., Musachio, J. L., Chin, F. T., Toyama, H., Seidel, J., Green, M. V, Thanos, P. K., Ichise, M., Pike, V. W., Innis, R. B. & McKay, R. D. G. Persistent dopamine functions of neurons derived from embryonic stem cells in a rodent model of Parkinson disease. *Stem Cells* **25,** 918–928 (2007).

212. Dezawa, M., Kanno, H., Hoshino, M., Cho, H., Matsumoto, N., Itokazu, Y., Tajima, N., Yamada, H., Sawada, H., Ishikawa, H., Mimura, T., Kitada, M., Suzuki, Y. & Ide, C. Specific induction of neuronal cells from bone marrow stromal cells and application for autologous transplantation. *The Journal of Clinical Investigation* **113,** 1701–1710 (2004).

213. Parish, C. L., Castelo-branco, G., Rawal, N., Tonnesen, J., Toft, A., Salto, C., Kokaia, M., Lindvall, O. & Arenas, E. Wnt5a-treated midbrain neural stem cells improve dopamine cell replacement therapy in parkinsonian mice. *The Journal of Chemical Physics* **118,** 149–160 (2008).

214. Kim, J., Auerbach, J. M., Rodríguez-Gómez, J. A., Velasco, I., Gavin, D., Lumelsky, N., Lee, S.-H., Nguyen, J., Sánchez-Pernaute, R., Bankiewicz, K. & McKay, R. Dopamine neurons derived from embryonic stem cells function in an animal model of Parkinson ' s disease. *Nature* **418,** 50–56 (2002).

215. Roy, N. S., Cleren, C., Singh, S. K., Yang, L., Beal, M. F. & Goldman, S. A. Functional engraftment of human ES cell-derived dopaminergic neurons enriched by coculture with telomerase-immortalized midbrain astrocytes. *Nature Medicine* **12,** 1259–1268 (2006).

216. Tabar, V., Tomishima, M., Panagiotakos, G., Wakayama, S., Menon, J., Chan, B., Mizutani, E., Al-Shamy, G., Ohta, H., Wakayama, T. & Studer, L. Therapeutic cloning in individual parkinsonian mice. *Nature Medicine* **14,** 379–381 (2008).

217. Takagi, Y., Takahashi, J., Saiki, H., Morizane, A., Hayashi, T., Kishi, Y., Fukuda, H., Okamoto, Y., Koyanagi, M., Ideguchi, M., Hayashi, H., Imazato, T., Kawasaki, H., Suemori, H., Omachi, S., Iida, H., Itoh, N., Nakatsuji, N., Sasai, Y., *et al.* Dopaminergic neurons generated from monkey embryonic stem cells function in a Parkinson primate model. *The Journal of Clinical Investigation* **115,** 102–109 (2005).

218. Shim, J.-W., Park, C.-H., Bae, Y.-C., Bae, J.-Y., Chung, S., Chang, M.-Y., Koh, H.-C., Lee, H.-S., Hwang, S.-J., Lee, K.-H., Lee, Y.-S., Choi, C.-Y. & Lee, S.-H. Generation of functional dopamine neurons from neural precursor cells isolated from the subventricular zone and white matter of the adult rat brain using Nurr1 overexpression. *Stem cells* **25,** 1252–1262 (2007).

219. Krabbe, C., Courtois, E., Jensen, P., Jørgensen, J. R., Zimmer, J., Martínez-Serrano, A. & Meyer, M. Enhanced dopaminergic differentiation of human neural stem cells by synergistic effect of Bcl-xL and reduced oxygen tension. *Journal of Neurochemistry* **110,** 1908–20 (2009).

220. Amatore, C., Arbault, S., Guille, M. & Lemaître, F. Electrochemical monitoring of single cell secretion: vesicular exocytosis and oxidative stress. *Chemical Reviews* **108,** 2585–2621 (2008).

221. Gandhi, S. P. & Stevens, C. F. Three modes of synaptic vesicular recycling revealed by single-vesicle imaging. *Nature* **423,** 607–613 (2003).

222. Neher, E. & Marty, A. Discrete changes of cell membrane capacitance observed under conditions of conditions of enhanced secretion in bovine adrenal chromaffin cells. *Proceedings of the National Academy of Sciences of the United States of America* **79,** 6712–6716 (1982).

223. Douglas, B. Y. W. W. & Rubin, R. P. The mechanism of cathecolamine release from the adrenal medulla and the role of calcium in stimulus-secretion coupling. *The Journal of Physiology* **167,** 288–310 (1963).

224. Kirpekar, S. M. & Wakade, A. R. Release of noradrenaline from the cat spleen by potassium. *The Journal of Physiology* **94,** 595–608 (1968).

225. Wightman, M., May, L. J. & Michael, A. C. Detection of dopamine dynamics in the brain. *Analytical Chemistry* **60,** 769–799 (1988).

226. Kibiuk, L. V. & Stuart, D. http://www.brainfacts.org/brain-basics/neuroanatomy/articles/2012/the-neuron/.

227. Wightman, R. M., Jankowski, J. A., Kennedy, R. T., Kawagoe, K. T., Schroeder, T. J., Leszczyszyn, D. J., Near, J. A., Diliberto, E. J. & Viveros, O. H. Temporally resolved catecholamine spikes correspond to single vesicle release from individual chromaffin cells. *Proceedings of the National Academy of Sciences of the United States of America* **88,** 10754–10758 (1991).

228. Zerby, S. & Ewing, A. G. Electrochemical monitoring of individual exocytotic events from the varicosities of differentiated PC12 cells. *Brain Research* **712,** 1–10 (1996).

229. Amatore, C., Arbault, S., Guille, M. & Lemaître, F. Electrochemical monitoring of single cell secretion: vesicular exocytosis and oxidative stress. *Chemical Reviews* **108,** 2585–2621 (2008).

230. Soo, J.-C., Zhang, J., He, Q., Agarwal, S., Li, H., Zhang, H. & Chen, P. Surface immobilized cholera toxin B subunit (CTB) facilitates vesicle docking, trafficking and exocytosis. *Integrative Biology* **2,** 250–257 (2010).

231. Spégel, C., Heiskanen, A., Acklid, J., Wolff, A., Taboryski, R., Emnéus, J. & Ruzgas, T. On-chip determination of dopamine exocytosis using mercaptopropionic acid modified microelectrodes. *Electroanalysis* **19,** 263–271 (2007).

232. Dias, A. F., Dernick, G., Valero, V., Yong, M. G., James, C. D., Craighead, H. G. & Lindau, M. An electrochemical detector array to study cell biology on the nanoscale. *Nanotechnology* **13,** 285–289 (2002).

233. Amatore, C., Arbault, S., Chen, Y., Crozatier, C., Lemaître, F. & Verchier, Y. Coupling of electrochemistry and fluorescence microscopy at indium tin oxide microelectrodes for the analysis of single exocytotic events. *Angewandte Chemie (International Edition)* **45,** 4000–4003 (2006).

234. Cui, H.-F., Ye, J.-S., Chen, Y., Chong, S.-C. & Sheu, F.-S. Microelectrode array biochip: tool for in vitro drug screening based on the detection of a drug effect on dopamine release from PC12 cells. *Analytical Chemistry* **78,** 6347–6355 (2006).

235. Spégel, C., Heiskanen, A., Pedersen, S., Emnéus, J., Ruzgas, T. & Taboryski, R. Fully automated microchip system for the detection of quantal exocytosis from single and small ensembles of cells. *Lab on a chip* **8,** 323–329 (2008).

236. Liu, X., Barizuddin, S., Shin, W., Mathai, C. J., Gangopadhyay, S. & Gillis, K. D. A microwell device for targeting single cells to electrochemical microelectrodes for high-throughput amperometric detection of quantal exocytosis. *Analytical Chemistry* **83,** 2445–2451 (2011).

237. Chuang, M.-C., Lai, H.-Y., Ho, J. A. & Chen, Y.-Y. Multifunctional microelectrode array (mMEA) chip for neural-electrical and neural-chemical interfaces: Characterization of comb interdigitated electrode towards dopamine detection. *Biosensors and Bioelectronics* **41,** 602–607 (2013).

238. Sasso, L., Heiskanen, A., Diazzi, F., Dimaki, M., Castillo-León, J., Vergani, M., Landini, E., Raiteri, R., Ferrari, G., Carminati, M., Sampietro, M., Svendsen, W. E. & Emnéus, J. Doped overoxidized polypyrrole microelectrodes as sensors for the detection of dopamine released from cell populations. *Analyst* **138,** 3651–3659 (2013).

239. Riaz, S. S., Jauniaux, E., Stern, G. M. & Bradford, H. F. The controlled conversion of human neural progenitor cells derived from foetal ventral mesencephalon into dopaminergic neurons in vitro. *Developmental Brain Research* **136,** 27–34 (2002).

240. Bökel, C. & Brown, N. H. Integrins in development: moving on, responding to, and sticking to the extracellular matrix. *Developmental Cell* **3,** 311–321 (2002).

241. Geiger, B., Bershadsky, A., Pankov, R. & Yamada, K. M. Transmembrane extracellular matrix–cytoskeleton crosstalk. *Nature Reviews* **2,** 793–805 (2001).

242. Jamora, C. & Fuchs, E. Intercellular adhesion, signalling and the cytoskeleton. *Nature Cell Biology* **4,** E101–8 (2002).

243. Giancotti, F. G. Integrin signaling. *Science* **285,** 1028–1033 (1999).

244. Guilak, F., Cohen, D. M., Estes, B. T., Gimble, J. M. & Chen, C. S. Control of stem cell fate by physical interactions with the extracellular matrix. *Cell Stem Cell* **5,** 17–26 (2010).

245. Flaim, C. J., Chien, S. & Bhatia, S. N. An extracellular matrix microarray for probing cellular differentiation. *Nature Methods* **2,** 119–125 (2005).

246. Discher, D. E., Mooney, D. J. & Zandstra, P. W. Growth factors, matrices, and forces combine and control stem cells. *Science* **324,** 1673–1677 (2009).

247. Ghibaudo, M., Trichet, L., Le Digabel, J., Richert, A., Hersen, P. & Ladoux, B. Substrate topography induces a crossover from 2D to 3D behavior in fibroblast migration. *Biophysical journal* **97,** 357–368 (2009).

248. Mandeville, J. T., Lawson, M. A. & Maxfield, F. R. Dynamic imaging of neutrophil migration in three dimensions: mechanical interactions between cells and matrix. *Journal of Leukocyte Biology* **61,** 188–200 (1997).

249. Isacson, O. & Breakefield, O. X. Benefits and risks of hosting animal cells in the humain brain. *Nature Medicine* **3,** 964–969 (1997).

Paper I

Fabrication of high-aspect ratio SU-8 micropillar arrays

Letizia Amato, Stephan S. Keller, Arto Heiskanen, Maria Dimaki, Jenny Emnéus, Anja Boisen, Maria Tenje, Microelectronic Engineering, Volume 98, October 2012, Pages 483-487.

Microelectronic Engineering 98 (2012) 483–487

Contents lists available at SciVerse ScienceDirect

Microelectronic Engineering

journal homepage: www.elsevier.com/locate/mee

Fabrication of high-aspect ratio SU-8 micropillar arrays

Letizia Amato *, Stephan S. Keller, Arto Heiskanen, Maria Dimaki, Jenny Emnéus, Anja Boisen, Maria Tenje

DTU Nanotech, Department of Nano- and Microtechnology, Technical University of Denmark, Ørsteds Plads 345b, 2800 Kgs. Lyngby, Denmark

ARTICLE INFO

Article history:
Available online 24 July 2012

Keywords:
High-aspect ratio SU-8
Micropillars
UV photolithography

ABSTRACT

SU-8 is the preferred photoresist for development and fabrication of high aspect ratio (HAR) three dimensional patterns. However, processing of SU-8 is a challenging task, especially when the film thickness as well as the aspect ratio is increasing and the size of the features is close to the resolution limit of photolithography. This paper describes process optimization for the fabrication of dense SU-8 micropillar arrays (2.5 μm spacing) with nominal height ⩾20 μm and nominal diameter ⩽2.5 μm (AR ⩾8). Two approaches, differing in temperature, ramping rate and duration of the baking steps were compared as part of the photolithographic processing, in order to evaluate the effect of baking on the pattern resolution. Additionally, during the post-processing, supercritical point drying and hard baking were introduced yielding pillars with diameter 1.8 μm, AR = 11 and an improved temporal stability.

1. Introduction

SU-8 is a chemically enhanced, negative tone photoresist, based on the EPON® SU-8 resin and composed of epoxy oligomers. The resin contains the photo-acid generator (up to 10 wt%) triarylsulfonium hexafluoroantimonate salt, and is dissolved in an organic solvent to enable spin coating [1,2]. Typically, SU-8 processing comprises spin coating, solvent removal, UV-exposure, polymerization, and development [3–5]. The lithographic performance of SU-8 (resolution, delamination, cracking, etc.) is affected by the parameters of every process step, each strongly influencing the obtained results and requiring individual tailoring for a desired application to obtain well-resolved and stable microstructures [6–11]. Therefore, values of parameters described in literature vary in a wide range depending on the different structural features.

The goal of this work was to fabricate dense arrays of high-aspect ratio (HAR) (⩾8) SU-8 micropillars with spacing and diameter approaching the resolution limit of standard UV photolithography. Possible applications of such SU-8 micropillars can comprise superhydrophobic surfaces [12] and carbon MEMS [13]. However, to our knowledge, HAR (⩾8) micropillars fabricated with UV photolithography have been reported only for diameters ⩾5 μm [13–15]. In the case of smaller diameters, the photolithographic resolution becomes critical, and lack of mechanical stability of the structures leads to cracking, collapsing and delamination from the substrate. Furthermore, the required thickness of an SU-8 layer to obtain a sufficient AR for small-diameter pillars causes a challenge by significantly reducing the photolithographic resolution. Thereby, when approaching the resolution limit even incremental progresses are difficult to achieve.

Micro- and nanopillars with AR much higher than 10 can be achieved using X-ray, e-beam and two-photon lithography [15,16]. However, these methods are very costly, require long processing times, and are hardly applicable for high-throughput fabrication of arrays. Additionally, in the case of X-ray lithography, the difficult access to synchrotron radiation strongly restricts the availability of this technique.

In photolithographic processing, conventionally soft-bake (SB) and post-exposure bake (PEB) are performed at an elevated temperature (between 60 and 100 °C) for a short time (3–5 min) [1,17]. However, previously published results have shown that SB at a lower temperature (between the ambient and 50 °C), combined with a low-temperature PEB at 50 °C minimizes thermal stress and thus also delamination and cracking [18,19].

In this paper, two processing approaches with different temperature, ramping rate and duration of SB and PEB are compared for the fabrication of SU-8 micropillars with height ⩾20 μm. CO_2 supercritical point drying and hard baking after the lithographic process are evaluated as means to overcome the collapsing of the structures and to achieve a high temporal stability.

2. Materials and methods

Preliminary experiments showed that delamination of the micropillars from the substrate is a major issue independent of the processing parameters. Therefore, a thin SU-8 underlayer (5 μm) was added in the processing.

* Corresponding author.
E-mail address: leta@nanotech.dtu.dk (L. Amato).

0167-9317/$ - see front matter © 2012 Elsevier B.V. All rights reserved.
http://dx.doi.org/10.1016/j.mee.2012.07.092

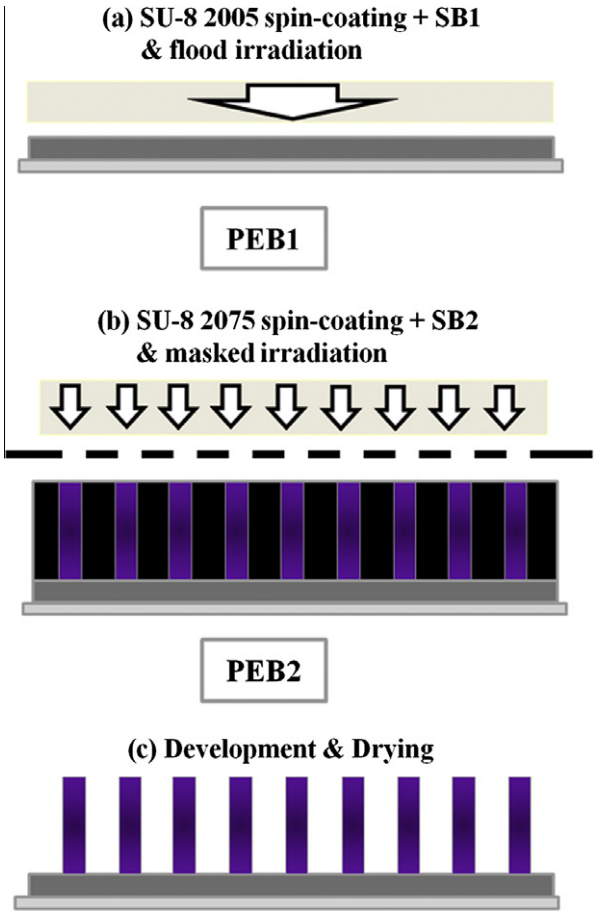

Fig. 1. A schematic flow of the lithographic process.

Using a surface micromachining approach, SU-8 resists of different viscosities from Micro Resist Technology (Germany) were sequentially processed and simultaneously developed to fabricate the thin underlayer (SU-8 2005) and the micropillars (SU-8 2075). The process flow is schematically illustrated in Fig. 1.

Si (100) wafers were chosen as substrates for fabrication of all the structures. Spin coating of the photoresists was done using a RC8 spin-coater (Karl-Süss, France). For the exposure steps, a MA6/BA6 aligner (Karl-Süss, France) was used. The aligner was equipped with a mercury lamp filtered at 365 nm (i-line filter, 20 nm FWHM) because the increased absorption of the SU-8 at shorter wavelengths would jeopardize the resolution.

To prepare the underlayer film with the nominal thickness of 5 μm, approximately 3 ml of SU-8 2005 were manually dispensed onto the substrate and spun at 2000 rpm for 30 s with an acceleration of 5000 rpm s^{-1}. The film was then flood exposed administering the exposure dose (D) of 500 mJ cm^{-2} as two single exposures of 250 mJ cm^{-2}.

In the case of the film for patterning of the micropillars, approximately 4 ml of SU-8 2075 were manually deposited in the central part of the substrate and the coating was performed using a two-step spin process. A spread cycle of 30 s at 1000 rpm with 200 rpm s^{-1} acceleration was applied to ensure that the deposited SU-8 was spread across the entire wafer. Subsequently, the wafer was spun at 4000 rpm for 120 s with 500 rpm s^{-1} acceleration, yielding a 23 μm thick film. The second layer of SU-8 was patterned by exposure in hard contact mode through a mask. The mask design included hole arrays of various dimensions (ranging from 1.5 to 15 μm) with a spacing equal to the hole diameter in each array. This design allowed for monitoring of the lithographic resolution of the corresponding process. The exposure dose (D) was optimized to achieve the highest resolution. D from 100 to 200 mJ cm^{-2} was tested and D = 150 mJ cm^{-2} was selected.

To determine the effect of the baking steps on the micropillar fabrication, temperature, ramping rate (R), and baking time of SB as well as PEB were varied in the experiments. A programmable hotplate (Harry Gestigkeit GmbH, Germany) for parallel processing of four samples was used for all the baking steps. The wafers were placed on a cold hotplate and ramped to the baking temperature. At the end of the baking time, the wafers were allowed to cool on the hotplate to room temperature by natural cooling over a period of 1.5–2 h. The two approaches of SU-8 processing that were compared in this work are denoted by "high temperature" (HTP) and "low temperature" procedure (LTP). The baking parameters are summarized in Table 1. A two-step baking at 60 and 90 °C was performed in the HTP. For the LTP, the final bake temperature was 50 °C.

The development in propylene glycol methyl ether acetate (PGMEA) was performed in two steps. First a rough development to remove most of the unexposed SU-8 was done for 5 min, after which each wafer was transferred to a second developer bath for another 5 min. Development was terminated by an isopropanol rinse for 30 s and subsequently the wafers were dried by evaporation of the rinse solvent, either in air or using supercritical drying with CO_2. For the supercritical drying, the specimens were placed in an isopropanol bath directly after development and then transferred to an Autosamdri-810 CO_2 supercritical point dryer (Tousimis, USA).

After drying, an additional two-step flood exposure with the total D = 500 mJ cm^{-2} and a hard-bake at 90 °C for 15 h in an oven were tested. This procedure has been used earlier to minimize residual stress and enhance temporal-stability of SU-8 cantilevers [19].

Imaging of the pillars was done using a FEI Nova 600 scanning electron microscope (SEM) in low-vacuum mode, at the pressure of 0.6 mbar to minimize charging of the non-conducting polymer samples.

3. Results

Fig. 2 shows that the resolution limit for the two processes was different. Micropillars with the nominal diameter ($N\varnothing$) = 3 μm processed with the HTP show irregular deformation and bending (Fig. 2A). Furthermore, the features are characterized by spikes of crosslinked SU-8 connecting them in the proximity of their base. The comparable structures with the LTP are well resolved and straight with an effective $\varnothing = 2.6 \pm 0.1$ μm (Fig. 2B). Micropillars with $N\varnothing$ = 2.5 μm fabricated with HTP were not well resolved forming an indistinct block of photoresist with stretched pillars

Table 1
Baking parameters of the "high temperature" and "low temperature" procedure. SB = soft-bake; PEB = post-exposure bake; R = ramping rate.

	Baking step	High temperature procedure (HTP)	Low temperature procedure (LTP)
Underlayer (SU-8 2005)	SB	5 min at 60 °C, R = 2 °C/min; 5 min at 90 °C, R = 2 °C/min	2 h at room temperature
	PEB	5 min at 60 °C, R = 2 °C/min; 5 min at 90 °C, R = 2 °C/min	1 h at 50 °C, R = 15 °C/min
Pillars (SU-8 2075)	SB	2 min at 60 °C, R = 2 °C/min; 5 min at 90 °C, R = 2 °C/min	1 h at 50 °C, R = 15 °C/min
	PEB	1 min at 60 °C, R = 2 °C/min; 5 min at 90 °C, R = 2 °C/min	2 h at 50 °C, R = 15 °C/min

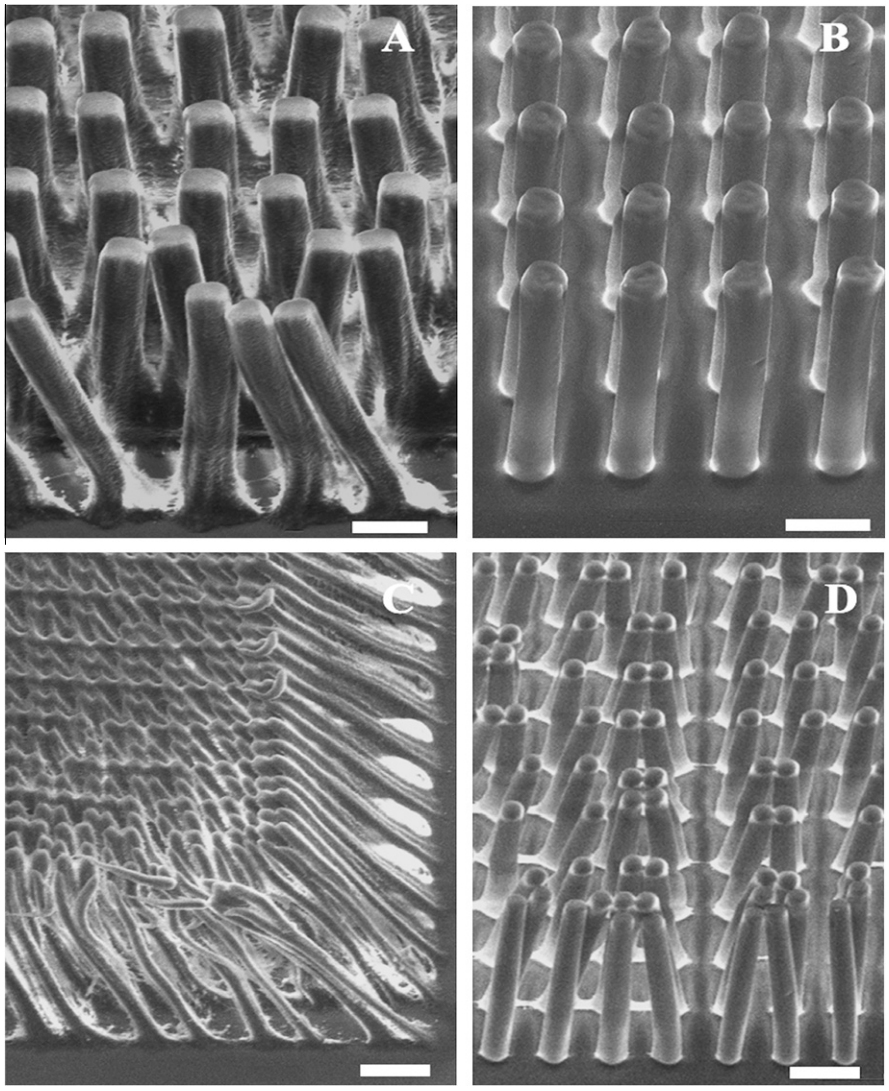

Fig. 2. SEM images of pillars processed with the HTP (A and C) and with the LTP (B and D). Micropillars with *N*Ø 3 μm (top) and 2.5 μm (bottom). Scale bars: 5 μm.

on the edges (Fig. 2C). For the LTP, well defined structures were achieved. However, neighboring pillars were leaning towards each other (Fig. 2D).

The results demonstrate that the pillars processed with the LTP have a higher structural stability than the ones fabricated with the HTP. The residual solvent content during polymerization of the photoresist is high for the LTP due to a lower temperature of the SB. The consequences are enhanced diffusion of photo-acid and mobility of the monomers in the polymer matrix, both promoting crosslinking of the SU-8 [19]. Apparently, the enhanced diffusion due to the higher residual solvent content does not seem to affect the photolithographic resolution of the LTP.

In comparison, the high-temperature SB in the case of the HTP results in low residual solvent content. The observed lack of structural stability of the micropillars indicates insufficient crosslinking even though the PEB is performed at a higher temperature compared to the LTP. On the other hand, the high temperature during the PEB of the HTP sufficiently enhances diffusion of photo-acid and photoresist polymerization in non-exposed regions causing loss of resolution of the structures. For pillars with *N*Ø = 3 μm, the lack of resolution at the lower part of the pattern is probably caused by temperature and solvent gradients in the SU-8 layer. During baking on a hot plate, the resist is heated from below by heat conduction, and a temperature gradient is developed in the resist layer, with a higher temperature at the bottom of the photoresist. This results in higher diffusion of photo-acid in the volume close to the silicon substrate, which affects the resolution. These considerations are even more significant for pillars with *N*Ø = 2.5 μm indicated by partial merging of the neighboring pillars.

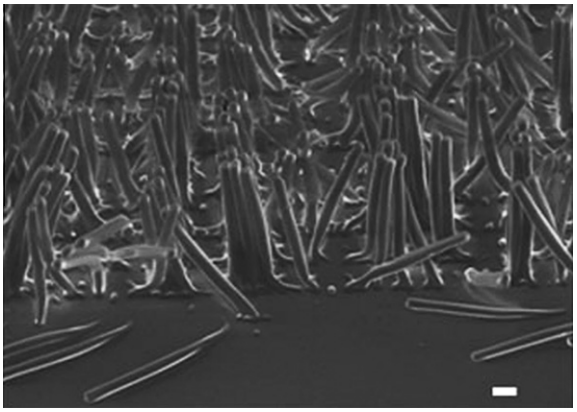

Fig. 3. SEM image of unresolved and delaminated micropillars with nominal Ø 2 μm fabricated using the LTP. Scale bar: 10 μm.

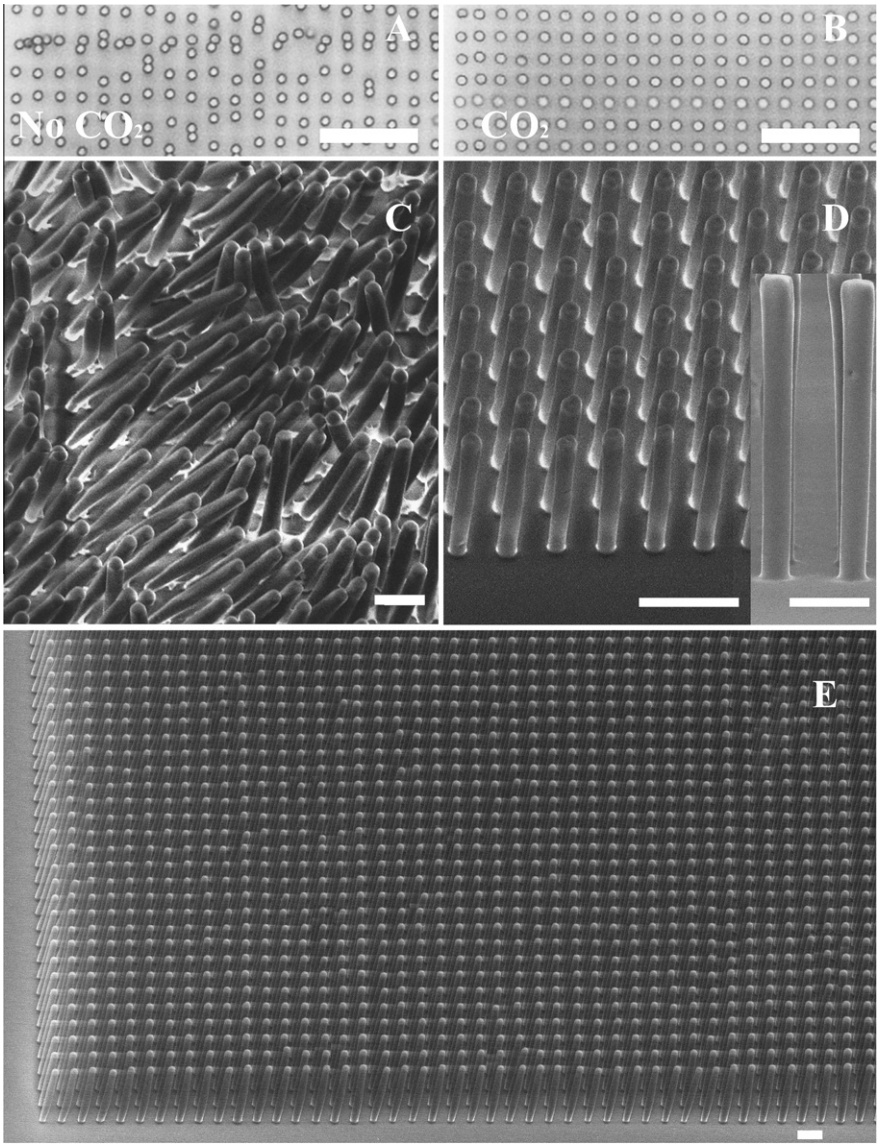

Fig. 4. Pillars with AR 11. Top: Optical microscope image of air dried (No CO_2) and supercritically dried (CO_2) pillars (Scale bar: 20 μm). Bottom: SEM images of pillars 7 days after fabrication. (Scale bar: 5 μm) (C) Collapsed pillars without hard bake. (D) Hard baked standing pillars. Inset: micropillars with aspect ratio 11 (Ø 1.8 μm and height 20 μm). (E) Zoom-out of standing pillars.

In the case of pillars with *NØ* = 2 μm, only a single block of SU-8 with no defined structures was observed when using the HTP (results not shown). The LTP yielded well-resolved standing pillars forming aggregates mixed with structures delaminated from the substrate (Fig. 3). Micropillars with *NØ* = 1.5 μm and *NØ* = 1 μm could not be fabricated.

3.1. CO_2 drying

The observed collapsing of the pillars with *NØ* of 2.5 μm (Fig. 2D) is due to the capillary forces, caused by the surface tension of the rinse liquid during the drying step after the development process [21,22]. The capillary forces act on the resist walls during solvent evaporation and cause bending and sticking of neighboring features. The collapse of the pattern is related to the mechanical properties of the resist and therefore to the lack of strength of the structures compared to the forces during drying. In addition, the longer the distance between the pillars, the smaller is the force on the structures, thus reducing the collapse [23]. This explains the collapse of the 2.5 μm pillars having a small spacing of only 2.5 μm.

To prevent the collapsing of the patterns, increasing the structural stability is limited whereas reduction of the surface tension due to the rinse liquid is the most plausible approach. Supercritical drying with CO_2 was tested to reduce the surface tension. Fig. 4 shows the comparison between samples dried with air (No CO_2) and supercritically dried (CO_2). When using supercritical drying, the isopropanol, which is used for rinsing after the development, is soluble in CO_2. This eliminates the surface tension and hence the capillary force becomes nonexistent, resulting in straight pillars (CO_2).

3.2. Hard baking

A few days after the processing, the pillars started to collapse, despite the fact that the samples had been dried with CO_2 (Fig. 4C). Moisture absorption and thermal vibrations during storage may explain the collapsing of the pillars. Further experiments showed that an additional flood exposure and a hard-baking step increase the temporal stability of the structures (Fig. 4D). The structural stability of the pillars is due to enhanced crosslinking

of the SU-8 and reduction of the residual solvent content. The densification during this process results in shrunken structures with Ø 1.8 μm (±0.1) and AR 11.

4. Conclusions

We have demonstrated that performing the baking steps at low temperature (50 °C) for long time (1–2 h) is essential for the fabrication of HAR structures with dimensions close to the resolution limit of photolithography. The obtained high structural stability is facilitated by enhanced crosslinking and high resolution is achieved due to limited diffusion.

The proposed method yields well resolved but collapsed pillars. The collapsing of structures can be eliminated by subsequent critical point drying and hard baking after the lithographic process. The optimized process yields standing micropillars with Ø 1.8 μm, AR = 11 having high temporal stability.

References

[1] N. Labianca, J. Delorme, Proc. SPIE 2438 (1995) 846.
[2] H. Lorenz, M. Despont, P. Vettiger, P. Renaud, Microsyst. Technol. 4 (1998) 143.
[3] J.M. Shaw, J.D. Gelorme, N.C. LaBianca, W.E. Conley, S.J. Holmes, IBM J. Res. Dev. 41 (1997) 81.
[4] J.V. Crivello, J. Polym. Sci. A 37 (1999) 4241.
[5] W.H. Teh, U. Dürig, U. Drechsler, C.G. Smith, H.-J. Güntherodt, J. Appl. Phys. 97 (2005) 054907.
[6] B. Eyre, J. Blosiu, D. Wiberg, Proc. MEMS (1998) 218.
[7] Z.G. Ling, K. Lian, L. Jian, Proc. SPIE 2 (2000) 1019.
[8] J. Zhang, K.L. Tan, H.Q. Gong, Polym. Test. 20 (2001) 693.
[9] S.J. Hong, S. Choi, Y. Choi, M. Alien, G.S. Proc. IEEE/ASMC 404, 2004.
[10] J.D. Williams, W. Wang, J. Microlithogr, Microfabric. Microsyst. 3 (2004) 563.
[11] J. Zhang, M.B. Chan-Park, S.R. Conner, Lab. Chip 4 (2004) 646.
[12] N.J. Shirtcliffe, S. Aqil, C. Evans, G. McHale, M.I. Newton, C.C. Perry, P. Roach, J. Micromech. Microeng. 14 (10) (2004) 1384.
[13] C. Wang, M. Madou, Biosens. Bioelectr. 20 (2005) 2181.
[14] H. Sato, Y. Houshi, S. Shoji, Microsyst. Technol. 10 (2004) 440.
[15] A. del Campo, C. Greiner, J. Micromech. Microeng. 17 (2007) R81.
[16] V.J. Cadarso, K. Pfeiffer, U. Ostrzinski, J.B. Bureau, G.A. Racine, A. Voigt, G. Gruetzner, J. Brugger, J. Micromech. Microeng. 21 (2010) 017003.
[17] C.H. Lin, G.B. Lee, B.W. Chang, G.L. Chang, J. Micromech. Microeng. 12 (2002) 590.
[18] T.A. Anhoj, A.M. Jorgensen, D.A. Zauner, J. Hübner, J. Micromech. Microeng. 16 (2006) 1819.
[19] S. Keller, G. Blagoi, M. Lillemose, D. Haefliger, A. Boisen, J. Micromech. Microeng. 18 (2008) 125020.
[21] T. Tanaka, M. Morigami, N. Atoda, Jpn. J. Appl. Phys. 32 (1993) 6059.
[22] Y. Jincao, M.A. Mattews, C.H. Darvin, Ind. Eng. Chem. Res. 40 (2001) 5585.
[23] H.J. Lee, J.T. Park, J.Y. Yoo, I. An, H.K. Oh, JKPS 42 (2003) S202.

Paper II

Dense High-Aspect Ratio 3D Interdigitated Carbon Pillar Microelectrode Arrays

Letizia Amato, Arto Heiskanen, Rasmus Hansen, Maria Tenje, Lauge Gammelgaard, Tomas Rindzevicius, Anja Boisen, Jenny Emnéus, Stephan S. Keller

Manuscript

Dense High-Aspect Ratio 3D Interdigitated Carbon Pillar Microelectrode Arrays

Letizia Amato[1], Arto Heiskanen[1], Rasmus Hansen[1], Maria Tenje[2], Lauge Gammelgaard[3], Tomas Rindzevicius[1], Anja Boisen[1], Jenny Emnéus[1], Stephan S. Keller[1*]

[1]*Department of Micro and Nanotechnology, Technical University of Denmark (DTU-Nanotech), Kgs. Lyngby, Denmark*
[2]*Department of Electrical Measurements, Lund University, Lund, Sweden*
[3]*Capres A/S, Diplomvej 373, DK-2800 Kgs. Lyngby, Denmark*

**Corresponding author: Stephan S. Keller (email: Stephan.Keller@nanotech.dtu.dk)*

1. Introduction

For miniaturised and portable electrochemical sensors, maximizing the electrode area on a micro-sized footprint is essential, and can be facilitated by three-dimensional (3D) electrodes. Several methods have enabled fabrication of 3D electrode arrays[1–4]. Fabrication of 3D metal electrodes requires the use of metal electroplating, sputtering or evaporation equipment, which often limits fabrication throughput and results in expensive devices that are not amenable for mass-production. An alternative and attractive method for 3D electrode fabrication is based on the carbon MEMS technique[5], a very simple, high-yield and cost-effective process that is based on pyrolysis of lithographically patterned polymeric precursors with strictly defined or arbitrary geometries. Polymer derived carbon is electrochemically and structurally similar to glassy carbon (GC): the microstructure contains graphitic (C atoms form sp^2 bonds as in graphite) and amorphous zones (C atoms form sp^3 bonds) [6–9]. The graphitic content of pyrolysed carbon can be tuned by tailoring the parameters during fabrication of the polymer precursor template[10–12] and the pyrolysis conditions[13,14]. Pyrolysed carbon electrodes exhibit a wide electrochemical potential window[15], chemical inertness towards a wide variety of solvents and electrolytes[16], good biocompatibility[17], and outstanding as well as tunable mechanical properties[16,18]. All these features make them the

ideal material choice for applications such as chemical sensing[19], heavy metal detection[20], biosensors[21–23], cell culture and differentiation[17,24,25], and microbatteries[26–28].

This work is the first report on fabrication and characterization of 3D electrode arrays in SU-8 derived pyrolysed carbon with a spacing and diameter approaching the resolution limit of standard UV photolithography (diameter 1.4 μm, spacing 5 μm, and aspect ratio of about 8). SU-8, the polymer precursor in our study, is a negative photoresist that is commonly used to fabricate high-aspect ratio (HAR) micro- and nanostructures[29–34]. Although pyrolysed micropillar arrays with aspect ratio higher than 10 have been fabricated before, their diameter and spacing were larger than 10 μm[34].

Our aim was to fabricate 3D carbon electrodes on wafer-scale, consisting of HAR pillars finely patterned in an interdigitated electrode (IDE) format (3D-IDE). Different types of 2D and 3D pyrolysed carbon structures were fabricated, followed by thorough characterisation of surface- and microstructures, as well as investigation of electrical and electrochemical properties.

The surface exposure and pyrolysis history of pyrolysed carbon electrodes can be critical for its performance, reproducibility, and stability. Most carbon surfaces[35] are prone to oxidize upon exposure to air and to adsorb impurities, leading to varying surface[6,36] and electronic[37] properties with time. Most of the proposed methods[38–41] for electrode regeneration produce changes in the structure[39,41] and properties of carbon electrodes and cannot be directly employed for microfabricated 3D electrodes.

Here, we demonstrate a relation between increased oxygen content and increased resistivity upon exposure of the electrode to air and present a method to efficiently regenerate the surface and electrical properties of the carbon electrodes.

2. Experimental section

2.1. Microfabrication of carbon electrodes

2.1.1. Materials

The negative epoxy photoresist SU-8 was purchased from Microresist GmbH (Berlin, Germany). SU-8 2005 (solid content 14 wt.%) and SU-8 2075 (solid content 73wt.%) were used as received. SU-8 2035 (solid content 70 wt.%) was diluted with cyclopentanone (BioReagent) to 56 wt.%. Phosphate buffered saline (PBS), potassium ferricyanide ($[Fe(CN)_6]^{3-}$), hexaammineruthenium(III) chloride and hexaammineruthenium(II) chloride were purchased from Sigma-Aldrich Corporation (St. Louis, MO, USA). Potassium ferrocyanide ($[Fe(CN)_6]^{4-}$) was purchased from Fluka BioChemica (Buchs, Germany). All solutions used for electrochemical characterization were prepared in ultrapure water (resistivity 18.2 Mohm cm) from a Milli-Q ® water purification system (Millipore Corporation, Billerica, MA, USA).

2.1.2 Preparation of unpatterned pyrolysed carbon films

For detailed characterization of the carbon electrode material properties, unpatterned SU-8 films with three different thicknesses were prepared and pyrolysed. 5 µm thick films of SU-8 2005 and 9 µm thick films of diluted SU-8 2035 were investigated as potential thicknesses of the precursor layer for the definition of the 2D interdigitated electrodes. 22 µm thick films of SU-8 2075 were characterized because films with this thickness were later used for the fabrication of the precursor structures of the 3D carbon pillar microelectrodes. The detailed method for the processing of SU-8 films was described earlier[29]. Briefly, the resist films were spin coated on top of 4-inch silicon wafers with a 2 µm thick thermal silicon dioxide layer. This was followed by soft baking on a hotplate and flood exposure with UV radiation (i-line, 365 nm). The exposed samples were subjected to a post-exposure-bake (PEB) on a hotplate and the uncrosslinked SU-8 was developed in Propylene Glycol Monomethyl Ether Acetate (PGMEA). The processing parameters for the SU-8 films with different thicknesses are summarized in Table 1.

The different SU-8 films were pyrolysed in a PEO-601 furnace (ATV Technologie GmbH, Vaterstetten, Germany) in nitrogen atmosphere. The pyrolysis protocol featured two stages: (i) a temperature ramp from room temperature to 200°C followed by a 30 min dwell time at 200°C to allow for any residual oxygen to be evacuated from the chamber and prevent combustion of the polymer as the temperature is increased further; and (ii) a temperature ramp from 200 to 900°C with 1 h dwell time at 900°C to complete the carbonization. The samples were heated and cooled down to room temperature at a ramp of 2°C /min.

Table 1 – Processing parameters for unpatterned SU-8 films with different thicknesses

SU-8 type	2005	2035 (dil.)	2075
SU-8 thickness	5 µm	9 µm	22 µm
Spin coating I: Spread cycle	2000 rpm/30 s 5000 $rpms^{-1}$	1000 rpm/30 s 200 $rpms^{-1}$	1000 rpm/30 s 200 $rpms^{-1}$
Spin coating II: Thinning cycle	None	4000 rpm/120 s 500 $rpms^{-1}$	4000 rpm/120 s 500 $rpms^{-1}$
Soft bake	2 h at RT (solvent evaporation)	15 min at 50 °C	1 h at 50 °C
Exposure	500 mJ/cm^2	500 mJ/cm^2	500 mJ/cm^2
Post bake	1 h at 50 °C	1 h at 50 °C	2.5 h at 50 °C

2.1.3 Fabrication of 3D carbon micropillar arrays

Large arrays of carbon micropillars with various dimensions were designed and fabricated to allow for initial characterization of electrical and electrochemical properties of 3D microelectrodes. For this purpose, SU-8 micropillar arrays were defined on unpatterned SU-8 films following a procedure previously described in detail[29] and subsequently pyrolysed . A 5 µm thick layer of SU-8 2005 simulating the 2D bottom layer of the final device and a 22 µm thick 3D pillar layer of SU-8 2075 were processed as described in Table 1. An air gap between the mask and the resist caused by the presence of an edge bead (EB) can severely reduce the lithographic resolution and the batch-to-batch reproducibility of HAR pillars. Thus, an EB removal (EBR) step was performed after spin coating of the pillar layer to minimize the height of EB. The EBR was optimized resulting in an EB of 4.6 µm (± 0.1; average ± SD, n=4) compared to 6.9 µm (± 0.1; average ± SD, n=4) without EBR.

The pillar layer was exposed with 150 mJ/cm^2 through a test mask with hole arrays of different diameters ranging from 3 to 15 µm. After development, the sample was dried in supercritical CO_2. In order to completely crosslink the resist, samples were flood exposed with 500 mJ/cm^2 and hard baked on a hotplate at 90 ° C for 15 h[42]. Finally, the SU-8 structures were pyrolysed following the process described above.

2.1.4 Fabrication of 3D interdigitated carbon microelectrodes (3D-IDE)

To obtain the final 3D interdigitated carbon microelectrodes, a polymer precursor structure with SU-8 micropillars on a patterned SU-8 film was fabricated using a multistep process

(Fig. 1a-d) followed by pyrolysis (Fig. 1e). Prior to SU-8 processing, alignment marks were photolithographically patterned in a positive photoresist (AZ©5214E from Micro- Chemicals GmbH, Ulm, Germany) using an image reversal process, followed by metal deposition (10 nm thick Cr adhesion layer and 150 nm thick Au layer) via electron beam evaporation and lift off in acetone (Fig. 1a). SU-8 photolithography was performed in two steps: (1) Patterning of planar interdigitated fingers in SU-8 2005 with 5 µm thickness, 5 µm width and 5 µm spacing (Fig. 1b). The process parameters were the ones described in Table 1 with an exposure dose of 140 mJ/cm^2. (2) Fabrication of SU-8 2075 pillars with 22 µm height and 3 µm diameter on top of the planar interdigitated fingers (Fig. 1c-d) as described in section 2.1.3.

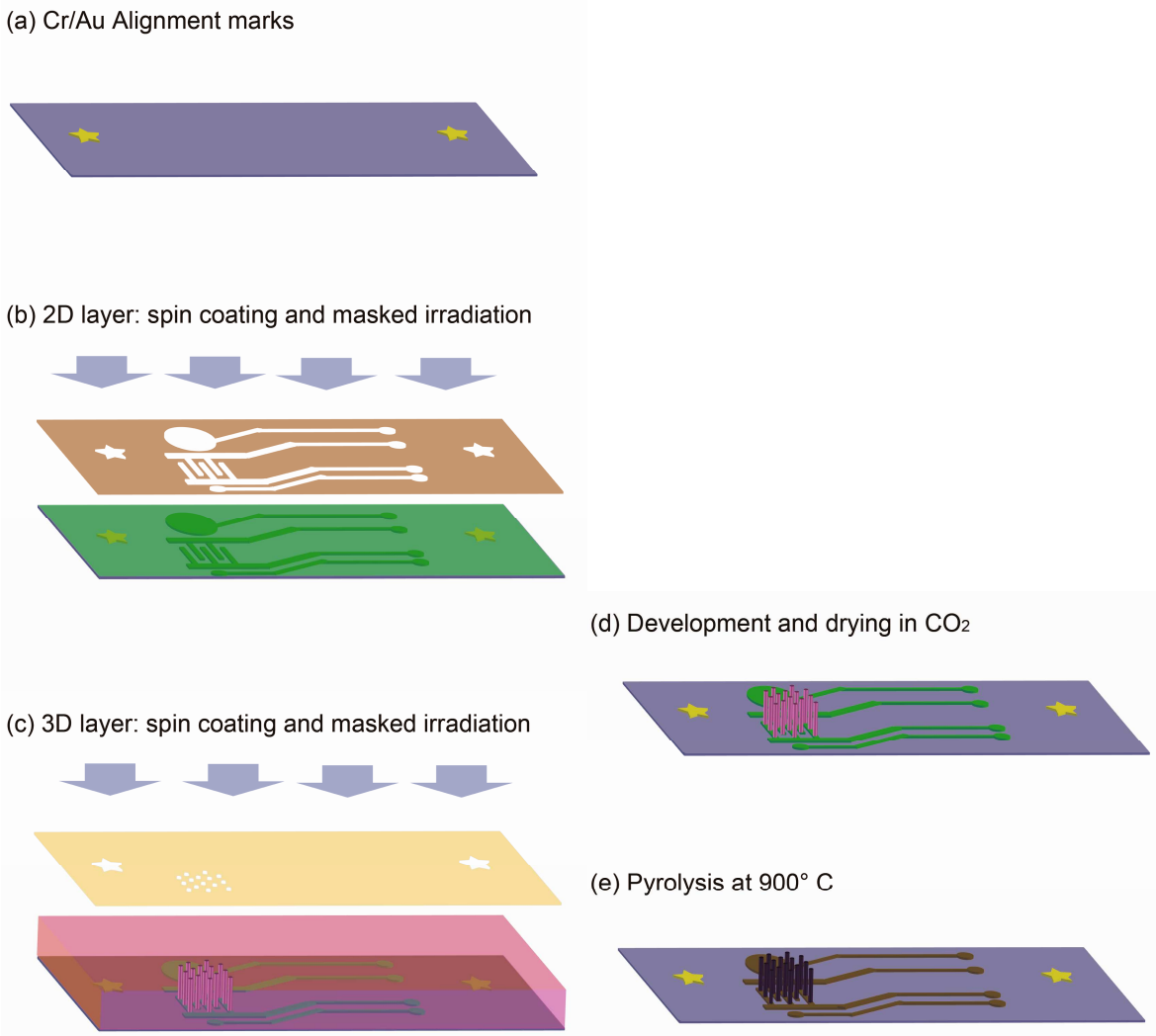

Figure 1. Schematic view of the fabrication process

2.1.5 Electrode regeneration

For regeneration of carbon structures after exposure to air contamination, temperature treatment of carbon was performed at 800 °C for 30 min with a heating and cooling rate of 10°C /min, similarly to a previously reported procedure[43].

2.2. Characterization of carbon electrodes

A range of techniques was used to characterise the structural-, electrical- and electrochemical properties of the unpatterned carbon films and the carbon microelectrodes.

2.2.1. Shrinkage measurements using SEM and profilometer

A scanning electron microscope (Zeiss Supra VP 40) was used for imaging of the carbon micropillar arrays (section 2.1.3) and the 3D-IDE (section 2.1.4). To evaluate the shrinkage of the micropillars, the structure height and diameter were characterized before and after pyrolysis For the same purpose, the height and width of the IDE structures interconnecting the pillars were measured before and after pyrolysis using a Dektak 8 stylus profiler (Veeco). The % shrinkage *s* was expressed as[44]

$$s = 1 - \frac{d_c}{d_{SU8}} \quad (1)$$

where d_{SU8} is a dimensional parameter of the SU-8 microstructure before pyrolysis such as the thickness, length, width or diameter and d_c the corresponding parameter of the carbon microstructure after pyrolysis.

2.2.3. Raman spectroscopy

The bulk structure of carbon films obtained from 5 µm and 22 µm thick SU-8 layers was analysed by visible Raman Spectroscopy performed using a Raman microscope (Model DXR, Thermo Fisher Scientific Inc, Denmark) with an excitation wavelength of 532 nm. All the spectra were recorded with a 10x long working distance objective and 5 mW laser power. The Raman spectra were analysed using OMNIC software from Thermo Scientific.

2.2.4. X-ray Photoelectron Spectroscopy (XPS)

The surface composition of carbon films obtained from 5 µm SU-8 layers at day 1 and day 90 after pyrolysis was characterized using XPS. The analysis was carried out in a Thermo K-

Alpha XPS instrument with a monochromatic Al–Kα-source and charge compensation. For each sample a binding energy survey from 0 to 1350 eV was performed followed by detailed spectral analysis in the C_{1s} binding energy ranges. The atomic concentrations of surface elements were extracted, using the software package Advantage provided by Thermo Fisher Scientific.

2.2.5. Electrical characterization

Four-point probe (4PP) measurements on unpatterned carbon films obtained from 5 µm, 9 µm and 22 µm thick SU-8 layers were carried out with a CAPRES microRSP-M150 using a lock-in technique[45]. The current set-point was 200 µA and the frequency 13 Hz. The static contact micro-four point probe used in these experiments consisted of micro-machined L-shaped cantilevers extending from the edge of a silicon support[45]. Electrical characterization on carbon films obtained from 5 µm thick SU-8 layers was done at different days after pyrolysis (1, 13, 26, 90 days). An identical approach was approach was used for electrical characterisation of the pillars and the flat underlayer carbon sheet (Fig. 2). For these measurements, cantilevers of a four-point probe with a pitch matching the one of a micropillar array were placed on top of the carbon pillars as shown in Fig 2B.

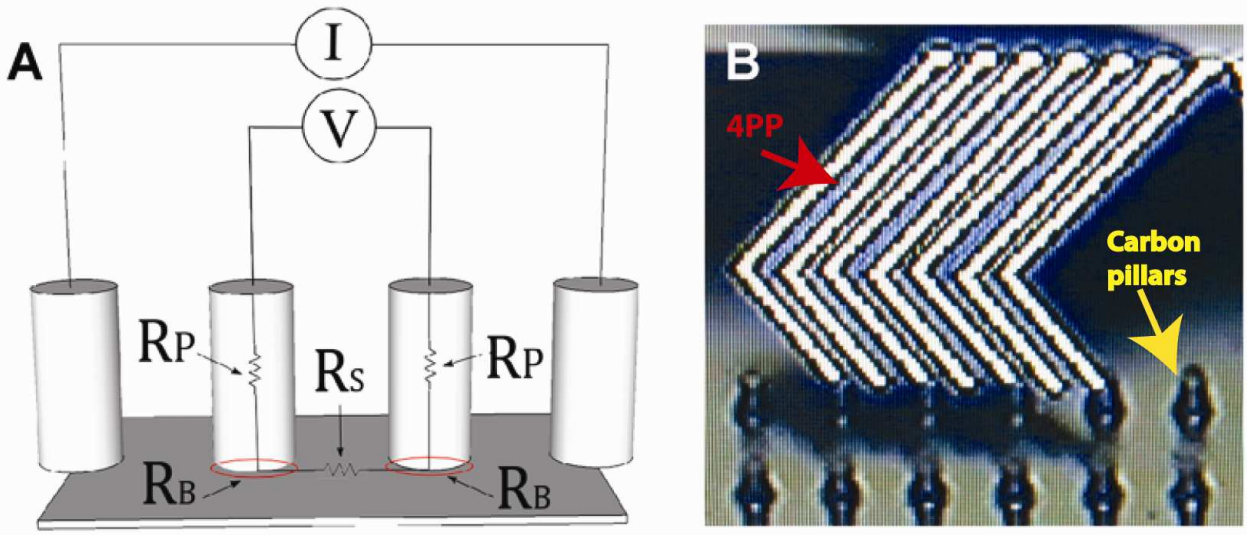

Figure 2. (A) Conceptual illustration of the four-point probe (4PP) measurements on top of the pillars. (R_P = pillar resistance; R_B = contact resistance between the pillars and the underlayer interface; R_S = resistance of underlayer). (B) A micrograph of a 4-point probe aligned on top of the carbon pillars.

2.2.6 Electrochemical characterization

Electrochemical characterization was performed on unpatterned carbon films obtained from 5 µm and 9 µm SU-8 layers using electrochemical impedance spectroscopy (EIS) and cyclic voltammetry (CV). The impedance spectra were acquired in the frequency range 0.1 - 10^6 Hz. The carbon electrode chips were placed in a micromilled poly(methylmethacrylate) (PMMA) holder. The holder (Supporting Information, S1) formed a 70-µL vial on top of the electrode chip to facilitate liquid handling during experiments. Interconnections between the electrode chip and the potentiostat (Reference 600 from Gamry Instruments, Warminster, PA, USA) were obtained using a tailor-made PCB having gold plated spring loaded pins (Mill-Max Mfg. Corp., Oyster Bay, NY, USA). Cr/Au pads on the carbon film chip served as electrical contacts for easy interface with an electrochemical system set-up. The Cr/Au metal layers (20/200nm) were patterned through a shadow mask by sputtering. In all experiments, an Ag/AgCl electrode served as pseudo-reference electrode (RE) and a platinum wire served as a counter electrode (CE). The EchemAnalyst software from Gamry was used to analyse the acquired impedance spectra.

3. Results and Discussion

3.1. Microfabrication of carbon micropillar arrays and interdigitated electrodes

As shown in Fig. 3 and 4, 3D micropillar arrays and 3D interdigitated carbon electrodes in different dimensions derived from SU8 were successfully fabricated. Below follows the charachterisation of these structures before and after pyrolysis using various characterisation techniques such as profilometry, SEM, 4PP, XPS, Raman spectroscopy, EIS, and CV.

Usually during pyrolysis a significant loss of material takes place due to evaporation of hydrocarbons, CO_2, and other gaseous products upon decomposition of photoresist and aromatization. These events result in weight loss and densification, leading to shrinkage of the structures[46]. In order to investigate the shrinkage of SU8 during pyrolysis, unpatterned SU-8 films with the three different thicknesses used for making the final 3D pillar structures were first prepared, pyrolysed and characterised. Table 2 summarizes the thickness values measured before and after pyrolysis.

Table 2 – Thickness of unpatterned films before and after pyrolysis measured with profilometer

Material	SU-8 [µm]	Carbon [µm]
SU-8 2005	5	0.4
SU-8 2035	9.2	1.6
SU-8 2075	22	11

Next, arrays of SU-8 micropillars with various pillar diameters were fabricated and successfully pyrolysed, as schematically described in Fig. 1. Fig. 3 shows micropillars before and after pyrolysis. We investigated the vertical and lateral shrinkage of the pillar structures by SEM imaging before (Fig. 3A and C) and after pyrolysis (Fig. 3B and D). The dimensions of the micropillars before and after pyrolysis are summarised in Table 3.

Table 3 – Dimensions (average ± s.e.m., n=48) of micropillars before and after pyrolysis evaluated from SEM images; ND=Nominal diameter on the lithographic mask; C=Carbon

	Pillar diameter		Pillar height	
ND [µm]	SU-8 [µm]	C [µm]	SU-8 [µm]	C [µm]
3	3.07 ± 0.02	1.44 ± 0.02	23.44 ± 0.07	11.1 ± 0.1
3.5	3.49 ± 0.03	1.66 ± 0.02	23.5 ± 0.2	11.37 ± 0.04
4	4.16 ± 0.03	1.98 ± 0.04	24.5 ± 0.2	11.69 ± 0.06
5	4.97 ± 0.04	2.50 ± 0.03	24.4 ± 0.1	11.77 ± 0.06
10	9.35 ± 0.06	5.08 ± 0.03	24.13 ± 0.08	11.98 ± 0.06
15	13.7 ± 0.1	7.58 ± 0.05	24.0 ± 0.1	11.20 ± 0.08

Figure 3E depicts the ratio between the height and width of SU-8 and their corresponding carbon structures. Different dimensions of the SU-8 structures induce different degree of shrinkage during pyrolysis. For instance, SU-8 pillars with diameter ranging from 3 to 4 µm shrunk isometrically, i.e. the height and diameter of the pillars shrank in the same proportion (~50%).

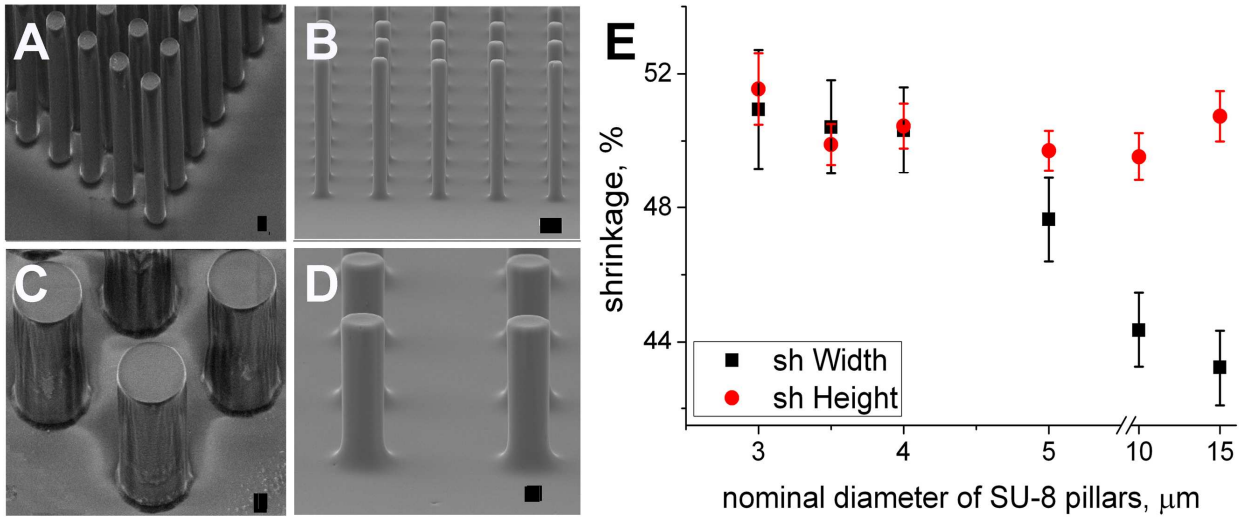

Figure 3. SEM images of SU-8 (A and C) and carbon pillars (B and D) (Scale bars: 2 µm). (E) % shrinkage in width (sh Width) and height (sh Height) of pillars with different diameters (data are average ± sem, n=48).

Finally, 3D-IDEs were fabricated (Fig. 4). For the interdigitated 2D structures that interconnect the pillars, the shrinkage calculated from profilometer analysis exhibited a decrease of 91.7±0.5% vertically and only 27.2±3.2% laterally (average ± s.e.m., n=23), yielding fingers in carbon of 0.4 µm in height and 3.6 µm in width. The carbon pillars on the IDE were 1.4 µm in height and 11 µm in diameter.

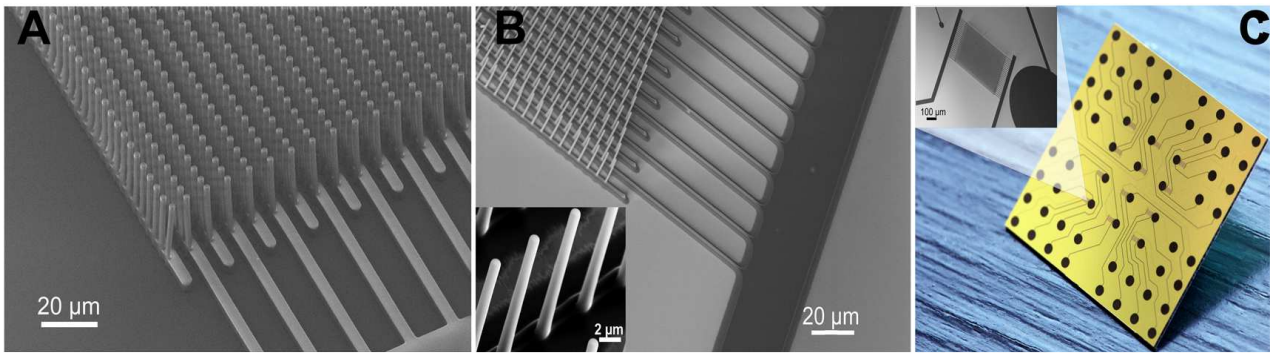

Figure 4. SEM images of 3D-IDEs with carbon pillars interconnected by interdigitated structures (A) before and (B) after pyrolysis. (C) Photograph of a silicon chip with the pyrolysed carbon electrode array structures (12 three-electrode systems at the centre with surrounding contact pads). Inset: SEM image of a three-electrode system.

3.2. Raman spectroscopy of unpatterned carbon films

In order to evaluate the microstructure and graphitization (i.e. disorder and crystallite formation) of the pyrolysed carbon constituting the 3D electrode chip, Raman spectra of

carbon films with two thicknesses, 0.4 µm and 11 µm were analysed (Table 2). Fig. 5 compares Raman spectra of the two carbon films recorded using identical experimental conditions. The spectra featured both the graphitic band (G-band) and the disorder-induced (amorphous) band (D-band), characteristic for carbon materials[47,48]. The D-band at 1350 cm^{-1} is ascribed to the microcrystallite graphite due to the enhanced double resonance Raman scattering. The G-band at 1590 cm^{-1}, which is close to the Raman line of single graphitic crystals at 1575 cm^{-1}, is the band of bond stretching motion pairs of sp^2 C atoms present in aromatic rings as well as in olefinic chains[49]. The slight frequency shift (~15 cm^{-1}) observed for the G-band in the spectra could be due to extremely small crystallite size[50]. It is known that the peak intensity ratio of the D and G peaks varies inversely with L_a ($I_D/I_G \propto 1/L_a$) where L_a is the crystallite size and I_D and I_G are the intensities of the D and G peak, respectively[50]. Hence, the higher the microstructural disorder of the carbon matrix (and thereby the higher the number of defects) is, the higher is the D peak intensity and thus the smaller L_a[48,49]. The I_D/I_G value for both spectra was 1.1, indicating a similar microstructure for the two layers, and thereby a comparable amount of amorphous regions.

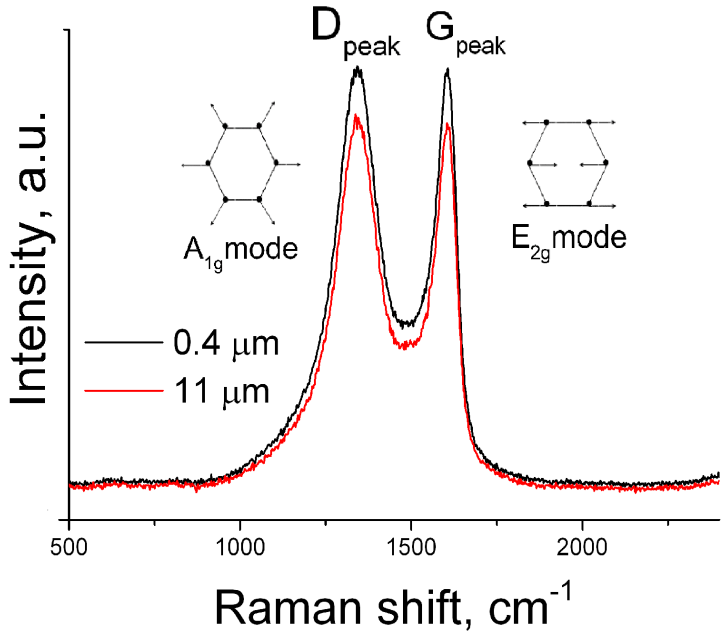

Figure 5. Raman spectra of carbon layers with a thickness of 0.4 µm and 11 µm. The spectra indicate the presence of D and G bands, similarly to glassy carbon and other pyrolysed carbon materials.

3.3. Electrical characterization of unpatterned carbon films and 3D carbon pillars

Electrical characterization using 4PP measurements was conducted on unpatterned carbon films with the three different carbon film thicknesses shown in Table 2 (0.4, and 1.6 and 11 µm). On 11 µm thick carbon films no measurements were possible. This could be explained by tendency of thicker carbon films to present increased roughness, as evidenced by AFM measurements (Supporting Information S2), which hindered proper contact between the probe and the carbon surface. Generally, all measurements on the two thinner films showed a phase change of less than 0.2 degree indicating a good ohmic contact to the sample and a surface layer with a good conductivity.

The resistivity values of the 0.4 µm film ($1.6 \pm 0.3 \times 10^{-2}$ Ωcm; average ± s. e. m., n=9) were higher than the resistivity values of 1.6 µm film ($3.9 \pm 0.04 \times 10^{-3}$ Ωcm; average ± s. e. m., n=9), suggesting a correlation between electrode resistivity and carbon film thickness. This phenomenon has previously been observed for pyrolysed carbon from SU-8[20] and other carbon-based films such as carbon nanotube composites[51] and graphene[51,52]. Park et al.[53] reported very similar resistivity values for ~ 0.4 µm thick films derived from SU-8. However, for 1.6 µm thick carbon films they showed a resistivity more than one order of magnitude higher than the one reported here. It was speculated that thick layers might impede efficient degassing of various hydrocarbons and carbon oxide, slowing down the increase of the relative amount of carbon in the film. The inverse behaviour with a lower resistivity for thicker carbon films observed in our case could be related to the slow heating during the pyrolysis process (2°C/min). The low heating rate could facilitate the outgassing of the non-carbonizing compounds and the build-up of the crystalline carbon structure[26], leading to lower resistivity of the thicker carbon film.

The resistivity of the 3D-carbon pillars and the flat underlayer carbon sheet was determined. No significant difference was seen between the measured resistance of the underlayer carbon film (Fig. 2) (R_S =39.8 Ω ± 0.7 Ω; average ± s.e.m., n=4) and the resistance through the pillars (R_P=39.7 Ω ± 0.9 Ω average ± s.e.m., n=4), indicating a negligible resistance at the pillar-underlayer sheet interface (R_B). This essentially means that there is a good connection between the pillars and the underlayer film.

3.4. Ageing of carbon and its regeneration

In preliminary experiments, changes of electrical and electrochemical behaviour with time were observed. Therefore, the dependence of the 0.4 µm carbon film resistivity on film ageing and surface oxidation was evaluated. After storage of samples in ambient air for 90 days, high-resolution XPS C_{1s} spectra revealed appearance of a "shoulder" in the region from 286 to 289 eV (Fig. 6A), which has been ascribed to adsorbates[40,54]. This was accompanied by higher O/C ratio (from 0.02 to 0.1) in the survey spectra of stored samples (Supporting Information, S3). Samples pyrolysed in the presence of nitrogen atmosphere have an oxygen terminated surface, which tends to adsorb impurities[40]. Contamination by adsorbates increases the O/C ratio on samples exposed to the ambient atmosphere in the laboratory, a phenomenon that has also been observed for glassy carbon[7] and pyrolysed positive photoresist[6]. Possible mechanisms responsible for adsorption of nonpolar adsorbates are e.g. creation of induced dipoles[55].

Resistivity measurements using 4PP measurements conducted on carbon films at different days after pyrolysis (Fig. 6B) showed increased resistivity values for longer air exposure. The higher resistivity may be caused by the increased oxidation level of the surface, leading to decreased conductivity of the surface layer. After film regeneration for 30 min at 800° C, the resistivity was $1.700 \pm 0.002 \times 10^{-2}$ Ω cm (average ± s.e.m., n=9), which is comparable to the initial value (1.6×10^{-2} Ω cm). During the thermal treatment, the initial oxidation condition might be regenerated and the initial electrical properties of the carbon film were effectively restored.

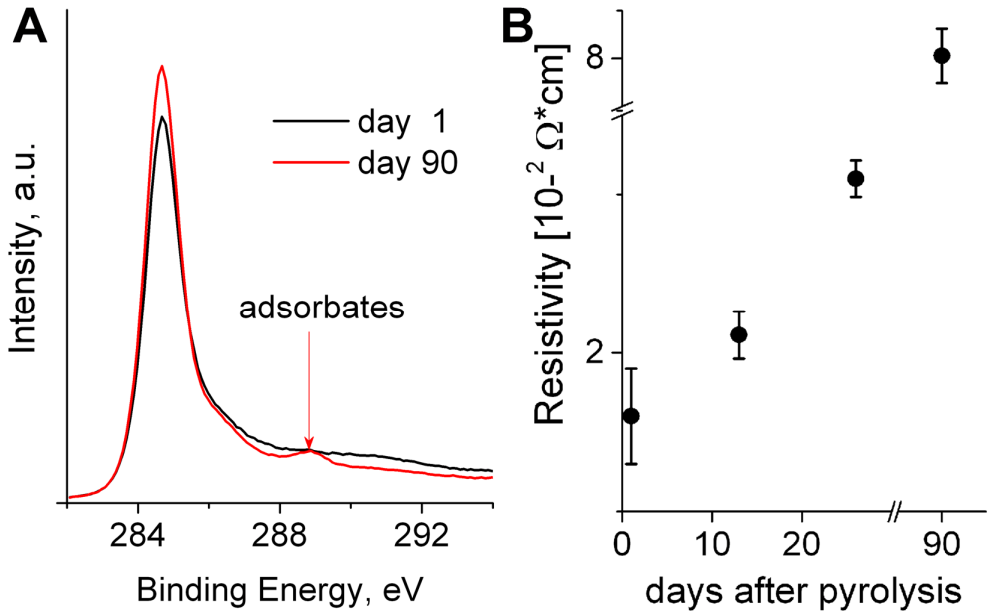

Figure 6. (A) Representative C_{1s} spectra of 0.4 µm carbon film after 1 and 90 days from pyrolysis. (B) Increase in resistivity of 0.4 µm carbon film with the number of days of exposure to ambient air. The error bars represent the standard error of mean, n = 9.

3.5. Electrochemical Characterization

It is known that the resistivity of pyrolysed carbon electrodes is related to their electrochemical response[20,53]. However, the electrochemical behaviour of materials is dependent on other factors, such as the capability of the surface to participate in electron transfer and the presence of possible inhomogeneity influencing the capacitive properties. Hence, characterization of a material using electroactive probes can give information beyond mere conductance measurements. The electrochemical behaviour of the unpatterned pyrolysed carbon films was evaluated using CV and EIS with the redox probe $Fe(CN)_6^{3-/4-}$. The acquired CVs (Fig. 7A) showed lower ΔE_p values (difference in peak-to-peak potential) for 1.6 µm carbon films (152±8 mV; average ± SD, n=4) compared to 0.4 µm films (210±22 mV; average ± SD, n=4). Fig. 7A also depicts an increase in peak current for the 1.6 µm film. The decrease in ΔE_p values and increase in peak current with increased film thickness are likely due to decreased resistivity for thicker films, which are thus more favourable for electron transfer at the electrode surface.

Although CVs are widely used for characterization of electrode materials and electrode processes, the obtained information cannot convey a detailed understanding of the behaviour of an electrode material. EIS has been applied widely for characterization of electrode

materials and modifications due to the richness of obtained information. Especially in the case of micro- and nanofabricated systems, EIS can yield information of the conductance of the system, which can be affected by material properties and prepared interfacing to measurement instrumentation. Moreover, when applying EIS using electroactive probes, such as $Fe(CN)_6^{3-/4-}$, both capability for faradaic electron transfer processes and material capacitive properties can be characterized independently of the general contribution of material conductance, as illustrated by the presented results below. Figs. 7B and C show typical Nyquist plots for the two film thicknesses obtained using EIS. The impedance spectra of the thin 0.4 μm carbon film shows a small capacitive semi-circle (Fig. 7B) in the high frequency region, which disappears in the Nyquist plot of the 1.6 μm thick carbon films (Fig. 7C). This capacitive semi-circle was independent of composition of the solution (Supporting Information, S4) and seems to be only related to the bulk properties of the pyrolysed carbon. Due to its inherent nature, pyrolysed carbon contains a mixture of sp^2 and sp^3 carbon regions, which at molecular level could be pictured as patches of conducting (sp^2 region) and insulating areas (sp^3 region). In the bulk carbon material this leads to distributed resistances and capacitances, which can be modelled as several capacitors and resistors in parallel, and hence as an equivalent resistor R_B in parallel with an equivalent capacitor C_B (Fig. 3B). Two equivalent circuits, both related to the modified Randles model and depicted as insets in Figs. 7B and 7C, were used to fit the impedance spectra obtained for the two different carbon thicknesses. In Figs. 7B and C both the experimental results and the fitted curves are presented, showing that the given two equivalent circuits fitted the experimental results very well throughout the entire frequency range. This proves that the given equivalent circuits were suitable for interpreting the spectra. The equivalent circuits for boron-doped diamond electrodes have shown similar characteristics as the one for the 0.4 μm thick carbon film[56].

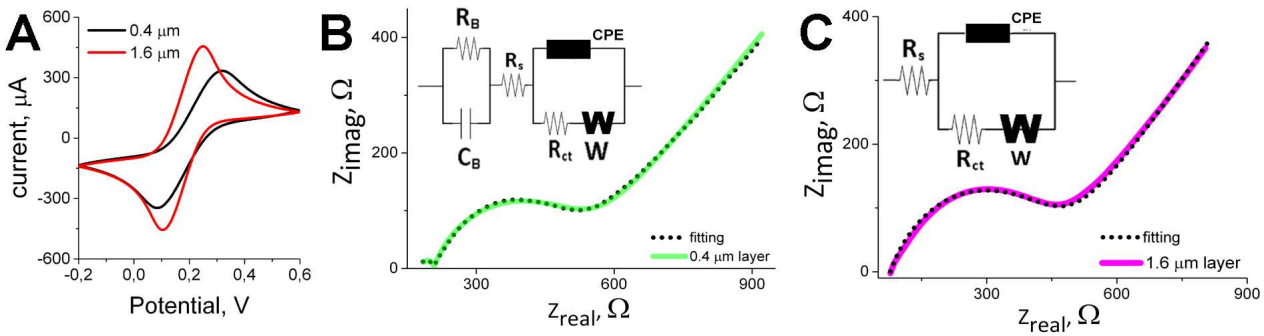

Figure 7. (A) Representative cyclic voltammograms at carbon films of 0.4 µm and 1.6 µm thickness (in 10 mM potassium hexacyanoferrate (II/III) in PBS pH7, scan rate 100 mV s^{-1} versus Ag/AgCl pseudo-reference electrode). Nyquist plots of 0.4 µm (B) and 1.6 µm (C) carbon films in 10 mM potassium hexacyanoferrate (II/III) in PBS pH 7. Insets are the corresponding equivalent circuits. R_S is the solution resistance; CPE is constant phase element, R_{CT} is the charge transfer resistance, C_B and R_B are the capacitance and resistance respectively corresponding to the incomplete capacitive semi-circle at high frequencies.

Table 4 summarizes the values obtained from the fitting: R_S is the solution resistance; Q is the magnitude of the constant phase element (CPE) at frequency ω=1, and α is the multiplication factor of the phase angle, R_{CT} is the charge transfer resistance, C_B and R_B are the capacitance and resistance respectively corresponding to the capacitive semi-circle in the high frequency region.

Generally, the R_S value indicates the magnitude of the solution resistance. However, for microfabricated systems R_S can comprise additional resistance related to the system. The R_S values derived from the fitting are higher for 0.4 µm carbon films than for 1.6 µm thick films. In our system the same electrolyte solution and redox probe concentration was used during spectra acquisition, hence aside from the presence of extra capacitive and resistive components in the equivalent circuit, the increased R_S value for the thinner carbon films could be related to the higher overall resistance of the system, as indicated by the CVs and the electrical measurements. Generally, for increased surface inhomogeneity, such as roughness and presence of both edge and basal graphitic planes in pyrolysed carbon electrode[57] (leading to inhomogeneous electron transfer reaction rates of redox systems at pyrolysed carbon surfaces[58]), α decreases. Similarly, in our case the decreasing α value (Table 4) seems to be related to the roughness increase for thicker films.

Table 4. Values obtained from the fitting of the acquired EIS spectra. The relevant values are C_B, R_B, R_S, and α.

	C_B (F)	R_B (Ω)	R_S (Ω)	R_{CT} (Ω)	W ($S*s^{½}$)	Q ($S*s^{α}$)	α
0.4 µm	2,03E-10	1,38E+03	207,4	330,8	2,21E-03	4,19E-05	0,731
1.6 µm	N/A	N/A	78,13	395,4	2,51E-03	4,06E-05	0,695

Albeit the increased resistance, indicated by electrical and electrochemical measurements of the thin carbon film, the electrochemical behaviour of the 3D-IDE carbon structure with 0.4 µm thick IDE (Fig. 8) is still suitable for further application. However, by increasing the thickness of the carbon IDE underlayer it could be possible to improve the electrochemical performance of the 3D-IDE electrode.

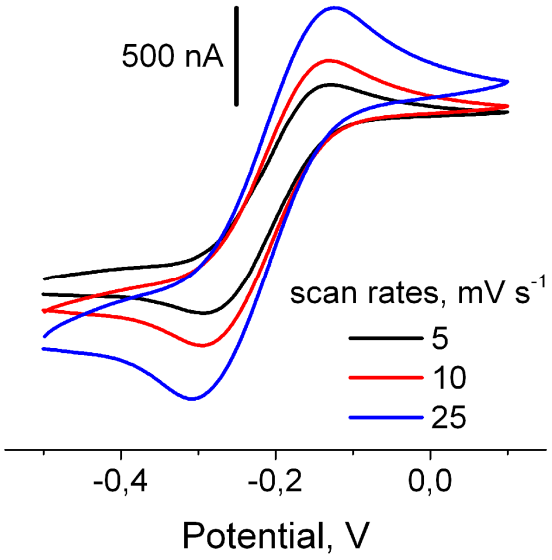

Figure 8. Representative cyclic voltammograms at carbon 3D-IDE with 0.4 µm thick IDE recorded at different scan rates versus Ag/AgCl pseudo-reference electrode in 1mM ruthenium (II/III) hexamine in PBS pH7.

4. Conclusions

Pyrolysed carbon is an excellent material for electrochemical applications that can be optimized employing different fabrication conditions. C-MEMS technique can facilitate various 2D and 3D electrode designs suitable for a wide range of next generation electrochemical sensors. The results presented here show the fabrication and thorough characterization of the 2D and 3 D electrodes from the precursor SU-8. The 3D structures

were high-aspect ratio micropillars with dimensions close to the resolution of UV lithography (1.4 µm in diameter and ~11 µm in height) which were patterned on large areas. The electrodes were characterized with various techniques for their shrinkage, and different properties: electrical, electrochemical, bulk microstructure (i.e. disorder and crystallite formation). Moreover, micropillar arrays were finely patterned on IDE structure to obtain 3D IDE carbon microelectrodes. Due to their good properties, the obtained 2D and 3D electrodes can be further used for bioelectrochemical applications.

Acknowledgements

Thomas Aarøe Anhøj from Danchip is acknowledged for helpful discussion on the EBR and SU-8 processing. Claudia Gritti from DTU Fotonik is acknowledged for help with AFM analysis. Marc Madou and Rodrigo Martinez Duarte are acknowledged for valuable discussion on the pyrolysis process.

References

1. Baure, G., Kwon, C. W., Lee, G. G., Chamran, F., Kim, C. J. & Dunn, B. Fabrication of 3D half-cell electrode arrays. in *Electrichemical Society Proceedings* 36–43 (2003).

2. Voldman, J., Gray, M. L., Toner, M. & Schmidt, M. A. A microfabrication-based dynamic array cytometer. *Analytical Chemistry* **74,** 3984–3990 (2002).

3. Patel, J. N., Gray, B. L., Kaminska, B. & Gates, B. D. Flexible three-dimensional electrochemical glucose sensor with improved sensitivity realized in hybrid polymer microelectromechanical systems technique. *Journal of diabetes science and technology* **5,** 1036–1043 (2011).

4. Long, J. W., Dunn, B., Rolison, D. R. & White, H. S. Three-dimensional battery architectures. *Chemical reviews* **104,** 4463–92 (2004).

5. Madou, M., Lal, A., Schmidt, G., Song, X., Kinoshita, K., Fendorf, M., Zettl, A. & White, R. Carbon micromachining (C-MEMS). in *Electrichemical Society Proceedings* **97-19,** 61–69 (1997).

6. Ranganathan, S., McCreery, R., Majji, S. M. & Madou, M. Photoresist-derived carbon for microelectromechanical systems and electrochemical applications. *Journal of The Electrochemical Society* **147,** 277–282 (2000).

7. Kim, J., Song, X., Kinoshita, K., Madou, M. & White, R. Electrochemical studies of carbon films from pyrolyzed photoresist. *Journal of the Electrochemical Society* **145,** 2314–2319 (1998).

8. Singh, A., Jayaram, J., Madou, M. & Akbar, S. Pyrolysis of negative photoresists to fabricate carbon structures for microelectromechanical systems and electrochemical applications. *Journal of The Electrochemical Society* **149,** E78–E83 (2002).

9. Pesin, L. A. Structure and properties of glass-like carbon. *Journal of Materials Science* **7,** 1–28 (2002).

10. Sharma, C. S., Katepalli, H., Sharma, A. & Madou, M. Fabrication and electrical conductivity of suspended carbon nanofiber arrays. *Carbon* **49,** 1727–1732 (2011).

11. Sharma, S., Sharma, A., Cho, Y.-K. & Madou, M. Increased graphitization in electrospun single suspended carbon nanowires integrated with carbon-MEMS and carbon-NEMS platforms. *ACS applied materials & interfaces* **4,** 34–39 (2012).

12. Du, R., Ssenyange, S., Aktary, M. & McDermott, M. T. Fabrication and characterization of graphitic carbon nanostructures with controllable size, shape, and position. *Small* **5,** 1162–1168 (2009).

13. Schueller, O. J. A., Brittain, S. T. & Whitesides, G. M. Fabrication of glassy carbon microstructures by pyrolysis of microfabricated polymeric precursors. *Advanced Materials* **9,** 477–480 (1997).

14. Park, B. Y., Taherabadi, L., Wang, C., Zoval, J. & Madou, M. J. Electrical Properties and Shrinkage of Carbonized Photoresist Films and the Implications for Carbon Microelectromechanical Systems Devices in Conductive Media. *Journal of The Electrochemical Society* **152,** J136–J143 (2005).

15. Wang, C., Taherabadi, L. H. & Madou, M. J. A novel method for the fabrication of high-aspect ratio C-MEMS structures. *Journal of Microelectromechanical Systems* **14,** 348–358 (2005).

16. Cowlard, F. C. & Lewis, J. C. Vitreous Carbon - A new form of carbon. *Journal of Materials Science* **2,** 507–512 (1967).

17. Teixidor, G. T., Gorkin, R., Tripathi, P. P., Bisht, G. S., Kulkarni, M., Maiti, T. K., Battacharyya, T. K., Subramaniam, J. R., Sharma, A., Park, B. Y. & Madou, M. Carbon microelectromechanical systems as a substratum for cell growth. *Biomedical Materials* **3,** 1–16 (2008).

18. Kawamura, K. & M, J. G. Mechanical properties of glassy carbon fibres derived from phenolic resin. *Journal of Materials Science* **7,** 1099–1112 (1972).

19. K. Zachek, M., Takmakov, P., Moodya, B., Wightman, R. M. & McCarty, G. S. Simultaneous decoupled detection of dopamine and oxygen using pyrolyzed carbon microarrays and FSCV. *Analytical Chemistry* **81,** 6258–6265 (2010).

20. Mardegan, A., Kamath, R., Sharma, S., Scopece, P., Ugo, P. & Madou, M. Optimization of carbon electrodes derived from epoxy-based photoresist. *Journal of the Electrochemical Society* **160,** B132–B137 (2013).

21. Xu, H., Malladi, K., Wang, C., Kulinsky, L., Song, M. & Madou, M. Carbon post-microarrays for glucose sensors. *Biosensors & Bioelectronics* **23,** 1637–1644 (2008).

22. Lee, J. a, Hwang, S., Kwak, J., Park, S. Il, Lee, S. S. & Lee, K.-C. An electrochemical impedance biosensor with aptamer-modified pyrolyzed carbon electrode for label-free protein detection. *Sensors and Actuators B: Chemical* **129,** 372–379 (2008).

23. Bisht, G. S., Holmberg, S., Kulinsky, L. & Madou, M. Diffusion-free mediator based miniature biofuel cell anode fabricated on a carbon-MEMS electrode. *Langmuir* **28,** 14055–14064 (2012).

24. Zhou, H., Gupta, A., Zou, T. & Zhou, J. Photoresist derived carbon for growth and differentiation of neuronal cells. *Molecular Science* **8,** 884–893 (2007).

25. Mitra, J., Jain, S., Sharma, A. & Basu, B. Patterned growth and differentiation of neural cells on polymer derived carbon substrates with micro/nano structures in vitro. *Carbon* **65,** 140–155 (2013).

26. Teixidor, G. T., Zaouk, R. B., Park, B. Y. & Madou, M. J. Fabrication and characterization of three-dimensional carbon electrodes for lithium-ion batteries. *Journal of Power Sources* **183,** 730–740 (2008).

27. Min, H.-S., Park, B. Y., Taherabadi, L., Wang, C., Yeh, Y., Zaouk, R., Madou, M. J. & Dunn, B. Fabrication and properties of a carbon/polypyrrole three-dimensional microbattery. *Journal of Power Sources* **178,** 795–800 (2008).

28. Wang, C., Taherabadi, L., Jia, G., Madou, M., Yeh, Y. & Dunn, B. C-MEMS for the Manufacture of 3D Microbatteries. *Electrochemical and Solid-State Letters* **7,** A435–A438 (2004).

29. Amato, L., Keller, S. S., Heiskanen, A., Dimaki, M., Emnéus, J., Boisen, A. & Tenje, M. Fabrication of high-aspect ratio SU-8 micropillar arrays. *Microelectronic Engineering* **98,** 483–487 (2012).

30. Campo, A. Del & Greiner, C. SU-8: a photoresist for high-aspect-ratio and 3D submicron lithography. *Journal of Micromechanics and Microengineering* **17,** R81–R95 (2007).

31. López-Romero, D., Barrios, C. a., Holgado, M., Laguna, M. F. & Casquel, R. High aspect-ratio SU-8 resist nano-pillar lattice by e-beam direct writing and its application for liquid trapping. *Microelectronic Engineering* **87,** 663–667 (2010).

32. De Volder, F. L., Vansweevelt, R., Wagner, P., Reynaerts, D., Hoof, C. Van & Hart, A. J. Hierarchical carbon nanowire microarchitectures made by plasma-assisted pyrolysis of photoresist. *ACS Nano* **5,** 6593–6600 (2011).

33. Wang, Chunlei; Madou, J. M. Carbon as a MEMS material: micro and nanofabrication of pyrolysed photoresist carbon. *International Journal Manufacturing Technology and Management* **13,** 360–375 (2008).

34. Kassegne, S., Wondimu, B., Majzoub, M. & Shin, J. High-efficiency microarray of 3D carbon MEMS electrodes for pathogen detection systems. *Proceedings of SPIE* **7266,** 726615, 1–6 (2008).

35. McCreery, R. L. in *Voltammetric Methods in Brain Systems* (Boulton, A. A. & Baker, G. B.) **27,** 1–26 (Humana Press, 1995).

36. Ranganathan, S. & McCreery, R. L. Electroanalytical performance of carbon films with near-atomic flatness. *Analytical chemistry* **73,** 893–900 (2001).

37. Collins, P. G. Extreme Oxygen Sensitivity of Electronic Properties of Carbon Nanotubes. *Science* **287,** 1801–1804 (2000).

38. Strand, A. M. & Venton, B. J. Flame etching enhances the sensitivity of carbon-fiber microelectrodes. *Analytical chemistry* **80,** 3708–15 (2008).

39. Takmakov, P., Zachek, M. K., Keithley, R. B., Walsh, P. L., Mccarty, G. S. & Wightman, R. M. Carbon Microelectrodes with a Renewable Surface. *Analytical Chemistry* **82,** 2020–2028 (2011).

40. Ranganathan, S., Kuo, T.-C. & McCreery, R. L. Facile preparation of active glassy carbon electrodes with activated carbon and organic solvents. *Analytical Chemistry* **71,** 3574–3580 (1999).

41. Mcdermott, M. T., Mcdermott, C. A. & Mccreery, R. L. Scanning tunneling microscopy of carbon surfaces: relationships between electrode kinetics , capacitance , and morphology for glassy carbon electrodes. *Analytical Chemistry* **65,** 937–944 (1993).

42. Keller, S., Blagoi, G., Lillemose, M., Haefliger, D. & Boisen, A. Processing of thin SU-8 films. *Journal of Micromechanics and Microengineering* **18,** 1–10 (2008).

43. Fagan, D. T., Hu, I. F. & Kuwana, T. Vacuum heat-treatment for activation of glassy carbon electrodes. *Analytical Chemistry* **57,** 2759–2763 (1985).

44. Martinez-Duarte, R., Renaud, P. & Madou, M. J. A novel approach to dielectrophoresis using carbon electrodes. *Electrophoresis* 2385–2392 (2011).

45. Petersen, D. H., Hansen, O., Hansen, T. M., Petersen, P. R. E. & Bøggild, P. Static contact micro four-point probes with <11 nm positioning repeatability. *Microelectronic Engineering* **85,** 1092–1095 (2008).

46. Jenkins, G. & Kawamura, K. *Polymeric Carbons - Carbon Fibre, Glass and Char*. (Cambridge University Press, 1976).

47. Kostecki, R., Schnyder, B., Alliata, D., Song, X., Kinoshita, K. & Kotz, R. Surface studies of carbon films from pyrolyzed photoresist. **396,** 36–43 (2001).

48. Ferrari, A. C. Raman spectroscopy of graphene and graphite: Disorder, electron–phonon coupling, doping and nonadiabatic effects. *Solid State Communications* **143,** 47–57 (2007).

49. Ferrari, A. & Robertson, J. Interpretation of Raman spectra of disordered and amorphous carbon. *Physical Review B* **61,** 14095–14107 (2000).

50. Tuinstra, F. & Koenig, J. L. Raman spectrum of graphite. *The Journal of Chemical Physics* **53,** 1126–1130 (1970).

51. Han, G. H. E. E., Kim, K. I. K., Kim, E. U. N. S., Chae, S. J. I. N., Park, M. I. N. H. O., Jeong, H., Lim, S. C. H. U. & Lee, Y. H. E. E. LARGE-AREA GRAPHENE-BASED FLEXIBLE. **4,** 83–90 (2009).

52. Bae, S., Kim, H., Lee, Y., Xu, X., Park, J.-S., Zheng, Y., Balakrishnan, J., Lei, T., Kim, H. R., Song, Y. Il, Kim, Y.-J., Kim, K. S., Ozyilmaz, B., Ahn, J.-H., Hong, B. H. & Iijima, S. Roll-to-roll production of 30-inch graphene films for transparent electrodes. *Nature Nanotechnology* **5,** 574–8 (2010).

53. Park, B. Y., Taherabadi, L., Wang, C., Zoval, J. & Madou, M. J. Electrical Properties and Shrinkage of Carbonized Photoresist Films and the Implications for Carbon Microelectromechanical Systems Devices in Conductive Media. *Aerospace Engineering* 136–143 (2005). doi:10.1149/1.2116707

54. Kerber, P., Porter, L. M., McCullough, L. a., Kowalewski, T., Engelhard, M. & Baer, D. Study of surface cleaning methods and pyrolysis temperatures on nanostructured carbon films using x-ray photoelectron spectroscopy. *Journal of Vacuum Science & Technology A: Vacuum, Surfaces, and Films* **30,** 0614071–6 (2012).

55. Kuo, T. & McCreery, R. L. Surface chemistry and electron-transfer kinetics of hydrogen-modified glassy carbon electrodes. *Electroanalysis* **71,** 1553–1560 (1999).

56. Trouillon, R. & O'Hare, D. Comparison of glassy carbon and boron doped diamond electrodes: Resistance to biofouling. *Electrochimica Acta* **55,** 6586–6595 (2010).

57. McCreery, R. L. Advanced carbon electrode materials for molecular electrochemistry. *Chemical reviews* **108,** 2646–2687 (2008).

58. McCreery, R. L. in *Eletroanalytical Chemistry* (Bard, A. J.) 221–374 (Marcel Dekker, 1991).

Supplementary information

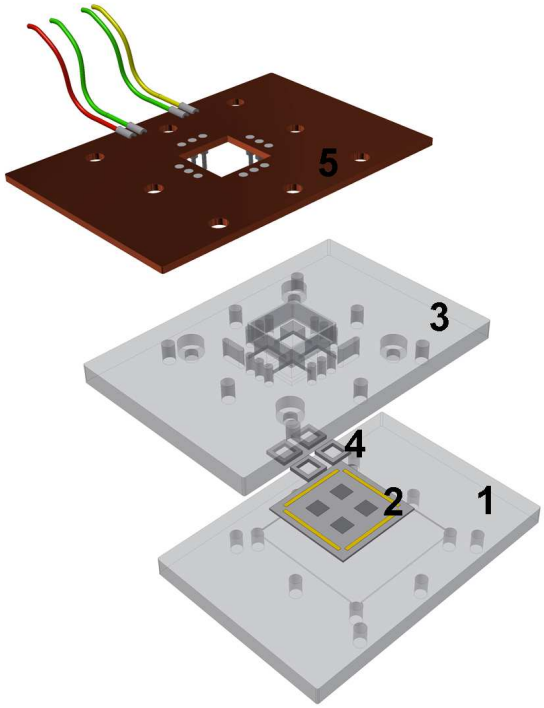

Figure S1. Conceptual drawing of the micromilled electrochemical cell used during electrochemical characterization. Exploded view of the different parts: (1) bottom plate with place for (2) the electrode chip with 4 different WE areas, (3) mid-plate defining 4 WE vials with (4) o-rings on top, and (5) a PCB as a top plate with spring loaded pins for connection to Cr/Au pads connected to the WEs.

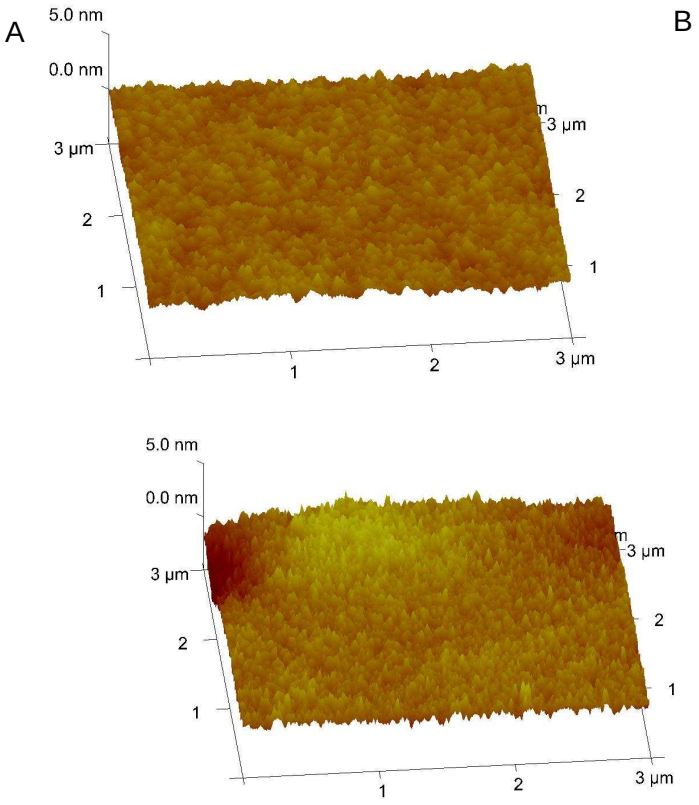

Figure S2. The roughness of carbon films of 0.4 µm (A) and 1.6 µm (B) was measured using AFM. The AFM measurements were performed using a Dimension 3100 platform AFM (Bruker AXS, Germany). The surface topography images of samples were acquired in tapping-mode with a silicon tip. Scan size was 3µm × 3µm. The roughness was 0.21 nm for 0.4 µm film and 0.44 nm for the 1.6 µm film

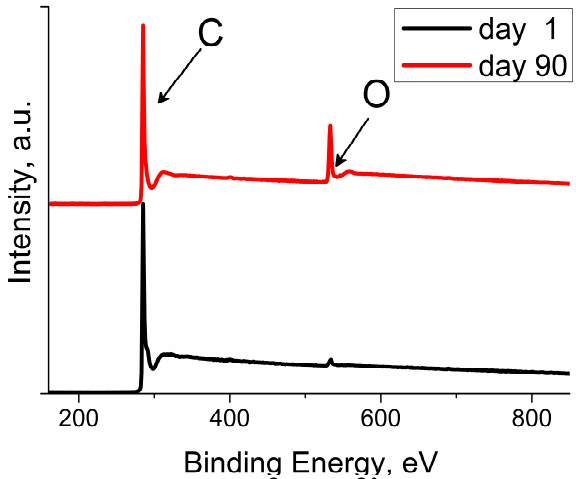

Figure S3. XPS Survey spectra of carbon films at 1 day and 90 days after pyrolysis. The spectra show increased oxygen content with exposure to the laboratory atmosphere.

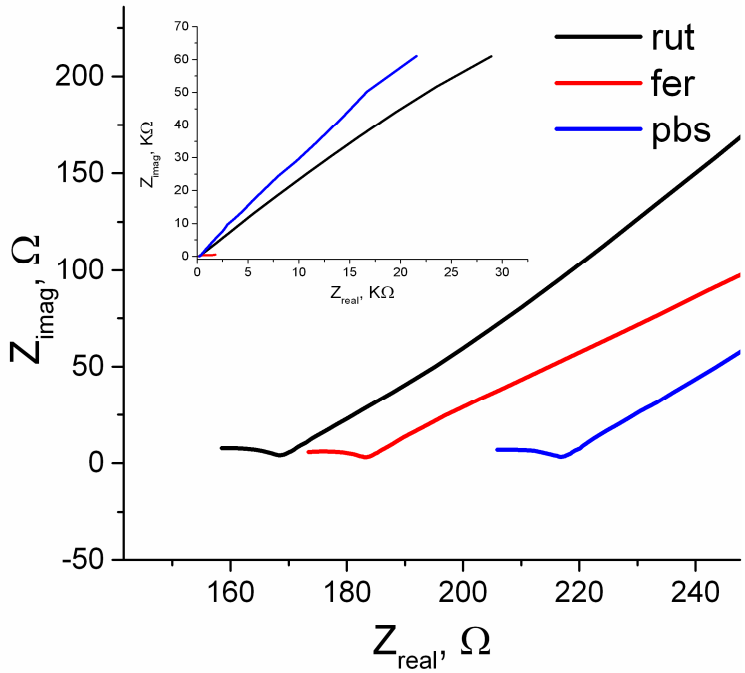

Figure S4. Zoom-in of the Nyquist plots for 0.4 um carbon film in 1 mM ruthenium (II/III) hexaammine (rut), 10 mM potassium hexacyanoferrate (II/III) (fer), and PBS pH7. The spectra show the presence of a capacitive semicircle regardless of the electrolyte solution. Inset: zoom-out of the same Nyquist plots.

Paper III

Tailoring the Surface of 2D and 3D Pyrolysed Carbon Structures Using Plasma Treatment and Electrochemical Reduction of an Aryl Diazonium Compound for Bioelectrochemistry

Letizia Amato, Arto Heiskanen, Niels Bent Larsen, Anja Boisen, Stephan Sylvest Keller, Jenny Emnéus

Manuscript

Tailoring the Surface of 2D and 3D Pyrolysed Carbon Structures Using Plasma Treatment and Electrochemical Reduction of an Aryl Diazonium Compound for Bioelectrochemistry

Letizia Amato, Arto Heiskanen, Niels Bent Larsen, Anja Boisen, Stephan Sylvest Keller, Jenny Emnéus

Department of Micro and Nanotechnology, Technical University of Denmark (DTU-Nanotech), Kgs. Lyngby, Denmark

Introduction

Different carbon allotropes have been used as electrode material[1,2], such as graphite, boron doped diamond, carbon nanotubes (CNTs) and glass-like carbons. The latter are carbons obtained through pyrolysis, which is carbonization of organic polymers[1] at high temperature in an inert atmosphere. Glassy carbon (GC) electrodes are obtained by pyrolysis of polyacrylonitrile or phenol formaldehyde polymeric resin precursors at 1000-3000 °C. GC electrodes exhibit excellent electrochemical properties and thus are often used as the 'gold standard' to compare the electrochemical behaviour of other electrodes. Photoresist-derived pyrolysed carbon (PC) electrodes are structurally and electrochemically similar to GC[3–7] and are very attractive for preparation of patterned electrodes of different sizes and shapes. Moreover, the use of the negative photoresist SU-8 enables fabrication of three dimensional (3D) micro- and nanoelectrodes[6,8–11] in pyrolysed carbon (3D-PC).

The surface chemistry of carbon electrodes is important for determining their electrochemical behaviour, as well as for their further application. Hence, significant work has been devoted to characterization and functionalization of carbon electrodes[1,12]. For instance, functionalization can provide tethering points for subsequent immobilization of DNA[10,13–15], enzymes[16,17], antibodies[18,19], and electroactive groups[20]. Moreover, due to the inherent hydrophobicity of 3D micro- and nanostructures[21], increasing hydrophilicity, and hence wettability, conveyed by the introduced surface functionalities is required to allow interfacing of 3D-PC structures for electrochemistry and for cell-based work[22].

Characterization of the surface wettability is thus necessary. Evaluation of surface wettability, expressed as the contact angle (CA) between the liquid and the surface, gives information about e.g. hydrophobicity, roughness, and surface heterogeneity[21,23].

To introduce surface functionalities, which confer properties suitable for a desired application, carbon materials can be modified using different physical and chemical treatments, such as polymer coating[24,25], plasma modification[26–29], UV-assisted modification[10,13,30], oxidation using strong acids[28,31] or anodization[1,32], electrochemical oxidation of amines and reduction of diazonium salt[33]. Plasma treatment of carbon surfaces is a rapid, effective, and versatile method that can be easily tuned to introduce a wide range of functional groups by varying plasma parameters, such as power, pressure, gas mixture, and treatment time[26,28,29,34]. Furthermore, plasma treatment can be performed on large areas. The excited species within different plasmas, i.e. electrons, radicals, and ions, strongly interact with carbon materials, breaking, e.g. C=C and C-C bonds, and hence creating active sites that react with atoms present in the plasmas[35]. The complex mixture of functionalities introduced by plasma treatment influence the physical and chemical properties of a surface. Specifically, it results in a dramatic change in the surface energy[36] and roughness, which alter the wetting characteristics of the surface.

Aryl diazonium modification is performed by *in situ* generation of an aryl diazonium salt from the corresponding aniline derivative which is then electrochemically grafted onto the electrode surface in a single step[37]. By synthesizing diazonium salts with different functional groups, the variety can be increased further and it is possible to more strictly control the introduced functionalization. Electrochemical reduction of diazonium salt thus offers a versatile and selective grafting of functional groups on a carbon surface. Moreover, since the reaction is performed electrochemically, it is possible to limit and direct the modification to a specific working electrode in an array of individually addressable electrodes. Electrochemical reduction of aryl diazonium salt was first applied to GC electrodes[38]. Since then, this method has been successfully used on other carbon materials (e.g. CNTs[39], graphite[40], graphene[41], and PC[42,43]), as well as semiconductor materials and metals (e.g. silicon[44,45], stainless steel[46], copper, gold, and platinum[47]). This method yields very stable surface functionalization, requiring mechanical abrasion for its removal, indicative of the covalent nature of the molecular attachment[48].

Previous studies have provided very useful information regarding the properties of plasma- and aryl diazonium modified PC electrodes[26–28,42,43]. The purpose of this work was to investigate differences in functionalization methods of two dimensional (2D) and 3D PC structures by electrochemical grafting of diazonium salt of 4-aminobenzoic acid and plasma treatment with oxygen (O_2) and water vapour/oxygen (H_2O/O_2) mixture. The 3D structures were high-aspect ratio carbon micropillars with 1.4 µm in diameter and 11 µm in height[49]. For this purpose, X-ray photoelectron spectroscopic (XPS) analysis, electrochemical characterization with different electrochemical probes and CA measurements were performed on the PC structures before and after surface modification.

Methods

Chemicals

Hydrochloric acid (HCl) (BioReagent), sodium nitrite ($NaNO_2$), phosphate buffered saline (PBS), 4-aminobenzoic acid (4-ABA), potassium ferricyanide ($[Fe(CN)_6]^{3-}$), hexaammineruthenium(III) chloride,,and hexaammineruthenium(II) chloride were purchased from Sigma-Aldrich Corporation (St. Louis, MO, USA). Potassium ferrocyanide ($[Fe(CN)_6]^{4-}$) was purchased from Fluka BioChemica (Buchs, Germany). All solutions used for electrochemical characterization were prepared in ultrapure water (resistivity 18.2 Mohm cm) from a Milli-Q ® water purification system (Millipore Corporation, Billerica, MA, USA)

Diazonium salt modification

Modification of PC electrodes by introduction of carboxylic acid functional groups was achieved by electrochemical reduction of the diazonium cation generated *in situ* from 4-ABA[50,51]. Briefly, 1 mM of $NaNO_2$ was added into a 1 mM acidic solution (0.5 M HCl) of 4-ABA to generate the diazonium cation. The solution was kept in complete darkness and in an ice bath and allowed to react for 5 min under nitrogen and stirring. Surface derivatization was carried out in the diazonium cation-generating solution by scanning from 1 V to -1 V vs. a Ag/AgCl pseudo-reference electrode (RE) at 100 mV s^{-1} for two cycles.

Plasma treatment

The plasma treatment was carried out in an Atto Plasma System (Diener Electronic GmbH, Ebhausen, Germany) under O_2 or H_2O/O_2 atmosphere. The chamber was first evacuated to below 15 Pa before introduction of the gases. After the pressure of the chamber had stabilized at 30 Pa upon application of gases, a glow discharge plasma was initiated at a radio frequency of 13.56 MHz by setting the electrical power at 50 W. Immediately after plasma treatment for 1 min, the carbon structures were characterised.

XPS

X-ray photoelectron spectroscopy (XPS) analysis was done on 2D PC films with a K-Alpha spectrometer (Thermo Fisher Scientific, UK) using a 400 µm wide monochromatized AlKa X-ray spot and by collecting the emitted photoelectrons at a pass energy of 200 eV for survey spectra and 50 eV for high resolution spectra. The software package Avantage of the instrument manufacturer allowed elemental composition and high-resolution carbon spectrum fitting. For deconvolution of C_{1s} spectra, a Shirley type background[52,53] was used. After baseline subtraction, an asymmetrical Gaussian–Lorentzian sum (30%) function served for curve fitting using an optimized peak shape.

Electrochemical characterization

Electrochemical characterization was performed on 2D PC films using electrochemical impedance spectroscopy (EIS) and cyclic voltammetry. The impedance spectra were acquired in the frequency range 100 kHz - 0.1 Hz. The measurements were performed using a computer controlled Reference 600 potentiostat from Gamry Instruments (Warminster, PA). Presentation and analysis of recorded impedance spectra and cyclic voltammograms (CVs) were performed using EchemAnalyst (V. 5.5) from Gamry Instruments. CVs were recorded using a three-electrode system having a Ag/AgCl pseudo-reference electrode (RE), and a platinum wire counter electrode (CE). For EIS measurements a two-electrode system was used.

CA Measurements

CA measurements on films and 3D carbon surfaces were performed with water as wetting agent using an OCA 20 goniometer (DataPhysics Instruments GmbH, Filderstadt, Germany), controlled by the manufacturer's SCA-20 software package. Static, advancing and receding CA were measured after applying a 2-µl drop of water on the surface. The CA of water drops deposited on the carbon structures were measured before and immediately after plasma treatment and diazonium salt modification.

AFM Analysis

Atomic force microscopic (AFM) characterization was performed on flat PC surfaces using a Dimension 3100 system (Bruker AXS GmbH, Karlsruhe, Germany). The surface topography images of samples were captured in tapping-mode with a silicon tip. Scan size was 3 µm x 3 µm.

Results and Discussions

XPS analysis

The surface elemental composition of untreated and plasma treated 2D PC films was determined by XPS survey spectra (Table 1). Both O_2 and H_2O/O_2 plasma treatment resulted in an increase in oxygen/carbon content ratio (O/C) compared to the untreated carbon surfaces. These findings are in accordance with what has previously been shown for O_2 plasma-treated PC[26–28] . Moreover, the results of our study demonstrate that O_2 plasma treatment results in a greater increase in the O/C than H_2O/O_2 plasma treatment.

Table 1. XPS analysis of untreated, O_2 and H_2O/O_2 plasma-treated PC films. (Average ± s.d. (n = 3))

Scope of analysis		**Analysis of samples**		
Retrieved parameter		Untreated	O_2 plasma	H_2O/O_2 plasma
Atomic composition[1]	O/C (%)	2.2 ± 0.2	29.7 ± 0.1	22.4 ± 0.3
Binding Energy (eV)[2]	Assigned Chemical Component (%)			
284.64 ± 0.06	C-C & C=C	63.1 ± 0.8	54.4 ± 0.5	56.8 ± 0.2
285.7 ± 0.1	C-O[3]	12.05 ± 0.04	12.3 ± 0.1	13.00 ± 0.05
287.12 ± 0.08	C=O[4]	8.8 ± 0.3	21.2 ± 0.3	16.6 ± 0.3
289.01 ± 0.03	O–C=O[5]	N/A	12.2 ± 0.4	13.5 ± 0.1
290.20 ± 0.04	shake-up	16.0 ± 0.6	N/A	N/A

[1] The atomic composition was obtained from survey spectra.
[2] The relative percentage of chemical components was obtained from C_{1s} peaks by deconvolution.
[3] e.g. alcohol, ether species.
[4] e.g. ketone, aldehyde species.
[5] e.g. carboxylic, ester species.

XPS analysis was also used to determine the relative percentage of the chemical components[35,54] that define the composition of PC films (Fig. 1).

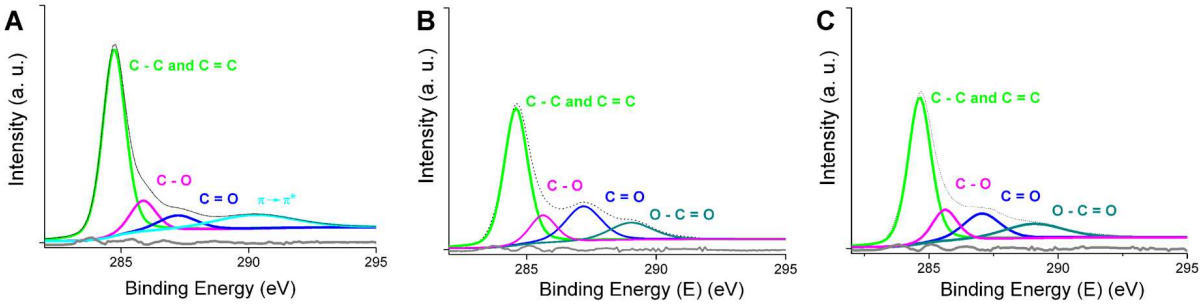

Figure 1. Fitting of high resolution C_{1s} spectra for **A**) untreated PC films, **B**) O_2, **C**) H_2O/ O_2 plasma treated films. For all the recorded spectra, the residuals (grey line) were low indicating a good fit between the fitted curves and the spectrum.

Table 1 lists the assigned chemical components, which were considered for curve fitting of the C_{1s} spectrum and the calculation of the percentages. Deconvolution of the C_{1s} spectrum

gives at most five individual component groups. The main peak corresponds to sp^2-hybridized graphite-like carbon (C=C) atoms and sp^3-hybridized carbon (C-C) atoms[54]. The other peaks are considered to originate from oxygen functionalities representing carbon atoms linked to one or more oxygen atoms that are electronegative and hencet are withdrawing electrons from the carbon atom. The C_{1s} spectra of untreated PC present shake-up satellite peaks due to π–π^* transitions in the aromatic rings of the graphitic areas[54]. The area of this region in the untreated sample was 16%.

Aside from graphitic carbon, alcoholic groups were the most abundant functionalities (12%) on the untreated surfaces. As a consequence of plasma treatment, the relative content of the main carbon peak decreases, whereas those of O–C=O, C=O, and C–O bonds increase. In the collective main C_{1s} peak, the C=C is more reactive than C-C and is hence expected to be the primary target of the plasma modification[35]. The results indicate that plasma induces oxidation primarily of the C=C bonds thus facilitating introduction of new surface functionalities on PC surfaces. Specifically, the relative percentage of C-O groups slightly increases compared to the untreated counterpart, especially on the H_2O/O_2 plasma-treated surfaces. Although C=O groups were the least predominant (~9%) on untreated surfaces, their content increased after plasma treatment, being higher on O_2 plasma-treated surfaces (~21%) compared to H_2O/O_2 plasma-treated ones (~17%). Shake-up satellite peaks disappear on all plasma-treated surfaces with the subsequent appearance of peaks representing carboxylic functionalities, which show higher intensity on H_2O/O_2 plasma treated samples.

Electrochemical evaluation of plasma treatment and diazonium salt modification

In diazonium salt modification, the molecule used during the reaction is commonly a substituted benzene ring. In our case, the substituent was a carboxylic group. The modification (Fig. 2) involves reaction of 4-aminobenzoic acid with sodium nitrite to form a phenyl diazonium ion, capable of undergoing electrochemically induced one-electron reduction on carbon electrodes. This generates a 4-carboxyphenyl radical and N_2, the former of which reacts with the carbon surface by coupling to an unsatisfied valence or adding to a double bond, yielding a 4-carboxyphenil (4CP)-terminated surface[33,55,56].

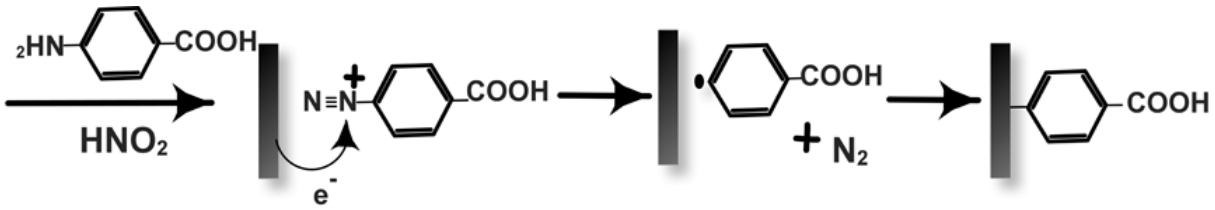

Figure 2. Modification of carbon surfaces by reduction of aryl diazonium reagents illustrated by the reaction of 4-aminobenzoic acid with nitrous acid.

The changes in surface characteristics of PC after plasma modification and electrochemical reduction with diazonium salt were monitored using cyclic voltammetry and EIS. Fig. 3 depicts cyclic voltammograms (CVs) of $[Fe(CN)_6]^{3-/4-}$ recorded at an untreated PC films and the same surface after 4-CP modification, H_2O/O_2 and O_2 plasma treatment.

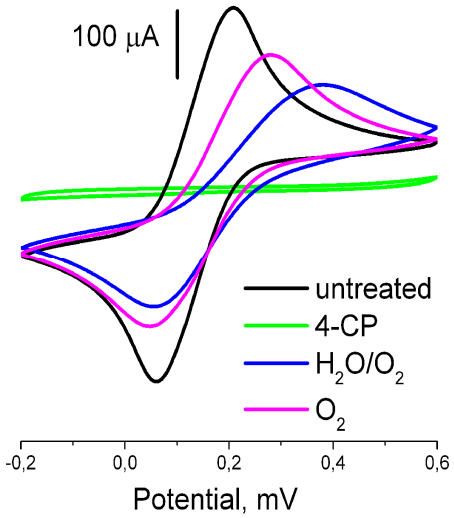

Figure 3. Representative CVs at an untreated PC film and after 4-CP modification, H_2O/O_2, and O_2 plasma treatment (in 10 mM $[Fe(CN)_6]^{3-/4-}$ in PBS pH 7, scan rate 50 mV s^{-1}, potential versus RE).

For the untreated surface, the CV shows quasi-reversible behaviour, while for the surface modified with 4-CP the anodic and cathodic peak related to the redox reactions of $[Fe(CN)_6]^{3-/4-}$ are not visible. This significant blocking effect is caused by surface passivation as a consequence of 4-CP modification[56–58].

Different factors contribute to the blocking effect of the diazonium modification and depend on the parameters used during diazonium modification, such as aryl substituent,

concentration of the diazonium salt, applied potential and its duration[56–58]. In our case, the presence of the tethered 4-CP layer causes electron transfer limitation due to electrostatic repulsion of $[Fe(CN)_6]^{3-/4-}$ as well as generates a physical barrier that hinders the access of $[Fe(CN)_6]^{3-/4-}$ to the carbon electrode (Figure 4A). The pK_a of the carboxylic group of 4-CP is close to 2.8 when 4-CP is surface-bound[57]. Hence, at a neutral pH the carboxylic group is deprotonated, which renders the net charge negative on the 4-CP modified surface. This negative charge at the electrode-electrolyte interface repels the $[Fe(CN)_6]^{3-/4-}$ anions, thus blocking the diffusion of the redox probe to the electrode surface. Consequently, this blocking causes a severe decrease in the electron-transfer kinetics of the redox probe[56,57]. The physical barrier formed by the tethered 4-CP layer could be explained by good barrier properties of closely-packed monolayers due to van der Waals interactions between the aromatic rings[57]. This phenomenon is analogous to the one reported for alkyl chains of thiol layers[59–61] forming tightly packed self-assembled monolayers (SAMs).

For structurally disordered SAMs on gold electrodes, the blocking effect is affected by possible defect sites[59] (Fig. 4B), which shorten the tunnelling distance as well as result in decreased electrostatic repulsion due to an increased spacing between charged functionalities (e.g. carboxylic groups). These events together increase the probability of electron transfer and hence of faradaic current.

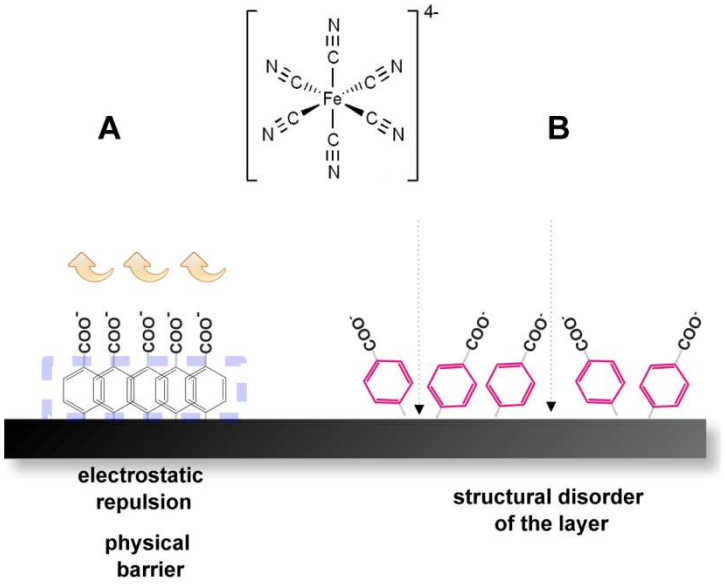

Figure 4. Schematic showing the effect of a 4-CP layer electrochemically tethered on a carbon surface. A) Highly ordered 4-CP layer with blocking effect due to electrostatic repulsion and physical barrier; B) Disordered 4-CP layer which increase the probability of electron transfer.

While 4-CP modification of PC surfaces seems to significantly hinder electron transfer, both plasma treatments have only a small effect, resulting in slightly lower peak current and higher peak potential separation (ΔEp) in the CVs of plasma treated samples (Fig. 3 and table 2). For the plasma treated surfaces, the density of negatively charged functionalities, such as deprotonated carboxylic groups (at neutral pH in PBS) introduced by the plasma treatment, is lower compared to the outcome of the electrochemical reduction of aryl diazonium salt. Interestingly, the ΔEp values are higher for H_2O/O_2 plasma treatment compared to treatment with O_2 plasma, which could be related to the higher density of carboxylic functionalities, as demonstrated by XPS analysis (Table 1).

Table 2. Values (average ± s.e.m, n=4) of ΔEp, anodic and cathodic peak currents derived from CVs recorded at untreated PC film and after 4-CP modification, H_2O/O_2, and O_2 plasma treatment (in 10 mM $[Fe(CN)_6]^{3-/4-}$ in PBS pH 7, scan rate 50 mV s^{-1}, potential versus RE).

	ΔEp (mV)	anodic peak (μA)	cathodic peak (μA)
untreated	177 ± 10	288 ± 4	-300 ± 7
O_2	252 ± 12	192 ± 11	-199 ± 11
H_2O/O_2	296 ± 13	185 ± 7	-214 ± 12
4-CP	N/A	N/A	N/A

The effect of the 4-CP layer and the functional groups introduced by the plasma treatments on PC electrodes was also evaluated by EIS. Figure 5 shows the impedance spectra of the carbon films for the untreated and modified electrode. The Nyquist plots of untreated and plasma treated PC surfaces (Fig. 5A) are characterized by a semicircle in the high-frequency domain, representing the capacitive behaviour, and a Warburg line in the low-frequency domain, characteristic of a diffusion limited process. The semicircle diameter represents the charge-transfer resistance, R_{CT}, i.e. the electron transfer limitation

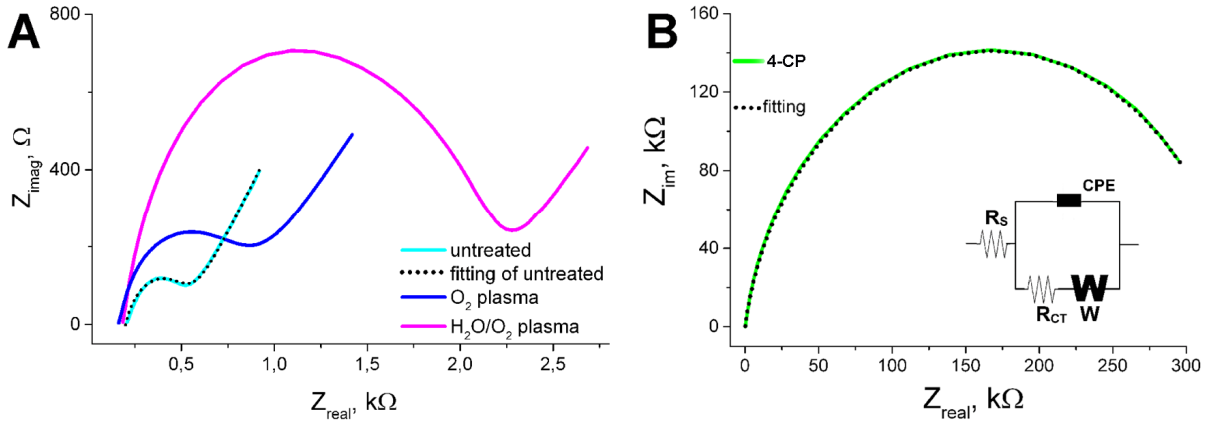

Figure 5. (A) Representative Nyquist plots recorded at untreated PC films and after modification of PC films with O_2 plasma, H_2O/O_2 plasma, and (B) 4-CP groups (in 10 mM $[Fe(CN)_6]^{3-/4-}$ in PBS pH 7). Inset: Randles modified equivalent circuit used to model the acquired EIS spectra. The circuit includes the ohmic resistance of the electrolyte solution (R_S), the Warburg impedance (W), the charge transfer resistance (R_{CT}), the constant phase element (CPE).

A Randles equivalent circuit[62] modified by replacing the double layer capacitance with a constant phase element (CPE) facilitates modelling of interfacial phenomena and was used to fit experimental EIS spectra for both untreated and modified electrodes (inset in Figure 5B).

The modified Randles model comprises four elements: (i) the ohmic resistance of the electrolyte solution (R_S); (ii) the Warburg impedance (W) due to diffusion limitation of ions from the bulk electrolyte to the electrode interface; (iii) the charge transfer resistance (R_{CT}) which exists if a redox probe is present in the electrolyte solution; (iv) the CPE at the electrode-electrolyte interface includes the double layer capacitance of the surface and is related to the surface condition of the electrode. The CPE was employed instead of a pure capacitor[63] due to surface inhomogeneity of carbon electrodes[64], originating from the presence of both edge and basal graphitic planes[1]. The electron transfer reaction rates of

redox systems at basal planes are more sluggish compared to the ones at the edge planes[65], resulting in inhomogeneous reaction rates and hence giving rise to non-ideal capacitive behaviour, modelled as CPE.

The acquired spectra were fitted to the equivalent circuit using nonlinear least-squares regression (dotted line in Figure 5). The fitting indicated good agreement of the equivalent circuit model with the acquired data over the entire applied frequency range. Table 3 shows the extracted parameters.

Table 3. Values extracted from the analysis of EIS spectra acquired at untreated and 4-CP modified PC films (spectra recorded in 10 mM $[Fe(CN)_6]^{3-/4-}$ in PBS pH 7). C_{DL} values were calculated using equation 2.

	untreated	4-CP modified
R_S	2,1E+02	2,1E+02
Q	4,0E-05	1,2E-06
α	7,4E-01	9,1E-01
R_{CT}	3,3E+02	3,3E+05
C_{DL}	**6,2E-06**	**5,3E-07**

The untreated carbon film reveals the smallest semicircle domain, implying a low R_{CT} (330 Ω). The R_{CT} value is of the same order of magnitude as for bare glassy carbon electrodes[57]. After plasma treatment, the observed increase in the semicircle diameter in the Nyquist plots indicates the increase in R_{CT}. These results can also be analysed by considering the electrochemical basis of the R_{CT}, as indicated in Eq. 1[66]:

$$R_{CT} = \frac{RT}{C^* n^2 F^2 A k^0_{app}} \qquad \text{Equation 1}$$

where R is the molar gas constant, T is the absolute temperature of the system, C^* is the equal concentration of the oxidized and reduced form of the used redox probe, n is the number of electrons involved in the redox process, F is Faraday's constant, A is the area of the electrode surface available for the redox process and k^0_{app} is the apparent standard rate constant of the redox process at very small overpotential (for an electrochemical system at equilibrium).

In this specific case, k^0_{app} in eq.1 can be primarily affected by surface modifications. Generally, for electrode surface modifications, the primary effect is either an increase or

decrease in the rate of a redox process. The repulsion between the negatively charged carboxylic groups on the surface and the $[Fe(CN)_6]^{3-/4-}$ anions reduces the ability of the redox probe to access the electrode surface, and thus decreases the kinetics of the redox probe, which results in an increase in R_{CT}[56,57]. In the case of H_2O/O_2 plasma modification the increase in R_{CT} is more pronounced than on O_2 plasma modified surfaces. These results are in agreement both with the parameters extracted from the CVs, shown in Table 2, as well as higher density of carboxylic functionality shown by XPS analysis as a consequence of H_2O/O_2 plasma treatment (Table 1).

In agreement with the cyclic voltammetry data of Table 2, Nyquist plots of plasma modified surfaces (Figure 5A) exhibit a considerably lower R_{CT} than the one on 4-CP-modified surfaces. The blocking effect of the 4-CP film significantly increases the R_{CT} on the surface ($3.3 \times 10^5 \Omega$) compared to the untreated electrode surface. Moreover, the Warburg line is not visible due to hindered electron transfer and hence mass transfer limitation is not manifested. These results are similar to the ones reported for GC electrodes modified with 4-CP groups [56,57].

Aside from R_{CT}[67,68] and k^0_{app}, determination of the capacitance (C_{DL}) from the CPE[63,69] can be employed to evaluate the effect of electrode modifications[57,67,70]. In this work, the C_{DL} value was calculated from the parameters derived from the fitting (table 3) using Eq. 2[63,71]:

$$C_{DL} = \left(\frac{Q\, R_S\, R_{CT}}{R_S + R_{CT}}\right)^{1/\alpha} \frac{R_S + R_{CT}}{R_S\, R_{CT}} \qquad \text{Equation 2}$$

Where Q is the magnitude of CPE at frequency ω=1, α is the multiplication factor of the phase angle and is an empirically derived constant. The other parameters are the same as previously described.

The value of α can vary between 1 (pure capacitive behaviour) and 0 (pure resistive behaviour). For untreated PC carbon films, α is quite low (0.74) in comparison with untreated smooth e-beam evaporated gold surfaces (~0.9)[68] and increases upon modification with diazonium salt (0.91), indicating that the degree of inhomogeneity decreases. Moreover, the C_{DL} value calculated for 4-CP modified PC films was lower compared to the C_{DL} value of the untreated film. Generally, any chemical modification causes a decrease in the overall double

layer capacitance ($C_{DL,tot}$), which, similarly to metal electrodes, comprises a series of individual capacitive contributions, described by the mathematical relation in Eq. 3[72]:

$$\frac{1}{C_{DL,tot}} = \frac{1}{C_{DL,PC}} + \frac{1}{C_{DL,MOD}} \qquad \text{Equation 3}$$

In our system, the CPE consists of the contribution of the untreated PC film to the double layer capacitance ($C_{DL,PC}$) as well as the additional series capacitor of the surface modification ($C_{DL,MOD}$).

Depending on the mechanism of electron transfer taking place between the electrode and the electroactive species[73,74], two different classes of reactions can be distinguished: (1) Outer sphere redox system, at which chemical interaction between the electrode and the electroactive species can be considered as non-existent. (2) Inner sphere redox system at which the electrode and the electroactive species are in direct contact and therefore the electron transfer occurs directly.

The $Fe(CN)_6^{3-/4-}$ couple studied above is considered a non-'ideal' outer sphere system[1], due to its sensitivity to impurities and negatively charged surface oxides (e.g. carboxylates) [1,74–76], as is clearly evidenced by the above results. The $Ru(NH_3)_6^{3+/2+}$ redox system, on the other hand, is considered as outer sphere and should not be influenced by impurities and different surface characteristics of electrodes, since it does not interact with any surface sites or functional groups on the electrode[74–76]. The $Ru(NH_3)_6^{3+/2+}$ redox system was therefore used to compare a 2D PC surface and a 3D PC pillar surface with the same basic footprint before and after 4-PC modification. The grey and red CVs seen in Fig. 6 for the untreated 2D and 3D PC surfaces show no increase of the peak current in spite of the fact that the surface area of the 3D PC surface is 1.9 times that of the 2D PC surface, indicating that the pillar surface was not sufficiently wetted or accessible to the electrochemical probe. This was subsequently confirmed, as indicated in the blue CV in Fig. 6 for the 3D PC surface after 4-CP modification, showing approximately 60% increase of the peak current as compared to the untreated 3D PC surface. It can be observed that the ΔEp is slightly increased after 4-CP modification, indicating a more sluggish electron transfer, which corroborates the above results that 4-CP seems to have a somewhat passivating effect on the electron transfer.

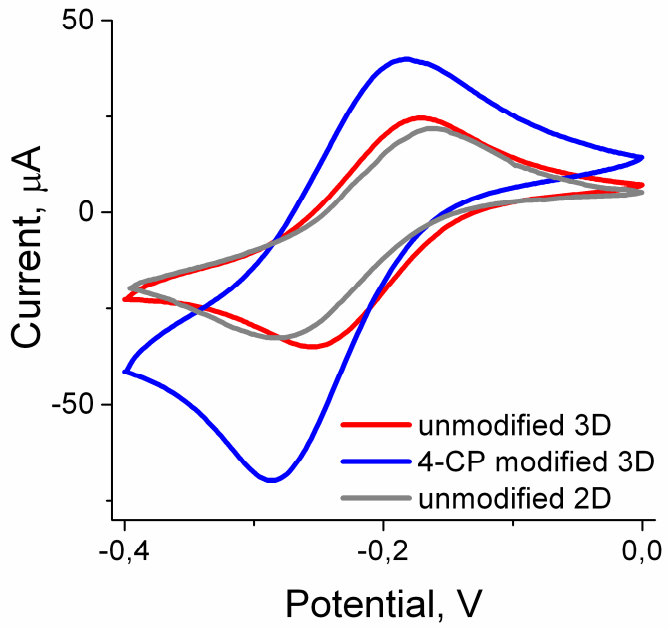

Figure 6. Representative CVs for $Ru(NH_3)_6^{3+/2+}$ at an untreated 2D surface and for untreated and 4-CP modified 3D PC pillar electrode (pillar diameter 1.4 um). 5 mM $Ru(NH_3)_6^{3+/2+}$ in PBS pH 7, scan rate 50 mV s^{-1}, potential versus Ag/AgCl RE.

Contact angle (CA) analysis

In order to study the degree of wettability of the 2D and 3D PC surfaces after surface modification, contact angle (CA) measurements were performed. For determination of the CA, the sessile drop method involves measuring the CA θ directly from a liquid drop profile after placing it on the surface. θ is the equilibrium CA, described by Young's equation[23], which is only valid for ideal systems, e.g. chemically homogeneous and smooth surfaces at atomic scale. In these cases, a single unique CA exists[23]. The failure of the system to meet the ideal conditions is the theoretical basis for the hysteresis, which is defined as the difference between the advancing, θ_A, and the receding contact angle, θ_R , $\Delta\theta = \theta_A - \theta_R$[21,23]. The equilibrium CA is between θ_A and θ_R. Hence, a drop on a surface has CA values ranging from θ_A to θ_R. Aside from the static CA (Fig. 7A-B), which is the equilibrium CA, the CA hysteresis should also be evaluated to better describe the surface heterogeneity[21] in terms of e.g. roughness, as well as surface functionalization.

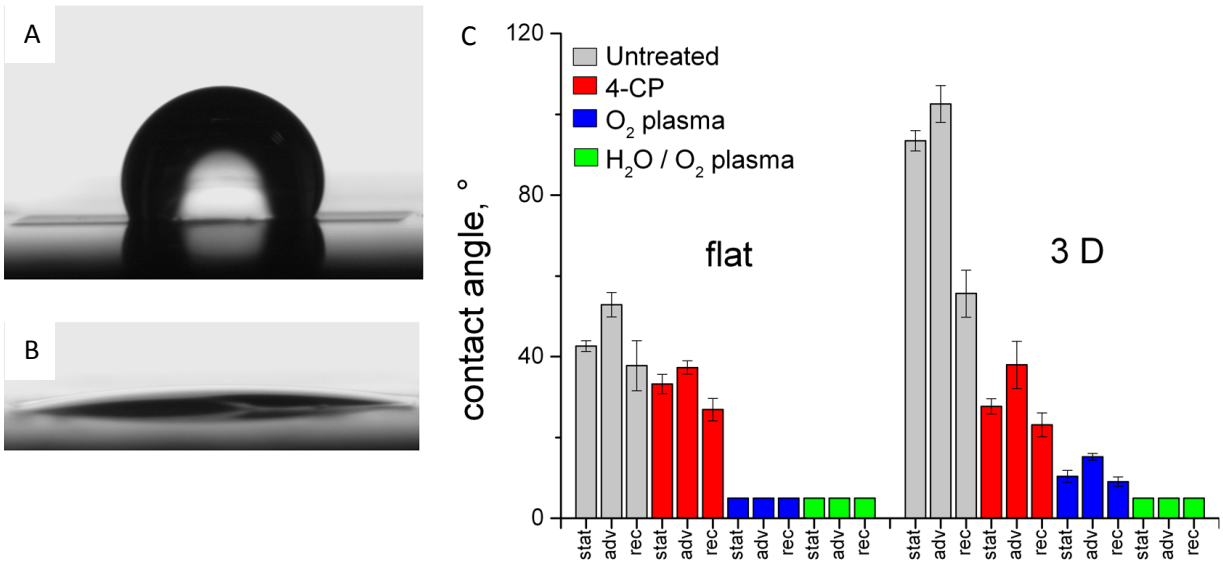

Figure 7. Representative photographs of static CA measurements on pillar structures before (A) and after (B) O_2 plasma treatment. (C) Static (stat), advancing (adv), and receding (rec) CA measurements on 2D PC (flat) and micropillars (3D) surfaces before (untreated) and after modification with O_2 plasma, H_2O/O_2 plasma, and 4-CP. The bars indicate the average ± s.e.m. (n=4).

Here, the effect of the surface modifications on the wetting characteristics of 2D PC surfaces and PC areas of 3D carbon pillar arrays (pillar diameter of 1.4 µm and 6 µm center-to-center spacing[77], Fig. 8) was studied using static, advancing and receding CA measurements.

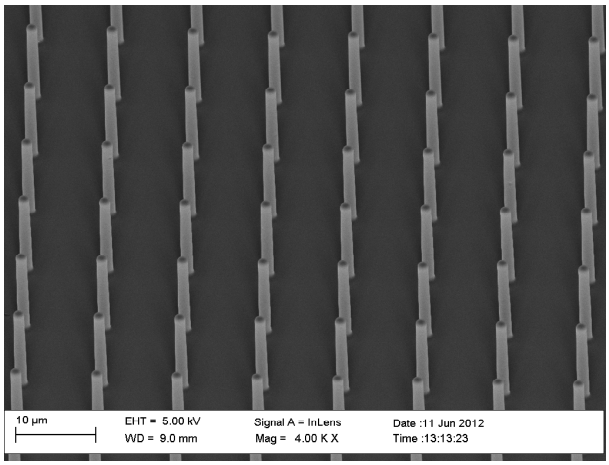

Figure 8. Scanning electron microscope image of carbon pillar arrays with 1.4 µm diameter and 6 µm center-to-center spacing.

For untreated surfaces, the CA was normally higher for 3D structures compared to 2D structures, a phenomenon previously observed for surfaces having micro- and nanosized patterns[78]. Generally, all samples after treatment show a decrease in CA (Figure 7C). This is mainly due to the oxygen functionalities introduced by the plasma modifications and not due

to a change in surface roughness, as shown by AFM images (Supporting Information, S1). However, in the case of tethered 4-CP, the decrease in CA is less pronounced, which may be explained by the partially exposed aromatic rings of the 4-CP film conferring hydrophobic characteristics. The results support however the findings in Fig. 6 that the 4-CP modification leads to improved wetting of the 3D PC surface. Experiments designed to better understand these phenomena are currently underway in our laboratory.

The hysteresis is more pronounced on 3D structures than on flat surfaces, as is expected for heterogeneous surfaces with microtopographies[23]. After both plasma treatments and 4-CP modification, the hysteresis decreases due to the homogeneity introduced by each surface modification. These results demonstrate that surface modification has a dominant effect on hysteresis compared to pillar topography.

Conclusions

The presented results show the possible purpose of using a certain functionalization method for a specific application. For instance, applications requiring voltammetry can benefit from plasma modifications whereas impedance based applications can benefit from effective tethering using diazonium salt as well as the multitude of functionalities with good stability and control on the homogeneity of functionalization in comparison with plasma.

Aknowledgments

FrancescoFumagalli from Istituto Italiano di Tecnologia is acknowledged for helpful discussion about plasma modifications.

References

1. McCreery, R. L. Advanced carbon electrode materials for molecular electrochemistry. *Chemical reviews* **108,** 2646–2687 (2008).

2. Falcao, E. H. L. & Wudl, F. Carbon allotropes: beyond graphite and diamond. *Journal of Chemical Technology and Biotechnology* **82,** 524–531 (2007).

3. Ranganathan, S., McCreery, R., Majji, S. M. & Madou, M. Photoresist-derived carbon for microelectromechanical systems and electrochemical applications. *Journal of The Electrochemical Society* **147,** 277–282 (2000).

4. Kim, J., Song, X., Kinoshita, K., Madou, M. & White, R. Electrochemical studies of carbon films from pyrolyzed photoresist. *Journal of the Electrochemical Society* **145,** 2314–2319 (1998).

5. Hebert, N. E., Snyder, B., McCreery, R. L., Kuhr, W. G. & Brazill, S. a. Performance of pyrolyzed photoresist carbon films in a microchip capillary electrophoresis device with sinusoidal voltammetric detection. *Analytical Chemistry* **75,** 4265–4271 (2003).

6. Wang, C. & Madou, M. From MEMS to NEMS with carbon. *Biosensors & bioelectronics* **20,** 2181–7 (2005).

7. Ranganathan, S. & McCreery, R. L. Electroanalytical performance of carbon films with near-atomic flatness. *Analytical chemistry* **73,** 893–900 (2001).

8. Wang, C., Taherabadi, L., Jia, G., Madou, M., Yeh, Y. & Dunn, B. C-MEMS for the manufacture of 3D microbatteries. *Electrochemical and Solid-State Letters* **7,** A435–A438 (2004).

9. Teixidor, G. T., Zaouk, R. B., Park, B. Y. & Madou, M. J. Fabrication and characterization of three-dimensional carbon electrodes for lithium-ion batteries. *Journal of Power Sources* **183,** 730–740 (2008).

10. De Volder, F. L., Vansweevelt, R., Wagner, P., Reynaerts, D., Hoof, C. Van & Hart, A. J. Hierarchical carbon nanowire microarchitectures made by plasma-assisted pyrolysis of photoresist. *ACS Nano* **5,** 6593–6600 (2011).

11. Kassegne, S., Wondimu, B., Majzoub, M. & Shin, J. High-efficiency microarray of 3D carbon MEMS electrodes for pathogen detection systems. *Proceedings of SPIE* **7266,** 726615, 1–6 (2008).

12. McCreery, R. L. in *Voltammetric Methods in Brain Systems* (Boulton, A. A. & Baker, G. B.) **27,** 1–26 (Humana Press, 1995).

13. Sun, B., Colavita, P. E., Kim, H., Lockett, M., Marcus, M. S., Smith, L. M. & Hamers, R. J. Covalent photochemical functionalization of amorphous carbon thin films for integrated real-time biosensing. *Langmuir* **22,** 9598–605 (2006).

14. Kowalczyk, A., Nowicka, A., Jurczakowski, R., Fau, M., Krolikowska, A. & Stojek, Z. Construction of DNA biosensor at glassy carbon surface modified with 4-aminoethylbenzenediazonium salt. *Biosensors & bioelectronics* **26,** 2506–2512 (2011).

15. Lee, J., Hwang, S., Kwak, J., Park, S. Il, Lee, S. S. & Lee, K.-C. An electrochemical impedance biosensor with aptamer-modified pyrolyzed carbon electrode for label-free protein detection. *Sensors and Actuators B: Chemical* **129,** 372–379 (2008).

16. Bourdillon, C., Delamar, M., Demaille, C., Hitmi, R., Moiroux, J. & Pinson, J. Immobilization of glucose oxidase on a carbon surface derivatized by electrochemical reduction of diazonium salts. *Journal of Electroanalytical Chemistry* **336,** 113–123 (1992).

17. Alonso-Lomillo, M. A., Domínguez-Renedo, O., Hernández-Martín, A. & Arcos-Martínez, M. J. Horseradish peroxidase covalent grafting onto screen-printed carbon electrodes for levetiracetam chronoamperometric determination. *Analytical biochemistry* **395,** 86–90 (2009).

18. Corgier, B. P., Marquette, C. a & Blum, L. J. Diazonium-protein adducts for graphite electrode microarrays modification: direct and addressed electrochemical immobilization. *Journal of the American Chemical Society* **127,** 18328–32 (2005).

19. Hayat, A., Barthelmebs, L. & Marty, J.-L. Electrochemical impedimetric immunosensor for the detection of okadaic acid in mussel sample. *Sensors and Actuators B: Chemical* **171-172,** 810–815 (2012).

20. Ghodbane, O., Chamoulaud, G. & Bélanger, D. Chemical reactivity of 4-bromophenyl modified glassy carbon electrode. *Electrochemistry Communications* **6,** 254–258 (2004).

21. Yan, Y. Y., Gao, N. & Barthlott, W. Mimicking natural superhydrophobic surfaces and grasping the wetting process: a review on recent progress in preparing superhydrophobic surfaces. *Advances in Colloid and Interface Science* **169,** 80–105 (2011).

22. Amato, L., Heiskanen, A., Caviglia, C., Shah, F., Zor, K., Skolimovskij, M., Madou, M., Gamelgaard, L., Hansen, Jul Rasmus Ramos, M., Moreno, T. R., Martinez-Serrano, Alberto Boisen, A., Keller, S. & Emnéus, J. Conducting structured 3D-carbon scaffolds for enhanced differentiation of neural stem cells and dopamine detection. *submitted* (2013).

23. Good, R. J. Contact angle, wetting, and adhesion: a critical review. *Journal of Adhesion Science and Technology* **6,** 1269–1302 (1992).

24. Min, H.-S., Park, B. Y., Taherabadi, L., Wang, C., Yeh, Y., Zaouk, R., Madou, M. J. & Dunn, B. Fabrication and properties of a carbon/polypyrrole three-dimensional microbattery. *Journal of Power Sources* **178,** 795–800 (2008).

25. Xu, H., Malladi, K., Wang, C., Kulinsky, L., Song, M. & Madou, M. Carbon post-microarrays for glucose sensors. *Biosensors & bioelectronics* **23,** 1637–44 (2008).

26. Teixidor, G. T., Gorkin, R., Tripathi, P. P., Bisht, G. S., Kulkarni, M., Maiti, T. K., Battacharyya, T. K., Subramaniam, J. R., Sharma, A., Park, B. Y. & Madou, M. Carbon

microelectromechanical systems as a substratum for cell growth. *Biomedical Materials* **3,** 034116 (8pp) (2008).

27. Hirabayashi, M., Mehta, B., Khosla, A. & Kassegne, S. Functionalization of pyrolyzed carbon microstructures for bio-nanoelectronics platforms. *ECS Transactions* **50,** 325–331 (2012).

28. Hirabayashi, M., Mehta, B., Vahidi, N. W., Khosla, A. & Kassegne, S. Functionalization and characterization of pyrolyzed polymer based carbon microstructures for bionanoelectronics platforms. *Journal of Micromechanics and Microengineering* **23,** 1–11 (2013).

29. Evans, J. F. & Kuwana, T. Introduction of functional groups onto carbon electrodes via treatment with radio-frequency plasmas. *Analytical Chemistry* **51,** 358–365 (1979).

30. Yang, J.-H., Penmatsa, V., Tajima, S., Kawarada, H. & Wang, C. Direct amination on 3-dimensional pyrolyzed carbon micropattern surface for DNA detection. *Materials Letters* **63,** 2680–2683 (2009).

31. Banerjee, S., Hemraj-Benny, T. & Wong, S. S. Covalent surface chemistry of single-walled carbon nanotubes. *Advanced Materials* **17,** 17–29 (2005).

32. Alsmeyer, D. C. & Mccreery, R. L. In situ raman monitoring of electrochemical graphite intercalation and lattice damage in mild aqueous acids. *Analytical Chemistry* **64,** 1528–1533 (1992).

33. Downard, A. J. Electrochemically assisted covalent modification of carbon electrodes. *Electroanalysis* **12,** 1085–1096 (2000).

34. Chen, Q., Dai, L., Gao, M., Huang, S. & Mau, A. Plasma Activation of Carbon Nanotubes for Chemical Modification. *The Journal of Physical Chemistry B* **105,** 618–622 (2001).

35. Hussain, S., Amade, R., Jover, E. & Bertran, E. Functionalization of carbon nanotubes by water plasma. *Nanotechnology* **23,** 385604 (2012).

36. Wan, Y., Yang, J., Yang, J., Bei, J. & Wang, S. Cell adhesion on gaseous plasma modified poly-(L-lactide) surface under shear stress field. *Biomaterials* **24,** 3757–3764 (2003).

37. Baranton, S. & Bélanger, D. Electrochemical derivatization of carbon surface by reduction of in situ generated diazonium cations. *The journal of physical chemistry. B* **109,** 24401–10 (2005).

38. Delamar, M., Hitmi, R., Pinson, J. & Savéant, J. M. Covalent modification of carbon surfaces by grafting of functionalized aryl radicals produced from electrochemical reduction of diazonium salts. *Journal American Chemical Society* **114,** 5883–5884 (1992).

39. Bahr, J. L., Yang, J., Kosynkin, D. V, Bronikowski, M. J., Smalley, R. E. & Tour, J. M. Functionalization of Carbon Nanotubes by Electrochemical Reduction of Aryl Diazonium Salts: A Bucky Paper Electrode. *Journal of the American Chemical Society* **123,** 6536–6542 (2001).

40. Liu, Y. & Mccreery, R. L. Reactions of organic monolayers on carbon surfaces observed with unenhanced raman spectroscopy. *Journal American Chemical Society* **117,** 11254–11259 (1995).

41. Paulus, G. L. C., Wang, Q. H. & Strano, M. S. Covalent electron transfer chemistry of graphene with diazonium salts. *Accounts of chemical research* **46,** 160–70 (2013).

42. Anariba, F., DuVall, S. H. & McCreery, R. L. Mono- and multilayer formation by diazonium reduction on carbon surfaces monitored with atomic force microscopy "scratching". *Analytical chemistry* **75,** 3837–44 (2003).

43. Brooksby, P. a & Downard, A. J. Electrochemical and atomic force microscopy study of carbon surface modification via diazonium reduction in aqueous and acetonitrile solutions. *Langmuir* **20,** 5038–45 (2004).

44. De Villeneuve, C. H., Pinson, J., Bernard, M. C., Allongue, P. & Physique, L. De. Electrochemical formation of close-packed phenyl layers on Si (111). *Journal of Physical Chemistry B* **101,** 2415–2420 (1997).

45. Flavel, B. S., Garrett, D. J., Lehr, J., Shapter, J. G. & Downard, A. J. Chemically immobilised carbon nanotubes on silicon: Stable surfaces for aqueous electrochemistry. *Electrochimica Acta* **55,** 3995–4001 (2010).

46. Deniau, G., Azoulay, L., Bougerolles, L., Palacin, S. & Cedex, F.-G. V. Surface electroinitiated emulsion polymerization: grafted organic coatings from aqueous solutions. *Chemistry of Materials* **18,** 5421–5428 (2006).

47. Bernard, M., Chausse, A., Cabet-deliry, E., Chehimi, M. M., Pinson, J., Podvorica, F. & Vautrin-ul, C. Organic layers bonded to industrial, coinage, and noble metals through electrochemical reduction of aryldiazonium salts. *Chemical Materials* **15,** 3450–3462 (2003).

48. Allongue, P., Delamar, M., Desbat, B., Fagebaume, O., Hitmi, R., Pinson, J. & Savéant, J.-M. Covalent modification of carbon surfaces by aryl radicals generated from the electrochemical reduction of diazonium salts. *Journal of the American Chemical Society* **119,** 201–207 (1997).

49. Amato, L., Heiskanen, A., Hansen, R., Tenje, M., Gammelgaard, L., Rindzevicius, T., Boisen, A., Emnéus, J. & Keller, S. S. Dense high-aspect ratio 3D interdigitated carbon pillar microelectrode arrays. *manuscript* 1–16

50. Lyskawa, J. & Bélanger, D. Direct Modification of a Gold Electrode with Aminophenyl Groups by Electrochemical Reduction of in Situ Generated Aminophenyl Monodiazonium Cations. *Chem. Mater*. 4755–4763 (2006).

51. Liu, G., Chockalingham, M., Khor, S. M., Gui, A. L. & Gooding, J. J. A comparative study of the modification of gold and glassy carbon surfaces with mixed layers of in situ generated aryl diazonium compounds. *Electroanalysis* **22,** 918–926 (2010).

52. Kalakodimi, R. P., Nowak, A. M. & Mccreery, R. L. Carbon / Molecule / Metal and Carbon / Molecule / Metal Oxide Molecular Electronic Junctions. *Chem. Mater.* **17,** 4939–4948 (2005).

53. Du, R., Ssenyange, S., Aktary, M. & McDermott, M. T. Fabrication and characterization of graphitic carbon nanostructures with controllable size, shape, and position. *Small* **5,** 1162–8 (2009).

54. Desimoni, E., Casella, G. I., Morone, a. & Salvi, a. M. XPS determination of oxygen-containing functional groups on carbon-fibre surfaces and the cleaning of these surfaces. *Surface and Interface Analysis* **15,** 627–634 (1990).

55. Pinson, J. & Podvorica, F. Attachment of organic layers to conductive or semiconductive surfaces by reduction of diazonium salts. *Chemical Society reviews* **34,** 429–439 (2005).

56. Baranton, S. & Bélanger, D. Electrochemical derivatization of carbon surface by reduction of in situ generated diazonium cations. *The journal of physical chemistry. B* **109,** 24401–10 (2005).

57. Saby, C., Ortiz, B., Champagne, G. Y. & Bélanger, D. Electrochemical Modification of Glassy Carbon Electrode Using Aromatic Diazonium Salts . 1 . Blocking Effect of 4-Nitrophenyl and 4-Carboxyphenyl Groups. *Langmuir* **7463,** 6805–6813 (1997).

58. Downard, A. J. & Prince, M. J. Barrier Properties of Organic Monolayers on Glassy Carbon Electrodes. *Langmuir* **17,** 5581–5586 (2001).

59. Diao, P., Guo, M., Jiang, D., Jia, Z., Cui, X., Gu, D., Tong, R. & Zhong, B. Fractional coverage of defects in self-assembled thiol monolayers on gold. *Journal of Electroanalytical Chemistry* **480,** 59–63 (2000).

60. Miller, C., Cuendet, P. & Grätzel, M. Adsorbed ω-Hydroxy Thiol Monolayers on Goid Electrodes: Evidence for Electron Tunneling to Redox Species in Solution. *J. Phys. Chem.* **95,** 877–886 (1991).

61. Miller, C. & Grätzel, M. Electrochemlstry at o-Hydroxy Thiol Coated Electrodes . 2 . Measurement of the Density of Electronic States Distributions for Several Outer-Sphere Redox Couples. *J. Phys. Chem.* **95,** 5225–5233 (1991).

62. Randles, J. E. B. Kinetics of rapid electrode reactions. *Discussion of the Faraday Society* **1,** 11–19 (1947).

63. Brug, G. J., Van Den Eeden, A. L. G., Sluyters-Rehbach, M. & Sluyters, J. H. The analysis of electrode impedances complicated by the presence of a constant phase element. *Journal of Electroanalytical Chemistry* **176,** 275–295 (1984).

64. Kim, C.-H., Pyun, S.-I. & Kim, J.-H. An investigation of the capacitance dispersion on the fractal carbon electrode with edge and basal orientations. *Electrochimica Acta* **48,** 3455–3463 (2003).

65. McCreery, R. L. in *Eletroanalytical Chemistry* (Bard, A. J.) 221–374 (Marcel Dekker, 1991).

66. Bard, A. J. & Faulkner, L. R. *Electrochemical methods*. (Wiley, New York, 2001).

67. Heiskanen, A. R., Spégel, C. F., Kostesha, N., Ruzgas, T. & Emnéus, J. Monitoring of saccharomyces cerevisiae cell proliferation on thiol-modified planar gold microelectrodes using impedance spectroscopy. *Langmuir* **24,** 9066–9073 (2008).

68. Pardo-Yissar, V., Katz, E., Lioubashevski, O. & Willner, I. Layered polyelectrolyte films on au electrodes: characterization of electron-transfer features at the charged polymer interface and application for selective redox reactions. *Langmuir* **17,** 1110–1118 (2001).

69. Hsu, C. H. & Mansfeld, F. Technical note: concerning the conversion of the constant phase element parameter Yo into a capacitance. *Corrosion* **57,** 747–748 (2001).

70. Boubour, E. & Lennox, R. B. Insulating properties of self-assembled monolayers monitored by impedance spectroscopy. *Langmuir* **16,** 4222–4228 (2000).

71. Lvovich, V. F. *Impedance spectroscopy*. (Wiley-Interscience, 2012).

72. Katz, E. & Willner, I. Probing biomolecular interactions at conductive and semiconductive surfaces by impedance spectroscopy: routes to impedimetric immunosensors, DNA-sensors, and enzyme biosensors. *Electroanalysis* **15,** 913–947 (2003).

73. Zanello, P. *Inorganic electrochemistry*. *Practice* (The Royal Society of Chemistry, 2003).

74. McCreery, R. L., Cline, K. K., McDermott, C. A. & McDermott, M. T. Control of reactivity at carbon electrode surfaces. *Colloids and Surfaces A: Physicochemical and Engineering Aspects* **93,** 211–219 (1994).

75. Cline, K. K., Mcdermott, M. T. & McCreery, R. L. Anomalously slow electron transfer at ordered graphite electrodes: influence of electronic factors and reactive sites. *J. Phys. Chem.* **98,** 5314–5319 (1994).

76. Chen, P. & McCreery, R. L. Control of electron transfer kinetics at glassy carbon electrodes by specific surface modification. *Analytical Chemistry* **68,** 3958–3965 (1996).

77. Amato, L., Heiskanen, A., Hansen, R., Tenje, M., Gammelgaard, L., Rindzevicius, T., Boisen, A., Emnéus, J. & Keller, S. S. Dense high-aspect ratio 3D interdigitated carbon pillar microelectrode arrays. *To be determined* 1–16

78. Strobel, M. & Lyons, C. S. An essay on contact angle measurements. *Plasma Processes and Polymers* **8,** 8–13 (2011).

Supporting information

S1. AFM

AFM analysis of not-treated and plasma-treated surface provided information about treatment effect on carbon film morphology. Analysis of these surfaces over an area of 3 μm×3 μm showed that the root-mean square (rms) roughness after O_2 plasma (3.0 Å; fig S1B) and H_2O/O_2 plasma (2.8 Å; Fig. S1C) were still below nanometer level similarly to the untreated counterpart (2.1 Å; Fig. S1A).

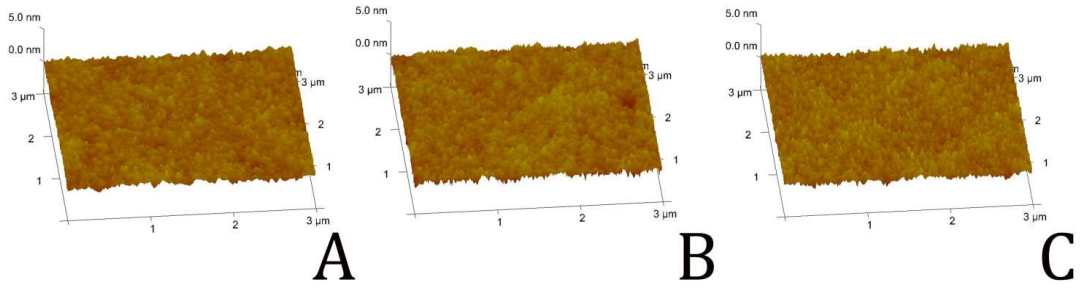

Acknowledgments

Claudia Gritti from DTU Fotonik is acknowledged for help with AFM imaging.

Paper IV

Conducting 3D-carbon scaffolds for enhanced differentiation of neural stem cells and dopamine detection

Letizia Amato, Arto Heiskanen, Claudia Caviglia, Fozia Shah, Kinga Zór, Maciej Skolimowski, Marc Madou, Lauge Gammelgaard, Rasmus Jul Hansen, Emma G. Seiz, Milagros Ramos, Tania Ramos Moreno, Alberto Martínez-Serrano, Anja Boisen, Stephan Keller, Jenny Emnéus

Submitted

Conducting 3D-carbon scaffolds for enhanced differentiation of neural stem cells and dopamine detection

Letizia Amato[1], Arto Heiskanen[1], Claudia Caviglia[1], Fozia Shah[1], Kinga Zór[1], Maciej Skolimowski[1,#], Marc Madou[2], Lauge Gammelgaard[3], Rasmus Jul Hansen[1], Emma G. Seiz[4], Milagros Ramos[4], Tania Ramos Moreno[4,§], Alberto Martínez-Serrano[4], Anja Boisen[1], Stephan Keller[1], Jenny Emnéus[1,]*

[1]Technical University of Denmark, Department of Micro- and Nanotechnology (DTU Nanotech), Produktionstorvet 423, DK-2800 Kgs. Lyngby, Denmark

[2]Department of Mechanical & Aerospace Engineering, University of California, Irvine, California 92697, USA

[3]Capres A/S, Diplomvej 373, DK-2800 Kgs. Lyngby, Denmark

[4]Departmento de Biología Molecular and Centro de Biología Molecular "Severo Ochoa" (CBMSO), Universidad Autónoma de Madrid – C.S.I.C., Cantoblanco, 28049-Madrid, Spain

Corresponding author

*Prof. Jenny Emnéus, Technical University of Denmark, Department of Micro- and Nanotechnology, Produktionstorvet 423, DK-2800 Kgs. Lyngby, Denmark, Phone: +45-45-256 867, Fax: +45-45, e-mail: jenny.emneus@nanotech.dtu.dk.

Present address

[#]University of Groningen, Department of Pharmacy, Antonius Deusinglaan 1, Postbus 196, 9700 AD Groningen, The Netherlands

[§]Lund University, Wallenberg Neurocentrum, BMC, Sölvegatan 17, SE-22100 Lund, Sweden

Abstract

Development of three dimensional (3D) scaffolds for tissue and cell engineering comprises a range of materials, and recently the significance of conductive scaffolds has been recognized in published research. On virtue of the conductive properties, different carbon allotropes, such as grapheme foam, have shown potentials in the development of conductive 3D scaffolds for tissue and cell engineering. In this paper, we demonstrate the first time an application of pyrolysed carbon derived from 3D patterned photoresist (SU-8) structures as a conductive scaffold for cell engineering. The scaffolds are used to study growth and differentiation of clinically relevant neural stem cells developed for cell replacement therapy of Parkinson's disease. The obtained results show that the pyrolysed carbon strongly increases the cells' development to mature dopamine releasing neurons and the 3D environment enhances the growth of neurites. Due to the conductive properties of the 3D-carbon scaffolds, these are optimal for electrochemical detection of exocytotic dopamine release from stem cell populations, functioning as a dopamine trap capable of detecting a much larger quantity of the released dopamine compared to conventional microchip-based systems relying on planar electrode configuration.

Dopamine, a member of the catecholamine family, acts as a neurotransmitter in the central nervous system (CNS), modulating vital CNS functions, such as voluntary movement. In patients with Parkinson's disease, dopamine releasing (dopaminergic) neurons in the CNS are dysfunctional or dying, causing a lack of dopamine in the target territories, which leads to impaired motor functions[1]. One of the suggested therapeutic approaches to restore dopamine production in Parkinson's patients is transplantation of human neural stem cells (hNSCs) (cell replacement therapy, CRT) into the brain of these patients[2]. In development of hNSCs able to differentiate into a dopaminergic neuronal lineage, an important goal is that a large fraction of the hNSCs will acquire dopaminergic properties (phenotype). Novel materials, structures and tools enabling to boost differentiation, as well as determining the fate of hNSCs to dopaminergic neurons is therefore essential for the field of stem cell research and CRT.

A range of different materials[3,4] is currently being explored for building three-dimensional (3D) scaffold structures for tissue engineering and biomedical research. The 3D environment is envisaged to provide a better mimic of the natural *in vivo* environment, leading to more physiologically realistic and reliable biomedical research tools than currently used standard 2D cell based assay formats[5]. Moreover, in a longer perspective, 3D scaffolds will be the key to building artificial tissues, organs, and implants[3].

Conductive 3D scaffolds have emerged as a new approach that provides both structural support and means to electrically stimulate and/or monitor the cell population therein[6–8]. These scaffolds are of particular interest in neuroscience due to the inherent electro-activity of neurons. Carbon nanomaterials, e.g., carbon nanotubes (CNTs), have primarily been used in 2D scaffolds/substrates, where they have shown to increase activity of neuronal networks[9], direct the differentiation of progenitor and stem cells toward specific neuronal lineages, and facilitate stimulation of differentiated NSCs[10]. Recently, graphene foam was found to be excellent for growth and differentiation of NSCs, as well as for electrical stimulation of neural activity[8].

The fabrication of pyrolysed carbon structures from polymer precursors was pioneered already in the 1970s[11]. Since then, micro-[12–14] and nanometer-sized[13–15] pyrolysed carbon structures have emerged for various applications, e.g. biosensors[16], microbatteries[13], cell culture substrates[17]. A number of advantages can be envisaged that make pyrolysed carbon an ideal material for constructing conducting 3D scaffolds for cell and tissue engineering: (1) Organised[18] and random[19] structured scaffolds can be fabricated in a simple process at small or semi-large scale with high-reproducibility, high-yield and cost-effectiveness. Micro/nanostructures can be placed in precisely defined positions without restrictions in shape or cross section and the features and scale depend on the process used for making the polymer precursor[13]. (2) By changing the chemical composition of the polymer precursor and the pyrolysis conditions, the carbon conductivity can be tailored[12,20]. (3)

Similarly, the mechanical properties of the scaffold can be tuned[13] to match the stiffness cells experience *in vivo*[21]. This fabricational degree of freedom provides possibilities for mass production, facilitating novel custom-made designs with unique properties to support various biomedical and pharmaceutical applications.

Here, we report for the first time the fabrication of dense high-aspect ratio (HAR~8) conducting 3D carbon scaffolds (3D-carbon scaffolds) with dimensions approaching the resolution limit of standard UV-lithography. This is a conceptually new approach where our pyrolysed 3D-carbon scaffold has three significant functions: (1) Mechanical support for clinically relevant hNSC growth and differentiation; the pillars serve as anchor points for the growth of neurites, facilitating formation of neuronal networks. (2) The pyrolysed carbon material itself serves as a next-generation substrate for biomedical devices[22] that not only facilitates but significantly enhances the differentiation of hNSCs toward dopaminergic neurons. (3) A neurotransmitter trap, enabling oxidation of a larger fraction of the dopamine released by the stem cell-derived neurons than on conventional 2D electrode substrates (compare 2D and 3D carbon surfaces in Fig. 1).

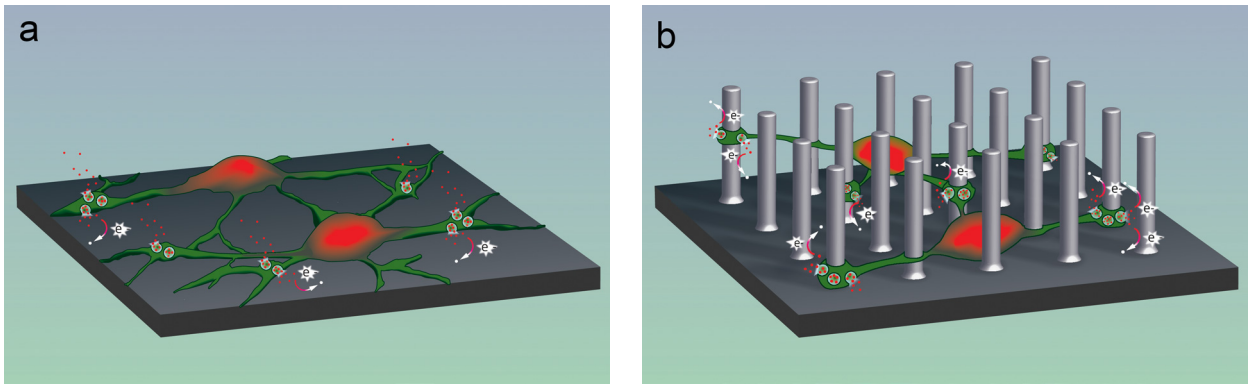

Figure 1 | Schematic view of dopamine sensing from hNSCs using pyrolysed carbon structures. a, Traditional measurement mode on a 2D substrate where only a fraction of dopamine reaches the electrode surface and can be detected, while most of the released dopamine diffuses away without being detected. **b,** New approach using 3D-carbon scaffold where the cells differentiate at the bottom or between pillars that therefore function as dopamine traps, allowing detection of a larger fraction of the released dopamine than on a 2D substrate (**a**).

Design, fabrication and characterization of 3D-carbon scaffolds. 3D-carbon scaffolds were fabricated using pyrolysis by carbonizing polymeric micropillar structures patterned in the polymer SU-8 (3D-SU8 scaffold), an epoxy-based negative photoresist on 4-inch silicon wafers. 3D-SU8 scaffolds (Fig. 2a) were fabricated using a two-step photolithography process, involving first depositing and crosslinking a flat SU-8 layer and then patterning a second SU-8 micropillar layer on top (Supplementary Information S1), as previously described[23]. During pyrolysis, the 3D-SU8 scaffold is decomposed with concomitant gas evolution and aromatization, causing weight loss and densification[11]. This results in ~50% isometric shrinkage of the 3D-SU8 scaffold[18]. The 3D-SU8

scaffolds were patterned on silicon wafers to form arrays of four scaffolds (each having the foot print of 4 mm x 4 mm) located in the centre of chips with dimension 22 mm x 22 mm (9 chips per wafer). The dimensions of the pillars in the 3D-SU8 scaffolds were designed so that the final pillars in the 3D-carbon scaffolds had certain features: (1) Pillar height tall enough for cells to grow interlaced within the pillars, in this way creating a trap for collecting most of the released dopamine. (2) Two different pillar diameters and spacings, allowing investigations of how the cells migrate, find residence and differentiate in between the pillars with different constraints.

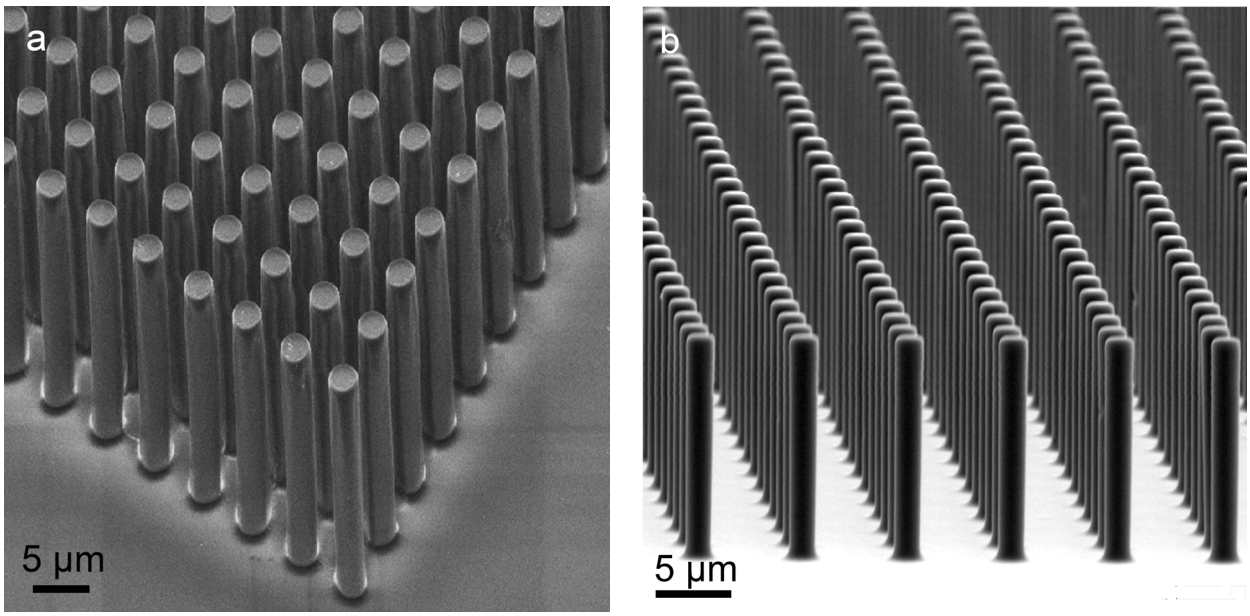

Figure 2 | Representative Scanning Electron Microscopic (SEM) images of 3D-scaffolds. a, 3D-SU8 scaffold having pillars with 3-µm diameter and 22-µm height. **b,** 3D-carbon scaffold obtained after pyrolysis of the scaffold in (**a**). The SU8 pillar diameter and height shrank to 1.4 µm and 11 µm, respectively. The inter-pillar spacing increased from 3 µm to 4.6 µm. Scale bars, 5 µm.

Is the pyrolysed carbon material suitable for adherence, spreading and proliferation of hNSCs? Surface wettability, topography and roughness are important factors affecting biological behaviour of cells on different materials[24]. Cellular adhesion and spreading, as well as proliferation and differentiation (e.g. neurite formation) of anchor dependent cells are often less pronounced and delayed on strongly hydrophobic or hydrophilic substrates[25]. Pyrolysed carbon materials can be modified chemically and physically to present specific surface functionalities that improve wettability and biocompatibility[26,27]. Increased wettability, due to oxygen plasma treatment, has shown to improve adhesion, spreading, and growth of neural cells[28], as well as nerve growth factor induced differentiation of PC12 cells[25]. Here, oxygen plasma treatment was employed for enhancing the wettability of the 3D-carbon scaffolds, and the resulting structures were characterized in terms of surface chemistry, wettability, adhesion and proliferation of hNSCs.

XPS spectra of untreated and oxygen plasma treated flat carbon surfaces (Fig. 3a) leads to a striking increase in the oxygen to carbon content ratio (O/C) from 0.022 ± 0.002 to 0.297 ± 0.001 (average ± standard deviation, n=3), resulting in increased surface energy[28]. The wettability of the pyrolysed carbon structures was further investigated using contact angle (CA) measurements (Fig. 3b). The CA of untreated 3D-carbon scaffolds is higher than that of flat carbon surfaces (93°±2 (1.4 μm pillars), 59°±4 (5.1 μm pillars) and 43°±1 (flat); average ± s.e.m, n=4), as expected for surfaces having micro- and nanosized roughness[29]. After plasma treatment, the CA on all structures decreases dramatically compared to untreated structures to values below 20°, indicating that the hydrophilicity, and hence the wettability, of all the structures increases. This is mainly attributed to oxidation of carbon and not to an increased surface roughness, as indicated by AFM imaging (Supplementary Information S2).

hNSCs require an adhesion factor, such as a cationic polyelectrolyte (e.g. poly-L-Lysine (PLL)), to adhere, grow and differentiate on commercial tissue culture polystyrene (TCPS)[30]. Therefore, two types of flat pyrolysed carbon samples (untreated and plasma treated) were tested with and without PLL-coating for their ability to promote hNSC adhesion, spreading and growth (Fig. 3c-f), and compared with hNSCs grown on PLL-coated TCPS (Fig. 3g). Representative micrographs after 24-h culturing of hNSCs clearly indicate that plasma treatment combined with PLL-coating most effectively promotes hNSC adhesion, spreading and growth (Fig. 3f), resulting in an even cell distribution and well-defined cell morphology (compare Fig. 3g). Although hNSCs seem to grow well on the PLL-coated pyrolysed carbon surface (Fig. 3e), the observed cell morphology and clustering indicates that PLL adhesion directly on pyrolysed carbon is not optimal. On untreated or plasma treated (Fig. 3c and d) pyrolysed carbon surfaces, hNSCs adhere poorly, forming clusters that do not promote cell spreading to acquire the proper morphology. Oxygen functionalities on plasma treated surfaces provide anchoring points for improved physisorption of the primary amine groups of PLL that mediate cell attachment. The above results demonstrate that the pyrolysed carbon material from SU8 precursor can easily be modified to suitably interface to hNSCs studies.

Does pyrolysed carbon influence dopaminergic properties of growing hNSCs? Indirect means are used in most studies to confirm dopaminergic phenotype of stem cell-derived neurons, one of which is immunocytochemistry for the enzyme tyrosine hydroxylase (TH)[30], the rate-limiting enzyme for catecholamine production in neurons. Previous reports have shown that for the hNSC cell line hVM1-Bcl-XL as studied here, the highest obtained percentage of TH positive cells for growing cells and after induced differentiation was ~2 and 17.2 % on PLL-coated TCPS, respectively[30]. A recent report indicates that pyrolysed carbon may be able to enhance neurite outgrowth of neuroblastoma cells[17]. In our study, immunocytochemistry for TH was conducted for

hNSCs growing on PLL-coated TCPS (as control) and oxygen plasma treated PLL-coated flat pyrolysed carbon to see if the carbon material itself has any ability to induce dopaminergic properties in growing hNCSs. Fig. 3 shows confocal fluorescence images of hNSC grown on TCPS (h) and on pyrolysed carbon (i). As seen, cells grown on pyrolysed carbon result in a previously unseen increase in the number of TH positive cells up to 75.2% ± 9.2% as compared to 2.4% ± 0.5 % on PLL-coated TCPS (±SD and n = 5). This is a result that may have important implications for finding new materials and improved protocols for effective implementation of CRT.

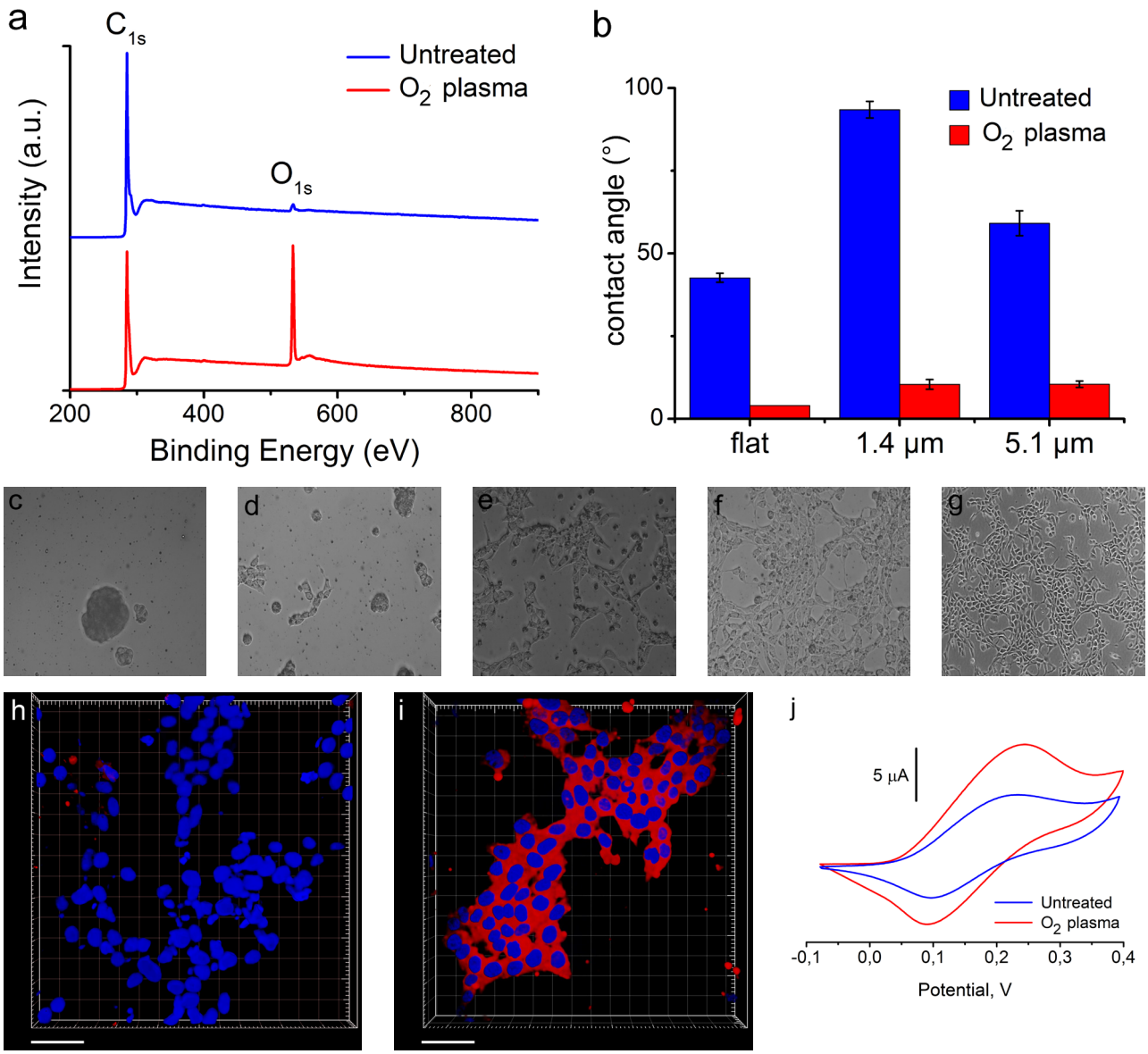

Figure 3 | Characterization of surface properties of pyrolysed carbon structures and their influence on hNSC behaviour. a, Characteristic XPS survey spectra of flat carbon before and after oxygen plasma treatment. The appearing peaks correspond to C_{1s} (285 eV) and O_{1s} (532 eV). **b,** Static contact angle measurements on flat carbon (flat) and 3D-carbon scaffolds with pillar diameter of 1.4 µm and 5.1 µm. The error bars represent the standard error of mean, n = 4 for all carbon structures. **c-g,** Representative bright

field images of ventral mesencephalon–derived hNSCs (hVM1-Bcl-XL). The cells are growing (48 h) on (**c**) untreated, (**d**) oxygen plasma treated, (**e**) PLL-coated, (**f**) oxygen plasma treated and PLL-coated flat carbon surfaces, and (**g**) PLL-coated TCPS. **h,i,** Representative confocal fluorescence images showing immunocytochemistry for tyrosine hydroxylase (TH, red) and nuclei (blue) in hVMbcl-x_L hNSCs growing (48h) on (**g**) PLL-coated TCPS and (**h**) oxygen plasma treated and PLL-coated flat carbon surfaces. Scale bars, 40 μm. **j**, Characteristic cyclic voltammograms of dopamine (5 mM) in PBS (pH 7) on a 3D-carbon scaffold (1.4-um pillars) before and after oxygen plasma treatment (V vs. Ag/AgCl pseudoreference electrode; potential sweep rate, 50 mVs^{-1}).

Is the 3D-carbon scaffold sufficiently conductive to function as an electrode material? The electrical properties of pyrolysed carbon depend on many parameters, including viscoelasticity and chemical composition of the precursor polymer[20], fabrication and templation method[13], as well as pyrolysis temperature[20,31,32] and atmosphere[31]. The resistivity of the 3D-carbon scaffold was determined using a microscopic four-point probe[18] and was found to be $1.6 \pm 0.3 \times 10^{-4}$ Ωm (average ± s.e.m., n=9), which is of the same order of magnitude as previously reported for carbonised SU-8 films[32] (5-7 $\times 10^{-4}$ Ωm). This can be compared with other carbon based electrode materials, such as nitrogen doped diamond-like carbon[33] (9.4×10^{-3} Ωm), boron doped diamond[34] ($0.5\text{-}1.0 \times 10^{-3}$ Ωm), glassy carbon[35] ($1\text{-}8 \times 10^{-5}$ Ωm), and graphite[36] (basal plane: $2.5\text{-}5.0 \times 10^{-6}$ Ωm).

Dopamine electrochemistry on flat carbon and 3D-carbon scaffolds before and after oxygen plasma treatment was investigated using cyclic voltammetry (CV). Fig. 3j shows the CV for the 3D-carbon scaffold with 1.4 μm diameter pillars. The redox behaviour of dopamine is quasi-reversible before and after plasma treatment; however, both the anodic and cathodic peak current is clearly increasing after plasma treatment. Similar results are obtained for both flat carbon and 3D-carbon scaffold with 5.1 μm diameter pillars (Supplementary Information S3). The observed increase in current can be explained by two factors: (1) The optimal orientation of the electroactive OH-groups of dopamine is mediated by the increased carbonyl and carboxyl functionalities obtained at plasma treated carbon surface, thereby improving the sensitivity for dopamine in an analogous manner as described for chemically modified metal electrodes[37–39]. (2) The effect of plasma treatment on the 3D scaffolds is more substantial in terms of increased current compared to flat carbon (Supplementary Information S3). This can be attributed to an increased exposure of the pillar surface to the dopamine solution as a result of enhanced wettability. The above results demonstrate that the pyrolysed carbon scaffolds from SU8 precursor are sufficiently conductive to facilitate dopamine electrochemistry.

Is the conducting 3D-carbon scaffold suitable for monitoring dopamine exocytosis from cell populations? Confirmation of true dopaminergic phenotype of stem cell-derived neurons requires detection of the actually released dopamine in response to depolarization with e.g., elevated K^+ concentration. Single-cell studies using fluorescence detection[40] and electrophysiology[41], have revealed the mechanism of quantal neurotransmitter release – exocytosis - involving fusion of storage vesicles with cellular plasma membrane. However, only electrochemical detection allows real-time monitoring of exocytotic release of dopamine and other catecholamines. This has been demonstrated on single cells and cell populations belonging to different model cell lines (e.g. chromaffin and pheochromocytoma (PC12) cells) using either carbon fiber microelectrodes[42,43] or planar (2D) microelectrode chips[38,39,44,45].

The capabilities of the 3D-carbon scaffolds for monitoring of dopamine exocytosis from populations of growing and differentiating cells were first investigated using PC12 cells, a model cell line designed to study neuronal functions, such as catecholamine exocytosis[46] with the most abundant catecholamine being dopamine[47]. Growth (24 h) and differentiation (120 h) of PC12 cell were carried out in parallel on oxygen plasma treated and laminin modified carbon structures, having the footprint of 4 mm x 4 mm. Fig. 4a shows a typical current-time trace recorded during amperometric detection of K^+ induced dopamine exocytosis from a population of growing PC12 cells. The current represents the sum of responses related to oxidation of dopamine released from individual fusing vesicles upon membrane depolarization triggered by elevated K^+ concentration. Performed control experiments clearly show that the recorded current-time traces are due to exocytosis from a depolarised population of PC12 cells and not caused by ionic current artefacts due to fluid addition or cell movement on the carbon surfaces (Supplementary Information S4).

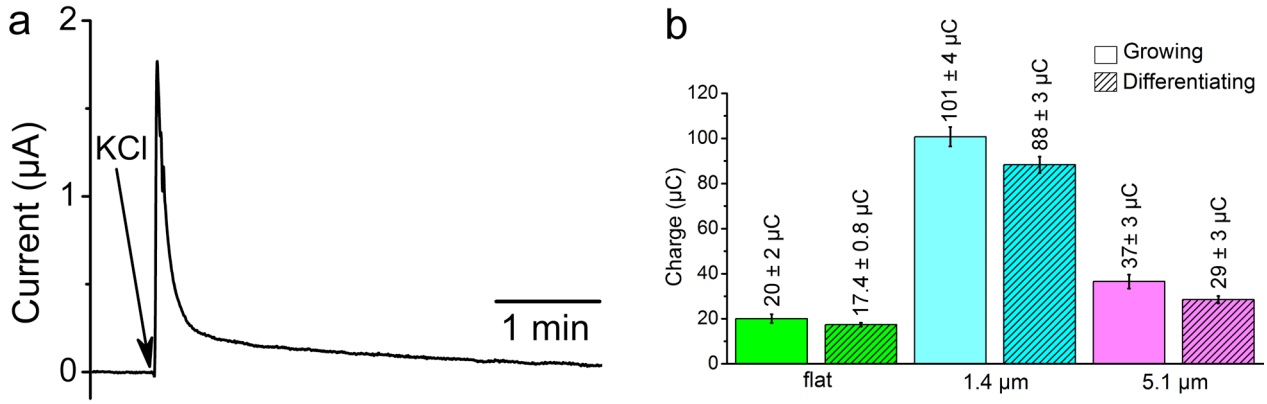

Figure 4 | Detection of dopamine release from PC12 cells on different carbon scaffold topographies. a, A characteristic current-time trace recorded during amperometric detection of dopamine released by a population of growing PC12 cells on oxygen plasma treated and laminin modified flat carbon, when the cells were depolarised by elevated K^+ concentration. Time scale bar, 1 min. The arrow indicates the time of addition of high-K^+ buffer (KCl). **b,** Calculated average charge related to the amount of detected dopamine

released by growing (24 h) and differentiating PC12 cells (120 h) on flat carbon surfaces and 3D-carbon scaffolds (1.4-µm and 5.1-µm pillars). Error bars represent the standard error of mean, n = 4 for flat carbon surfaces and n = 6 for each type of the 3D-carbon scaffold.

Similarly, as shown for current-time traces originating from single-cell exocytosis measurements[48], the amount of signalling substance (ultimately number of molecules) detected/released by a cell population can be determined by integrating the recorded current[39]. The results for populations of growing and differentiated PC12 cells on the different carbon surfaces (Fig. 4b) show two clear trends. The average charge is significantly higher for (1) 3D-carbon scaffolds than for flat carbon surfaces, 1.4-µm pillars yielding the highest charge, and (2) for growing PC12 cells compared to differentiated cells irrespective of the type of carbon surface studied.

The 3D carbon scaffolds have larger surface area compared to flat carbon (for 5.1 µm pillars and 1.4 µm pillars the increase in surface area is 1.6 and 1.9 fold, respectively, all chips having a 22 × 22 mm^2 footprint), which normally could explain the first trend, i.e., a higher electrochemical response. However, this is not valid here since the cell population on the different carbon structures had the same cell number. It is more likely that the 3D carbon scaffold serves as an efficient dopamine trap. When dopamine is released in a 3D scaffold acting as a 3D sensor, the dopamine molecules encounter the surrounding carbon pillars (Fig. 1b), leading to oxidation of a larger number of molecules than on a flat carbon surface where most of the molecules diffuse away without being detected (Fig. 1a). This effect more pronounced for the 1.4 µm than the 5.1 µm scaffold due the more densely structured scaffold, i.e., less distance between pillars, and more likelihood that a dopamine molecule will encounter a pillar and be oxidized. The second trend is in accordance with previous reports[43,49] and is due to a change in location of the exocytotic zones in differentiating PC12 cells (from the cell body to the neurite-like structures). The above results demonstrate that the pyrolysed carbon scaffolds are indeed suitable as electrodes for detection of exocytotic events, as well as a tool to discriminate biological differences between cell populations.

Does the 3D-carbon scaffold topography influence the fate of stem-derived neurons towards dopaminergic phenotype? The suitability for growth, differentiation and subsequent detection of dopaminergic phenotype of clinically relevant hNSCs was investigated using a combination of SEM, confocal fluorescence imaging (TH and nuclei) and electrochemical detection of dopamine exocytosis.

SEM images of growing hNSCs on the different carbon pillar structures in Fig. 5b-c show that the pillar topography leads to formation of elongated neurites, which are using the pillars as

effective anchoring points. These elongated neurites are not observed on flat carbon (Fig. 5a). Confocal images, on the other hand, show that the growing hNSCs (in the absence of differentiation inducing conditions) on all surfaces (Fig. 5d-f) effectively become TH-positive (75-82 %, details in Supplementary Information S5).

If we compare SEM images of growing (Figs. 5a-c) and differentiated hNSCs (Figs. 5g-i), in all cases the neurite elongation is more prominent after hNSCs have been exposed to differentiation conditions, and most significantly so for the 1.4 um pillars. Visual inspection of confocal images (Fig. 5j-l) seems to indicate that the number of TH positive cells has increased compared to growing cells (Figs. 5d-f). This can be explained by the fact that the total number of cells has increased since the proliferation of hNSCs does not completely stop during the first few days of differentiation, which is in accordance with previous studies[30]. In reality, the number of TH positive differentiated hNSCs was found not to be significantly different (72-75 %) from growing cells based on student t-test (details in Supplementary Information S5). This can be compared to 24.1 % TH positive differentiated hNSCs on TCPS (Fig. 5m). These observations show that the carbon material definitely induces dopaminergic properties whereas the topography seems to further enhance neurite formation.

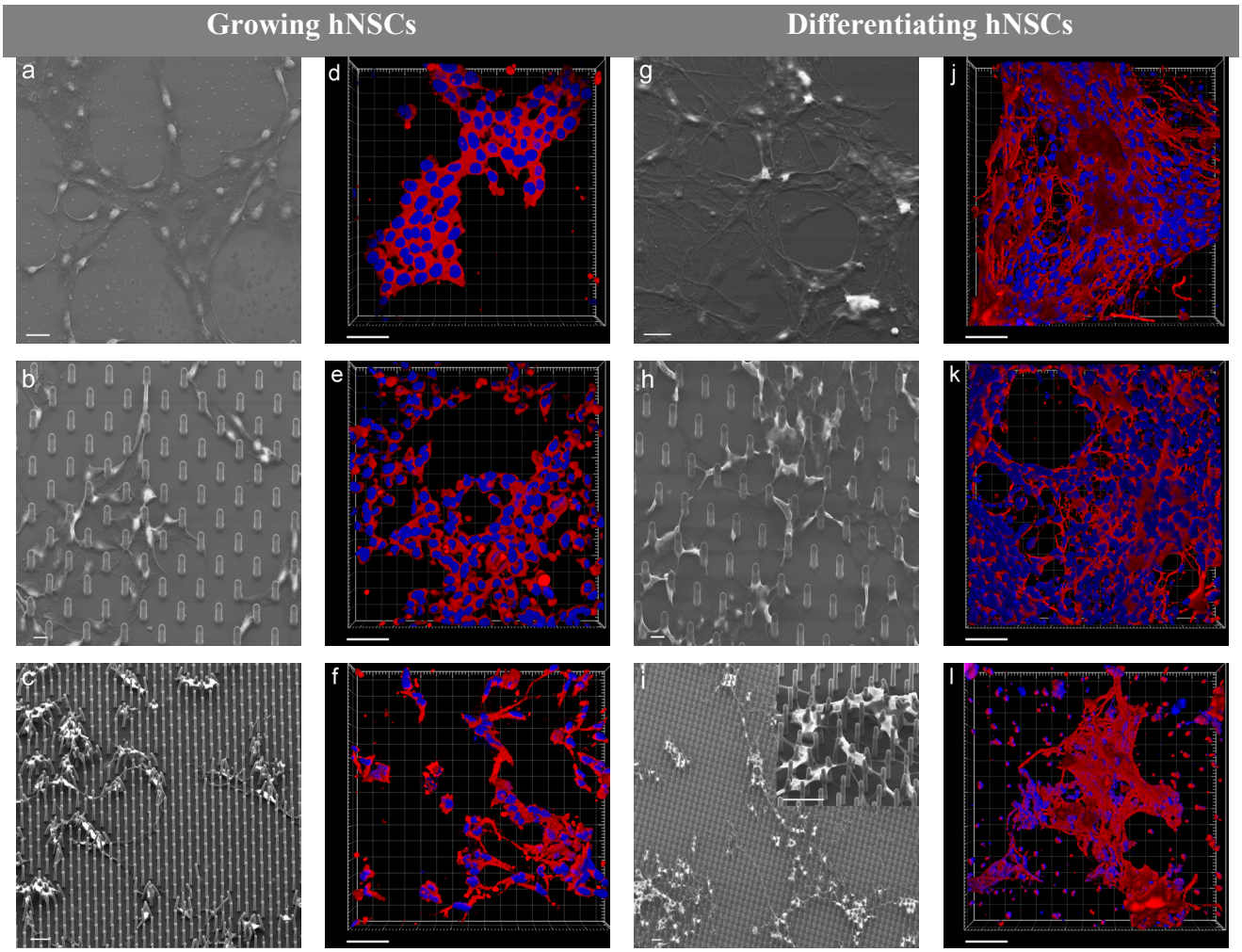

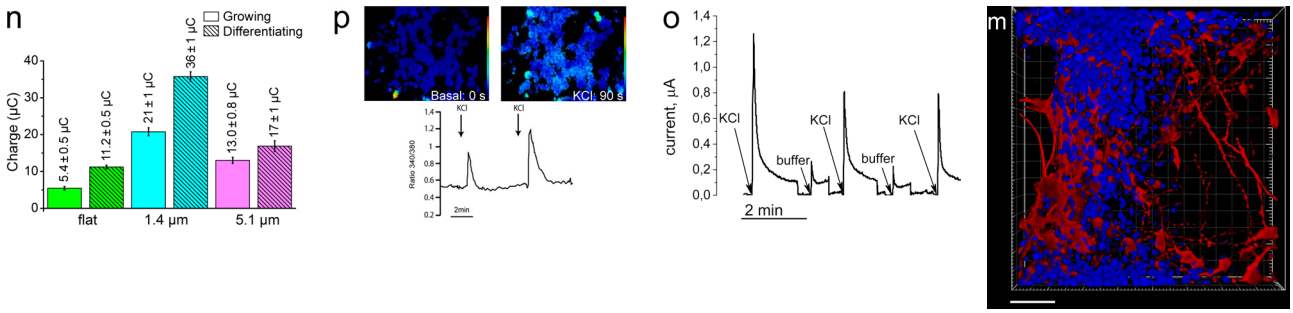

Figure 5 | Characterization of hNSCs on different carbon scaffold topographies. a-c,g-i, Representative SEM images of growing (48 h) (**a-c**) and differentiating (10 days) (**g-i**) hNSCs on flat carbon (**a,g**), 5.1-µm (**b,h**), and 1.4-µm (**c,i**) 3D-carbon scaffolds. Inset of i: magnification of hNSCs interacting with carbon pillars. Scale bars, 20 µm (**a,g**) and 10 µm (**b,c,h,i,inset of i**). **d-f,j-m** Representative confocal fluorescence images showing immunocytochemistry for tyrosine hydroxylase (TH, red) and nuclei (blue) in growing (48 h) (**d-f**) and differentiating (10 days) (**j-m**) hNSCs on flat carbon (**d,j**), 5.1-µm (**e,k**), and 1.4-µm (**f,l**) 3D-carbon scaffolds as well as on TCPS (**m**). Scale bars, 40 µm. **n,** Calculated average charge related to the amount of detected dopamine released by growing and differentiating hNSCs on flat carbon surfaces and 3D-carbon scaffolds (1.4-µm and 5.1-µm pillars). Error bars represent the standard error of mean, n = 4 for the flat carbon surfaces and n = 6 for each type of 3D-carbon scaffold. **o,** Representative confocal fluorescence images of Ca^{+} influx into differentiating hNSCs (10 days) on TCPS upon multiple K^{+}-induced depolarization steps. Time scale bar, 2 min. The arrows indicate the time of addition of high-K^{+} buffer (KCl). **p,** Characteristic current-time trace recorded during amperometric detection of dopamine from a population of differentiating hNSCs (10 days) on a flat carbon surface upon multiple K^{+}-induced depolarization steps. Time scale bar, 2 min. The arrows indicate the time of addition of high-K^{+} buffer (KCl) and low-K^{+} buffer (buffer).

What is the advantage of using conducting 3D-carbon scaffolds to study the fate of hNSC-derived neurons towards dopaminergic phenotype? The studied hNSCs produce only dopamine since they do not express the enzyme dopamine-beta-hydroxylase, which is needed for transition into the noradrenergic and adrenergic pathways[30]. Moreover, they are strictly anchorage dependent; hence, single-cell studies cannot be conducted to evaluate their dopaminergic properties. Traditionally, their capability to release dopamine, is determined by quantifying the released dopamine upon collecting samples of culture medium followed by subsequent HPLC analysis[30]. Here, we show amperometric detection of the released dopamine from depolarised growing and differentiated hNSCs (presented as the charge in Fig. 5n). To our knowledge, this is the first demonstration of electrochemical real-time detection of dopamine exocytosis from populations of stimulated hNSCs. Similarly as for the PC12 cell experiments (Fig. 4b), the results clearly demonstrate that the 1.4 um pillar structure functions as a very efficient dopamine trap. We also see that growing cells on all surfaces have clearly acquired the capability of exocytotic dopamine release even though no differentiation conditions have been applied. The apparently higher charge

obtained for differentiated hNSCs on all structures could have two explanations: (1) The most apparent reason is that the imposed differentiation conditions increase the cells' ability to exocytotically release dopamine. (2) The fact that the cells continue proliferation during the first few days of differentiation means that the total number of cells increases and thus a larger quantity of dopamine can be released. To differentiate between the significance of these two contributions, further studies will be pursued.

Mature neurons have the ability to re-establish the resting membrane potential and close the voltage-gated Ca^{2+} channels after K^{+}-induced depolarization[50], i.e. they are able to undergo repetitive depolarization. This cellular property is traditionally verified by fluorescence microscopic imaging of Ca^{2+} influx, as seen in Fig. 5o for hNSCs differentiated on the PLL-coated TCPS. However, this is a characteristic feature of all neurons undergoing exocytosis, not only dopaminergic neurons[50]. In Fig. 5p, the effect of repetitive depolarization of hNSCs differentiated on 3D-carbon scaffold is demonstrated using electrochemical detection, verifying that dopaminergic hNSCs have become mature neurons, each depolarization step, indeed, leading to dopamine release. It is clearly so that immunocytochemistry gives indirect visual information that cells are developing into dopaminergic phenotype (TH^{+}), and that Ca^{2+} imaging shows that cells have become mature neurons. However it gives no evidence of the cells' ability to exocytotically release dopamine and that the dopamine releasing cells are mature dopaminergic neurons. The combination of the 3D conductive carbon scaffold and electrochemistry makes this possible.

Collectively, this work represents a new direction in hNSC research and opens up new possibilities in stem cell research and therapy, and is to date the first report on electrochemical real time detection of dopamine exocytosis from hNSCs-derived neurons. The combination of a conducting 3D carbon scaffold and electrochemistry gives unique possibilities to enhance hNSCs differentiation into TH^{+} phenotype (material) and neurite elongation (3D topography), and at the same time enables direct confirmation of true dopaminergic phenotype and neuronal maturation (electrochemical dopamine trap).

Methods

Cell culture. Details of cell culture and differentiation protocols are given in the Supplementary Information S6.

Chemicals used in experimental work. Potassium chloride (BioXtra), sodium chloride (BioReagent), magnesium chloride hexahydrate (BioReagent), calcium chloride dehydrate (BioReagent), glucose (BioXtra), 4-(2-hydroxyethyl)piperazine-1-ethanesulfonic acid (HEPES) (1 M solution; BioReagent), 2-(3,4-dihydroxyphenyl)ethylamine hydrochloride (Dopamine),

glutaraldehyde (25 % in water, specifically purified for use as cell fixative in electron microscopy), cell culture tested phosphate buffered saline (PBS), Triton X-100 (10 % solution in water; BioUltra), formaldehyde (36 % solution in water; BioReagent), goat serum, monoclonal mouse anti-tyrosine hydroxylase antibody (anti-TH), cell culture tested water were purchased from Sigma-Aldrich Corporation (St. Louis, MO, USA). Alexa Fluor® 488 goat anti-mouse IgG antibody (anti-mouse), TO-PRO®-3 stain were from Life Technologies Ltd. (Paisley, UK).

Pyrolysis of SU-8 structures. Pyrolysis of SU-8 structures was performed using a PEO-601 open-end furnace from ATV Technologie GmbH (Vaterstetten, Germany) under a nitrogen atmosphere. The pyrolysis protocol comprised three stages: (i) Temperature was ramped from room temperature (RT) to 200 °C followed by 30-min dwelling time at 200 °C to allow for any residual oxygen to be removed from the furnace chamber (prevention of combustion during further processing at higher temperatures). (ii) Temperature was ramped from 200 °C to 900 °C followed by 1-h dwelling time at 900 °C to complete carbonization. (iii) The pyrolysed samples were allowed to cool from 900 °C down to RT. Temperature ramping during heating and cooling was done at the rate of 2 °C/min.

Preparation of electric contacts. Fabrication details of metallized electric contacts are given in the Supplementary Information S7.

Scanning Electron Microscopic (SEM) imaging. SEM imaging of the carbon structures and growing/differentiating cells was performed using a Zeiss Supra VP 40 microscope. In preparation for cell imaging, cells were fixed for 1 hour in 2% glutaraldehyde solution diluted in PBS, followed by rinsing with PBS (twice for 15 min) and cell culture tested water (twice for 5 min). Gradual dehydration of the cell samples was performed by exposing the chips with fixed cells to a series of ethanol-water solutions from 40% to 100% ethanol (absolute ethanol).

Plasma treatment. The plasma treatment was carried out using an Atto Plasma System from Diener Electronic GmbH (Ebhausen, Germany) equipped with a 13.56 MHz RF generator. The chamber was evacuated to an initial pressure below 15 Pa before introducing the process gas (O_2). After the pressure of the chamber had stabilized at 30 Pa upon introduction of O_2, the plasma was ignited. The applied power was 50W and the process time was 1 min. Immediately after plasma treatment, the carbon structures were used for either characterization or cell-based experiments.

Resistance measurements. Resistance measurements were conducted using a CAPRES microRSP-M150 system with a static contact microscopic four-point probe (M4PP). The measurements were

carried out using lock-in technique (current set-point: 200 µA; frequency: 13 Hz). Generally, all measurements showed a phase change of less than 0.2 degree indicating that the contact to the sample was good.

X-ray photoelectron spectroscopic (XPS) characterization. XPS analysis was done on a K-Alpha spectrometer (Thermo Fisher Scientific, UK) using a 400 µm wide monochromatized AlKa X-ray spot with collection of the emitted photoelectrons at a pass energy of 200 eV for survey spectra. The instrument manufacturer's Avantage software package allowed for elemental composition analysis. The XPS analysis was conducted before and immediately after plasma treatment.

Contact angle (CA) characterization. CA measurements at the carbon structures (flat surfaces and 3D-carbon scaffolds) were performed using an OCA 20 goniometer (DataPhysics, Germany) with water as the wetting agent. Static CA was measured after applying a 2-µl drop of water on the characterized surface. The CA of the water drop deposited on the carbon structures was measured before and immediately after plasma treatment. The instrument was controlled using the manufacturer's SCA-20 software package.

Characterization of dopamine electrochemistry. 5 mM dopamine solutions for cyclic voltammetric (CV) characterization were prepared immediately before use in nitrogen purged PBS (purging was started at least 20 min before preparation of the dopamine solution). The CVs were acquired using a micromilled poly(methyl methacrylate) (PMMA) chip holder (Supplementary Information 8), having a 70-µl vial for each quadrant of the silicon chip with carbon structures (Supplementary Information 7). Electric connections to the potentiostat (CHI 1030 from CH Instruments Inc., Austin TX, USA) were formed as described in the Supplementary Information (S7 and S8). An Ag/AgCl wire and a Pt wire were used as the pseudo-reference electrode and counter electrode, respectively.

Exocytosis measurements. The low-K^+ buffer contained 10 mM HEPES, 5 mM glucose, 1.2 mM Mg^{2+}, 2 mM Ca^{2+}, 150 mM Na^+, and 5 mM K^+. The high-K^+ buffer differed from the low-K+ buffer in terms of Na^+ and K^+ concentration, which were 5 mM and 450 mM, respectively. Both buffers were sterile-filtered (0.22-µm syringe filter) before use.

The open vial in the chip holder where cells were cultured/differentiated (Supplementary Information S6 and S8) facilitated the addition of the necessary buffer solutions during exocytosis measurements. Before starting exocytosis measurements, the medium was immediately replaced by

55 µL of the low-K^+ buffer to record a baseline for the measurements. Two platinum wires served as reference electrode (RE) and counter electrode (CE). The carbon working electrode (WE) was poised at 350 mV vs. the platinum RE. After a stable baseline had been recorded, exocytosis was triggered by pipetting 15 µL of the high-K^+ buffer directly into the vial to elevate the K^+ concentration to 100 mM. The current–time traces corresponding to the oxidation of the dopamine released by the cells were obtained immediately after triggering the exocytosis. Recording of the exocytotic events was done once in each quadrant of the silicon chips with carbon structures (Supplementary Information S7). Exocytosis experiments were carried out on 6 chips having 3D-carbon scaffolds and on 4 chips with flat carbon surfaces. All the amperometric recordings were performed using a CHI 1030 potentiostat at room temperature (~22 °C). All calculated results from cell-based measurements are presented ± (s.e.m.), with n being the number of carbon scaffold electrodes having cell populations subjected to exocytosis measurements.

Immunocytochemistry and confocal microscopic imaging of cells. Cells were fixed for 15 min at room temperature (RT) in 4% formaldehyde in PBS followed by rinsing with PBS (three times for 5 min). To permeabilize cell membranes and block unspecific binding of antibodies, the fixed cells were incubated at RT for 1 h in solution containing 10 % goat serum and 0.25 % Triton X-100 in PBS. After removal of the blocking solution, the cells were incubated with anti-TH primary antibody (diluted 1:1000 in PBS containing 1 % goat serum and 0.25 % Triton X-100) overnight at 4 °C followed by rinsing three times for 10 min in each rinsing solution (1° PBS containing 1 % goat serum and 0.25 % Triton X-100; 2° PBS containing 0.25 % Triton X-100; 3° PBS). Incubation with Alexa Fluor® 488 -conjugated anti-mouse secondary antibody (diluted 1:500 as described for primary antibody) was done at RT for 30 min followed by rinsing with PBS (twice for 10 min). Cell nuclei were counterstained with TO-PRO®-3 (diluted 1:1000 in PBS). Confocal laser scanning microscopy was performed using a Leica TCS SP5 microscope (Leica Microsystems, Wetzlar, Germany) equipped with a 50x/0.75 W objective. Five images were acquired from each prepared sample. A 488 nm Ar laser was used for exciting Alexa Fluor® 488, and a 633 nm HeNe laser for TOPRO®-3. All the acquired images were analysed and treated using the Imaris 7.4.2 software package (Bitplane AG, Zürich, Switzerland).

References

1. Jankovic, J. Parkinson's disease: clinical features and diagnosis. *J. Neurol. Neurosurg. Psychiatry* **79,** 368–376 (2008).

2. Ganz, J., Lev, N., Melamed, E. & Offen, D. Cell replacement therapy for Parkinson's disease: how close are we to the clinic? *Expert Rev. Neurother.* **11,** 1325–1339 (2011).

3. Carletti, E., Motta, A. & Migliaresi, C. in *3D Cell Cult. Methods Protoc.* (Haycock, J. W.) 17–39 (Humana Press Inc., 2011). doi:10.1007/978-1-60761-984-0

4. Zorlutuna, P. *et al.* Microfabricated biomaterials for engineering 3D tissues. *Adv. Mater.* **24,** 1782–1804 (2012).

5. Pampaloni, F., Reynaud, E. G. & Stelzer, E. H. K. The third dimension bridges the gap between cell culture and live tissue. *Nat. Rev. Mol. Cell Biol.* **8,** 839–845 (2007).

6. Yow, S.-Z., Lim, T. H., Yim, E. K. F., Lim, C. T. & Leong, K. W. A 3D Electroactive Polypyrrole-Collagen Fibrous Scaffold for Tissue Engineering. *Polymers (Basel).* **3,** 527–544 (2011).

7. Shin, S. R. *et al.* Carbon-Nanotube-Embedded Hydrogel Sheets for Engineering Cardiac Constructs and Bioactuators. *ACS Nano* **7,** 2369–2380 (2013).

8. Li, N. *et al.* Three-dimensional graphene foam as a biocompatible and conductive scaffold for neural stem cells. *Sci. Rep.* **3,** 1604 (6pp) (2013).

9. Lovat, V. *et al.* Carbon nanotube substrates boost neuronal electrical signaling. *Nano Lett.* **5,** 1107–1110 (2005).

10. Kam, N. W. S., Jan, E. & Kotov, N. A. Electrical stimulation of neural stem cells mediated by humanized carbon nanotube composite made with extracellular matrix protein. *Nano Lett.* **9,** 273–278 (2009).

11. Jenkins, G. M. & Kawamura, K. *Polymeric Carbons: Carbon Fibre, Glass and Char*. (Cambridge University Press, 1976).

12. Schueller, O. J. A., Brittain, S. T. & Whitesides, G. M. Fabrication of glassy carbon microstructures by pyrolysis of microfabricated polymeric precursors. *Adv. Mater.* **9,** 477–480 (1997).

13. Wang, C. & Madou, M. From MEMS to NEMS with carbon. *Biosens. Bioelectron.* **20,** 2181–2187 (2005).

14. De Volder, M. F. L. *et al.* Hierarchical Carbon Nanowire Microarchitectures Made by Plasma-Assisted Pyrolysis of Photoresist. *ACS Nano* **5,** 6593–6600 (2011).

15. Du, R., Ssenyange, S., Aktary, M. & McDermott, M. T. Fabrication and characterization of graphitic carbon nanostructures with controllable size, shape, and position. *Small* **5,** 1162–1168 (2009).

16. Xu, H. *et al.* Carbon post-microarrays for glucose sensors. *Biosens. Bioelectron.* **23,** 1637–1644 (2008).

17. Mitra, J., Jain, S., Sharma, A. & Basu, B. Patterned growth and differentiation of neural cells on polymer derived carbon substrates with micro/nano structures in vitro. *Carbon N. Y.* **65,** 140–155 (2013).

18. Amato, L. *et al.* Dense high-aspect ratio 3D interdigitated carbon pillar microelectrode arrays *To be Determ.* 1–16 (2013)

19. Mohanty, S. *et al.* Conducting pyrolysed carbon scaffold for tissue engineering. in *Proceeding 39th Int. Conf. Micro- Nano-Engineering* (2013).

20. Park, B. Y., Taherabadi, L., Wang, C., Zoval, J. & Madou, M. J. Electrical Properties and Shrinkage of Carbonized Photoresist Films and the Implications for Carbon Microelectromechanical Systems Devices in Conductive Media. *J. Electrochem. Soc.* **152,** J136–J143 (2005).

21. Georges, P. C. & Janmey, P. A. Cell type-specific response to growth on soft materials. *J. Appl. Physiol.* **98,** 1547–1553 (2005).

22. Helmus, M. N., Gibbons, D. F. & Cebon, D. Biocompatibility: meeting a key functional requirement of next-generation medical devices. *Toxicol. Pathol.* **36,** 70–80 (2008).

23. Amato, L. *et al.* Fabrication of high-aspect ratio SU-8 micropillar arrays. *Microelectron. Eng.* **98,** 483–487 (2012).

24. Alves, N. M., Pashkuleva, I., Reis, R. L. & Mano, J. F. Controlling cell behavior through the design of polymer surfaces. *Small* **6,** 2208–2220 (2010).

25. Lee, S. J., Khang, G., Lee, Y. M. & Lee, H. B. The effect of surface wettability on induction and growth of neurites from the PC-12 cell on a polymer surface. *J. Colloid Interface Sci.* **259,** 228–235 (2003).

26. Downard, A. J. Electrochemically Assisted Covalent Modification of Carbon Electrodes. *Electroanalysis* **12,** 1085–1096 (2000).

27. Hirabayashi, M., Mehta, B., Khosla, A. & Kassegne, S. Functionalization of Pyrolyzed Carbon Micro Structures for Bio-nanoelectronics Platforms. *ECS Trans.* **50,** 325–331 (2012).

28. Khorasani, M. T., Mirzadeh, H. & Irani, S. Plasma surface modification of poly (l-lactic acid) and poly (lactic-co-glycolic acid) films for improvement of nerve cells adhesion. *Radiat. Phys. Chem.* **77,** 280–287 (2008).

29. Yan, Y. Y., Gao, N. & Barthlott, W. Mimicking natural superhydrophobic surfaces and grasping the wetting process: a review on recent progress in preparing superhydrophobic surfaces. *Adv. Colloid Interface Sci.* **169,** 80–105 (2011).

30. Krabbe, C. *et al.* Enhanced dopaminergic differentiation of human neural stem cells by synergistic effect of Bcl-xL and reduced oxygen tension. *J. Neurochem.* **110,** 1908–20 (2009).

31. Ranganathan, S., McCreery, R., Majji, S. M. & Madou, M. Photoresist-Derived Carbon for Microelectromechanical Systems and Electrochemical Applications. *J. Electrochem. Soc.* **147,** 277 (2000).

32. Singh, A., Jayaram, J., Madou, M. & Akbar, S. Pyrolysis of Negative Photoresists to Fabricate Carbon Structures for Microelectromechanical Systems and Electrochemical Applications. *J. Electrochem. Soc.* **149,** E78 (2002).

33. Gao, Y., Chen, X., Gupta, S., Gillis, K. D. & Gangopadhyay, S. Magnetron sputtered diamond-like carbon microelectrodes for on-chip measurement of quantal catecholamine release from cells. *Biomed. Microdevices* **10,** 623–9 (2008).

34. Fryda, M. *et al.* Fabrication and application of Diachem electrodes. *Diam. Relat. Mater.* **12,** 1950–1956 (2003).

35. Kaufman, A. B. Electrical characteristics of vitreous vs common carbons. *Appl. Phys. Lett.* **21,** 231 (1972).

36. Pierson, H. O. *Handbook of Carbon, Graphite, Diamond and Fullerenes*. Ch. 3 (Noyes Publications, 1993).

37. Dalmia, A., Liu, C. C. & Savinell, R. F. Electrochemical behavior of gold electrodes modified with self-assembled monolayers with an acidic end group for selective detection of dopamme. *J. Electroanal. Chem.* **430,** 205–214 (1997).

38. Spégel, C. *et al.* On-Chip Determination of Dopamine Exocytosis Using Mercaptopropionic Acid Modified Microelectrodes. *Electroanalysis* **19,** 263–271 (2007).

39. Sasso, L. *et al.* Doped overoxidized polypyrrole microelectrodes as sensors for the detection of dopamine released from cell populations. *Analyst* **138,** 3651–3659 (2013).

40. Gandhi, S. P. & Stevens, C. F. Three modes of synaptic vesicular recycling revealed by single-vesicle imaging. *Nature* **423,** 607–613 (2003).

41. Neher, E. & Marty, A. Discrete changes of cell membrane capacitance observed under conditions of conditions of enhanced secretion in bovine adrenal chromaffin cells. *Proc. Natl. Acad. Sci. U. S. A.* **79,** 6712–6716 (1982).

42. Wightman, R. M. *et al.* Temporally resolved catecholamine spikes correspond to single vesicle release from individual chromaffin cells. *Proc. Natl. Acad. Sci. U. S. A.* **88,** 10754–10758 (1991).

43. Zerby, S. & Ewing, A. G. Electrochemical monitoring of individual exocytotic events from the varicosities of differentiated PC12 cells. *Brain Res.* **712,** 1–10 (1996).

44. Dias, A. F. *et al.* An electrochemical detector array to study cell biology on the nanoscale. *Nanotechnology* **13,** 285–289 (2002).

45. Liu, X. *et al.* A microwell device for targeting single cells to electrochemical microelectrodes for high-throughput amperometric detection of quantal exocytosis. *Anal. Chem.* **83,** 2445–2451 (2011).

46. Westerink, R.H.; Ewing, A. G. The PC12 cell as model for neurosecretion. *Acta Physiol.* **192,** 273–285 (2008).

47. Koike, T. & Takashima, A. Clonal Variability of PC12 Pheochromocytoma Cells with Respect to Catecholamine Biosynthesis. *J. Neurochem.* **42,** 1472–1475 (1984).

48. Amatore, C., Arbault, S., Guille, M. & Lemaître, F. Electrochemical Monitoring of Single Cell Secretion: Vesicular Exocytosis and Oxidative Stress. *Chem. Rev.* **108,** 2585–2621 (2008).

49. Greene, L. A. & Rein, G. Release, Storage and Uptake of Catecholamines by a Clonal Cell Line of Nerve Growth Factor (NGF) Responsive Pheochromocytoma Cells. *Brain Res.* **129,** 247–263 (1977).

50. Tønnesen, J. *et al.* Functional properties of the human ventral mesencephalic neural stem cell line hVM1. *Exp. Neurol.* **223,** 653–656 (2010).

Acknowledgments

A.H. acknowledges Ørsted postdoctoral fellowship and Lundbeck Foundation (R69-A6408) for financial support. Nanna Bild from DTU Nanotech is acknowledged for the artwork in Fig. 1.

A.M.S. acknowledges financial support from EU (NMP-SL-2008-214706, EXCELL), MINECO (PLE2009-0101 and SAF2010-17167), TerCel (RD12/0019/0013), Neurostem-CM (S2010-BMD-2336), and institutional grant from Fundación Ramón Areces to the CBMSO.

Author contributions

L.A., A.H., A.B., S.K. and J.E. designed the fabrication and characterization; L.A., A.H., A.M.S. and J.E. designed the biological application; T.R.M. and A.M.S. provided the stem cell line for the biological application; M.M. introduced L.A. to pyrolysis of SU-8, L.A. performed the work under supervision of A.H., A.B., S.K. and J.E. with some contribution in the biological experiments from C.C., F.S., E.G.S., and M.R., electrochemical experiments from A.H. and K.Z., and confocal microscopy from M.S.; L.A. analysed the data with some contribution from A.H., K.Z., T.R.M, A.M.S. and J.E. L.A., A.H. and J.E. wrote the paper.

Additional information

Supplementary Information is available in the online version of the paper. Reprints and permissions information is available online at www.nature.com/reprints. Correspondence and requests for materials should be addressed to J.E.

Competing financial interests

The authors declare no competing financial interests.

SUPPLEMENTARY INFORMATION

Conducting 3D-carbon scaffolds for enhanced differentiation of neural stem cells and dopamine detection

Letizia Amato[1], Arto Heiskanen[1], Claudia Caviglia[1], Fozia Shah[1], Kinga Zór[1], Maciej Skolimowski[1,#], Marc Madou[2], Lauge Gammelgaard[3], Rasmus Jul Hansen[1], Emma G. Seiz[4], Milagros Ramos[4],Tania Ramos Moreno[4,§], Alberto Martínez-Serrano[4], Anja Boisen[1], Stephan Keller[1], Jenny Emnéus[1,]*

[1]Technical University of Denmark, Department of Micro- and Nanotechnology (DTU Nanotech), Produktionstorvet 423, DK-2800 Kgs. Lyngby, Denmark

[2]Department of Mechanical & Aerospace Engineering, University of California, Irvine, California 92697, USA

[3]Capres A/S, Diplomvej 373, DK-2800 Kgs. Lyngby, Denmark

[4]Departmento de Biología Molecular and Centro de Biología Molecular "Severo Ochoa" (CBMSO), Universidad Autónoma de Madrid – C.S.I.C., Cantoblanco, 28049-Madrid, Spain

Corresponding author

*Prof. Jenny Emnéus, Technical University of Denmark, Department of Micro- and Nanotechnology, Produktionstorvet 423, DK-2800 Kgs. Lyngby, Denmark, Phone: +45-45-256 867, Fax: +45-45, e-mail: jenny.emneus@nanotech.dtu.dk.

Present address

[#]University of Groningen, Department of Pharmacy, Antonius Deusinglaan 1, Postbus 196, 9700 AD Groningen, The Netherlands

[§]Lund University, Wallenberg Neurocentrum, BMC, Sölvegatan 17, SE-22100 Lund, Sweden

Content

S-1 Schematic overview of 3D-carbon scaffold fabrication

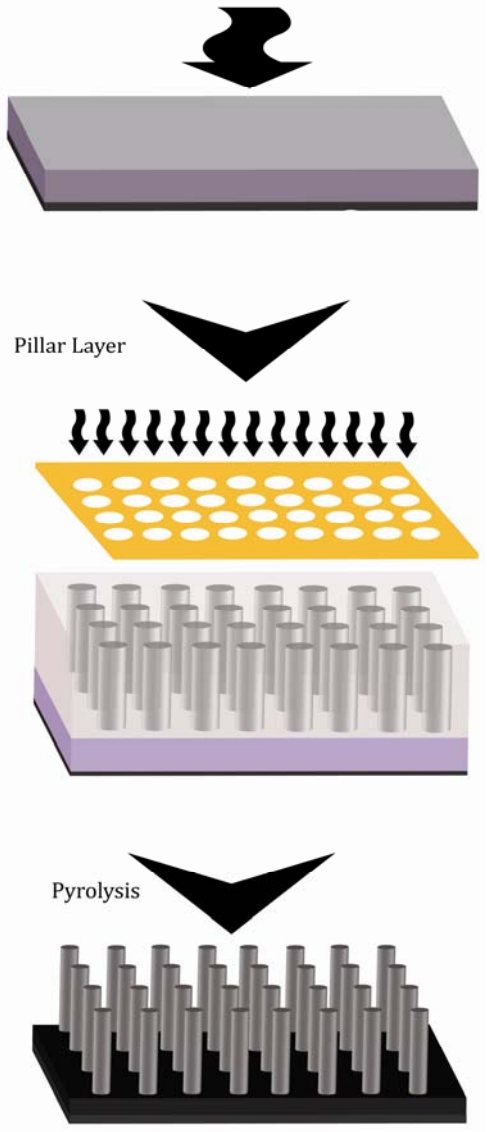

Figure S1 | Schematic view of 3D-carbon scaffold fabrication. An underlying SU-8 layer undergoes UV exposure (flood exposure). A second SU-8 layer is deposited and patterned using a lithographic mask. After subsequent development, baking, and critical point drying (CO_2) the 3D-SU8 scaffold is pyrolysed to obtain the final 3D-carbon scaffold.

S-2 Atomic Force Microscopic (AFM) characterization of pyrolysed carbon surfaces

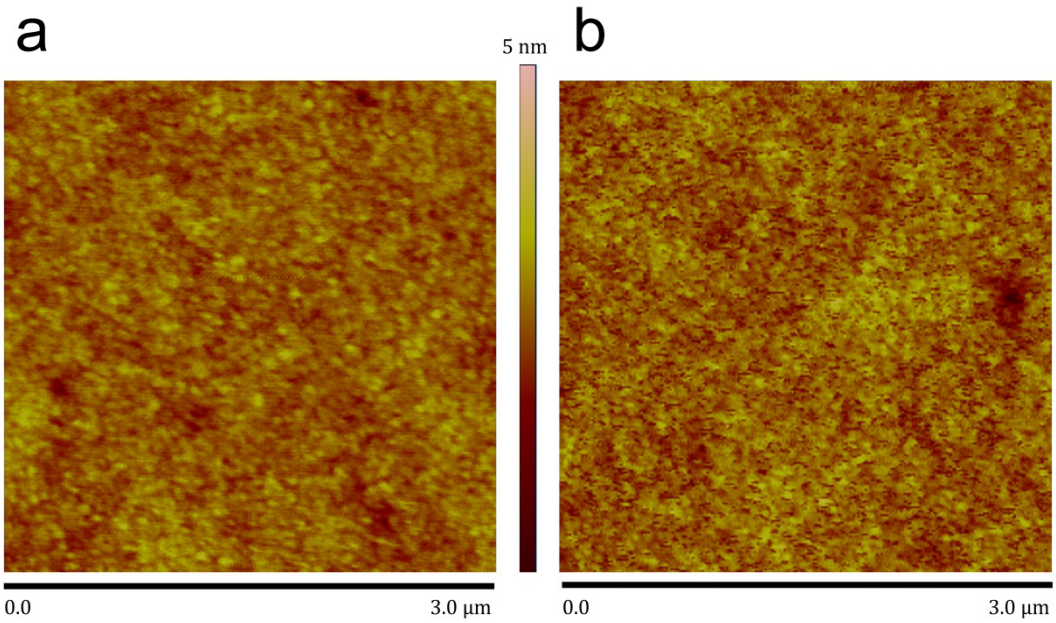

Figure S2 | Effect of O_2 plasma treatment on surface roughness. Representative Atomic Force Microscopic (AFM) images of **a,** untreated and **b,** O_2 plasma treated flat pyrolysed carbon surface (3 µm x 3 µm).

AFM characterization was performed using a Dimension 3100 system from Bruker AXS GmbH (Karlsruhe, Germany). The instrument was equipped with a silicon tip. The images were acquired using tapping mode by scanning 3 µm x 3 µm areas. The obtained results revealed that untreated pyrolysed carbon surfaces had a relatively smooth and uniform structure free of cracks (**Fig. S3a**). Statistical analysis of this surface showed a root-mean square (rms) roughness of 2.1 Å over an area of 3 × 3 µm. This structure is typical of carbon films obtained by pyrolysis at 700 °C–1000 °C in an inert atmosphere[1] and comparable to pyrolytic graphite surfaces having rms surface roughness of 2.4 Å[2]. The oxygen plasma treated surfaces (**Fig. S3b**) featured a rms roughness of 3.9 Å, increases the surface roughness. Generally, rms surface roughness of untreated pyrolysed carbon surfaces has been shown to be below 5 Å[1]. This indicates that despite the increased surface roughness as a consequence of O_2 plasma treatment the determined rms value is, nevertheless, in the range reported for untreated surfaces. Other surface treatments, such as mechanical polishing of glassy carbon, increase surface roughness more significantly resulting in rms value of 20.4[2].

S-3 Dopamine electrochemistry on pyrolysed carbon structures

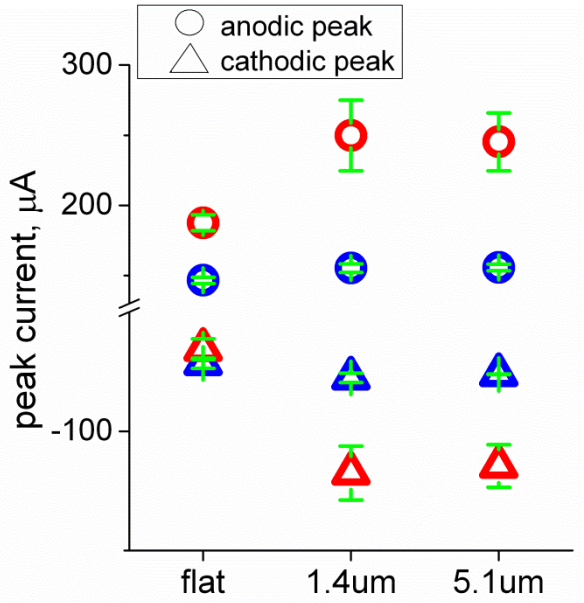

Figure S3 | Effect of O_2 plasma treatment on dopamine electrochemistry. Comparison of anodic and cathodic peak current derived from recorded cyclic voltammograms (CV) of dopamine (5 mM in PBS) on pyrolysed carbon surfaces (flat) and 3D-carbon scaffolds with 1.4-µm and 5.1-µm pillars before (blue) and after O_2 plasma treatment (red). Error bars represent s.d., n=2.

The obtained results lead to two significant conclusions on the effect of O_2 plasma treatment on dopamine electrocheistry: (1) The anodic peak current increases significantly on all carbon structures, i.e. both flat carbon surfaces and 3D-carbon scaffolds. (2) A significant increase in cathodic peak current is observed only in the case of 3D-carbon scaffolds.

Since the entire area of flat carbon surfaces is accessible to the introduced electrolyte and dissolved dopamine, the increased anodic peak current after O_2 plasma treatment can be explained by the influence of the formed oxygen functionalities, such as carbonyl and carboxylic groups. In the case of chemical modification of gold electrodes (carboxylic acid functionalized thiol self-assembled monolayers (SAM)[3,4] and overoxidized polypyrrole[5]), these functionalities have been shown to enhance the anodic peak current. This effect has been attributed to hydrogen bond –mediated orientation of the catechol moiety of dopamine. Especially in the studies focusing on the thiol SAMs[3,4], the effect of the modification on the cathodic peak current was not pronounced.

Based on the fabrication process of 3D-carbon scaffolds (**Fig. S1**), these comprise both an underlying carbon layer and vertically aligned carbon pillars. Pyrolysed carbon structures are inherently hydrophobic. In the case of 3D-carbon scaffolds, this can lead to limited wetting of

the interpillar space close to the flat underlying carbon layer, due to which dopamine electrochemistry does not take place on the entire geometric area of the scaffolds. The O_2 plasma treatment-induced increase in the surface density of oxygen functionalities can improve wetting. Hence, both anodic and cathodic peak current can increase due to the increased accessible electrode area. **Table S3** shows a statistical comparison of the increase in anodic and cathodic peak current as a consequence of O_2plasma treatmnet. This indicates that the increase in the anodic peak current on the 3D-carbon scaffolds (1.4-µm pillars and 5.1-µm pillars) is significantly higher than the observed increase in the cathodic peak current (one-tailed student's t-test, 90 % confidence level). This significantly more increased anodic peak current can be explained by the simultaneous effect of oxygen functionalities on oxidation of dopamine, as presented above for flat carbon surfaces.

Table S3. Comparison of O_2 plasma-induced increase in anodic (i_a) and cathodic (i_c) peak current of dopamine CVs on different 3D-carbon scaffolds.

3D-carbon scaffold	Increase in peak current		Student's t-test (one-tailed[2])
	Δi_a (µA)[1]	Δi_a (µA)[1]	p (90 % confidence level)
1.4-µm pillars	94 ± 25	40 ± 11	0.0547
5.1-µm pillars	89 ± 21	38 ± 9	0.0428

[1] Presented as average ± s.d., n = 2.
[2] One-tailed t-test was applied based on the assumption that in all cases $\Delta i_a > \Delta i_c$.

S-4 Control experiments: amperometric current-time traces

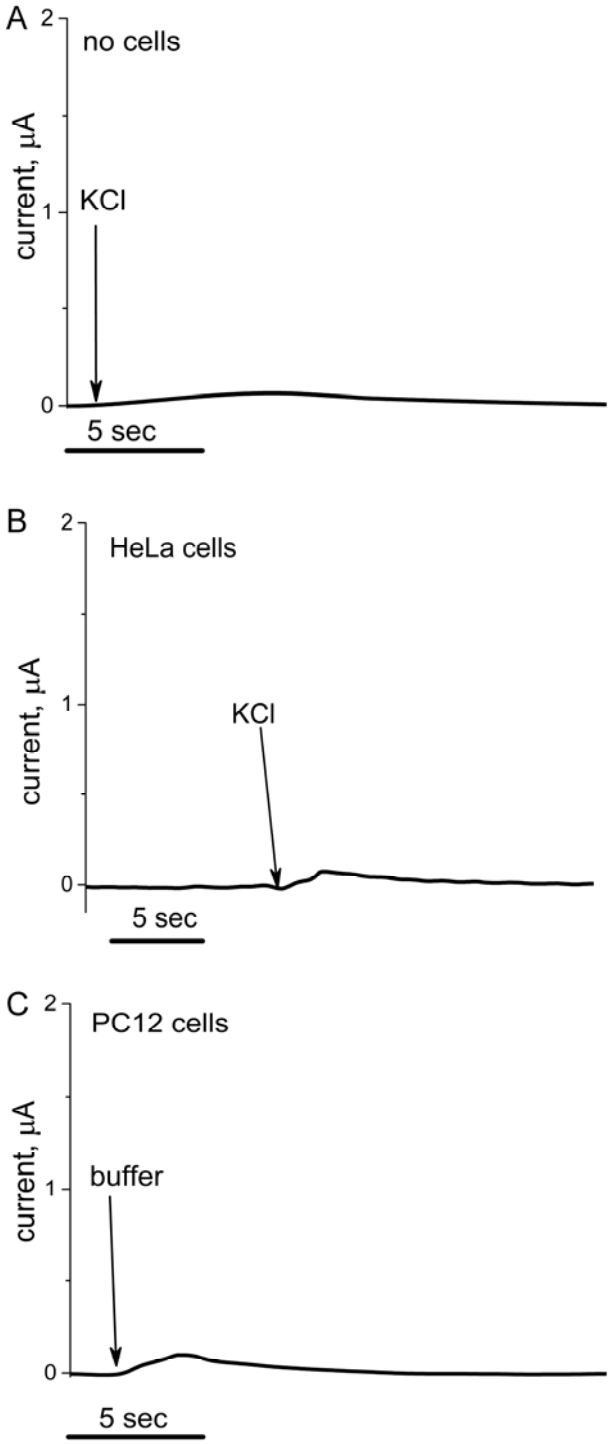

Figure S4 | Influence of fluid handling and the presence of cells on recorded current-time trances. Representative current-time traces showing the effect of **a,b,** addition of high-K^+ buffer to a carbon electrode without cells (**a**) and in the presence of HeLa cells (**b**), which are not dopamine releasing, and **c,** addition of low-K^+ buffer to a carbon electrode in the presence of PC12 cells.

When conducting electrochemical measurements by making transient addition of buffer directly to an electrode surface, there is a possibility that a significant part of the recorded current is due to movement of ions. Furthermore, if the electrode surface is covered by cells, the additional possibility is that movement of cells due to fluid addition can perturb the electrode-electrolyte interface contributing to the recorded current. The results of the three control experiments presented in **Fig. S4a-c** lead to the following significant conclusions: (1) Addition of high-K^+ buffer used to depolarize cells to trigger exocytosis does not cause a current response which can affect exocytosis measurements in the presence of dopamine releasing cells. (2) The addition of high-K^+ buffer to an electrode surface having non-dopaminergic HeLa cells does not significantly perturb the electrode-electrolyte interface, which could obscure exocytosis measurements. Moreover, the result also indicates that the addition of high-K^+ buffer does not cause any other cellular responses, which could result in a significant current response. (3) Dopaminergic PC12 cells do not generate a significant current response only due to addition of a buffer (low-K^+ buffer). Hence, current responses recorded in the presence of PC12 cells upon addition of high-K^+ buffer are due to oxidation of the released dopamine.

S-5 Statistical analysis of TH-positive (TH^+) hNSCs on different substrates

Table S6-1. Percentage of TH^+ hNSCs in populations of growing and differentiating cells on tissue culture polystyrene (TCPS) and pyrolysed carbon structures (flat carbon and 3D-carbon scaffolds with 1.4-µm and 5.1-µm pillars).

Substrate material	Growing hNSCs[1] (% of population ± s.d.)	Differentiation hNSCs[2] (% of population ± s.d.)
TCPS	2.5 ± 0.6	24 ± 2
Flat carbon	75 ± 9	74 ± 9
3D-carbon scaffold 1.4-µm pillars	82 ± 7	75 ± 14
3D-carbon scaffold 5.1-µm pillars	80 ± 8	73 ± 9

[1] The cells were allowed to grow for 48 h prior to analysis.
[2] The cells were allowed grow for 48 h, after which the differentiation conditions were induced by change of medium. Differentiation conditions were maintained for 10 days prior to analysis.

The obtained results (**Table S6-1**) show clearly that the percentage of TH^+ cells is higher on all the carbon structures in comparison with populations grown and differentiated on TCPS. Based on preliminary inspection of the percentages on the different carbon structures, the obtained values are clearly very close to each other. To evaluate whether there is any significant difference between the populations, growing cells on flat carbon surfaces were chosen as the control for comparison, which was performed using two-tailed student's t-test. Each population average was compared to the one obtained for growing cells on flat carbon surfaces. Furthermore, based on performed F-test, the variances of each population in comparison with the ones growing on flat carbon surfaces were shown to be equal, due to which the performed t-test in each case was homoscedastic.

The performed t-test for each population indicated that with 95 % confidence level none of the average percentages of TH^+ cells significantly differed from the value obtained for the populations of growing cells on flat carbon surfaces. The obtained t-test results are shown in **Table S6-2**. Each of the probabilities is > 0.05.

Table S6-2. Student's t-test for comparison of the average percentage of TH^+ positive (growing or differentiating) hNSCs with the average obtained for growing cells on flat carbon surfaces.

Substrate material	Growing hNSCs (p, 95 % confidence level)	Differentiation hNSCs (p, 95 % confidence level)
Flat carbon	N/A	0.835
3D-carbon scaffold 1.4-µm pillars	0.232	0.982
3D-carbon scaffold 5.1-µm pillars	0.393	0.694

S-6 Protocols of cell culture and differentiation

Culturing and differentiation of PC12 cells. Rat pheochromocytoma (PC12) cells were purchased from Deutsche Sammlung von Mikroorganismen und Zellkulturen GmbH (Braunschweig, Germany). Dulbecco's Modified Eagle Medium/Nutrient Mixture F-12 (DMEM/F12), Trypsin-EDTA (0.05 %) and penicillin/streptomycin (P/S) were purchased from Life Technologies Ltd. (Paisley, UK). All other cell culture reagents were from Sigma-Aldrich Corporation (St. Louis, MO, USA).

The passage number of PC12 cells was below 14 in all experiments. Subculturing was done in polyethylenimine (PEI: branched, average Mw ~25,000 kDa, 50 μg/ml, 2 – 3 h) coated T25 culture flasks (Nunc A/S, Roskilde, Denmark) using DMEM/F12 supplemented with 15 % horse serum (HS), 2.5 % fetal bovine serum (FBS), 1 % P/S, and 5 mM 4-(2-hydroxyethyl)piperazine-1-ethanesulfonic acid (HEPES). In the differentiation medium, the serum contents was lowered (0.5% HS and 0.5% FBS). 100 ng/ml of nerve growth factor from rat (NGF-β) was added to induce differentiation. All cell preparations were maintained in a humidified incubator 5 % CO_2 / 95 % air) at 37 °C. For the experiments with differentiated PC12 cells, 24 hours prior to seeding the cells onto an electrode chip, the cellular response to NGF-β was initiated by changing the growth medium for the differentiation medium.

Before preparation of the silicon chips with carbon structures (Supplementary Information S7) for cell-based experiments, they were treated with O_2 plasma. The chips and chip holders (Supplementary Information S8) were sterilized by immersion in 96 % ethanol (10 min) and 0.5 M NaOH (30 min), respectively, followed by rinsing with PBS trice. After sterilization, the chips were coated with laminin (20 mg/ml, 2 – 3 h), diluted in cell culture tested phosphate buffered saline (PBS) to promote cellular adhesion. PC12 cell suspensions for seeding onto the electrode chips were prepared by first washing the cells with PBS followed by 5 minutes incubation with trypsin-EDTA. Trypsinization was terminated by addition of an excess of culture medium. Cells were centrifuged for 5 min at 900 rpm at 20 °C and resuspended in culture medium. Cell density was determined using a standard hemocytometer and cells were seeded onto the coated electrode chips at a surface density of 1.5×10^5 cells per cm^2.

For growing and differentiating cells the measurements were performed 1 and 5 days after seeding respectively. In order to increase the dopamine load in the vesicles[6], 1 hour before

the measurements the cells on the chips were incubated with fresh medium containing 100 μM of L-DOPA.

Culturing and differentiation of human neural stem cells (hNSCs). The immortalized human Ventral Mesencephalic cell line overexpressing Bcl-XL (hVM-Bcl-XL) was cultured as described elsewhere[7]. AlbuMAX-I and N_2 supplement were purchased from Life Technologies Ltd. (Paisley, UK), recombinant human epidermal growth factor (EGF) and fibroblast growth factor (FGF) were from R&D Systems Europe, Ltd. (Abingdon, UK), and glial cell line-derived neurotrophic factor (GDNF) was from PeproTech EC Ltd. (London, UK). All other cell culture reagents were purchased as mentioned above for PC12 cells or from Sigma-Aldrich Corporation (St. Louis, MO, USA).

Cells from passages 41 to 46 were cultured on poly-L-lysine (PLL: Mw ~70,000 kDa, 10 μg/mL, 2 – 3 h) coated T25 culture flasks (Nunc A/S, Roskilde, Denmark) using proliferation medium DMEM/F12 containing 0.5 % (w/v) AlbuMAX-I, 5mM HEPES, 0.6 % (w/v) glucose, 1 % (v/v) N_2 supplement, 1 % (v/v) non-essential amino acids (stock solution: 40 mM L-alanine, L-asparagine, L-aspartic acid, L-glutamic acid, and L-proline), 1 % P/S, 20 ng/ml EGF and FGF. To induce differentiation of the cells, EGF and FGF in the proliferation medium were replaced by 2 ng/ml of GDNF and 1 μM of dibutyryl-cAMP (differentiation medium). All cell preparations were maintained in a humidified incubator 5 % CO_2 / 95 % air) at 37 °C.

Preparation of the silicon chips with carbon structures was done as described above for PC12 cells unless a specific deviation from general procedure was necessary as described in the results and discussion. The chips were coated with PLL (10 μg/ml, 2 – 3 h). Cells were seeded at the density of 30,000 cells/cm^2 in proliferation medium on the PLL coated chips and polystyrene multi-well plates (Nunc A/S). After 48-hour growth period the proliferation medium was removed and replaced by differentiation medium. Differentiation medium was changed every second day until cells had differentiated for 10 days.

S-7 Preparation of gold coated electric contacts for pyrolysed carbon

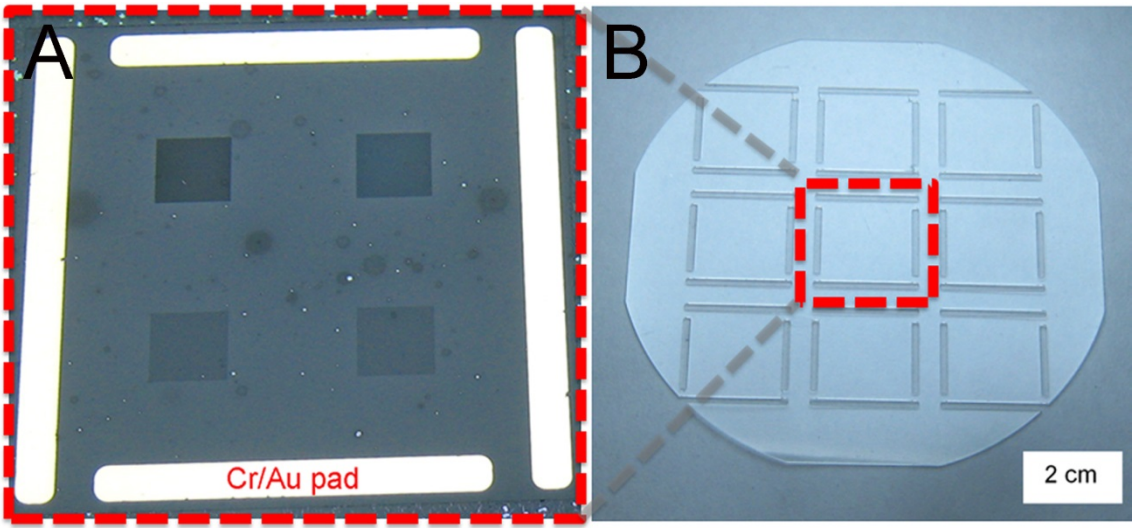

Figure S8 | Preparation of gold contact pads for electrode chips with pyrolysed carbon structures. a-b, Photograph of a chip with four contact pads (**a**) and a shadow mask (**b**) used to pattern the contact pads.

The prepared contact pads (**Fig. S8a**) (width: 1.5 mm) having 20 nm of chromium as an adhesion metal layer and 200 nm of gold were prepared by interfacing a 4-inch silicon wafer with pyrolysed carbon structures to a micromilled shadow mask made of 1-mm poly(methyl methacrylate) (PMMA) (**Fig. S8b**). The lower surface of the PMMA shadow mask was micromilled in such a way that 30-µm spacing was formed on the above of the wafer to avoid scratching of the carbon surface. Metal deposition was done using e-beam evaporation (QCL 800, Wordentec Ltd., United Kingdom). After deposition of the metals, the individual chips (22 mm x 22 mm) were obtained by manual scribing. Each chip (**Fig. S8a**) has a continuous pyrolysed carbon surface (light gray) and in the case of 3D-carbon scaffolds four quadrants (each having the footprint of 4 mm x 4 mm; dark gray) with defined pillar structures (dimensions determined by pyrolysis of the lithographically defined SU-8 pillars). The dimension of each quadrant with pillar structures is 4 mm x 4 mm.

S-8 Setup for cell culturing/differentiation and electrochemical exocytosis measurements

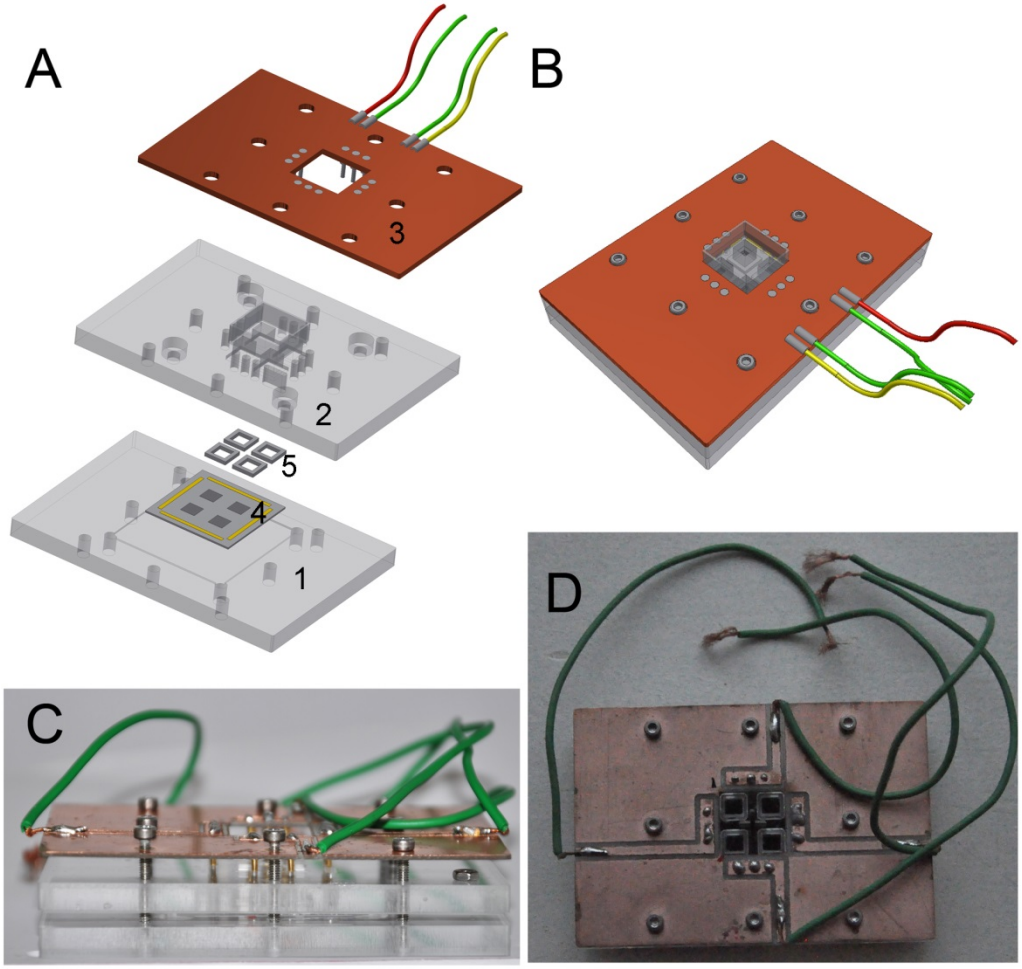

Figure S9-1 | Setup for cell handling and electrochemical exocytosis measurements. a-b, A schematic view of the setup components (**a**) and an assembled setup (**b**). **c-d,** Photos of the setup viewed from side (**c**) and above (**d**).

The setup for cell culturing/differentiation and electrochemical exocytosis measurements comprises three micromilled components (**Fig. S9-1a**): (**1**) A bottom, (**2**) an upper part with four vials (volume 70 µl), and (**3**) a circuit board for electric contacts. The bottom and upper part are made of 5 mm thick poly(methyl methacrylate) (PMMA). The bottom has an indentation for placement of a chip with pyrolysed carbon structures (**4 in Fig. S9-1a; Fig. S8a**). The vials of the upper part, one for each quadrant of the chip (4), are tightened on the using tailor-made square-shaped polydimethyl siloxane (PDMS) gaskets (thickness: 1 mm; width 1 mm; inner opening 4 mm x 4mm) (5). The circuit board has soldered spring loaded pins (Mill-Max Mfg. Corp., Oyster Bay, NY, USA) to form electric contact to the gold

contact pads of the chip. Each quadrant of the chip has three pins. The components of the setup are assembled together using 2-mm screws (**Fig. S9-1b-d**). **Fig. S9-1c** shows the three components of the setup and the assembly screws and spring loaded pins. **Fig. S9-1d** shows the leads (defined by micromilling) interfacing the spring loaded pins to the contact wires.

References

1. Brooksby, P. A. & Downard, A. J. Electrochemical and atomic force microscopy study of carbon surface modification via diazonium reduction in aqueous and acetonitrile solutions. *Langmuir* **20,** 5038–5045 (2004).

2. Mcdermott, M. T., Mcdermott, C. A. & Mccreery, R. L. Scanning tunneling microscopy of carbon surfaces: relationships between electrode kinetics , capacitance , and morphology for glassy carbon electrodes. *Analytical Chemistry* **65,** 937–944 (1993).

3. Dalmia, A., Liu, C. C. & Savinell, R. F. Electrochemical behavior of gold electrodes modified with self-assembled monolayers with an acidic end group for selective detection of dopamme. *Journal of Electroanalytical Chemistry* **430,** 205–214 (1997).

4. Spégel, C. *et al.* On-chip determination of dopamine exocytosis using mercaptopropionic acid modified microelectrodes. *Electroanalysis* **19,** 263–271 (2007).

5. Sasso, L. *et al.* Doped overoxidized polypyrrole microelectrodes as sensors for the detection of dopamine released from cell populations. *Analyst* **138,** 3651–3659 (2013).

6. Sombers, L. a, Maxson, M. M. & Ewing, a G. Loaded dopamine is preferentially stored in the halo portion of PC12 cell dense core vesicles. *Journal of neurochemistry* **93,** 1122–31 (2005).

7. Villa, A. *et al.* Generation and properties of a new human ventral mesencephalic neural stem cell line. *Experimental Cell Research* **315,** 1860–74 (2009).